

HZDR-119

ANNUAL REPORT 2021

Institute of Resource Ecology



Wissenschaftlich-Technische Berichte
HZDR-119 2022 . ISSN 2191-8708

HZDR
HELMHOLTZ ZENTRUM
DRESDEN ROSSENDORF

Wissenschaftlich-Technische Berichte
HZDR-119

Annual Report 2021

Institute of Resource Ecology

Editorial board:

Prof. Dr. Thorsten Stumpf

Dr. Harald Foerstendorf

Dr. Frank Bok

Dr. Anke Richter

HZDR

 **HELMHOLTZ**
ZENTRUM DRESDEN
ROSSENDORF

Impressum

Print edition: ISSN 2191-8708

Electronic edition: ISSN 2191-8716

The electronic edition is published under Creative Commons License (CC BY-NC-ND):

<https://www.hzdr.de/publications/Publ-34219>

<https://nbn-resolving.org/urn:nbn:de:bsz:d120-qucosa2-778408>

Published by Helmholtz-Zentrum Dresden–Rossendorf e.V.

Contact

Helmholtz-Zentrum Dresden–Rossendorf e.V.

Institute of Resource Ecology

Bautzner Landstraße 400

D-01328 Dresden

Germany

Phone: +49 (0) 351 260 3210

Fax: +49 (0) 351 260 3553

e-mail: contact.resourceecology@hzdr.de

<https://www.hzdr.de/fwo>

This report is also available at <https://www.hzdr.de/fwo>

Cover picture

The Institute of Resource Ecology now operates a Bruker Biospin ELEXSYS E50 Electron Paramagnetic Resonance (EPR) spectrometer in a radiochemistry laboratory. The device, equipped with an Oxford Instruments Mercury iTC He cryostat, supplements the spectrum of spectroscopic techniques at the institute. Radioactive samples can be investigated in solid or liquid state of aggregation. This precious tool will promote the characterization of actinide compounds. Particularly, the unequivocal identification oxidation and spin states of heavy metal ions is possible, allowing for a better understanding of the chemical reactivity of and molecular structures formed by actinide and transactinide ions.

Cover created by WERKSTATT X. Michael Voigt (www.werkstatt-x.de); pictures provided by B. Drobot and J. Kretzschmar.

Preface

THE INSTITUTE OF RESOURCE ECOLOGY (IRE) IS ONE OF the eight institutes of the Helmholtz-Zentrum Dresden-Rossendorf (HZDR). Our research activities are mainly integrated into the program “Nuclear Waste Management, Safety and Radiation Research (NUSAFE)” of the Helmholtz Association (HGF) and focus on the topics “Safety of Nuclear Waste Disposal” and “Safety Research for Nuclear Reactors”. The program NUSAFE, and therefore all work which is done at IRE, belong to the research field “Energy” of the HGF.

IRE conducts applied basic research to protect humans and the environment from the effects of radioactive radiation. For this purpose, we develop molecular process understanding using state-of-the-art methods of microscopy, spectroscopy, diffraction, numerical simulation, theoretical chemistry and systems biology. We implement this in a cross-institutional research environment at the HZDR. Our active interdisciplinarity combines radiochemistry, geosciences and biosciences as well as materials science and reactor physics. We provide knowledge that is applied in particular to reactor and repository safety as well as in radioecology.

We achieve this goal with a unique infrastructure comprising chemical and biological laboratories as well as hot cells in corresponding radiation and biology safety laboratories in Dresden, Leipzig and Grenoble. In Grenoble, at the European Synchrotron Radiation Facility (ESRF), the institute operates a beamline with four experimental stations for continuously advanced X-ray spectroscopy and diffraction of radioactive samples, which is also available to external users.

Again in 2021, the corona pandemic had an extraordinary influence on our work. The laboratories were closed for several weeks and the scientific exchange with collaborators, partners, and friends was reduced to a large extent. Nevertheless, 131 original papers were published in peer-reviewed international scientific journals with an average impact factor of 5.29 in 2021. The extraordinary broadness of research topics and activities is illustrated below by some selected highlights:

Within the framework of a national alliance, modeling tools were developed and validated based on integral experiments at the INKA test facility of Framatome GmbH, which replicates the passive decay heat removal system of the KERENA boiling water reactor at full scale. In addition, the entire INKA test facility, including all passive components, was modeled with the thermal hydraulic system model ATHLET and successful validation was performed for three different design-basis accident experiments (→ p. 78).

Ion irradiations, as a surrogate for hardly accessible neutron irradiations, are an indispensable tool for the investigation of the behavior of materials for nuclear environments. However, the ion-induced microstructural damage is limited to μm layers and exhibits intricate depth dependencies hampering the transferability to neutron irradiation. An important step towards improved transferability was made by systematic self-ion irradiations on a Fe-9Cr model alloy (proxy for candidate steels) clarifying these depth dependencies using STEM. Dislocation loops were found to be arranged in characteristic bands exhibiting noticeably different number densities and mean sizes of the loops and their positions correlating with the profiles of displacement damage and injected interstitials. The ion energy and depth range suitable for gaining meaningful information transferable to neutron irradiation was identified (→ p. 84). Moreover, these results bear valuable implications for the correct interpretation of

data obtained by methods that integrate over extended depth ranges, e.g. nanoindentation (→ p. 83). The work provides insight into the opportunities and limits of the use of ions to emulate neutron damage and provides recommendations for the design of experiments for optimal transferability.

Reliable prognostics concerning the migration patterns of radionuclides are significantly supported by the “smart- K_d ” approach developed under the lead of our institute during the last years. 2021 brought significant extensions of the thermodynamic database coupled to this approach. Namely the systems uranium-montmorillonite (with PSI → p. 43) and trivalent actinides/lanthanides-muscovite (→ p. 44) were successfully published milestones. Moreover, the smart- K_d is now implemented in the OpenGeoSys reactive transport software (→ p. 36) maintained by UFZ within the iCross network project.

The basis for understanding and predicting the behavior of radionuclides in the environment is a precise knowledge of the processes at the molecular level and the interplay between the geosphere and biosphere. This year, by combining state-of-the-art spectroscopic and microscopic techniques and instrumentation, we have succeeded for the first time in spatially resolving the speciation of europium in a multi-component system, namely europium/calcite/*Shewanella oneidensis*. Thus, the preferential interaction of europium with extracellular DNA and surface proteins of the bacterium was demonstrated (→ p. 63). This paves the way for future investigation of complex environmental samples.

Using spectroscopy, X-ray diffraction and theory studies regarding the fundamental properties of the actinides have explored new mechanisms for the *in situ* oxidation of tetravalent actinides (→ p. 17) and the coordinative properties of glucuronic acid, a simple biomolecule (→ p. 14). In collaboration with the University of Erlangen, we have also contributed to a study characterizing complexes of trivalent uranium with ligands containing S-donor atoms. First studies making use of the newly installed EPR spectrometer have revealed interesting electrochemical properties in a bimetallic complex containing Sb and Ru (→ p. 29).

Furthermore, we have expanded previous work investigating the retention properties of K-feldspar to include natural and synthetic Ca-feldspars (→ p. 47) and studied the impact of naturally occurring anions on the retention of trivalent rare earth and actinide elements (→ p. 44).

In a French-German cooperation together with the Université de Lille and the HZDR Computational Science Group, the complexation of trivalent curium with aqueous phosphates was newly investigated by spectroscopy and *ab initio* simulations. For the first time, in addition to $\text{Cm}(\text{H}_2\text{PO}_4)^{2+}$, the formation of $\text{Cm}(\text{H}_2\text{PO}_4)^{2+}$ was unambiguously established. The results are essential for understanding fundamental actinide coordination chemistry and clarifying the often-emphasized analogy of actinides and lanthanides as well as for predicting actinides migration behavior in a nuclear waste repository (→ p. 15). Starting in 2022, the successful collaboration is consolidated with a joint supervision of a doctoral thesis.

After a successful restart in 2020 at the world-wide first 4th generation synchrotron (EBS-ESRF), the Rossendorf Beamline has now all four experimental stations running in full user mode. XES, the 5-crystal spectrometer for high-energy-resolution X-ray absorption and emission spectroscopy (→ p. 23); XAFS, with the world’s first multi element Ge detector with CUBE amplifiers; XRD-1, the 6-circle Huber

diffractometer for surface and high-resolution powder diffraction; and XRD-2, the Pilatus 2M diffractometer for single-crystal and *in situ* diffraction (→ p. 19). On XES and XAFS, the first experiments involving trans-uranium actinides have been successfully conducted. Last but not least, both spectroscopy stations have demonstrated their superior performance by obtaining excellent spectra in the sub-ppm concentration range.

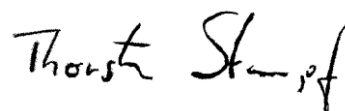
The surface reactivity of crystalline matter determines important properties such as the migration of radionuclides and the evolution of porosity and permeability. We present a novel parametrization of reactive transport models towards heterogeneous surface reactivity leading to improved quantitative predictability of dissolution reactions (→ p. 35). Another application is the valid quantification and prediction of the heterogeneous sorption of radionuclides on crystal surfaces, as shown by a combined experimental and numerical study (→ p. 38). Solute transport and fluid flow are governing factors in reactive transport. The upscaling of small-scale transport processes in complex geomaterials remains an important task for our research. For improved prediction of radionuclide migration in laminated and layered argillaceous rocks with complex diagenetic products, advanced numerical upscaling workflows are required, as demonstrated in the example of heterogeneous diffusive transport in Opalinus clay rocks (→ p. 37). The treatment of plastic waste by biodegradation is a very promising approach. This is impressively demonstrated by the first spatially resolved data sets of biodegradation kinetics using rate maps (→ p. 40). 2D and 3D materials are investigated, particularly with respect to their electronic properties and the possibility of tuning these properties to the desired applications. For instance, in the van der Waals heterostructures of transition-metal dichalcogenide monolayer with a 2D perovskite, we show a novel band alignment, allowing only hole transfer between

the two building blocks (→ p. 28). In other contributions, we investigated, together with experimental partners, novel noble-metal chalcogenides and metal-organic frameworks, which are promising for efficient photoelectrocatalytic water splitting and highly sensitive photodetectors, respectively (→ p. 31).

Beside these highlights, we obtained many other new scientific results in the past year, which are presented in this annual report.

In the last year, more than 180 scientists and technicians were employed at the Institute of Resource Ecology. Thereof, 49 Ph.D. students worked at the institute in 2021.

In retrospect of a challenging but at the end successful year 2021, I would like to thank the visitors, German and international ones, for their interest in our research and for their participation in the institute seminars. Although it was very limited in 2021, we will continue to encourage strongly the collaborations and visits by scientists in the future. Special thanks are due to the executive board of the HZDR, the Ministry of Science and Arts of the Free State Saxony (SMWK), the Federal Ministry of Education and Research (BMBF), the Federal Ministry for Economic Affairs and Climate Action (BMWK), the Deutsche Forschungsgemeinschaft (DFG), the European Commission, and other organizations for their support.



Prof. Dr. Thorsten Stumpf
Director of the
Institute of Resource Ecology

Contents

SCIENTIFIC CONTRIBUTIONS

Part I: The Chemistry of Long-Lived Radionuclides

Synthesis and characterization of a U(III) arene-anchored tris-thiophenolate complex	13
D. Pividori, M. E. Miehlich, B. Kestel, F. W. Heinemann, A. Scheurer, M. Patzschke, K. Meyer	
Structure and thermodynamics of Eu(III) and Cm(III) complexes with glucuronic acid	14
S. Reese, P. Kaden, C. J. Taylor, R. Kloditz, M. Schmidt	
Impact of temperature on the complexation of Cm(III) with H_2PO_4^- : insights from thermodynamics	15
N. Jordan, N. Huittinen, I. Jessat, F. Réal, V. Vallet, S. Starke	
Covalency trends in An(IV) mono(salen) complexes	16
M. K. Blei, L. K. Waurick, M. Patzschke, K. O. Kvashnina, J. März	
Synthesis of a uranyl(VI) pure <i>N</i> -donor complex <i>via</i> TEMPO mediated oxygen transfer.....	17
L. Köhler, J. Balas, J. März, M. Schmidt, T. Stumpf	
Uranyl(VI) citrates: comprehensive determination of aqueous solution molecular structures and complex formation constants	18
J. Kretzschmar, S. Tsushima, A. Rossberg, R. Steudtner, K. Müller, F. Bok, K. Schmeide, V. Brendler	
High temperature diffraction at ROBL	19
C. Hennig, V. Svitlyk, S. Findeisen	
Solid solutions and phase stability in (Th/Ce)-Y-zirconia systems	20
V. Svitlyk, S. Weiss, C. Hennig	
Incorporation of Cm^{3+} into hydrous zirconia at elevated temperatures.....	21
L. Opitz, N. Huittinen	
Oxidation of micro- and nanograined UO_2 pellets by <i>in situ</i> synchrotron XRD	22
E. De Bona, K. Popa, O. Walter, M. Cologna, C. Hennig, A. C. Scheinost, D. Prieur	
Study of fission product behavior in (U,Pu) O_{2-x} SIM fuel	23
R. Caprani, D. Prieur, P. Martin, J. Martinez, F. Lebreton, C. Aloin, M. Alibert, J.-R. Sevilla, L. Barnouin, P. Signoret, L. Picard, G. Gabriel, O. Miollan, N. Clavier	
High energy resolution X-ray spectroscopy methods at the Rossendorf beamline for actinide science	24
E. F. Bazarkina, K. O. Kvashnina	
Probing the 5f orbitals of hexavalent uranium by HERFD	25
L. Amidani, M. Retegan, A. Volkova, K. Popa, P. M. Martin, K. O. Kvashnina	
High Energy Resolution X-ray spectroscopy at the actinide $\text{M}_{4,5}$ edges	26
K. O. Kvashnina, S. M. Butorin	
Optimization of the U-O phase diagram with <i>in situ</i> XANES.....	27
D. Prieur, M.-M. Desagulier, D. R. Neuville, C. Guéneau, E. Epifano, K. Dardenne, J. Rothe, P. M. Martin	
Nonradiative energy transfer and selective charge transfer in $\text{WS}_2/(\text{PEA})_2\text{PbI}_4$ heterostructure	28
M. Karpinska, M. Liang, R. Kempt, K. Finzel, M. Kamminga, M. Dyksik, N. Zhang, C. Knodlseder, D. K. Maude, M. Baranowski, Ł. Kłopotowski, J. Ye, A. Kuc, P. Plochocka	
Coordination and electrochemical switching on paddle-wheel complexes containing an As-Ru or a Sb-Ru axis.....	29
R. Gericke, J. Wagler	
Lithium-assisted exfoliation of palladium thiophosphate nanosheets for photoelectrocatalytic water splitting.....	30
B. Wu, R. Kempt, E. Kovalska, J. Luxa, A. Kuc, T. Heine, Z. Sofer	

Oriented growth of in-oxo chain based metal-porphyrin framework thin film for high-sensitive photodetector	31
Y.-B. Tian, N. Vankova, P. Weidler, A. Kuc, T. Heine, C. Wöll, Z.-G. Gu, J. Zhang	

Part II: Long-Lived Radionuclides & Transport Phenomena in Geological Systems

Implementing heterogeneous crystal surface reactivity in reactive transport models.....	35
C. Fischer	
Radionuclide transport modelling: the Smart K_d -concept in reactive transport codes	36
M. Stockmann, R. Lu, A. Gehrke	
Effective diffusivity prediction of radionuclides in clay formations using an integrated upscaling workflow.....	37
T. Yuan, C. Fischer	
Heterogeneous sorption of radionuclides predicted by crystal surface nanoroughness	38
T. Yuan, S. Schymura, T. Bollermann, K. Molodtsov, P. Chekhonin, M. Schmidt, T. Stumpf, C. Fischer	
Observation of fluid injection into tight barrier material with GeOPET	39
J. Kulenkampff, S. Gruhne, D. Lösel	
Heterogeneous surface retreat during enzymatic PET degradation as revealed by Vertical Scanning Interferometry	40
H. Lippold, C. Sonnendecker, C. Fischer	
Estimating uncertainties of radionuclide migration in crystalline host rock – An interdisciplinary approach.....	41
S. Pospiech, V. Brendler	
Cm(III) sorption on single crystal orthoclase surfaces.....	42
M. Demnitz, S. Schymura, J. Neumann, M. Schmidt, K. Müller	
New insights into U(VI) sorption onto montmorillonite from batch sorption and spectroscopic studies at increased ionic strength	43
M. Stockmann, K. Fritsch, F. Bok, M. Marques Fernandes, B. Baeyens, R. Steudtner, K. Müller, C. Nebelung, V. Brendler, T. Stumpf, K. Schmeide	
Impact of sulfate on the sorption of trivalent actinides and rare earth elements (Am, Eu, Y) on the muscovite (001) basal plane	44
J. Neumann, S. S. Lee, H. Brinkmann, P. J. Eng, J. E. Stubbs, T. Stumpf, M. Schmidt	
Batch sorption studies of Np(V) onto ZrO ₂	45
I. Jessat, H. Foerstendorf, N. Jordan	
Uranium carbonates removal by layered double hydroxides	46
N. Mayordomo, G. Padberg, D. M. Rodriguez, K. Müller	
Retention of trivalent lanthanides (Eu, La) and actinides (Am, Cm) by natural and synthetic Ca-feldspars	47
J. Lessing, J. Neumann, F. Bok, J. Bezzina, J. Lützenkirchen, V. Brendler, T. Stumpf, M. Schmidt	
Structural modelling of Tc(IV) complexes with green rust: application of Fourier filtering algorithm combined with target factor analysis.....	48
A. Rossberg, N. Mayordomo	
Neural network analysis of EXAFS spectra to identify technetium chukanovite species	49
K. Schmeide, A. Rossberg, F. Bok, S. Shams Aldin Azzam, S. Weiss, A. C. Scheinost	
Spectro-electrochemical cell development for the investigation of redox mechanisms.....	50
D. M. Rodriguez, N. Mayordomo, V. Brendler, K. Müller	

Isothermal Titration Calorimetry (ITC) for surface processes – Thermograms correlate with classical batch experiments	51
H. Foerstendorf, N. Jordan	
Phase transformations in cerium-doped zirconia	52
L. B. F. dos Santos, N. Huittinen, V. Svitlyk, C. Hennig	
Production of monazite targets for heavy ion irradiation experiments	53
S. E. Gilson, A. A. Bukaemskiy, M. K. Henkes, G. L. Murphy, N. Huittinen	
Thermodynamic reference database THEREDA: 11. News in the 2021 data release and major developments	54
F. Bok, H. C. Moog, A. Richter, S. Zechel	

Part III: Long-Lived Radionuclides in Biological Systems

Binding of U(VI) to plant cells of <i>Brassica napus</i>	57
J. Jessat, R. Hübner, W. A. John, A. Rossberg, D. Prieur, S. Sachs	
Curium speciation studies in the presence of plant cells (<i>Brassica napus</i>)	58
H. Moll, M. Schmidt, S. Sachs	
Evidence of efficient uranium sorption by <i>Magnetospirillum magneticum</i> AMB-1 cells	59
E. Krawczyk-Bärsch, J. Ramtke, B. Drobot, R. Steudtner, J. Raff	
Interaction of U(VI) with <i>Nicotiana tabacum</i> cells – Role of Ca ion channels in U uptake into plant cells	60
F. Rajabi, S. Sachs	
Elucidation of metal-reducing proteins in plant cells using tobacco BY-2 suspension cultures	61
W. A. John, S. Matschi, S. Sachs	
Geochemical and microbiological characterization of mine water from two former uranium mines in Saxony/Germany	62
A. M. Newman-Portela, E. Krawczyk-Bärsch, M. Lopez-Fernandez, B. Drobot, A. Kassahun, J. Raff, M. L. Merroun	
Spatially resolved Eu(III) environments by chemical microscopy	63
R. Steudtner, M. Vogel, T. Fankhänel, J. Raff, B. Drobot	
Nanoscale membrane mimetics for structural investigations of membrane proteins	64
M. Subramanian, C. Kielar, S. Tsushima, K. Fahmy, J. Oertel	
Development of an in-house preparation route for vesicles	65
T. Fankhänel, R. Steudtner, L. Nucke, B. Drobot	
Selectivity of the natural lanthanide binding protein lanmodulin	66
B. Drobot, H. Singer, C. Zeymer, L. J. Daumann, R. Steudtner	
Interaction of Ferritin with Pu ⁴⁺	67
S. Tsushima, C. Zurita, C. Den Auwer	
Investigation of the structure and dynamics of gallium binding to high-affinity peptides elucidated by multi-scale simulation, quantum chemistry, NMR and ITC	68
C. J. Taylor, N. Schönberger, A. Lanikova, M. Patzschke, B. Drobot, L. Zidek, F. Lederer	
<i>In vivo</i> capture of bacterial cells by remote guiding	69
I. Rybkin, S. Pinyaev, O. Sindeeva, S. German, M. Koblar, N. Pyataev, M. Čeh, D. Gorin, G. Sukhorukov, A. Lapanje	
Dual-radiolabeling shows dissolution-based uptake pathway of CeO ₂ in freshwater shrimp	70
S. Schymura, I. Rybkin, S. S. Uygan, S. Drev, R. Podlipec, T. Rijavec, A. Mansel, A. Lapanje, K. Franke, M. Strok	
α - β -separation in liquid scintillation counting using small economical detectors	71
S. Stalke, R. Steudtner, K. Grossmann	

Part IV: Nuclear Reactor Safety Research

Neutronic benchmark solution of the FFTF Loss of Flow Tests – Preliminary results.....	75
E. Nikitin, A. Ponomarev, E. Fridman	
Optimization of multi-group energy structures for diffusion analyses of sodium-cooled fast reactors assisted by simulated annealing	76
Y. Bilodid, V. A. Di Nora, E. Fridman, E. Nikitin	
Plant modelling and applied safety analyses in NuScale Small Modular Reactor (SMR) with thermal-hydraulic system code ATHLET and CFD software.....	77
E. Diaz-Pescador, A. Grahn	
Numerical investigation of asymmetric cold-water injection into the primary circuit of a German KONVOI PWR during a Station Blackout sequence with ATHLET	78
E. Diaz-Pescador, F. Schäfer, S. Kliem	
Activation calculations of selected RPV components' segments	79
R. Rachamin, J. Konheiser	
Fracture mechanics investigation of reactor pressure vessel steel by means of small scale specimen technique.....	80
A. Das, E. Altstadt, P. Chekhonin, F. Obermeier	
Advanced microstructural characterization of reactor pressure vessel steels.....	81
P. Chekhonin, L. Lai	
Microstructure of oxide dispersion strengthened Fe-Cr-based tubes	82
A. Ulbricht, F. Bergner	
Microstructure-informed prediction and measurement of nanoindentation hardness of an Fe-9Cr alloy irradiated with Fe-ions of 1 and 5 MeV energy	83
G. Kapoor, P. Chekhonin, C. Kaden, K. Vogel, F. Bergner	
Depth distribution of irradiation-induced dislocation loops in an ion-irradiated Fe-9Cr model alloy	84
K. Vogel, C. Kaden, P. Chekhonin, F. Bergner	
Radiochemical analysis of ¹⁴ C and ⁶⁰ Co in the activated RPV steel samples of Greifswald Nuclear Power Plant	85
G. Yassin, A. Barkleit	
Greifswald NPP ex-vessel dosimetry revisited	86
E. Poenitz, J. Konheiser	
Neutron irradiated concrete: Material characterization and gamma dosimetry.....	87
Q. I. Roode-Gutzmer, A. Barkleit, J. Konheiser	
Examining zeta potential in the alkaline dissolution of quartz.....	88
Q. I. Roode-Gutzmer, R. Lessing	

PUBLICATIONS

○ Articles (peer-reviewed).....	91
○ Further Contributions.....	100
○ Editorial Work	100
○ Oral Presentations	101
○ Theses	103

SCIENTIFIC ACTIVITIES

- Contributions to the Framework of IAEA’s CPR2016: “Implementing Exploration Techniques for Paleochannel Sandstone-Hosted Uranium Deposits and Fluid-Rock Interaction in In-Situ Leaching Processes” 109
- Awards 109
- Seminars (Talks of Visitors) 110
- Teaching Activities..... 110

PERSONNEL 113

ACKNOWLEDGEMENTS 119

INDEX OF AUTHORS 124

SCIENTIFIC CONTRIBUTIONS (PART I)

Chemistry

The Chemistry of

**LONG-LIVED
RADIONUCLIDES**

Synthesis and characterization of a U(III) arene-anchored tris-thiophenolate complex

D. Pividori,¹ M. E. Miehlich,¹ B. Kestel,¹ F. W. Heinemann,¹ A. Scheurer,¹ M. Patzschke, K. Meyer¹

¹Friedrich-Alexander-University Erlangen-Nürnberg (FAU), Department of Chemistry and Pharmacy, Inorganic Chemistry, Erlangen, Germany

Large scale DFT and multi-reference calculations have been performed on U(III) complexes to gain deeper understanding of the U(III)-S bond.^[1]

The group of Karsten Meyer has long experience with anchored aryl-oxide ligands. In a recent series of experiments the oxygen in these was replaced by sulfur, leading to ligands of the general structure depicted in Fig. 1.

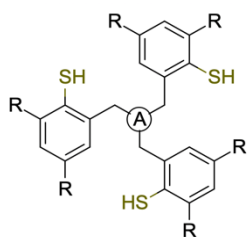


Figure 1. Schematic drawing of the ligand. The anchor A is mesitylene and R is the adamantyl rest.

METHODS. The anchor can be either triazacyclononane or mesitylene. The three thiophenolate groups carry two bulky adamantyl ligands each. The ligand synthesis is a seven step procedure starting from 2-adamantyl-4-methylphenol and has an overall yield of 12%. Adding [U(N-(SiMe₃)₂)₃] to a suspension of the ligand in cyclohexane yields the target complex. The identity of which was confirmed by NMR and SC-XRD. The target complex [U^{III}((SAr^{Ad,Me})₃mes)] shows interesting structural and magnetic properties which led to a computational investigation of the complex and its tris-aryloxide counterpart.

Optimizations of the structures of the two complexes were done at the DFT level of theory employing triple- ζ basis sets and the PBE0 functional. Dispersion corrections according to Grimme were used and scalar relativistic effects were taken into account by a small core ECP for uranium. The calculated structures agreed extremely well with crystal structures.

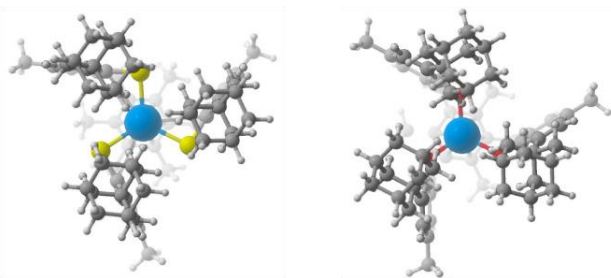


Figure 2. Structure of [U^{III}((SAr^{Ad,Me})₃mes)] (left) and [U^{III}((OAr^{Ad,Me})₃mes)] (right).

RESULTS. A striking first observation is the structural difference between the S and O complexes as depicted in Fig. 2, while the C–O–U bond angle is 126°, this changes to 93° for the C–S–U angle. The reason becomes evident from a look at the orbital contributions to the U–O and U–S bond. The U–S bond has a predominant p contribution from sulfur, while it is a clear sp³ hybrid for oxygen. The s–p hybridization does not work for sulfur as the energy difference between the 3s and 3p orbitals is too large.

This difference is even reflected in the magnetic properties of the complexes. The EPR spectra for both differ significantly.

While the U–O complex shows only a mildly oblate uranium with g values of 1.58, 1.46 and 1.2, the U–S complex shows a greatly increased axiality with g values of 3.06, 2.85 and 0.96. To corroborate the change in axiality, multi-reference calculations (CASSCF(3,7)) on a smaller model system were performed. In the model the adamantyl rests as well as the methyl groups of the mesitylene anchor were replaced by hydrogen. The resulting structure was optimized and then its electronic properties compared to the whole complex, only minor differences in the U(III) environment were found. The subsequent CAS calculation gave g values of 2.93, 2.93 and 1.03 for the U–S compound, in excellent agreement with experiment.

The U–S bond was further analyzed by the QTAIM (quantum theory of atoms in molecules) method and by the closely related method of interacting quantum atoms (IQA). These calculations showed, that the U–S bond is indeed quite strong with a delocalization index (DI) of 0.65, but, interestingly, still slightly weaker than the U–O bond (DI = 0.72). The IQA method was then employed to determine covalent contributions. While the U–O bond is predominantly ionic with a covalent contribution of 19% the U–S bond shows 39% of covalent contribution, which explains the much more oblate behavior of the U–S complex. This is of course another example of the HSAB concept at work, the relatively soft U(III) forms stronger covalent interactions with the softer sulfur ligand.

From the QTAIM analysis it also becomes apparent, that the mesitylene anchor also interacts with U(III). This interaction is relatively weak (DI = 0.2 for the U–S complex), but it shows a very high covalent contribution of 48%. This interaction becomes even visible in the spin-density of the complexes, here depicted for the U–S complex in Fig. 3. This interaction is comparable in both ligands. As can be seen in Fig. 2, the U(III) center is still approachable by other species, despite the bulky adamantyl rests, suggesting possibilities for interesting chemistry at the metal center, which will hopefully be revealed in further studies.

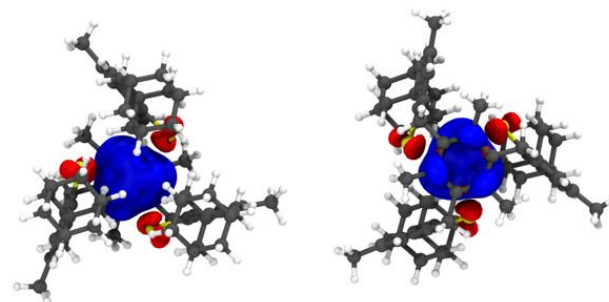


Figure 3. Spin density of [U^{III}((SAr^{Ad,Me})₃mes)], left viewed from the top through the adamantyl groups, right viewed through the mesitylene anchor. Blue alpha excess, red beta excess (spin polarization).

[1] Pividori, D. *et al.* (2021) *Inorg. Chem.* **60**, 16455–16465.

Structure and thermodynamics of Eu(III) and Cm(III) complexes with glucuronic acid

S. Reese, P. Kaden, C. J. Taylor, R. Kloditz, M. Schmidt

We have studied the interaction of Cm^{3+} and Eu^{3+} with glucuronic acid (GlcA), a simple sugar acid. Time-resolved laser-induced luminescence spectroscopy (TRLFS) shows that complexation at pH 5.0 occurs only at high ligand-to-metal ratios in the form of 1:1 complexes with standard formation constants $\log \beta^0 = 1.84 \pm 0.22$ for Eu^{3+} and $\log \beta^0 = 2.39 \pm 0.19$ for Cm^{3+} . A combination of NMR, QMMM, and TRLFS reveals the structure of the complex to be a “half-sandwich-structure” wherein the ligand binds through its carboxylic group, the ring oxygen, and a hydroxyl group. Surprisingly, Y^{3+} , prefers a different coordination geometry, bonding to the opposite side of a distorted GlcA molecule. QMMM simulations indicate that the differences in stability between Cm, Eu, and Y are related to ring strain induced by smaller cations.

Complexation by small organic ligands controls the bioavailability of radionuclides and influences their mobility in the geosphere. Glucuronic acid (GlcA) is a simple sugar acid, which is a common building block of extracellular polysaccharides (EPS), a ubiquitous biomolecule involved in numerous biochemical processes, e.g. biomineralization.^[1] Thus, we have studied the complex formation of GlcA with Cm(III) and Eu(III) using TRLFS and NMR spectroscopy, as well as QMMM calculations.^[2]

EXPERIMENTAL. All experimental and computational details are available in the literature.^[2] Briefly, three types of experiments were performed by TRLFS: (i) variable ligand concentration at fixed pH 5.0 and several ionic strengths (Cm and Eu), (ii) varying pH from 5–9 at $I = 0.1 \text{ M}$, and (iii) ligand concentration series in the presence of CO_2 (Eu only). All luminescence measurements were carried out in solution at room temperature. The samples were resonantly excited using a tunable OPO laser system pumped by a Nd:YAG laser (both Continuum, USA). Eu(III) was excited *via* its most intense absorption band corresponding to the (${}^7\text{F}_0 \rightarrow {}^5\text{L}_6$) transition at 394.0 nm, while the most intense (${}^8\text{S}_{7/2} \rightarrow {}^6\text{I}_{11/2}$) transition at 396.6 nm was used for Cm(III) excitation. NMR spectra were recorded on a Varian Inova 400 MHz spectrometer operating at 399.89 MHz for ${}^1\text{H}$ and 100.56 MHz for ${}^{13}\text{C}$, respectively. The solvent D_2O was used as internal standard. Equilibrium Quantum Mechanics/Molecular Modeling (QMMM) simulations were conducted of each of Eu(III), Cm(III), and Y(III) with each of the α and β anomers of glucuronic acid where the metal was placed either above or below each anomer for a total of twelve configurations.

RESULTS. TRLFS shows a continuous increase of the (${}^5\text{D}_0 \rightarrow {}^7\text{F}_2$)/(${}^5\text{D}_0 \rightarrow {}^7\text{F}_1$) peak ratio with increasing ligand concentration for Eu(III) and a corresponding peak shift to higher wavelength for Cm(III). Concurrently, lifetimes increase in both systems, indicating the occurring complexation reaction. Peak deconvolution with subsequent fluorescence intensity (FI) correction yields a speciation of the trivalent metals, which only reaches ~50% complexation even at very high ligand-to-metal (L/M) ratios ~200,000.

From this speciation complex, formation constants can be derived for both, Cm and Eu, by slope analysis and extrapolation to infinite dilution. The complex formation constants are found to be $\log \beta^0(\text{Cm}) = 2.39 \pm 0.19$ and $\log \beta^0(\text{Eu}) = 1.84 \pm 0.22$, respectively, for the $[\text{M}(\text{GlcA})]^{2+}$

complex. The difference between the constants is surprisingly large, corresponding to a ~3.5-fold increase for Cm. In addition to $\log \beta$, a specific ion interaction theory (SIT) interaction parameter was determined.

The origin of this difference in stability can be characterized by determining the structures of the formed complexes. TRLFS shows that 1:1 complexes form, which bear 5–6 water molecules in addition to GlcA, while pH dependent measurements indicate involvement of at least one OH-group in binding to Eu. Paramagnetic NMR spectroscopy in combination with QMMM simulations was used to identify which functional groups bind to each metal. NMR data analysis was complicated by the fact that the chosen diamagnetic reference, Y(III), exhibits a different structure than both Eu and Cm. Nonetheless, the NMR results suggest bonding of Eu through one or two OH-groups, the ring oxygen O-5 as well as possibly the carboxylic acid group on C-6 (Fig. 1D). On the other hand, Y(III) appears to bind to O-2 and O-4 on the opposite side of a distorted GlcA molecule (Fig. 1C).

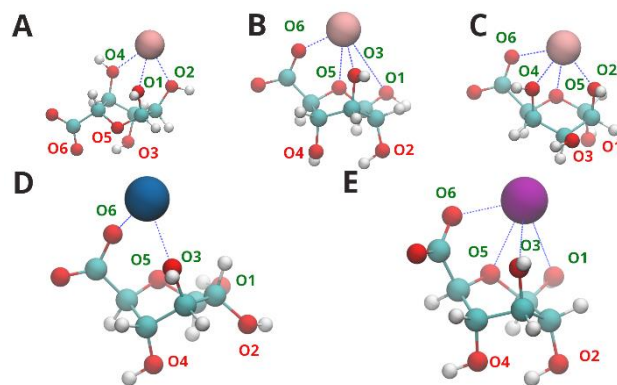


Figure 1. Depiction of Y(III) simulation starting geometries with (A) α -glucuronic acid (B) β -glucuronic acid and (C) the underside of a distorted α -glucuronic acid conformation. The most stable configurations from the QMMM simulations for (D) Eu and (E) Cm are shown below.

We applied QMMM simulations from various starting conditions for all three metals to determine likely complex structures. The simulations show that Cm consistently binds to O-3, O-5, and O-6. In contrast, Eu also binds to all three, but only maintains contact to the carboxyl O-6, while interactions with the ring oxygen O-5 and O-3 broke and re-formed over time. This difference is caused by the smaller ionic radius of Eu relative to Cm.^[3] The yet smaller Y cannot steadily interact with any GlcA conformer and forms a stable complex with a highly distorted molecule instead revealing interactions with O-2 and O-4 as well as carboxyl O-6 and ring O-5 (Fig. 1C), which would be found on opposite sides of the pyranoid ring in less distorted configurations (Fig. 1A).

[1] Arias, J. L. *et al.* (2008) *Chem. Rev.* **108**, 4475–4482.

[2] Reese, S. *et al.* (2021) *Inorg. Chem.* **60**, 14667–14678.

[3] Shannon, R. D. (1976) *Acta Crystallogr. A* **32**, 751–767.

Impact of temperature on the complexation of Cm(III) with H_2PO_4^- : insights from thermodynamics

N. Jordan, N. Huittinen, I. Jessat, F. Réal,¹ V. Vallet,¹ S. Starke²

¹University of Lille, CNRS, UMR 8523, PhLAM, Lille, France; ²Computational Science Group, Department of Information Services and Computing, HZDR

The complexation of Cm(III) with H_2PO_4^- was investigated at temperatures between 25 and 90 °C using laser-induced luminescence spectroscopy. Two complexes namely $\text{CmH}_2\text{PO}_4^{2+}$ and $\text{Cm}(\text{H}_2\text{PO}_4)_2^+$ were identified. The integrated van't Hoff equation was used to obtain molar enthalpies and entropies of reaction for both complexes.

EXPERIMENTAL. For the luminescence spectroscopic investigations ($\lambda_{\text{exc}} = 396.6\text{nm}$) performed at 25 °C, sample rows with $I = 0.5, 1.0$ and 2.0mol L^{-1} were prepared using NaClO_4 as background electrolyte. The concentration of ^{248}Cm was 8.76×10^{-8} or $1.15 \times 10^{-7}\text{mol L}^{-1}$. The proton concentration was $3 \times 10^{-3}\text{mol L}^{-1}$ in all samples. The phosphate concentration varied between 0 and 0.055mol L^{-1} . Additionally, experiments were performed at $-\log_{10}[\text{H}^+] = 3.44$ ($I = 1.0$ and 2.4mol L^{-1}) and 3.65 ($I = 3.0\text{mol L}^{-1}$). Furthermore, the impact of temperature (25 to 90 °C; $I = 1\text{mol L}^{-1}$) on the complexation was investigated.

RESULTS. With increasing phosphate concentration the emission spectra of Cm(III) at 25 °C were shifted towards higher wavelengths indicating an increasing complexation.^[1] After decomposition, the pure spectral components of the Cm^{3+} aquo ion, the $\text{CmH}_2\text{PO}_4^{2+}$ and the $\text{Cm}(\text{H}_2\text{PO}_4)_2^+$ complexes as well as their luminescence intensity corrected species distribution were obtained.^[1] The determination of the conditional stability constants at 25 °C was performed on the molal scale assuming the following chemical reaction ($n = 1$ and 2):



which was confirmed by slope analysis.^[1] The conversion from molar to molal scale and the derivation of molal concentration of the free H_3PO_4 was performed as described elsewhere.^[1,2] By applying the SIT equation,^[3] the following values at infinite dilution were derived: $\log_{10}\beta^0 = 0.45 \pm 0.04$ ($\text{CmH}_2\text{PO}_4^{2+}$) and $\log_{10}\beta^0 = 0.08 \pm 0.07$ ($\text{Cm}(\text{H}_2\text{PO}_4)_2^+$) (Fig. 1). Furthermore, the ion interaction coefficients, $\varepsilon(\text{CmH}_2\text{PO}_4^{2+}; \text{ClO}_4^-) = 0.17 \pm 0.04\text{kg mol}^{-1}$ and $\varepsilon(\text{Cm}(\text{H}_2\text{PO}_4)_2^+; \text{ClO}_4^-) = -0.10 \pm 0.06\text{kg mol}^{-1}$ were obtained. Our results clearly show, that any approach exclusively based on charge consideration and neglecting the size and structure of the complex (*e.g.*, its electron density distribution) to derive default values for non-available ion interaction coefficients, should be used extremely carefully.^[3,4]

With rising temperature an increasing Cm(III) complexation was observed.^[1] For the extrapolation to infinite dilution, the ion interaction coefficients derived at 25 °C were assumed to be constant in the temperature range from 25 to 90 °C.^[3] The integrated van't Hoff equation enabled us to derive positive standard molar enthalpies and entropies of reaction for both complexes (Tab. 1), indicating an endothermic and entropic driven complexation.^[5] For the first time, the formation of the $\text{Cm}(\text{H}_2\text{PO}_4)_2^+$ complex was spectroscopically assessed and consistent thermodynamic data was obtained. Similar studies were conducted for Europium, which will allow discussing how reliable the analogy between lanthanides and trivalent actinides is.^[6] Furthermore, the authors are aiming at exploring other aqueous Cm(III)/Eu(III)-phosphate species

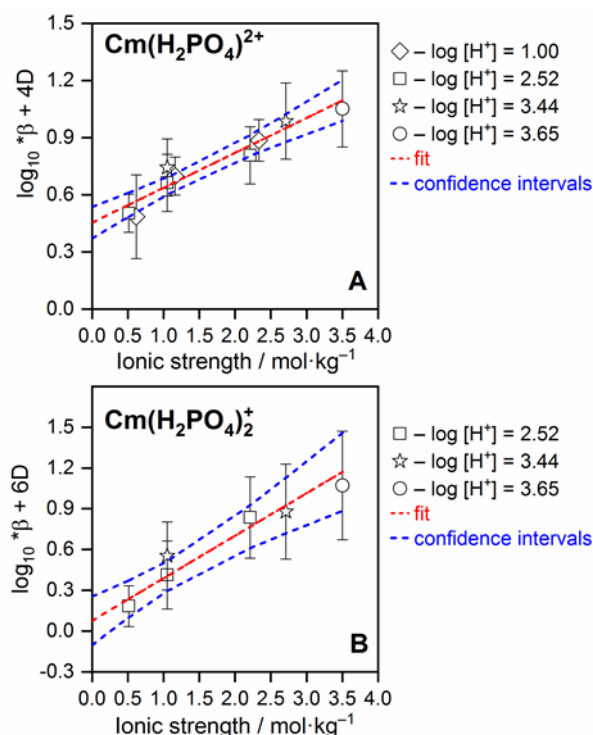


Figure 1. Linear SIT regression plot for the complexes of $\text{Cm}(\text{H}_2\text{PO}_4)_2^{2+}$ (A) and $\text{Cm}(\text{H}_2\text{PO}_4)_2^+$ (B) at 25 °C.

Table 1. Enthalpy and entropy values derived for the $\text{Cm}(\text{H}_2\text{PO}_4)_2^{2+}$ and $\text{Cm}(\text{H}_2\text{PO}_4)_2^+$ complexes using the integrated van't Hoff equation.

Complex	$\Delta_R H_m^0$ (kJ mol ⁻¹)	$\Delta_R S_m^0$ (J mol ⁻¹ K ⁻¹)
$\text{Cm}^{3+} + \text{H}_3\text{PO}_4 \rightleftharpoons \text{Cm}(\text{H}_2\text{PO}_4)_2^{2+} + \text{H}^+$	14.2 ± 1.1	56.1 ± 3.3
$\text{Cm}^{3+} + 2\text{H}_3\text{PO}_4 \rightleftharpoons \text{Cm}(\text{H}_2\text{PO}_4)_2^+ + 2\text{H}^+$	22.7 ± 1.8	77.3 ± 5.7

under circumneutral and slightly alkaline pH conditions. However, finding suitable solution conditions while avoiding Cm/Eu-phosphate precipitation will be challenging, even with a highly sensitive method such as luminescence spectroscopy.

- [1] Huittinen, N. *et al.* (2021) *Inorg. Chem.* **60**, 10656–10673.
- [2] Jordan, N. *et al.* (2018) *Inorg. Chem.* **57**, 7015–7024.
- [3] Grenthe, I. *et al.* (2020) *Second Update on the Chemical Thermodynamics of Uranium, Neptunium, Plutonium, Americium and Technetium. Chemical Thermodynamics Volume 14*, OECD Publications, Paris.
- [4] Thoenen, T. *et al.* (2014) PSI Bericht Nr. 14–04, Villigen, Switzerland.
- [5] Puigdomènech, I. *et al.* (1999), *Temperature Corrections to Thermodynamic Data and Enthalpy Calculations*, TDB-4, Issy-Les-Moulineaux, France: OECD Nuclear Energy Agency.
- [6] Jessat, I. *et al.* (2022), in preparation.

Covalency trends in An(IV) mono(salen) complexes

M. K. Blei, L. K. Waurick, M. Patzschke, K. O. Kvashnina, J. März

Series of U(IV) mono(salen) complexes of the type $[\text{UX}_2(\text{salen})(\text{THF})_2]$ were synthesized and characterized by HERFD-XANES (High Energy Resolution Fluorescence Detected X-ray Absorption Near Edge Structure) measurements to get a deeper understanding of the covalency trends induced by varying the halides (X). An increasing covalency in the U–X bond from F *via* Cl to Br was found.

Previous quantum chemical calculations showed unexpected large covalent contributions for actinide halide bonds.^[1] A deeper understanding of the binding character of these bonds can be derived from series of isostructural complexes, *e.g.* by using HERFD-XANES. The salen ligand has been found to be a suitable system (see Fig. 1), which is able to form 1:1 complexes with tetravalent actinides of the type $[\text{AnX}_2(\text{salen})(\text{solv})_2]$. The variation of the system of the mono(salen) complex offers the possibility to analyze the so far hardly described binding properties between halides and actinides.

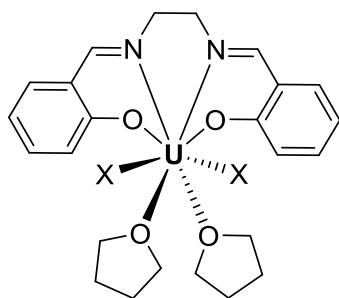


Figure 1. Mono(salen) uranium(IV) complex with two coordinated THF solvent molecules and two halides X (X = F, Cl, Br, I).

EXPERIMENTAL. U(IV) mono(salen) complexes were synthesized by dissolving 1 eq. U(IV) bis(salen) complex in MeOH and adding 1.1 eq. UCl_4 . By using the corresponding $[\text{U}_4(\text{Et}_2\text{O})_2]$ salt, the complex $[\text{U}_2(\text{salen})(\text{MeOH})_2]$ was synthesized. By evaporating MeOH and dissolving the complexes in anhydrous THF $[\text{UCl}_2(\text{salen})(\text{THF})_2]$ as well as $[\text{U}_2(\text{salen})(\text{THF})_2]$ was formed. $[\text{UBr}_2(\text{salen})(\text{THF})_2]$ was synthesized by dissolving $[\text{UCl}_2(\text{salen})(\text{MeOH})_2]$ in anhydrous THF and adding SiMe_3Br . The resulting suspension was centrifuged and remaining solvent was evaporated. The complex $[\text{UF}_2(\text{salen})(\text{THF})_2]$ was prepared by the addition of TBAF (*t*-butyl ammonium fluoride) to the dissolved complex $[\text{UBr}_2(\text{salen})(\text{THF})_2]$ in anhydrous THF by centrifuging the suspension and evaporating the remaining solvent.

In order to investigate the effects of the halide exchange on the binding situation at the U(IV) center, HERFD-XANES measurements were conducted at the Rossendorf Beamline (ROBL) of the ESRF.

By exciting the M_4 X-ray absorption edge of U(IV) at 3728 eV, on the one hand the number of *f* electrons of an actinide in the ground state and thus its oxidation state can be determined. Furthermore, such a measurement allows conclusions to be drawn about the electron density at the actinide and thus about the covalency of the coordinative bonds.^[2]

RESULTS. In Fig. 2, the HERFD-XANES spectra of the series of mono(salen) U(IV) complexes $[\text{UX}_2(\text{salen})(\text{THF})_2]$ with varying halide substituent X (X = F, Cl, Br, I) as well as UO_2

and UO_2^{2+} reference substances are shown. The strong absorption band around 3725 eV confirms the tetravalent oxidation state based on the UO_2 reference data. However, the broad absorption band including maxima at higher energies of complex $[\text{U}_2(\text{salen})(\text{THF})_2]$ point to at least one further oxidation state in addition to U(IV). Unfortunately, due to the different species, the absorption energy and intensity of the iodide complex cannot be used for comparison with the other complexes.

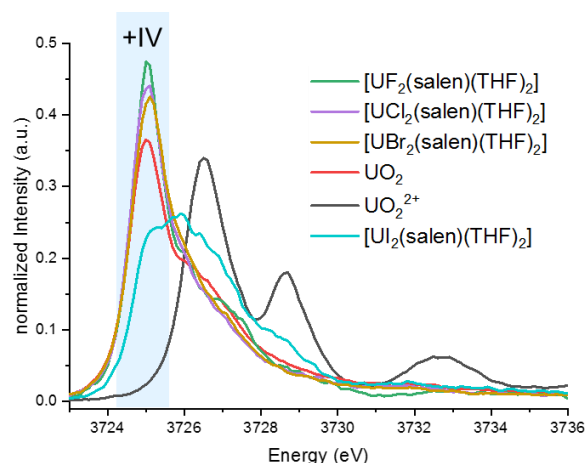


Figure 2. The normalized intensity against measured Energy of the complexes $[\text{UX}_2(\text{salen})(\text{THF})_2]$ (X = F, Cl, Br, I) and the reference samples UO_2 and UO_2^{2+} .

For the other complexes $[\text{UX}_2(\text{salen})(\text{THF})_2]$ (X = F, Cl, Br), the following trends become clear: The intensity of the energy maximum increases from the fluoride complex *via* the chloride to the bromide complex which indicates an increasing covalency of the halide bond to the uranium. This tendency is confirmed by a slightly decreasing absorption energy, which equates to an increasing electron density at U(IV). The increasing covalency in the An–X bond from F *via* Cl to Br can be explained by the increasing size of the halides and thus decreasing hardness, leading to a better polarizability of the halides.

A higher covalency and correspondingly higher electron density at the U(IV) is also confirmed by NBO (Natural Bond Orbital) analysis. This shows a decreasing charge (increasing electron density) on An(IV) (Th and U) within the mono(salen) halide series (F, Cl, Br, I) with a particularly large decrease between F and Cl. Therefore, it was found that the higher the polarizability of a donor (halide) the more covalent is the character of the bond with uranium.

[1] Radoske, T. *et al.* (2020) *Chem. Eur. J.* **26**, 16853–16859.

[2] Butorin, S. M. *et al.* (2016) *Proc. Natl. Acad. Sci. U.S.A.* **113**, 8093–8097.

Synthesis of a uranyl(VI) pure *N*-donor complex via TEMPO mediated oxygen transfer

L. Köhler, J. Balas, J. März, M. Schmidt, T. Stumpf

Synthesis of the hexavalent uranyl complex

$\text{Li}(\text{thf})_3[\text{UO}_2\text{Cl}(\text{pyren})]$ (**1**) with the *N*-donor ligand *N,N'*-ethylene-bis((pyrrole-2-yl)methanimine) (H_2L , H_2pyren) was achieved on the one hand *via* classical salt metathesis reaction. But on the other hand, oxidative oxygen transfer with (2,2,6,6-Tetramethylpiperidin-1-yl)oxyl (TEMPO) was shown to convert the tetravalent complexes $[\text{U}(\text{pyren})_2]$ (**2**) and $[\text{UCl}_2(\text{thf})_2(\text{pyren})]$ (**3**) to a hexavalent uranyl complex in 1:1 stoichiometry. The formation of similar uranyl complexes for the different routes was proven by NMR and a mechanism suggested.

Due to their different degrees of mobility in the environment, exploring the accessibility of the different oxidation states of uranium plays a crucial role in the risk assessment of future nuclear waste repositories. In deep geological formations with reducing conditions, the tetravalent state is expected to be predominant and least mobile. Nevertheless, formation of the mobile uranyl(VI) ion might be possible through organic oxygen transfer agents. Exemplarily, (2,2,6,6-Tetramethylpiperidin-1-yl)oxyl (TEMPO) is used in the following investigations, to see, if oxygen transfer can be realized through such compounds.

EXPERIMENTAL. A: *N,N'*-ethylene-bis((pyrrole-2-yl)methanimine) (H_2pyren) was deprotonated by the base lithium diisopropylamide (LDA) in thf and stirring at room temperature. After 20 minutes, UO_2Cl_2 in thf was added to the solution, leading to an immediate color change to intense dark red. After one day, volatiles were removed in vacuum and the product was received as red powder. Crystals were grown by layering a saturated complex solution in thf with cyclohexane.

B: An excess of TEMPO in thf was added to an orange suspension of $[\text{U}(\text{pyren})_2]$ and $[\text{UCl}_2(\text{thf})_2(\text{pyren})]$ in thf. After stirring for 3 h the reaction mixture slowly starts to turn red. The completeness of the reaction was accomplished after one day. Then all volatiles were removed in vacuum, yielding the product as red solid.

RESULTS. The synthesis of a uranyl complex in 1:1 stoichiometry with the pyren ligand was conducted *via* two different paths (see Fig. 1). One possibility is the reaction between uranyl chloride and the deprotonated ligand (path A). Interestingly, a complex anion is formed, exhibiting a cation-

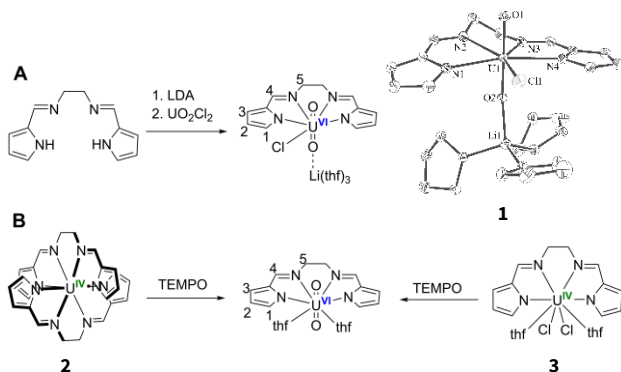


Figure 1. Synthesis paths leading to a uranyl complex with ligand pyren. Salt metathesis reaction resulting in the anionic complex $\text{Li}(\text{thf})_3[\text{UO}_2\text{Cl}(\text{pyren})]$ (**1**) (A). Oxidation of the tetravalent complexes through the oxygen transfer reagent TEMPO (B).

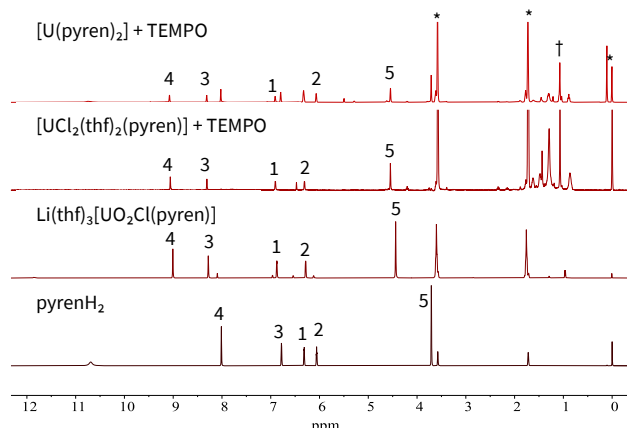


Figure 2. ^1H NMR spectra of the different reaction mixtures (top 2) in comparison to **1** and the protonated ligand (bottom 2) in thf- d_8 . *: signals of Thf and tms, †: signals of tetramethylpiperidine.

cation interaction between the uranyl oxo ligand O2 and a lithium ion (Fig. 1). Hence, an increased U–O2 bond length of 1.799(5) Å compared to U–O1 with 1.775(9) Å can be found, indicating bond weakening and thus potentially activation. Nevertheless, similar values for the different bond lengths are reported in literature.^[1,2] Analysis in solution by ^1H NMR shows only one signal set in a range typical for diamagnetic species, verifying that the highly symmetric anionic complex structure is preserved in solution.

Furthermore, the tetravalent uranium complexes **2** and **3** were chosen as starting material to synthesize a neutral hexavalent complex suitable for comparison (Fig. 2). ^1H NMR analysis of the reaction with TEMPO shows very good agreement with the spectrum of complex **1** (Fig. 2). With respect to this and charge balance for a +2-charged uranyl center, a suggestion of the formed product is given in Fig. 1. Impurities arise from ligand species in solution. Very small deviations of peak positions of 0.5 ppm in maximum could be explained by the formation of a neutral instead of an anionic complex. Regarding the reaction mechanism, oxygen atoms are subsequently transferred from TEMPO to the uranium in a redox reaction.^[3]

These investigations depict, that conversion of U^{IV} to $\text{U}^{\text{VI}}\text{O}_2^{2+}$ is possible *via* oxygen transfer agents even under reducing conditions. This might have an impact on the mobility of these species and should be considered in future risk assessments.

Following work will focus on crystal growth of the products from the reactions with the tetravalent complexes to verify the predicted structures and undertake bonding analysis as well as comparison to **1**. Furthermore, the reaction procedure will also be applied to other tetravalent actinide complexes, such as $[\text{NpCl}_2(\text{thf})_2(\text{pyren})]$, to investigate if oxidation is possible there as well.

[1] Klamm, B. E. *et al.* (2020) *Inorg. Chem.* **59**, 23–31.

[2] Cowie, B. E. *et al.* (2019) *Chem. Rev.* **119**, 10595–10637.

[3] Fortier, S. *et al.* (2011) *J. Am. Chem. Soc.* **133**, 14224–14227.

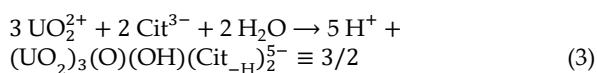
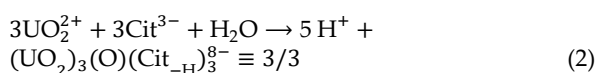
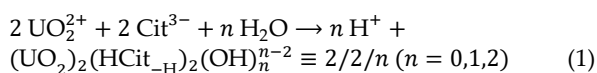
Uranyl(VI) citrates: comprehensive determination of aqueous solution molecular structures and complex formation constants

J. Kretzschmar, S. Tsushima, A. Rossberg, R. Steudtner, K. Müller, F. Bok, K. Schmeide, V. Brendler

This research addresses a subject discussed controversially for over 70 years. Both the molecular structures and the aqueous speciation of dimeric and trimeric uranyl(VI) citrate complexes were determined from acidic to alkaline pH ranges by means of a unique multi-method approach supported by DFT calculation. Species distribution calculations suggest that polynuclear U(VI) citrate species do not significantly increase U(VI) mobility in the environment.

EXPERIMENTAL. Sample preparation procedures, used spectroscopic techniques and details on quantum chemical calculations can be found in our recent papers.^[1,2]

RESULTS. The polynuclear U(VI) complexes forming with citric acid ($\text{H}_3\text{Cit}_{\text{H}^+0_{\text{aq}}}$) are characterized by tridentate coordination, involving the deprotonated hydroxyl group and two out of the three carboxylates. The remaining third carboxyl group can be either protonated ($\text{HCit}_{\text{H}^+3}$) or deprotonated (Cit_{H^+4}).



Combining ^{17}O NMR and DFT calculation allowed for unambiguous assignment of complex configurations, evidencing that the binary ($n = 0$) dimeric 2/2/0 complex exists as two diastereomers, with the *syn* isomer in aqueous solution strongly favored over the *anti* isomer. Upon increasing pH above ~4, at first ternary ($n = 1, 2$) dimeric mono- and bis-hydroxo U(VI) citrate 2/2/1 and 2/2/2 complexes form. Then, at neutral pH, ternary trimeric 3/3 and 3/2 complexes predominate. For all these species stability constants were determined (Tab. 1).

UV-Vis and ATR FT-IR spectra reveal the successive formation of ternary U(VI) citrate hydroxo dimeric species. Both spectroscopies refer to features directly correlated with uranyl(VI). In case of IR, the uranyl entities show a decrease in their antisymmetric stretching vibration frequency, $\nu_3(\text{UO}_2)$. The incremented increase in absorptivity in ligand-to-metal charge-transfer (LMCT) transitions observed in the UV-Vis spectra essentially refer to the uranyl(VI) as the chromophore. The structural changes occurring in direct vicinity of

the UO_2 entities upon deprotonation of the uranyl(VI)-coordinating water are caused by hydrolysis within the binary U(VI)-citrate dimeric complex according to $\text{U-OHH} \rightarrow \text{U-OH} + \text{H}^+$.

Increasing pH causes the 2/2/2 species to break down so that the $\text{HCit}_{\text{H}^+3}$ ligand is released, thereby forming Cit^{3-} . The consecutively emerging 3/3 complex then forms by reaction of the trinuclear uranyl(VI) hydrolysis species $(\text{UO}_2)_3(\mu_3\text{-O})(\text{OH})_3^+$ with three Cit^{3-} thereby (again) releasing the alcoholic hydroxyl protons to finally yield $(\text{UO}_2)_3(\mu_3\text{-O})(\text{Cit}_{\text{H}^+})_3^{8-}$. Upon further increasing pH, the complexes with U(VI)/Cit ratio equal to unity are displaced by $(\text{UO}_2)_3(\mu_3\text{-O})(\mu_2\text{-OH})(\text{Cit}_{\text{H}^+})_2^{5-}$, a species with U(VI)/Cit ratio of 1.5, which can be seen as the replacement of citrate by OH^- as ligand. The computed speciation distributions imply that in general the inorganic U(VI) hydrolysis species are the precursors for the polynuclear U(VI) citrate complex species. That is, even for 100-fold citrate excess no polynuclear species form as long as the U(VI) solution is sufficiently diluted, such as 10^{-7}M .

For U(VI) concentrations of about 10^{-7}M , corresponding to the $\mu\text{g L}^{-1}$ range, only the mononuclear 1/1 species, $(\text{UO}_2)(\text{HCit})^-$, plays a role. Taking into account that as of $5 \times 10^{-5}\text{M}$ U(VI) and excess ligand the formed U(VI) citrate complexes are polynuclear, in some technology-affected natural environments (issue of TENORM – technologically enhanced natural occurring radioactive materials) both the U(VI) and the (organic) ligand concentration probably reach values that promote formation of polynuclear complex species. However, these polynuclear complexes are still only minor components compared to competing inorganic U(VI) complexes, namely hydroxides, carbonates and hydroxycarbonates. Thus, calculations of the species distribution suggest that the characterized polynuclear U(VI) citrate species do not significantly increase uranium mobility in the environment. From a safety and risk assessment perspective, this is good news.

Additionally, uranyl(VI) citrate complexes are important for environmental remediation concepts of uranium-contaminated sites. For instance, in microbial degradation and immobilization these readily bioavailable species are well-suited electron-donor bearing precursors for biogenic reduction of mobile U(VI) complexes to immobile U(IV)-oxide species.

ACKNOWLEDGEMENTS. This work was funded by the European Union's Horizon 2020 research and innovation program (CORI project, no. 847593) as well as by the Federal Ministry for Economic Affairs and Climate Action (BMWK, GRaZ II, grant no. 02E11860B).

Table 1. Stability constants of aqueous dimeric and trimeric U(VI) citrate species, calculated for zero ionic strength according to the Davies equation.

Species	$\log \beta(I)^a$	
	$I = 0.1 \text{ M}$	$I \rightarrow 0$
2/2/0	19.7 ± 0.2^b	22.1 ± 0.2
2/2/1	13.8 ± 0.2^b	15.5 ± 0.2
2/2/2	6.5 ± 0.2^b	7.4 ± 0.2
3/3	$-(5.4 \pm 0.4)^b$	$-(8.6 \pm 0.4)$
3/2	$-(1.0 \pm 0.9)^c$	$-(1.0 \pm 0.9)$

^a: $\pm 2\sigma$; ^b: 0.1 M NaClO₄, UV-vis; ^c: 0.1 M NaCl, ATR FT-IR.

[1] Kretzschmar, J. et al. (2020) *Chem. Commun.* **56**, 13133–13136.

[2] Kretzschmar, J. et al. (2021) *Inorg. Chem.* **60**, 7998–8010.

High temperature diffraction at ROBL

C. Hennig, V. Svitlyk, S. Findeisen¹

¹HZDR, Mechanical Engineering, Dresden, Germany

In situ powder XRD, recently implemented at ROBL's XRD-2 diffractometer, is a powerful technique to study phase transitions and structural modifications as a function of temperature, with various applications in kinetics, catalysis and thermodynamics.

The diffractometer XRD-2 can be equipped either with a hot gas generator / Cyberstar (Fig. 1), or a heating chamber HTK1200N / Anton Paar (Fig. 2).^[1] The hot gas generator is able to heat a sample up to 850 °C using an Eurotherm controller. The temperature is remotely controlled with the Py-latus software.^[2] Samples can be measured exclusively in transmission mode using quartz glass capillaries of typically 0.3 mm in diameter. The capillary is rotated with one of the standard goniometers and can be aligned with the long-distance microscope (top right in Fig. 1).

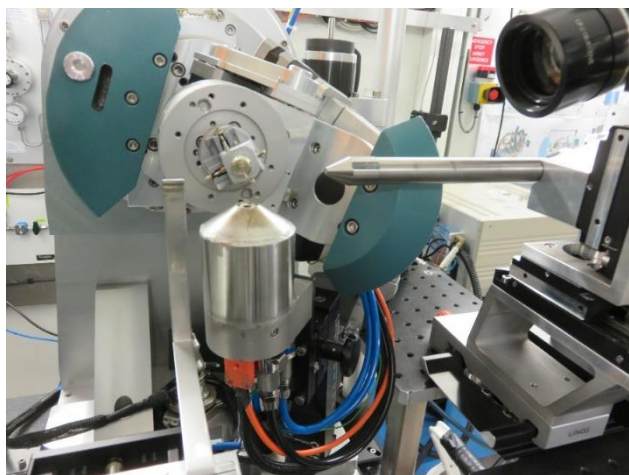


Figure 1. Hot gas generator/Cyberstar in Debye-Scherrer Geometry mounted at XRD-2.

The second option is the use of a heating chamber HTK1200N (Anton Paar) which reaches a temperature of 1200 °C (Fig. 2). This furnace can be used for measuring PXRD in reflection and in transmission geometries and can also be used for XANES and EXAFS measurements at ROBL's XAFS station.

A rotation module for glass capillaries can be mounted and enables measurements in transmission geometry. The capillary can be aligned with an external microscope before mounting the complete rotation module. For measurements

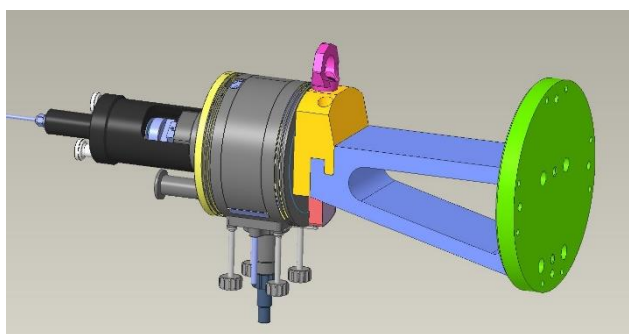


Figure 2. Heating chamber HTK1200N (grey) with rotation module for glass capillaries (black), adapter between heating chamber and support (yellow and blue), and support plate (green). The unit for measurements in reflection mode is mounted on the bottom of the chamber.

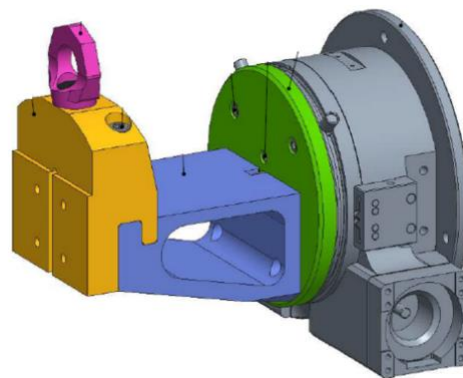


Figure 3. Modified goniometer support for samples in reflection geometry using HTK1200N. Goniometer/Huber (grey) mounting plate for the goniometer (green), adapter unit between heating chamber and support (yellow and blue).

in reflection geometry (Bragg-Brentano and grazing incidence), the heating chamber is mounted on a specially designed goniometer (Fig. 3).

The dehydration of $\text{CaSO}_4 \cdot 2\text{H}_2\text{O}$ is shown as example for a temperature-dependent phase transformation. $\beta\text{-CaSO}_4 \cdot 0.5\text{H}_2\text{O}$ (SG P3₁2₁) is formed by dehydration of $\text{CaSO}_4 \cdot 2\text{H}_2\text{O}$ (SG I2/a) at temperatures above 120 °C (Fig. 4/1). Soluble anhydrite (CaSO_4 , SG C222) forms around 130 °C (Fig. 4/2) and transfers around 350 °C (Fig. 4/3) into insoluble anhydrite (CaSO_4 , SG Amma). The experiment was performed with the hot gas generator with a heating rate of three degrees per minute. Figure 4 shows the registered pattern as function of temperature using the MEDVED software. MEDVED (Modulation-Enhanced Diffraction Viewer and EDitor) is compatible with ROBL's data format and allows inspecting each powder pattern separately or together.^[3]

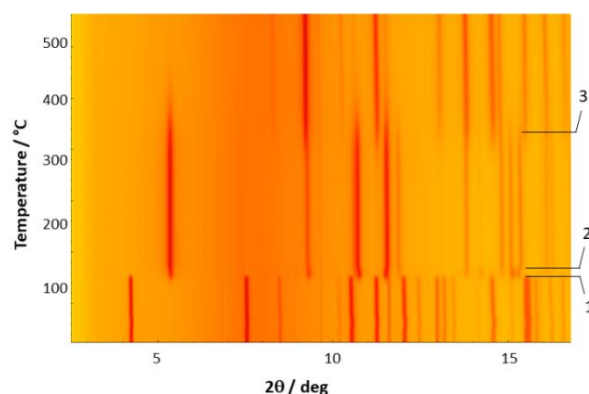


Figure 4. Dehydration of $\text{CaSO}_4 \cdot 2\text{H}_2\text{O}$. Powder diffraction patterns measured in transmission at 22 keV. The sequence of the powder patterns is depicted with MEDVED. Diffraction peak maxima are red.

[1] Scheinost A. C. *et al.* (2021) *J. Synchrotron Rad.* **28**, 333–340.

[2] Dyadkin, V. (2016) *J. Synchrotron Rad.* **23**, 825–829.

[3] Chernyshov, D. *et al.* (2016) *Acta Crystallogr. A* **72**, 500–506

Solid solutions and phase stability in (Th/Ce)-Y-zirconia systems

V. Svitlyk, S. Weiss, C. Hennig

Y-stabilized zirconia (YSZ) phases were found to incorporate Th atoms and the corresponding solubility ranges depend on the relative Y content. Cubic YSZ series can incorporate 20 % more of Th⁴⁺ ions compared to their tetragonal analogues with lower Y content. The larger Th-Zr/Y solubility range for phases with higher Y concentration is related to the associated symmetry increase which allows to stabilize longer Zr/Y–O bonding distances. Analogous Ce-YSZ phases exhibit excellent stability under extreme conditions of temperature and pressure. The YSZ phases are, therefore, potential candidates as host matrices for tetravalent radiotoxic elements like U, Th or Pu.

Derivatives of zirconium-based ceramics, in particular zirconia, ZrO₂, are promising materials as host matrices for spent nuclear fuel since these phases are known to remain stable in geological cycles of up to 10⁹ years.^[1] Scientific and technological goals for this research are to obtain zirconium-based ceramic materials containing maximum possible tetravalent actinides (An(IV)) without Zr/An(IV) phase separation. In addition, structural stability of these phases under various external parameters, e.g. temperature (*T*), pressure (*P*), irradiation and leaching resistance is essential in order to exclude possible discharge of the incorporated radioactive elements over a long time scale.

EXPERIMENTAL. For the current study, five series of samples based on Y-stabilized zirconia (YSZ) have been synthesized *via* co-precipitation method: Zr_xY_{0.11}Th_yO_{2-z} (*y* = 1–7%, ~1% step), Zr_xY_{0.14}Th_yO_{2-z} (*y* = 4, 7, 10, 12%), Zr_xY_{0.21}Th_yO_{2-z} (*y* = 0–11%, ~3% step), Zr_xY_{0.10}Ce_yO_{2-z} (*y* = 0–8%, ~1.5% step) and Zr_xY_{0.16}Ce_yO_{2-z} (*y* = 0–8%, ~1.5% step). Ambient, *T*- and *P*-dependent *in situ* synchrotron radiation diffraction experiments were performed at the ROBL BM20 beamline at ESRF, Grenoble. *HT* was obtained with hot gas blower and *HP* was generated using diamond anvil cells (DAC). Diffraction data were collected on high resolution XRD1 (Pilatus 100k) and multipurpose XRD2 (Pilatus3 X 2M, *HT* and *HP* experiments, Fig. 1) diffractometers of ROBL.^[2]

RESULTS. For the tetragonal phases with lower Y concentration of 14 at.-% a maximal possible Th intake on the Zr/Y metal site reached ca. 10 at.-%. Cubic phases with higher Y

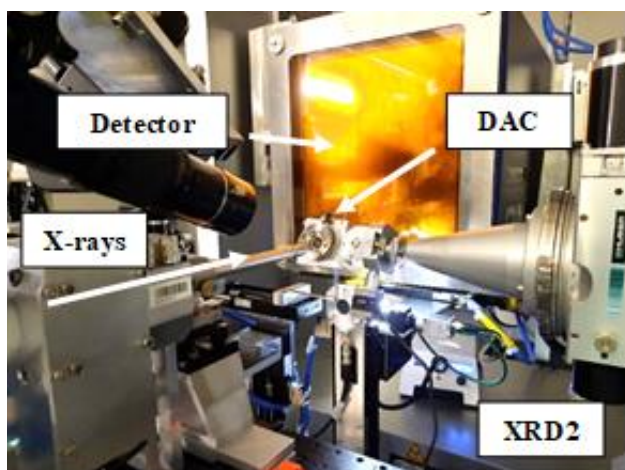


Figure 1. *In situ* HP diffraction experiment at XRD2 ROBL diffractometer.

content could dissolve up to ca. 12 at.-% Th. This behavior is explained by more symmetrical coordination of central Zr/Y metals by the surrounding O atoms in cubic YSZ, as concluded from the diffraction experiments. This results in easier accommodation of bigger Th atoms *via* structural stabilization of longer Zr/Y–O bonding distances. Thus, in these systems higher symmetry favors incorporation of larger An(IV).

T-dependent studies revealed excellent stability of the YSZ phases doped with guest Ce⁴⁺ ions used as surrogates for An(IV). Specifically, no phase decompositions and no mobility of incorporated Ce⁴⁺ ions have been observed during *in situ* measurements in a *RT* – 1150 K range. Nevertheless, application of *HP* induced transformation to higher cubic symmetry in Ce-YSZ phase with lower Yttrium content around 9 GPa. Remarkably, occupancy of the guest Ce⁴⁺ ions remained constant up to the maximal probed pressure of 14 GPa (Fig. 2). Cubic phase with higher Y content did not exhibit structural or phase changes until 11 GPa. This together with *T*-dependent data indicates excellent affinity of Ce atoms with the host YSZ matrices. The studied YSZ phases can be considered as promising materials for long-term and secure immobilization of radiotoxic actinide elements.

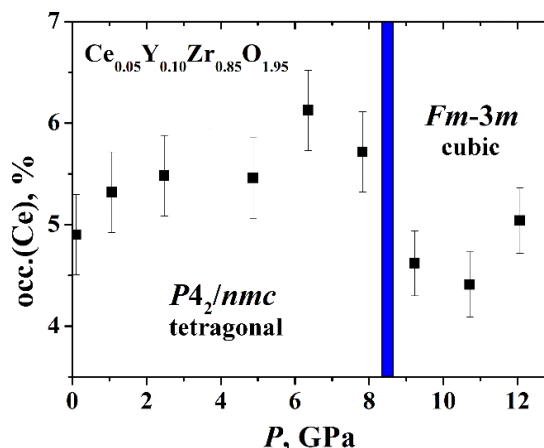


Figure 2. Occupancy of guest Ce⁴⁺ ions throughout the tetragonal-cubic transformation in Ce-YSZ at *HP*.

ACKNOWLEDGEMENTS. This project was supported by the Bundesministerium für Bildung und Forschung (BMBF) AcE grant (02NUK060). We also acknowledge the HZDR BM20 ROBL station at ESRF for providing beamtime in the frame of the AcE project. D.Naudet, J.Exner and N.Baumann are acknowledged for computing and technical support during experiments at BM20 beamline.

[1] Heaman, L. M. and LeCheminant, A. N. (1993) *Chem. Geol.* **110**, 95–126.

[2] Scheinost, A. C. et al. (2021) *J. Synchrotron Radiat.* **28**, 333–49.

Incorporation of Cm³⁺ into hydrous zirconia at elevated temperatures

L. Opitz, N. Huittinen

The incorporation of Cm³⁺ into zirconia and the crystallization of the solid phase has been monitored for thermal aging times of up to four months at 80 °C. The samples collected after different aging times were analyzed with PXRD and luminescence spectroscopy. The diffraction data showed partial crystallization of the hydrous zirconia after 16 days in solution, and a fully crystalline ZrO₂ material composed of mainly the monoclinic phase and a minor amount of the tetragonal polymorph after four months. Cm-TRLFS indicated a successful incorporation of the actinide into the amorphous and crystalline zirconia structures.

Water intrusion into a deep geological repository can lead to the mobilization of transuranium elements present in the spent nuclear fuel matrix (e.g. Pu, Np, Am, Cm). Different materials in the repository, such as Zircaloy-4, may act as retention barriers for the released elements and prevent their further migration into the biosphere. In this work, the interaction of the trivalent actinide curium with hydrous zirconia, i.e. the amorphous precursor to zirconia (ZrO₂) forming as a result of Zircaloy corrosion, has been studied.

EXPERIMENTAL. Zirconyl chloride octahydrate (100 mg) was dissolved in 400 µL HCl (0.01 M). Cm(III) stock solution was added to the mixture (82 µL, 10⁻⁴ M). The solution was inserted dropwise to 13.3 mL 0.5 M NaCl (pH 12) and the pH of the electrolyte was readjusted to its initial pH value with 2 N NaOH when necessary. The formed precipitate of Cm-containing hydrous zirconia was recovered by centrifugation and washed twice with 20 mL MilliQ-grade water. The powder was dried for 24 h in N₂ atmosphere. The dry powder was suspended in 13.3 mL 0.5 M NaCl (pH 12) and placed in a drying cabinet at 80 °C for a given amount of time. After removing the sample from the oven it was centrifuged and the powder was washed twice with 20 mL MilliQ-grade water. The resulting powder was dried for 24 h and ground in an agate mortar.

RESULTS. The recovered sample after one day at 80 °C, has a fully amorphous structure as deduced from the absence of any diffraction peaks (Fig. 1, bottom trace). The amorphous powder is hydrous zirconia which can be described with the chemical formula ZrO(OH)₂.^[1] Upon further increase of the thermal aging time, a transformation of the material into a crystalline ZrO₂ structure can be observed with PXRD (Fig. 1,

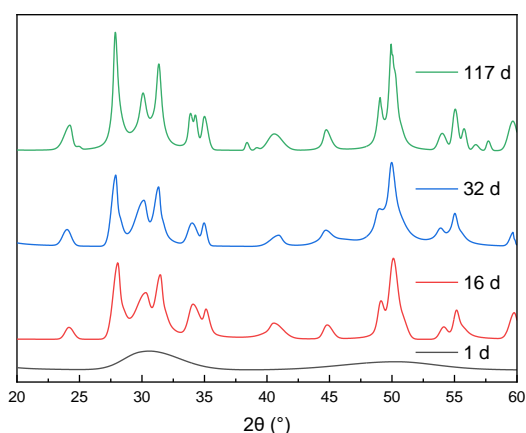


Figure 1. PXRD diffractograms of the Cm³⁺:ZrO₂ samples.

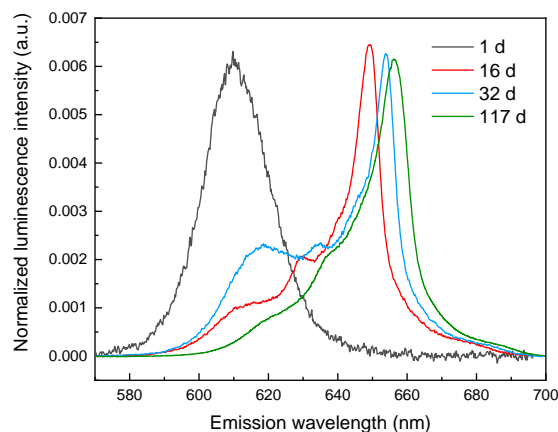


Figure 2. Emission spectra of the Cm³⁺:ZrO₂ samples at different thermal aging times.

upper traces). Phase identification showed the presence of both the monoclinic and the tetragonal phases, whereas the monoclinic phase is dominant with 76 % for the longest treated sample (24 % tetragonal ZrO₂). While the monoclinic phase is thermodynamically stable below 1170 °C, the tetragonal phase undergoes stabilization due to the surface energy of the small crystallites (< 20 nm).^[2] The spectroscopic results obtained with time-resolved laser-induced fluorescence spectroscopy (TRLFS) show a broad Cm emission signal at 615 nm after the short aging time of one day (Fig. 2, spectrum of 1 d). Following spectral decomposition, the emission peak could be described with two single component spectra arising from two different Cm environments in the amorphous structure of the Zr-phase. Upon further thermal aging TRLFS shows that with the beginning of the phase transformation a large bathochromic shift to wavelengths of up to 650 nm and beyond occurs, while the signal from the amorphous phase disappears (Fig. 2, spectra of 16–117 d). This points toward full incorporation of the Cm³⁺ cation into the structure of zirconia by replacing the host Zr⁴⁺ cation in both the monoclinic and tetragonal phase. To preserve charge neutrality, 0.5 oxygen vacancies are created per incorporated trivalent cation. Various hot band transitions can also be seen in Fig. 2 for all partly crystalline samples. The main signal at 650 nm cannot be decomposed into multiple species but the different peak widths and slightly asymmetric peaks allows for the assumption that several Cm³⁺ environments are present also in these crystalline samples. This is in agreement with recent results obtained in analogous experiments using the luminescent lanthanide Eu³⁺.^[3] The results show that the retention of lanthanides and actinides are possible with the zirconia barrier present in the spent nuclear fuel waste.

ACKNOWLEDGEMENTS. The support of BMBF for funding of the AcE project (02NUK060A) is greatly acknowledged.

[1] Huang, C. et al. (2001) *J. Am. Ceram. Soc.* **84**, 1637–1638.

[2] Kountouros, P. et al. (1993) *Science and Technology of Zirconia Vol. 5*, Technomic Publishing Company, Inc., Lancaster.

[3] Opitz, L. (2021) Master thesis, Technische Universität Dresden.

Oxidation of micro- and nanograined UO_2 pellets by *in situ* synchrotron XRD

E. De Bona,¹ K. Popa,¹ O. Walter,¹ M. Cologna,¹ C. Hennig, A. C. Scheinost, D. Prieur

¹Joint Research Centre, European Commission, Karlsruhe, Germany

The oxidation of three UO_2 pellets having equal density but different grain size was studied by *in situ* P-XRD. The UO_2 samples were produced by Spark Plasma Sintering and had grain sizes of $3.08 \pm 0.06 \mu\text{m}$, $478 \pm 17 \text{ nm}$, and $163 \pm 9 \text{ nm}$. After 21 h at 300°C , the first two samples were converted into U_3O_8 , while the one having the smallest grain size showed only the XRD peaks of U_3O_7 . This is particularly relevant for spent nuclear fuel safety as its grain size is similar to that of the high burnup structure (*i.e.*, the region at the rim of spent nuclear fuel pellets).

Despite over 50 years of studies on the oxidation of UO_2 in different forms (powder, sintered, single crystal) and under different conditions (temperature, oxygen partial pressure, radiation field), some crucial aspects remain unclear. Around 300°C , the temperature representative of dry storage conditions, UO_2 oxidizes to U_3O_8 following the reaction $\text{UO}_2 \rightarrow \text{U}_4\text{O}_9 \rightarrow \beta\text{-U}_3\text{O}_7 \rightarrow \text{U}_3\text{O}_8$.^[1] Excess oxygen atoms are first incorporated inside the lattice of the hyperstoichiometric phase UO_{2+x} , and after a certain threshold (increasing with temperature up to $x = 0.24$) start rearranging in cuboctahedral clusters with the formation of U_4O_9 (or U_4O_{9-y}).^[2] Further oxidation introduces more cuboctahedra leading to an anisotropic distortion of the lattice and the formation of tetragonal U_3O_7 .^[3] These stages involve diffusion-controlled processes (pseudo-parabolic weight gain curve), while the successive formation of U_3O_8 is driven by a combination of nucleation and growth, and microcracking (sigmoidal weight gain curve).^[4] These cracks, fundamental for the development of U_3O_8 , start appearing only after an incubation time, needed for the formation of a layer of U_3O_7 thick enough to induce stress due to the lattice mismatch with pristine UO_{2+x} .^[5] Recent studies showed that loose powders under a certain size (200 nm) did not develop U_3O_8 after being oxidized under air.^[6] In this work, similar results were obtained on sintered UO_2 pellets having grain size of $163 \pm 9 \text{ nm}$.

EXPERIMENTAL. The three UO_2 samples of different grain sizes were produced by Spark Plasma Sintering (SPS) under different conditions.^[7] The resulting samples had a density of 95 % TD, and grain sizes of $3.08 \pm 0.06 \mu\text{m}$ (*micro*), $478 \pm 17 \text{ nm}$ (*sub- μ*), and $163 \pm 9 \text{ nm}$ (*nano*). An annealing treatment (2 h, 600°C , Ar-4% H_2) was performed to reduce all stoichiometries to exactly $\text{UO}_{2.00}$.

A fragment of each pellet was prepared for P-XRD by manual milling in an agate mortar for one minute, and then poured into a glass capillary open at both ends to allow air-flow. These samples were then shipped to the ROBL-II beamline where the *in situ* oxidation study was performed. XRD patterns were continuously acquired during 21 h at 300°C , with an acquisition time of 10 s in the early stages and 30 s after some hours. Data were recorded using a Pilatus3X 2M detector (Dectris Ltd.), with a sensitive area of $253.7 \times 288.8 \text{ mm}^2$ (width \times height).

RESULTS. All three samples share a similar behavior in the initial phase of the oxidation experiment. The appearance of the reflections of U_4O_9 and U_3O_7 can be seen in Fig. 1. The formation of U_4O_9 leads to the appearance of shoulders on

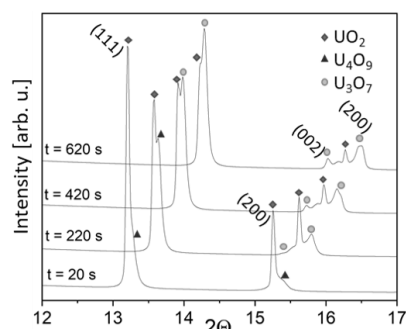


Figure 1. Evolution of the P-XRD pattern of the micrograined UO_2 sample in the first 620 s of the isothermal oxidative treatment. Patterns have been gradually shifted to higher 2θ for sake of readability.

the right side of the UO_2 peaks, while that of tetragonal U_3O_7 into the splitting of the 200 peak into the 200–002 doublet. Rietveld refinements of the XRD data allow calculating the volumetric fractions of each phase as oxidation proceeded. In each one of the three samples, U_4O_9 always remains below 20%, due to its prompt conversion to U_3O_7 , that is in all cases the main phase after about 10 min.

At this point, different oxidation behaviors can be observed, based on the grain size. The peaks of U_3O_8 start appearing in the micro and sub- μ samples after 15 and 30 min respectively. UO_2 completely disappears after 2.5 h in the nano and sub- μ sample, and after 10 h in the micro sample. In the nano sample, no U_3O_8 reflections can be detected at any stage of the experiment. Figure 2 shows a comparison of the initial and final stages of each sample.

This finding is particularly relevant for spent nuclear fuel safety, as the transformation of UO_2 into U_3O_8 involves a 36% volume expansion that can be detrimental to the integrity of the fuel pins.

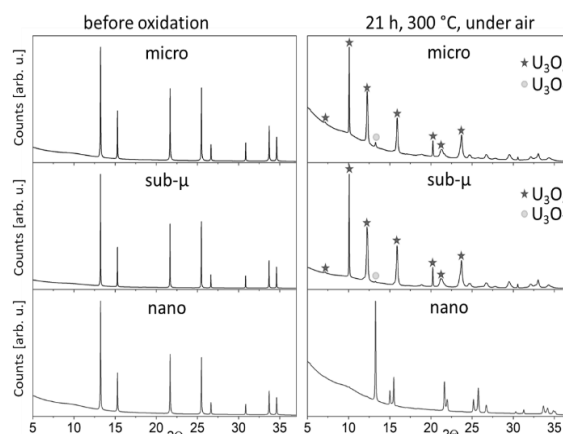


Figure 2. Comparison of the P-XRD patterns for the three samples before and after the oxidation treatment. Contrarily to the other two samples, no U_3O_8 was detected in the nano-sized compound after 21 h in air at 300°C .

- [1] Rousseau, G. *et al.* (2006) *J. Nucl. Mater.* **355**, 10–20.
- [2] Desgranges, L. *et al.* (2009) *Inorg. Chem.* **48**, 7585–7592.
- [3] Leinders, G. *et al.* (2016) *Inorg. Chem.* **55**, 9923–9936.
- [4] Quémard, L. *et al.* (2009) *J. Eur. Ceram. Soc.* **29**, 2791–2798.
- [5] Desgranges, L. *et al.* (2010) *J. Nucl. Mater.* **402**, 167–172.
- [6] Leinders, G. *et al.* (2016) *Inorg. Chem.* **55**, 3915–3927.
- [7] De Bona, E. *et al.* (2021) *J. Eur. Ceram. Soc.* **41**, 3655–3663.

Study of fission product behavior in (U,Pu)O_{2-x} SIM fuel

R. Caprani,^{1,2} D. Prieur,² P. Martin,¹ J. Martinez,¹ F. Lebreton,¹ C. Aloin,¹ M. Alibert,¹ J.-R. Sevilla,¹ L. Barnouin,¹ P. Signoret,¹ L. Picard,¹ G. Gabriel,¹ O. Miollan,¹ N. Clavier³

¹CEA, DES, ISEC, DMRC, Univ Montpellier, Marcoule, France; ²HZDR, Dresden, Germany; ³University of Montpellier, Montpellier, France

Investigating the fission products (FP) behavior in MOX fuel is critical to understand spent nuclear fuel behavior at the final repository stage. The fabrication of model materials consisting of fresh MOX fuel doped with stable FP isotopes was undertaken. The synthesized material is globally representative of fast reactor fuel, and of high Pu concentration regions in thermal reactor fuel. The samples showed microstructure and composition coherent with real irradiated fuel. Moreover, analysis techniques not available for spent fuel have been employed, furthering the understanding of FPs speciation in MOX fuel.

EXPERIMENTAL. We prepared mixed UO₂-PuO₂-FP powder by planetary milling. The powder was then pressed at 450 MPa and sintered at 1,700 °C under Ar + 4.3 % H₂ + 1,200 vpm H₂O to obtain cylindrical 5 × 5 mm² pellets. In order to separate the effect of selected FP, we produced a batch “S” containing only “soluble” FPs, and a batch “M” with the addition of FPs characteristic of the metallic inclusions observed in irradiated fuel.^[1] The Pu enrichment was set to Pu/U + Pu = 26 wt.-%; the full chemical composition is given in Tab. 1.

Table 1. Mass composition (wt.-%) of the two fabrication batches “S” and “M”. The difference from 100 is given by oxygen.

Element	S	M
Am	0.43	0.41
Ce	0.88	0.84
La	0.43	0.44
Mo	–	1.45
Nd	2.10	1.96
Pd	–	0.80
Pu	20.99	20.24
Rh	–	0.34
Ru	–	1.49
Sr	0.11	0.12
U	61.11	58.63
Y	0.11	0.10
Zr	1.00	1.18

Optical and Electronic Microscopy (OM, SEM), XRD, μ-Raman, and EPMA analysis have been performed at CEA Marcoule, while XANES data have been collected at the Rosendorf beamline at ESRF.

RESULTS. Globally the sample microstructures are representative of spent MOX fuel. In particular, EPMA measurements show that all soluble FPs are found in solid solution in the matrix, while the white phases (metallic inclusions) made of Mo, Pd, Rh, and Ru are observed as expected as separate phases (Fig. 1).

By XRD we found monophasic fluorite, which was the target structure of our fabrications. In fabrication M, although present, the metallic precipitates are not visible in the diffracted pattern because they remain below the concentration threshold for laboratory equipment (< 5 wt.-%).

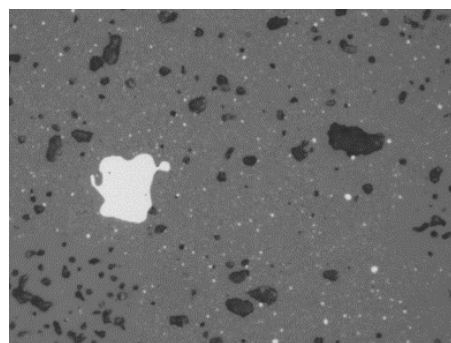


Figure 1. Optical image at magnification × 100 highlighting the metallic precipitates (white) found in samples of composition M. In black are the porosities, and in grey the (U,Pu,FPs)O₂ matrix.

The lattice parameter of the fluorite phase of all samples was found to be coherent with Duriez Law, adequately corrected accounting for the FP presence.^[2] XANES measurements at Mo, Pd, Rh and Ru K-edges confirmed that all these elements occur only in metallic form, in mixed alloys with varying composition.

The data collected at U, Pu and Am L_{III} edges, allowed us to compute their respective oxidation state and the O/HM (HM = U + Pu + Am) ratio in the system. The *as-sintered* O/HM is 2.011 for fabrication S, and 2.040 for fabrication M, respectively, remarkably close to the fabrication target of 2.00. On a local scale, the samples are found to respect the homogeneity specifications: no pure PuO₂ residue of fabrication has been found. Nevertheless, local Pu-hotspots are observed (Pu < 50 wt.-%) systematically enriched with soluble FP, in particular with Ce, La, Nd, and Zr (Fig. 2).

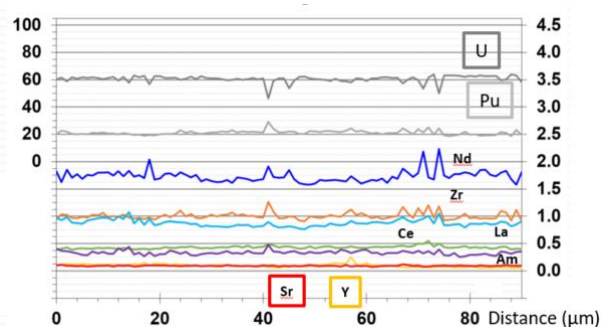


Figure 2. EPMA elemental mass concentration (wt.-%) quantitative profile. From top to bottom: U, Pu, Nd (blue), Zr (orange), Ce (cyan), La (green), Am (purple), Sr (red), and Y (yellow). U and Pu concentrations are plotted on the left axis, while all other elements are plotted on the right axis.

ACKNOWLEDGEMENTS. The authors acknowledge the ESRF facility, and the beamline ROBL in particular, for the provision of instruments and beam-time.

[1] Guerin, Y (2012) in: *Comprehensive Nuclear Materials*, p. 547–578, Elsevier, Oxford.

[2] Duriez, C. et al. (2000) *J. Nucl. Mater.* **277**, 143–158.

High energy resolution X-ray spectroscopy methods at the Rossendorf beamline for actinide science

E. F. Bazarkina, K. O. Kvashnina

The X-ray emission spectrometer opens analytical opportunities to study the electronic structure of actinides. The main techniques, which can be realized with help of the spectrometer, are HERFD-XANES, RIXS, and RXES. This report summarizes the technical details and main advantages of these techniques for actinide compounds.

XES is one of the four experimental end-stations available at ROBL (BM20, ESRF).^[1] It is suitable for such techniques as high-energy resolution fluorescence-detection X-ray absorption near-edge structure spectroscopy (HERFD-XANES), resonant inelastic X-ray scattering (RIXS), and/or resonant inelastic X-ray emission spectroscopy (RXES) at $M_{4,5}$ and $L_{1,2,3}$ edges. Compared to conventional XANES, the HERFD technique is in particular interesting for electronic structure studies, due to its capacity to improve the energy resolution of the detected spectra.^[1,2]

EXPERIMENTAL. The main optical elements of the XES spectrometer include five spherically bent crystal analyzers and the Ketek detector, mounted together with the sample in vertical Rowland circle geometry (1 m or 0.5 m diameter). When actinide atoms are excited by an initial X-ray at particular absorption edge, crystal analyzers select the emitted fluorescence according to Bragg's law and focus the diffracted monochromatic photons into the energy-selective detector. The dedicated PyXES software (©Vadim Dyadkin, SNBL@ESRF, <https://soft.snbl.eu/pyxes.html#>,^[1]) allows to choose the emission line of interest, and the corresponding crystal analyzer set (see available Si and Ge crystals in [1]), then based on the theoretical values it moves analyzers and detector into predefined positions, which needs to be adjusted for each crystal manually with the photons from the reference sample (*i.e.* using real X-ray beam). The spectrometer alignment has to be done for each change of emission line or each change of the incident energy. As an example, Si220 crystals in 75.17 Bragg angle are used for the U_{M4} edge, Ge220 crystals with 79.85 Bragg angle for the Th_{M4} edge, and Si220 with 66.00 Bragg angle for the Pu_{M4} edge. Sample environments include: (a) a cryostream (to avoid radiation damage of sample by cooling without signal loose); (b) a furnace for *in situ* measurements with tender X-rays under high temperature (up to 850 °C) and selected gas flow (*e.g.*, air, N_2 , He).

RESULTS. The main advantage of the emission spectrometer for actinides lays in the significant gain in spectral energy resolution. This is due to the fact that the width of the spectral features is defined by the smaller core-hole lifetime broadening in the final state of the spectroscopic process – in the emission process. Several factors impact the final resolution: (1) the selected Bragg angle of the analyzer, which is thus linked to the selected energy (the best resolution is obtained at Bragg angles close to 90° due to the geometrical effect of the Johann geometry of the spectrometer); (2) the vertical X-ray beam size for the vertical spectrometer geometry (50–100 μm at ROBL); (3) the choice between 0.5 m and 1 m diameter XES spectrometer configuration (the best resolution is obtained at 1 m, whereas 0.5 m allows recording weaker signals); (4) the selected emission line (see Fig. 1); (5) the length of air-filled part of the optical path (especially crit-

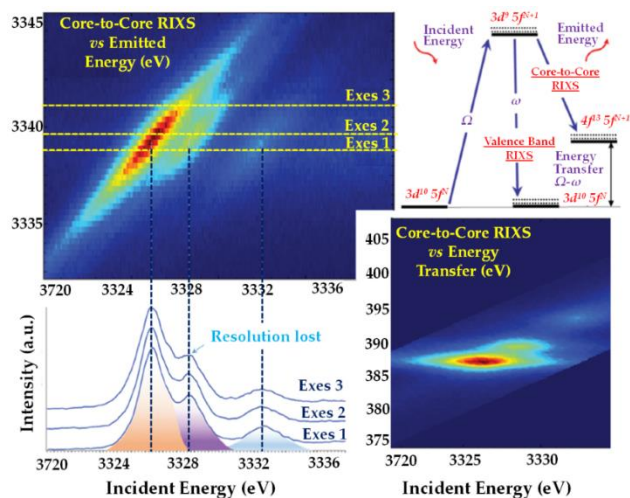


Figure 1. The 3d–4f RIXS of $UO_2(NO_3)_2 \cdot 6H_2O$ recorded near the maximum of the $U_{M\beta}$ emission line. The corresponding cuts through the RIXS plane at different emission energies (HERFD scans) and the energy diagram of the core-to-core and valence-to-core processes.^[2]

ical for the tender X-rays), the use of He-bag with the maximum filling of the optical path is favorable for better resolution, due to the rapid increase in the intensity of the detected signal. The resolution can be slightly improved by a homemade motorized slit in front of the detector.

The $M_{4,5}$ HERFD-XANES spectra allow fingerprinting the oxidation state of the actinides.^[2,3] The maximum of $M_{4,5}$ HERFD-XANES spectra is shifted by energy with oxidation state. The chemical shift between various oxidation states $U(III)$ – $U(IV)$ – $U(V)$ – $U(VI)$ is not linear, *i.e.* the shift between $U(IV)$ and $U(V)$ is much greater than the one between $U(V)$ and $U(VI)$. The coordination geometry may impact the energy shift only by 0.1–0.2 eV versus 1–2 eV which is observed for various U oxidation states. The L_3 HERFD-XANES spectroscopy of actinides benefits from the high penetration depth in the hard X-ray energy range (~17,000–18,000 eV) and probes the actinide 6d states (2p–6d transitions) which is strongly local-coordination-dependent. The quantification of different oxidation states/coordination in HERFD-XANES spectra can be done using iterative transformation factor analysis (ITFA).^[4,5] The detection limit at ROBL is currently 0.7 ppm.

The RIXS data represent 2D maps where the incident energy is plotted at the x-axis, and the emitted energy (E_e) is plotted at the y-axis (Fig. 1 top). Alternatively, the energy difference between the incident (E_i) and the emitted energies (E_e) may be plotted (Fig. 1 bottom). Variations of color in the plot represent scattering intensities. During the analysis, special attention has to be paid to the features that do not lie on the diagonal cut (related to HERFD), which provides finer details on the electronic structure. The main features of HERFD-XANES and RIXS spectra of actinides can be interpreted with the help of theoretical calculations.^[6]

- [1] Scheinost, A. C. *et al.* (2020) *J. Synchrotron Rad.* **28**, 333–349.
- [2] Kvashnina, K. O. *et al.* (2022) *Chem. Commun.* **58**, 327–342.
- [3] Kvashnina, K. O. *et al.* (2022) this report, p. 26.
- [4] Rossberg, A. *et al.* (2003) *Anal. Bioanal. Chem.* **376**, 631–638.
- [5] Rossberg, A. *et al.* (2009) *Environ. Sci. Technol.* **43**, 1400–1406.
- [6] Butorin, S. M. (2020) *Inorg. Chem.* **59**, 16251–16264.

Probing the 5f orbitals of hexavalent uranium by HERFD

L. Amidani, M. Retegan,¹ A. Volkova,² K. Popa,³ P. M. Martin,⁴ K. O. Kvashnina

¹ESRF, Grenoble, France; ²Lomonosov Moscow State University, Moscow, Russia; ³European Commission Joint Research Centre, Karlsruhe, Germany; ⁴CEA, DES, ISEC, DMRC, University of Montpellier, Bagnols sur Cèze, France

Measuring the M-edges of actinides with High-Energy-Resolution Fluorescence Detected X-ray Absorption Near-Edge Structure (HERFD-XANES) spectroscopy is a very powerful investigation tool since the unoccupied 5f states are directly probed. While its sensitivity to the actinide oxidation state is well established, the effects of local geometry have never been thoroughly investigated. We recently addressed this dependence for U⁶⁺. Experimental M₄-edge HERFD-XANES on a set of samples with U⁶⁺ in different local geometries were interpreted based on DFT and crystal field theory simulation of spectra.

Understanding the effects of local coordination on M_{4,5}-edges HERFD-XANES is necessary for a correct interpretation of the spectra. Studying U⁶⁺ largely simplifies the task due to the absence of 5f electrons. Under these circumstances, application of DFT-based methods, which naturally accounts for the effects of the surrounding atoms, is justified. Moreover, hexavalent uranium features a rich variety of coordination geometries, offering an ideal playground for systematic studies.^[1]

RESULTS. The set of U⁶⁺-bearing samples investigated is reported in Tab. 1. The local configuration goes from uranate (Sr₃UO₆) to uranyl (Cs₂UO₂Cl₄) and spans three U local symmetries, *i.e.* O_h, D_{3d} and D_{4h}. A scheme of U coordination is given in Fig. 1. Table 1 reports also bond lengths and the splitting of 5f states due to local symmetry. 3, 5 and 5 groups of f-orbitals are found for O_h, D_{3d} and D_{4h}, respectively. Experimental M₄ HERFD-XANES are shown in Fig. 1 and present marked differences. In particular, the high-energy feature (C) shifts to higher energies when going from uranate to uranyl (3.6 eV shift). Between the main peak (A) and C, an additional peak (B) can be distinguished for the uranate (Sr₃UO₆) and the prototypical uranyl case (Cs₂UO₂Cl₄). The spectra calculated with the DFT-based code FDMNES are reported as thin lines below the experimental curves.^[2] The code has as primary entry the atomic coordinates. The very good agreement indicates that spectral differences reflect the signature of the local environment. Inspection of the f-Density of States (DOS) and its components allows assignment of peaks to specific f-orbitals. For uranate, the three peaks correspond to the three groups of symmetry-split f-orbitals, with peak C given by the t_{1u} orbitals (f_{3,3}, f_{3,3}, and f_{2,3}). In all other samples, peak C corresponds to f_{2,3}, whose lobes point to the closest ligands. Further insight into peak assignment is provided by calculating the spectra with Crystal Field Theory (CTF) with the code Quanyty.^[3] To observe the correlation between specific symmetry-split f-orbitals and spectral peaks, we varied the energy of the orbital group and

Table 1. The set of samples measured, with the relative U local symmetry, bond length and splitting of 5f orbitals expected according to symmetry.

Sample	U sym.	U bond length (Å)	5f splitting
Sr ₃ UO ₆	O _h	2.069 × 2; 2.099 × 2; 2.103 × 2	a _{2u} , t _{2u} , t _{1u}
CaUO ₄	D _{3d}	1.961 × 2; 2.295 × 6	a _{1u} , e _u , e _u , a _{2u} , a _{2u}
β-SrUO ₄	D _{4h}	1.877 × 2; 2.186 × 2; 2.205 × 2	b _{1u} , b _{2u} , e _u , e _u , a _{2u}
Cs ₂ UO ₂ Cl ₄	D _{4h}	1.780 × 2; 2.665 × 2; 2.687 × 2	b _{1u} , b _{2u} , e _u , e _u , a _{2u}

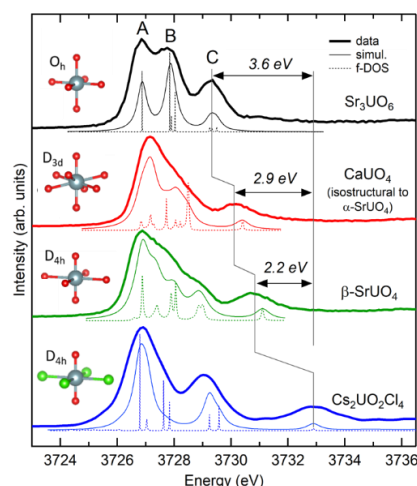


Figure 1. Experimental (thick line) and simulated (thin line) U M₄ HERFD-XANES. The corresponding U total f-DOS are reported below each calculation (dotted line). The progressive shift of peak C is highlighted by a vertical line. Sketches of the different symmetry groups are shown on the left.

observed which spectral peak was affected by the change (energies of the f-orbitals can be given as input in place of CFT parameters). Results are reported in Fig. 2 and confirm the assignment based on DFT calculations. For a detailed discussion of peak assignment, the reader is referred to our recent publication.^[4]

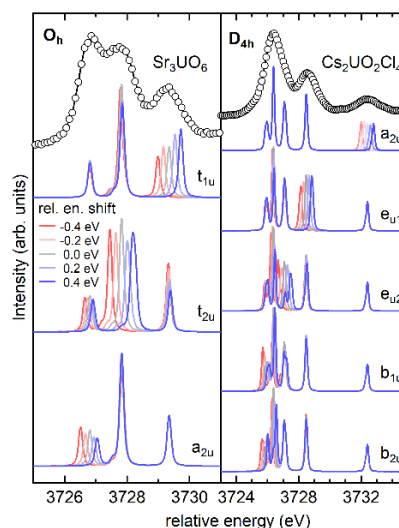


Figure 2. Crystal Field (CF) XANES calculations obtained by shifting the energy of each group of CF-split f-orbitals. Each group of calculations is labelled by the symmetry of the shifted orbitals. Experimental data are shown on top (open circles).

Our study clearly shows the sensitivity of M₄-edge HERFD-XANES to the local environment of U and provides a solid theoretical interpretation of spectral peaks as given by specific groups of symmetry-split f-orbitals.

- [1] Burns, P. C. (2005) *Can. Mineral.* **43**, 1839–1894.
 [2] Bunău, O. and Joly, Y. (2009) *J. Phys.: Condens. Matter* **21**, 345501.
 [3] Haverkort, M. W. et al. (2014) *EPL Europhys. Lett.* **108**, 57004.
 [4] Amidani, L. et al. (2021) *Inorg. Chem.* **60**, 16286–16293.

High Energy Resolution X-ray spectroscopy at the actinide $M_{4,5}$ edges

K. O. Kvashnina, S. M. Butorin¹

¹Condensed Matter Physics of Energy Materials, X-ray Photon Science, Department of Physics and Astronomy, Uppsala University, Uppsala, Sweden

In this article, we show that high-energy resolution X-ray spectroscopy at the actinide $M_{4,5}$ edges provides fingerprint information on both the actinides' oxidation states and their local symmetry.

More than 10 years have passed and more than 100 papers were published after the first X-ray spectroscopy experiment in high-energy resolution mode on uranium systems at the UM_4 edge (~ 3728 eV) at ID26 beamline of ESRF in 2009, where the X-ray emission spectrometer was utilized.^[1–3] Significant progress has been made meanwhile, and X-ray absorption spectroscopy (XAS) or X-ray absorption near edge structure (XANES) spectroscopy in the high-energy resolution fluorescence detection (HERFD) mode (also known as HR-XANES) is now a common technique for probing the electronic structure of actinides and for studying the physics and chemistry of the f-block elements.^[4] After the first experiment, several beamlines at various synchrotron facilities made an effort to adapt their experiment stations to the tender X-ray range and to equip them with X-ray emission spectrometers. All those efforts will surely be beneficial in terms of understanding the mechanisms of chemical reactions involving actinides at the atomic level, that the HERFD method at the tender $M_{4,5}$ X-ray range (3,500–4,000 eV) offers.

RESULTS. We review here the capacity of the HERFD method at the actinide $M_{4,5}$ edges. The highest demand of the use of this method is to probe the actinide oxidation state and 5f occupation. Figure 1a shows the HERFD data at the UM_4 edge of UO_2 , UO_3 and KUO_3 as representatives of tetravalent (UO_2), hexavalent (UO_3) and pentavalent (KUO_3) uranium systems. The energy of the HERFD-XANES maximum corresponds to the energy difference between the 3d and 5f levels. As soon as the 5f shell gains or loses more electrons, it causes a chemical shift in XANES that can be detected. It should be noted that the chemical shift between various oxidation states in the row U(IV)-U(V)-U(VI) does not follow a straight line.

At the same time, the energy position of the $UM_{4,5}$ HERFD spectra can be strongly influenced not only by the U oxidation state, but also by the coordination geometries and the

associated ligand field splitting of the 5f shell. However, the detectable difference will be in order of 0.1 eV versus 1–2 eV observable for U oxidation state changes. Figure 1b summarizes the position of the HERFD peak for several U-containing systems ordered along increasing energy and oxidation state. It shows that chemical state verification still can be done even in the presence of various geometries and ligands around the absorbing U atom.

Figure 1c reports the UM_4 HERFD data for tetravalent, pentavalent and hexavalent species. In case of tetravalent species, the energy position of the peak maximum increases from UO_2 to UCl_4 and is related to the ability of an element to attract the bonded electrons towards itself or in other words related to the variation of electronegativity. The difference in the energy position of the HERFD peak between KUO_3 and $NaUO_3$ is almost negligible, but noticeable. Figure 1c (right) shows that not only the energy position of the HERFD peak but also the shape changes significantly. Local symmetry and changes of the crystal parameters always influence the HERFD spectral shape. An example of when the crystal structure influence can be studied is the case of the hexavalent uranium species with $5f^0$ ground state configuration. The spectrum of $UO_2(NO_3)_2 \cdot 6H_2O$ contains three primary peaks separated by 2 and 4 eV between each other on the incident energy scale. These peaks reflect the splitting of the U 5f unoccupied states and were assigned to transitions to the nonbonding $5f_{d_{xy}}$ and $5f_{d_{yz}}$, antibonding $5f_{d_{xz}}$, and antibonding $5f_{d_{yz}}$ molecular orbitals. The second peak provides information about equatorial U–O bonds and the third one provides information on U–O axial bonds. The uranate $CaUO_4$ -HERFD spectrum shows a very different profile. Detailed information on the influence of local structure in hexavalent uranium species can be found in literature.^[5]

It has been demonstrated in our recent article that HERFD spectral features are shaped by the electron-electron interaction and directly depend on the number of available f electrons in the systems, thus allowing the unambiguous detection of the 5f occupancy and the oxidation state of complex actinide systems.^[4] In addition, HERFD experiments at the actinide $M_{4,5}$ edges allow for probing the crystal field, charge transfer effects, speciation and covalency effects in the crystal and electronic structure of actinides. Such fundamental knowledge is a key step towards solving the extreme complexity of the chemistry problems with radionuclides, which in turn may improve the prediction of the radionuclide behavior in the environment and the safety of nuclear waste disposals.

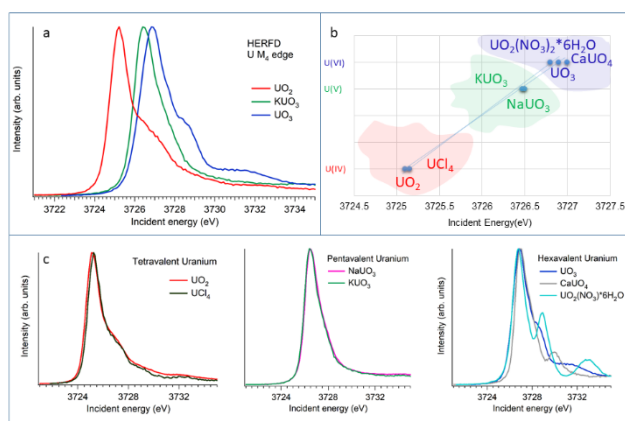


Figure 1. Uranium M_4 HERFD data of UO_2 , KUO_3 and UO_3 with U(IV), U(V) and U(VI) oxidation state respectively (a). The positions of the HERFD peak for several U-containing systems in the order of the increasing energy and oxidation state (b). UM_4 HERFD data for several tetravalent, pentavalent and hexavalent systems in different crystal structures (c).

[1] Kvashnina, K. O. *et al.* (2013) *Phys. Rev. Lett.* **111**, 253002.

[2] Kvashnina, K. O. and Butorin, S. M. (2009) *U M4 HERFD RIXS data UO2*, doi:10.1515/esrf-dc-450082049.

[3] Kvashnina, K. O. and Butorin, S. M. (2009) *Uranium M4 HERFD data*, doi:10.1515/esrf-dc-450082001.

[4] Kvashnina, K. O. and Butorin, S. M. (2022) *Chem. Commun.*, 327–342.

[5] Amidani, L. *et al.* (2021) *Inorg. Chem.* **60**, 16286–16293.

Optimization of the U-O phase diagram with *in situ* XANES

D. Prieur, M.-M. Desagulier,¹ D. R. Neuville,² C. Guéneau,³ E. Epifano,⁴ K. Dardenne,⁵ J. Rothe,⁵ P. M. Martin¹

¹CEA, DES, ISEC, DMRC, University of Montpellier, Marcoule, France; ²Université de Paris, Institut de physique du globe de Paris, CNRS, Paris, France; ³Université Paris-Saclay, CEA, Service de la Corrosion et du Comportement des Matériaux dans leur Environnement (SCCME), Gif-sur-Yvette, France; ⁴CIRIMAT laboratory, University of Toulouse, CNRS, INPT, UPS, ENSIACET, Toulouse, France; ⁵Karlsruhe Institute of Technology (KIT), Institute for Nuclear Waste Disposal, Karlsruhe, Germany

Here, we show how *in situ* XANES is suitable and relevant for phase diagram determination. New experimental data points have been collected using this method and discussed in regard to the available data. Comparing our experimental data with thermodynamic calculations, we observe that the current version of the U-O phase diagram misses some experimental data in specific domains. This lack of experimental data generates inaccuracy in the model, which can be overcome using *in situ* XANES.

EXPERIMENTAL. The *in situ* XANES measurements were conducted at the INE-Beamline of the KIT synchrotron light source. The measurements were conducted on square samples extracted from a UO_{2.00} dense pellet. A dedicated furnace was designed to collect *in situ* XAS data on radioactive samples in various atmospheres and up to 2000 K.^[1] The binary phase diagram and the oxygen potential evolution in function of the O/U ratio for temperature were calculated with the Thermo-Calc software using the model derived by Guéneau *et al.*^[2]

RESULTS. Figure 1 presents the range of temperature and oxygen potential in which experimental data have already been collected. Our study provides new experimental data and especially in condition domains which have not been studied before.

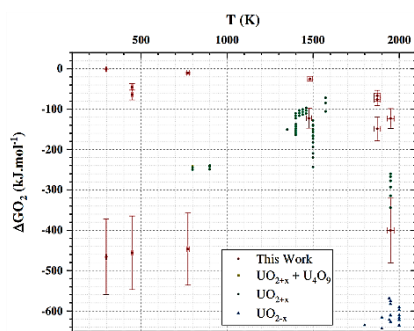


Figure 1. Oxygen potential and temperature of our experimental data and the selected experimental U-O thermodynamic data.

U_{LIII} XANES spectra have been collected for each data point. Figure 2 provides an example of XANES spectra recorded on a sample heated at 1873(19) K in different atmospheres. The sample heated at the most reducing conditions (dry Ar-H₂) is clearly stoichiometric. On the contrary, a shift towards higher energy, as well as a broadening, appears when heated

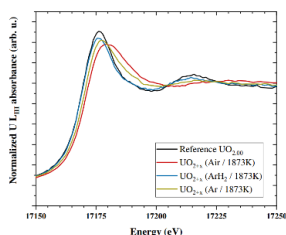


Figure 2. U_{LIII} XANES spectra of UO_{2+x} samples measured at 1,873(19) K in different oxygen potentials.

in more oxidizing conditions (*i.e.* Ar and air). These spectral changes indicate a modification of U oxidation state, and especially of oxidation in the presented case.

The U_{LIII} XANES spectra were fitted in order to determine the molar fraction of U^{IV}, U^V, and U^{VI}, as well as the O/U ratio. By plotting our O/U experimental values into the U-O phase diagram (Fig. 3), we can observe that our data are scattered in different domains: UO_{2+x}, UO₂-U₄O₉ and UO_{2+x}-U₃O₈. It is remarkable to note that, for each collected experimental point, the best XANES fitting results are systematically obtained using component species matching the end-members indicated in the phase diagram.

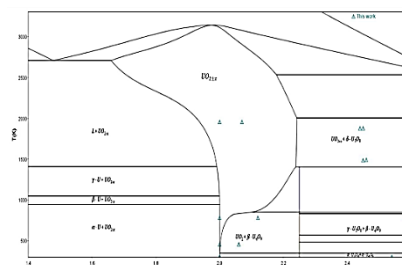


Figure 3. Our experimental points (blue triangles) in the calculated U-O phase diagram.

Figure 4 compares, for a given temperature, our experimental values (circle) with the oxygen potential curve (line) derived from the thermodynamic modelling. Note that the calculated data are extrapolated from the existing experimental data (squares) and the thermodynamic data of each U oxide end-members considered in the CALPHAD model.

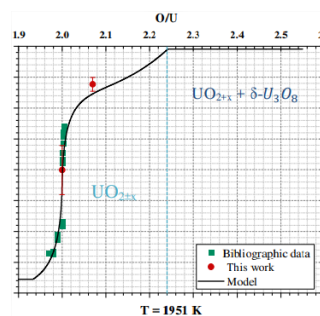


Figure 4. Comparison between the O/U calculated (line) and our experimental data (circle), and the selected experimental data (squares).

The *in situ* method is of huge interest for a wide range of applications in which the oxidation states drive the chemical processes. Here, we demonstrate that *in situ* XANES, coupled with thermodynamic calculations, is a proper combination to assess the phase diagram. Indeed, *in situ* XANES allows collecting relevant data close to the real thermodynamic conditions encountered in the nuclear fuel cycle.

[1] Prieur, D. *et al.* (2021) *J. Synchrotron Rad.* **6**, 1684–1691.
[2] Guéneau, C. *et al.* (2021) *J. Nucl. Mat.* **419**, 145–167.

Nonradiative energy transfer and selective charge transfer in $\text{WS}_2/(\text{PEA})_2\text{PbI}_4$ heterostructure

M. Karpińska,¹ M. Liang,² R. Kempt,³ K. Finzel,³ M. Kamminga,² M. Dyksik,¹ N. Zhang,¹ C. Knodlseedler,¹ D. K. Maude,¹ M. Baranowski,⁴ Ł. Kłopotowski,⁵ J. Ye,² A. Kuc, P. Plochocka¹

¹CNRS, Toulouse, France; ²University of Groningen, Groningen, The Netherlands; ³Technische Universität Dresden, Dresden, Germany; ⁴University of Wrocław, Wrocław, Poland; ⁵Polish Academy of Sciences, Warsaw, Poland

Van der Waals heterostructures are currently the focus of intense investigation; this is essentially due to the unprecedented flexibility offered by the total relaxation of lattice matching requirements and their new and exotic properties compared to the individual layers. Here, we investigated the hybrid transition-metal dichalcogenide (TMD)/2D perovskite heterostructure $\text{WS}_2/(\text{PEA})_2\text{PbI}_4$ (PEA - phenylethylammonium).^[1] We present the first density-functional theory (DFT) calculations of a heterostructure ensemble, which revealed a novel band alignment, where direct electron transfer is blocked by the organic spacer of the 2D perovskite. In contrast, the valence band forms a cascade from WS_2 through the PEA to the PbI_4 layer allowing hole transfer. These predictions are supported by optical spectroscopy studies, which provide compelling evidence for both charge transfer and nonradiative transfer of the excitation (energy transfer) between the layers. Our results show that TMD/2D perovskite heterostructures provide a flexible and convenient way to engineer the band alignment.

EXPERIMENTAL. Only the theory part performed by the group members from HZDR and TUD is shown here, experimental details are given in literature.^[1] A bilayer model structure of $\text{WS}_2/(\text{PEA})_2\text{PbI}_4$ (Fig. 1 left) was created in the Virtual NanoLab with less than 0.1 % strain on the individual layers, resulting in a superstructure with 239 atoms. The structure can be represented by supercell vectors $m_1 = (-3, -2)$, $m_2 = (4, 2)$, $n_1 = (-3, 8)$, and $n_2 = (2, -11)$ with a rotation angle of $\theta = 79^\circ$ and a vacuum spacing of 100 Å (other representation choices are possible). This model structure was relaxed using FHI-aims employing the PBE functional on tight tier 1 numeric atom-centered orbitals, including the nonlocal many-body dispersion correction and scalar relativistic corrections on a $4 \times 4 \times 1$ Γ -centered k-grid. The forces and stresses were minimized below 0.05 eV \AA^{-1} . The electronic band structure, the Mulliken projections, and the density of states were calculated including spin-orbit coupling and dipole correction on a $6 \times 6 \times 1$ Γ -centered k-grid.

RESULTS. We have presented the evidence for both charge and energy transfer in the $\text{WS}_2/(\text{PEA})_2\text{PbI}_4$ heterostructure at low temperatures. Due to particular band alignment be-

tween the $(\text{PEA})_2\text{PbI}_4$ and WS_2 layers, estimated from the DFT simulations, only the hole transfer is present from the TMD to the 2D perovskite. Simultaneously, the electron exchange between the layer is completely blocked. However, the excitation can be transferred from $(\text{PEA})_2\text{PbI}_4$ to WS_2 via an energy transfer process, which is especially efficient close to the B-exciton resonance in WS_2 . This is confirmed by photoluminescence excitation showing that WS_2 monolayer can be effectively sensitized by the $(\text{PEA})_2\text{PbI}_4$.

The DFT results in detail: our simulations consider the full structure and orbital hybridization of a TMDs/2D perovskite heterostructure. The band structure shows that the top of the valence band is mainly composed of orbitals from the PbI_4 slab, while the conduction band is dominated by the WS_2 states. Consequently, a type-II band alignment is formed between the TMD layer and the PbI_4 slab. The valence band maximum at Γ is localized mostly in the PbI_4 layer, while the conduction band minimum at Ω is localized in the WS_2 layer. The conduction band alignment provides a barrier for electron transfer between the WS_2 and the PbI_4 layer. Indeed, based on the Hirshfeld charge analysis, we find negligible charge transfer from the TMD layer to the organic spacers of $0.1 e^-$ averaged over the whole model structure consisting of 239 atoms. Moreover, in the valence band, we have an interesting situation: the peak of the PEA density of states is located around -6.5 eV ; however, a closer inspection of the density of states plot reveals that there are also states related to PEA slightly above WS_2 and below PbI_4 . The density of these states is comparable to the WS_2 density of states close to the top of valence band. Therefore, in the valence band, the WS_2 , PEA, and PbI_4 band edges form a cascade, which favors the transfer of photoinduced holes from WS_2 to the PbI_4 layer (Fig. 1, right). Thus, stacking WS_2 with $(\text{PEA})_2\text{PbI}_4$ leads to a novel band diagram, where only one type of carrier can be directly transferred between the layers, *i.e.*, holes. At the same time, strong excitonic effects in both materials, together with their proximity, should favor energy transfer from the perovskite layer to the TMD layer.

ACKNOWLEDGEMENTS. A.K., R.K., and K.F. gratefully acknowledge the Gauss Centre for Supercomputing e.V. (www.gauss-centre.eu) for funding this project by providing computing time through the John von Neumann Institute for Computing (NIC) on the GCS Supercomputer JUWELS at Jülich Supercomputing Centre (JSC). Furthermore, A.K., R.K., and K.F. gratefully acknowledge the support from GWK for funding this project by providing computing time through the Center for Information Services and HPC (ZIH) at TU Dresden. A.K. acknowledges the financial support from Deutsche Forschungsgemeinschaft (DFG, German Research Foundation) within SFB1415 project number 417590517 and the association with the SPP2244 (2DMP).

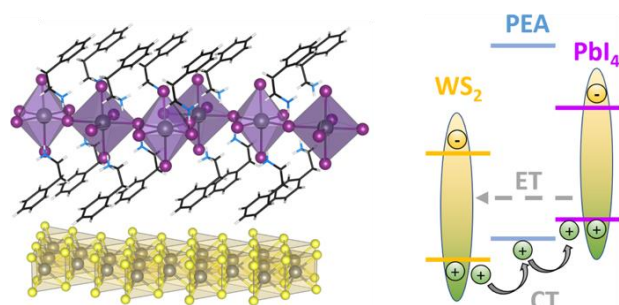


Figure 1. Atomic structure of $\text{WS}_2/(\text{PEA})_2\text{PbI}_4$ heterostructure. $(\text{PEA})_2\text{PbI}_4$ is the 2D perovskite with PbI_4 octahedra and PEA as organic spacers (left). Summary of the band alignment in the $\text{WS}_2/(\text{PEA})_2\text{PbI}_4$ heterostructure resulting from DFT calculations (right). The charge transfer (CT) and energy transfer (ET) paths are indicated.

[1] Karpińska, M. *et al.* (2021) *ACS App. Mater. Interface* **12**, 33677–33684.

Coordination and electrochemical switching on paddle-wheel complexes containing an As–Ru or a Sb–Ru axis

R. Gericke, J. Wagler¹

¹Institut für Anorganische Chemie, Technische Universität Bergakademie Freiberg, Freiberg, Germany

Inspired by the known complex $[\text{PhP}(\mu\text{-PyO})_4\text{Ru}(\text{CO})]$ (PyO = 2-pyridyloxy), the family of group 15 paddle-wheel complexes has been expanded to $[\text{PhPn}(\mu\text{-PyO})_4\text{Ru}(\text{L})]$ (Pn = P, As, Sb; L = NCMe, CO). Electrochemical investigations of the $[\text{PhSb}(\mu\text{-PyO})_4\text{Ru}(\text{L})]$ complexes showed reversible oxidation of the complexes with L = NCMe and back-formation of the complexes with L = NCMe upon oxidation of the complexes with L = CO in NCMe. The easily accessible complex $[\text{PhSb}(\mu\text{-PyO})_4\text{RuCl}]$ exhibits reversible electrochemical and coordinative exchange with its reduced analogue $[\text{PhSb}(\mu\text{-PyO})_4\text{Ru}(\text{NCMe})]$ under retention of the paddle-wheel motif and Sb–Ru bond properties.^[1]

EXPERIMENTAL. *Synthesis of $[\text{PhSb}(\mu\text{-PyO})_4\text{Ru}(\text{NCMe})]$ (Sb1).* A total of 100 mg (258 μmol) of $\text{PhSb}(\text{PyO})_2$ and 100 mg (262 μmol) of $[\text{Ru}(\text{PyO})_2(\text{nbnd})]$ (nbnd = norbornadiene) were suspended in NCMe (2 mL) and stirred under reflux for 10 min. The yellow suspension was cooled to ambient temperature, whereupon the solid product was filtered, washed with NCMe (2.5 mL), and dried in vacuo. Yield: 116 mg (153 μmol , 59%).

Synthesis of $[\text{PhSb}(\mu\text{-PyO})_4\text{Ru}(\text{Cl})]$ (Sb2). A total of 100 mg (258 μmol) of $\text{PhSb}(\text{PyO})_2$ and 100 mg (262 μmol) of $[\text{Ru}(\text{PyO})_2(\text{nbnd})]$ were dissolved in chloroform (3 mL) and stirred under reflux for 1 h. The resulting blue suspension was cooled to ambient temperature and filtered. The blue solid was washed with chloroform (0.5 mL) and dried in vacuo (42 mg). After 1 week of vapor diffusion of Et_2O into the filtrate, the supernatant was decanted off, and the remaining blue solid was washed with Et_2O (1 mL) and dried in vacuo (65 mg). Yield: 107 mg (171 μmol , 66%).

RESULTS. The cyclic voltametric curve of Sb2 exhibits a reduction peak at $E_{\text{pa}} = -0.39$ V (Fig. 1, black trace). Reverting to a more positive potential, the corresponding oxidation occurs with noticeably lower intensity, but the characteristic oxidation peak of Sb1 (red trace) appears, indicating the replacement of chloride at Sb2^- by NCMe with the formation of Sb1. Upon reverting to a more negative potential, the reduction peaks of both Sb1 and Sb2 could be detected, but this time the peak current of the reduction of Sb1^+ is less intense than the peak current of the oxidation of Sb1, which indicates that Sb1^+ undergoes replacement of NCMe by Cl to reform Sb2. When the scan rate was increased from 100 to 500 mV/s, which makes the diffusion and exchange processes less pronounced, the oxidation potential of Sb2^- at $E = -0.29$ V could be measured. Increasing the number of cycles did not change the trace, which indicates the presence of an electrochemical and coordinating “equilibrium” at a constant scan rate. This phenomenon is reminiscent of other types of molecular hysteresis, such as the exchange of Ru–O versus Ru–S coordination of sulfoxide ligands in combination with CV reduction and oxidation, as reported by Taube *et al.*^[2] Although in Sb2 the $\sigma(\text{Sb}^{\text{III}} \rightarrow \text{Ru}^{\text{II}})$ bonding situation has a predominant contribution as obtained from NBO analysis, for Sb1, the bond should be considered to consist of contributions by both canonical forms $\sigma(\text{Sb}^{\text{IV}}\text{-Ru}^{\text{I}})$ (X-type) and $\sigma(\text{Sb}^{\text{III}} \rightarrow \text{Ru}^{\text{II}})$ (L-type). Complex Sb2 carries an increased

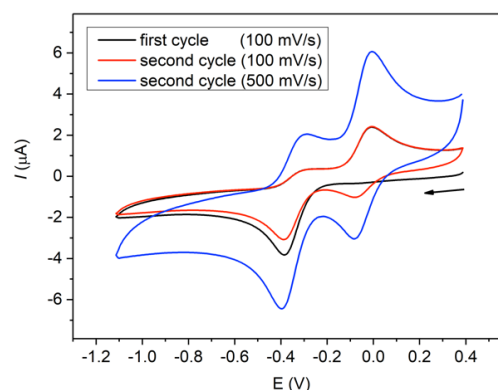


Figure 1. Cyclic voltametric curves of Sb2 in 100 mM $[\text{n-Bu}_4\text{N}]\text{PF}_6$ in NCMe at scan rates of 100 mV/s (black and red trace) and 500 mV/s (blue trace) The data was internally referenced to Fc/Fc^+ ; $E_{1/2} = 0$ V.

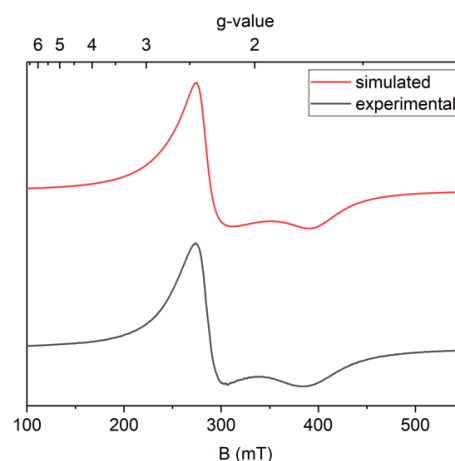


Figure 2. X-band EPR spectrum of Sb2 at 4 K (black) and the simulated spectrum (red). The spectrum was acquired from the solid powder sample at 2.0 mW microwave power, 0.3 mT modulation amplitude and 100 kHz modulation frequency.

natural charge at Ru ($\text{NC}_{\text{Ru}} = 0.48 e^-$), and the X-band electron paramagnetic resonance (EPR) spectrum of solid Sb2 at 4 K revealed an axial signal with $g_{\parallel} = 2.42$ and $g_{\perp} = 1.70$ (Fig. 2), well in agreement with an octahedrally coordinated Ru atom featuring four N donor atoms in the xy-plane and a Sb and Cl donor in z-axis, respectively. The Mulliken spin density exhibits 82.7% location at Ru (singly occupied molecular orbital (SOMO) from NBO calculation), which is in agreement with the EPR measurements. These observations are underlining the canonical form $\sigma(\text{Sb}^{\text{III}} \rightarrow \text{Ru}^{\text{II}})$. Because the Sb contribution to the Sb–Ru bond is 53% in Sb2 (NLMO), the canonical form $\sigma(\text{Sb}^{\text{IV}}\text{-Ru}^{\text{II}})$ with a covalent Sb–Ru bond should be taken into consideration as well. Interestingly, the atomic contributions to this NLMO are similar to those found in compound Sb1.

ACKNOWLEDGEMENTS. The authors are grateful to Dr. P. Kaden for support with EPR measurements.

[1] Gericke, R. *et al.* (2021) *Inorg. Chem.* **60**, 18122–18132.

[2] Taube, H. *et al.* (1991) *J. Am. Chem. Soc.* **113**, 2327–2328.

Lithium-assisted exfoliation of palladium thiophosphate nanosheets for photoelectrocatalytic water splitting

B. Wu,¹ R. Kempt,² E. Kovalska,¹ J. Luxa,¹ A. Kuc, T. Heine, Z. Sofer¹

¹University of Chemistry and Technology, Prague, Czech Republic; ²Technische Universität Dresden, Dresden, Germany

Efficient photoelectrocatalytic (PEC) water splitting could be the solution for environmental and energy problems by converting light energy into clean and renewable energy of H₂. Here, we explored 2D palladium thiophosphate Pd₃(PS₄)₂, which is a promising photocatalyst absorbing light in the visible range. We obtained a few-layer Pd₃(PS₄)₂ through lithium-assisted exfoliation from the bulk phase and characterized it employing Raman spectroscopy, XPS, AFM, and STM combined with DFT calculations. The measured band gap for as-obtained few-layer Pd₃(PS₄)₂ is 2.57 eV (indirect), and its band edges span the electrochemical potentials of the hydrogen and oxygen evolution reactions. The performance in the water-splitting reaction is studied under acidic, neutral, and alkaline conditions under violet irradiation at 420 nm. 2D palladium phosphochalcogenides semiconductor with bifunctional electrocatalytic and photoelectrocatalytic properties shows competitive performance compared with industrial Pt/C catalysts for solar-driven water splitting under acidic and alkaline conditions.

EXPERIMENTAL. Here, we present details of theoretical methods used in this project.^[1] Full structural optimization (relaxation of lattice vectors and atomic positions) was performed in FHI-AIMS employing the PBE functional on light tier 2 numeric atom-centered orbitals, including the many-body dispersion correction and scalar relativistic corrections on a 8 × 8 × 6 Γ -centered k -grid. Band structures and densities of states were calculated including spin-orbit coupling employing the HSE06 functional on tight tier 1 numeric atom-centered orbitals with added auxiliary diffuse basis functions. Raman spectra were predicted employing a Coupled Perturbed Kohn-Sham approach in Crystal17 including corrections for experimental conditions of 532 nm and 295 K.

RESULTS. In this work, we report the exfoliation of few-layer palladium thiophosphate Pd₃(PS₄)₂ in solution from its bulk crystal *via* lithium intercalation and mild ultrasonication. First, the Li-ions were intercalated into the layers of bulk crystal in nonpolar hexane by continuous sonication, followed by solvation in highly polar dimethyl sulfoxide (DMSO) to form a big solvated Li@DMSO group, which could effectively weaken the van der Waals forces between the 2D Pd₃(PS₄)₂ layers. Thus, exfoliated few-layer palladium thiophosphate sample could be achieved under further mild sonication. The red-purple bulk crystals were grown by chemical vapor transport. We measured the valence band position and an indirect band gap of 2.57 eV, indicating the suitability of the material for photoelectrocatalytic water splitting, which was confirmed by our DFT calculations. We further studied the electrochemical performance of HER and OER (oxygen evolution reaction) at pH 0, 7, and 14 under violet irradiation at 420 nm. Details are given in Wu *et al.*^[1] Simulation results in detail: our Raman simulations (Fig. 1) show that E_g¹/A_{1g}¹ signals around 200 cm⁻¹ and the E_g³ signal at 316 cm⁻¹ are characteristic for this material. They correspond to vibrational modes of the tetrathiosphosphate units and are in good agreement with the literature and theory. The A_{1g}³ mode corresponds to the P-S-bond stretching and is

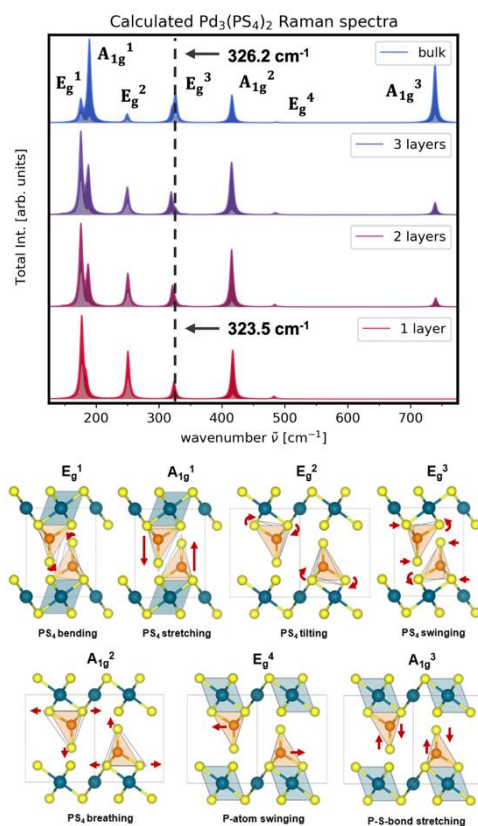


Figure 1. Morphology and structure characterization of layered Pd₃(PS₄)₂: calculated Raman spectra (top), Raman modes (bottom).

visible at 720 cm⁻¹ in the bulk sample but disappears for fewer layers as predicted by our calculations. Furthermore, the E_g³ mode shifts by 1.7 cm⁻¹ to lower wavenumbers in the exfoliated sample compared to the bulk sample, which agrees with the prediction from theory for fewer layers. The Raman spectra revealed that the structure of Pd₃(PS₄)₂ is maintained after exfoliation.

The calculated layer-dependent band gap results, the calculated indirect band gap of the bulk sample is 2.80 eV, which is above the values measured in our experiment and reported literature. With the reduction of thickness, the confinement-induced band gap varies from the bulk value of 2.80 eV to over 2.88 eV in monolayer, which agrees with the increased band gap of the exfoliated materials compared with the bulk.

Despite the indirect nature of the band gap, which consequently leads to low absorption coefficient of visible light, our results show that irradiation led to an enhancement of catalytic performance for both hydrogen evolution reaction (HER) as well as oxygen evolution reaction (OER).

ACKNOWLEDGEMENTS. This work was financially supported by BMBF (NobleNEMS, 16ES1121). We thank the Center for Information Services and High-Performance Computing (ZIH) at TU Dresden for computer time.

[1] Wu, B. *et al.* (2021) *ACS Appl. Nano Mater.* **4**, 441–448.

Oriented growth of in-oxo chain based metal-porphyrin framework thin film for high-sensitive photodetector

Y.-B. Tian,¹ N. Vankova,² P. Weidler,³ A. Kuc, T. Heine, C. Wöll,³ Z.-G. Gu,¹ J. Zhang¹

¹Fujian Institute of Research on the Structure of Matter, Fuzhou, China; ²Technische Universität Dresden, Dresden, Germany; ³Karlsruhe Institut für Technologie, Karlsruhe, Germany

The potential of metal–organic frameworks (MOFs) for applications in optoelectronics results from a unique combination of interesting photophysical properties and straightforward tunability of organic and inorganic units. Here, we demonstrated that using the MOF approach, chromophores can be assembled into well-ordered 1D arrays using metal-oxo strands as lead structure, and the resulting porphyrinic rows exhibit unique photophysical properties and allow the realization of highly sensitive photodetectors. A porphyrinic MOF thin film, In-TCPP surface-coordinated MOF thin films with [021] orientation, were fabricated by our experimental partners using a layer-by-layer method, from In(NO) and TCPP (5,10,15,20-(4-carboxyphenyl) porphyrin). Detailed experimental and theoretical analysis revealed that the assembly yields a structure where In-oxo strands running parallel to the substrate fix the chromophoric linkers to yield 1D arrays of porphyrins. The frontier orbitals of this highly anisotropic arrangement are localized in these columnar arrangements of porphyrins and result in high photoactivity, which is exploited to fabricate a photodetector with record (comparing with other organic materials) responsivity in visible regime of 7.28×10^{14} Jones and short rise/fall times (0.07/0.04 s). This oriented MOF thin film-based high-sensitive photodetector provides a new avenue to use inorganic, stable lead structures to assemble organic semiconductors into regular arrays, thus creating a huge potential for the fabrication of optoelectronic devices.

EXPERIMENTAL. Here, we show details of theoretical methods used in this project. More details are given by Tian *et al.*^[1] First-principle calculations based on density functional theory (DFT) were performed using the Crystal17 code. POB-TZVP basis sets and D3(BJ) dispersion corrections, to account for the London dispersion interactions, were used throughout the calculations. Relaxation of the atomic positions in both the In-TCPP SURMOF and the In-oxo based chain model was carried out using the Perdew–Burke–Ernzerhof (PBE) functional while keeping the lattice parameters the same as the previously reported crystallographic cell ($a = 7.17 \text{ \AA}$, $b = 32.67 \text{ \AA}$ and $c = 17.06 \text{ \AA}$ ($\alpha = \beta = \gamma = 90^\circ$)). Band structures, projected and integrated density of states (pDOS and IDOS, resp.) were then calculated at the same PBE-D3(BJ) level, but also using the Heyd-Scuseria-Ernzerhof (HSE06) screened hybrid functional. In all calculations, we used a k-point mesh of 52 k-points in the irreducible Brillouin zone according to the Monkhorst-Pack sampling scheme.

RESULTS. In this work, we demonstrated that In-TCPP, a porphyrinic MOF with a highly anisotropic architecture, has detectivities exceeding those reported previously. Whereas most MOFs consist of individual metal-oxo nodes linked by organic linkers, in the In-TCPP 1D MOF metal-oxo strands provide lead structures to which planar chromophores, TCPP are fixed *via* coupling units to well-ordered rows running along the [100] direction (cf. Fig. 1 bottom). The choice of In-oxo strands was motivated by the attractive properties of In_2O_3 regarding the fabrication of optical sensors and de-

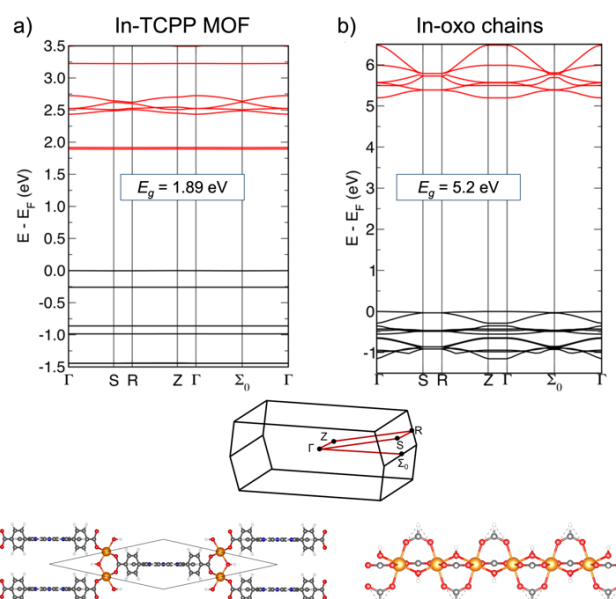


Figure 1. Band structure of In-TCPP MOF (a) and In-oxo-based chain models (b). Representation of the primitive Brillouin zone with the calculated path $\Gamma \rightarrow \text{S} \rightarrow \text{R} \rightarrow \text{Z} \rightarrow \Gamma \rightarrow \Sigma_0 \rightarrow \Gamma$ together with the structural models used in the calculations (bottom). Calculations using Crystal17 at the PBE-D3(BJ)/POB-TZVP level of theory.

vices. The chromophores used here, porphyrins, exhibit excellent electron-transfer and photoresponse properties and are often used in organic photovoltaic devices.

To understand the mechanism for the efficacy of photoexcited charge carrier conduction in In-TCPP, DFT calculations were carried out using the structural unit cells. The electronic bands of In-TCPP are displayed in Fig. 1a and for In-oxo chains in Fig. 1b, revealing the presence of a direct bandgap with 1.89 eV in the MOF. While this value agrees well with that determined from the Tauc plot of the experimental data, it must be noted that (i) the very flat nature of both conduction and valence bands do not allow a clear assignment of the bandgap character, and (ii) the used PBE functional generally underestimates optical gaps. However, it does not account for exciton binding energies which may be appreciable for MOF materials.

As demonstrated by the integrated density of states (IDOS), the frontier bands are both dominated by the porphyrinic units. Given the fact that both bands are extremely flat, there is negligible conjugation between neighboring molecules. Therefore, band transport is not possible, and the charge transport is deduced to be due to hopping transport along the porphyrin rows.

ACKNOWLEDGEMENTS. N. V., A. K., and T. H. gratefully acknowledge the Priority Program of the Deutsche Forschungsgemeinschaft COORNETS (SPP 1928). ZIH Dresden is thanked for a high-performance computing grant.

[1] Tian, Y.-B. *et al.* (2021) *Adv. Sci.* **2100548**, 1–8.

SCIENTIFIC CONTRIBUTIONS (PART II)

Geological Systems

Long-Lived Radionuclides & Transport Phenomena in

GEOLOGICAL SYSTEMS

Implementing heterogeneous crystal surface reactivity in reactive transport models

C. Fischer

The surface reactivity of crystalline matter determines important properties, *e.g.* the migration of radionuclides. Furthermore, the surface reactivity controls the development of physical parameters during fluid-solid reactions, such as porosity and permeability. These physical parameters feed back to the efficiency of chemical reactions in reactive transport processes. Reactive transport simulations are used to investigate the effects of reactivity heterogeneity, superimposed on fluid transport heterogeneity, on the effective dissolution rate.^[1] In this study, the models simulate the chemical reaction of calcite dissolution, solute transport, and the evolution of crystal surface geometry. Importantly, heterogeneous surface reactivity is finally included in the simulation of reactive transport.^[2,3] The parametrization of crystal surfaces with specific rate constants was tested,^[3] as was the surface slope factor as a surrogate value for intrinsic surface reactivity.^[2] Experimental data sets collected using vertical scanning interferometry validate the approaches. The novel parametrization enables simulation of surface-controlled heterogeneous reactivity in surface dissolution and is currently extended to more complex data sets, including geometries of porous rocks obtained from microcomputed tomography. Overall, the new parametrization of the reactive transport models will lead to a significant improvement in the predictability of material retention and release in the environment.

NUMERICAL. In the standard modeling of reactive transport, it is assumed that the dissolution reaction proceeds at a fixed rate at the surface of the crystal, *i.e.*, the normal flux from the surface is given by a function of the concentration at the surface. Under conditions far from equilibrium, and under the simplifying assumption of the dissolution rate as a single constant, the surface-normal fluxes are given by: $D \mathbf{n} \cdot \nabla c = R$ where R is the dissolution rate, D is the diffusion coefficient of the dissolving species in the fluid and \mathbf{n} is the surface normal of the interface. A first model for using multiple different surface rates is to apply a discrete set of dissolution rates. This is implemented using a set of surface dissolution rates assigned to specific voxels on the surface.^[3] An alternative numerical approach was chosen for the more general use of a rate continuum without the complex site-specific assignment of surface reactivity: The slope of the surface envelope curve of nano- and microtopographic crystal surfaces was calculated. The data serve as a proxy value for surface reactivity, as they reflect the density of the most highly reactive surface constituents. This proxy value was used as a first approximation of a reasonable rate variability as a prefactor (surface slope factor, SSF) in the simulation.^[2]

RESULTS. Figure 1 illustrates the results of the improved numerical approach. A comparison is given of how the rate result using the conventional case (single rate) on a nanostructured surface compares to the new parameterization (rate spectrum). In the first case, a homogeneous surface rate occurs. The total rate is thus too high and the resulting rate distribution is far too uniform. A proper prediction of the surface evolution is impossible. For applications, a prediction of the permeability evolution would fail. A small, negligible influence of the flow field can be detected. However, this is by no means suitable to explain the experimental findings (Fig. 1, bottom right). Calcite cement disso-

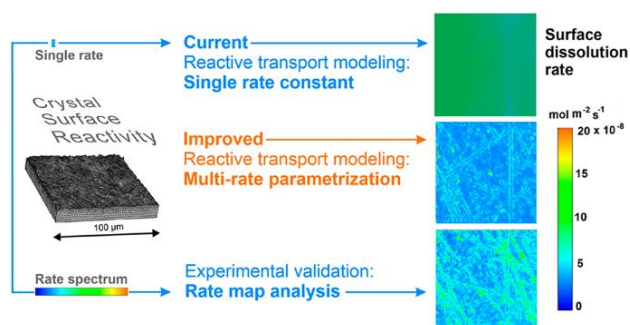


Figure 1. Comparison of results in previous and new parameterization of reactive transport models. Remarkable is the excellent agreement of the new approach with experimental results.

lution was simulated using the multi-rate model parameterized with dissolution rates from the literature.^[4] The reacting surface reflects the competing effect of edge and corner rates compared to crystal area rates.^[3] While this approach can serve as a first-order explanation for crystal evolution in pore space, it cannot yet be used to address the specific evolution of crystal faces with structural defects, including screw dislocations. Thus, a second approach was applied for this purpose, using the nanotopographic envelope of the crystal surface.^[3] The numerical result (Fig. 1, center right) is validated by the experimental result. The rate distribution shows how the influence of transport control contributes to the overall rate in competition with surface reactivity (Fig. 2).

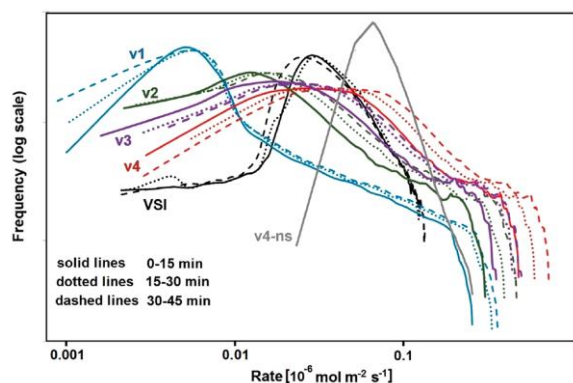


Figure 2. Comparison of simulated calcite dissolution rate spectra at different fluid velocities with measured rate spectra (VSI). As the flow rate increased (from v_1 to v_4), the maximum of the histogram shifted toward higher rates, showing the decreasing effect of transport control. Note the similar position of rate spectra maximum frequency of v_4 versus VSI data at about 10^{-8} to 10^{-7} mol $m^{-2} s^{-1}$.

OUTLOOK. Ongoing work aims to enable the use of parameterization presented here on complex geometries of porous materials from, *e.g.*, microcomputed tomography measurements.

- [1] Agrawal, P. *et al.* (2021) *Geochim. Cosmochim. Acta* **307**, 338–350.
- [2] Karimzadeh, L. & Fischer, C. (2021) *ACS Earth Space Chem.* **5**, 2408–2418.
- [3] Prill, T. *et al.* (2021) *Transp Porous Media* **140**, 535–557.
- [4] Bollermann, T. and Fischer, C. (2020) *Amer. J. Sci.* **320**, 53–71.

Radionuclide transport modelling: the Smart K_d -concept in reactive transport codes

M. Stockmann, R. Lu,¹ A. Gehrke²

¹Helmholtz Centre for Environmental Research – UFZ, Department of Environmental Informatics, Leipzig, Germany; ²Gesellschaft für Anlagen- und Reaktorsicherheit (GRS) gGmbH, Brunswick, Germany

In the framework of the iCross project, the smart K_d -concept is implemented in the transport code OpenGeoSys6 (OGS6) to describe variable radionuclide sorption in transport models as consequence of changing geochemical conditions over space and time.^[1-3] To validate this concept three benchmark calculations were performed, and results obtained with OGS6 were compared to independent simulations with the transport code d³f++ also including the smart K_d -approach and with fully coupled reactive transport models, *i.e.* OGS6#PhreeqC and PHAST.^[2-5]

MODEL DESCRIPTION. Benchmark calculations were performed based on a well-defined 2D test case for a typical sedimentary rock system covering potential repository host rock formations in Northern Germany.^[6] This serves as a comprehensive proof-of-concept and demonstrates the capability to describe the sorption behavior in dependence of changing geochemical conditions. The transport of several radionuclides was simulated through a 20 m long and 1 m high saturated column (Fig. 1). The domain is considered as homogeneous porous media (porosity = 0.2 and permeability = $1.01 \times 10^{-11} \text{ m}^2$) with a reactive surface associated to 85 wt.-% quartz, 10 wt.-% feldspar, 0.5 wt.-% mica, 0.5 wt.-% goethite, 0.5 wt.-% gibbsite and 1.5 wt.-% kaolinite. A constant inflow of $3 \times 10^{-5} \text{ m s}^{-1}$ in a 1 m wide window was set and open boundary is assumed at the end of the domain. In addition, it is assumed that calcite is present in the entire domain, being the only mineral that may dissolve or precipitate due to solution changes over time.

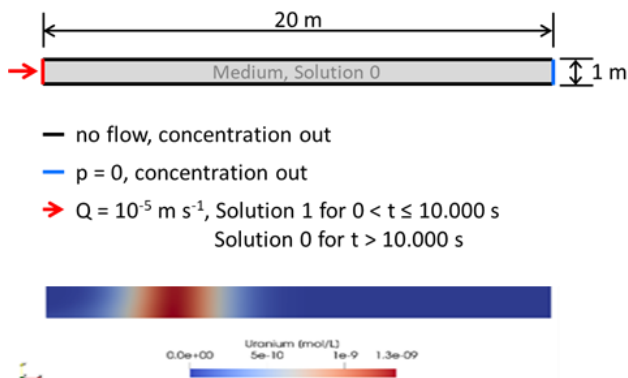


Figure 1. Model domain dimensions (above) and boundary conditions as well as transport of uranium through the model domain (below).

RESULTS. To validate the implemented smart K_d -concept in OGS6 and d³f++, benchmark calculations were performed stepwise. In the first benchmark, a non-sorbing tracer transport was simulated with consideration of the reactive transport equation in saturated porous media implemented in OGS6 and d³f++. Similar results were obtained with both transport codes for the flow and tracer calculations, which verified the model setup.

In a second benchmark, simulations with the new implemented smart K_d -concept (multidimensional look-up table approach) were performed based on a reduced system. Therefore, Ni and Np(V) were taken as injected radionuclides that could sorb on the different minerals. In Fig. 2, the spatial distribution is shown after 500,000 s calculated with

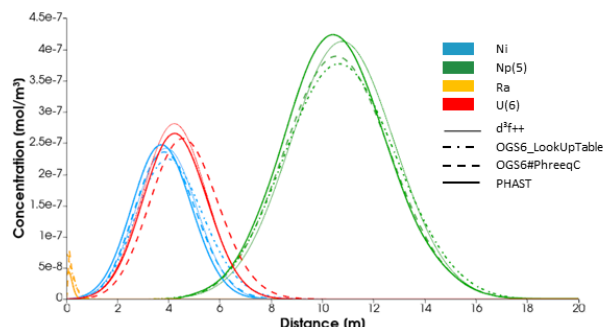


Figure 2. Spatial distribution of the radionuclides after 500,000 s simulation time.

the new implemented smart K_d -approach. As can be seen, the profiles of Ni and Np(V) obtained from d³f++ and OGS6 lie nearly perfectly one upon another. This implies that the look-up table approach works well.

In a third benchmark, fully coupled reactive transport models were used, *i.e.* the direct coupling OGS6#PhreeqC (version 3.5.0) and PHAST. A case similar to the previous one was modelled but apart from Ni and Np(V), five additional radionuclides, Cs, Am, Th, U(VI) and Ra were included simultaneously. Good agreement between both codes and d³f++ is observed. The spatial distributions after 500,000 s reflect a radionuclide-specific retardation effect as can be seen clearly in Fig. 2. Neptunium has the weakest sorption of all considered radionuclides with the peak maximum at a distance of 11 m from the inflow. Cesium, Americium and Thorium have the strongest sorption and accumulated nearby the injection boundary (therefore not shown in Fig. 2). We are able to reflect the radionuclide-specific retardation effect. This real application case serves as a benchmark for field-scale transport simulations.

ACKNOWLEDGEMENTS. This work based on two projects: The iCross project is funded by the German Federal Ministry of Education and Research (BMBF) (Grant 02NUK053B) and the Helmholtz Association (Grant SO-093). The SMILE project is funded by the Federal Ministry for Economic Affairs and Climate Action (BMWK) under grant No. 02E11668A-C.

- [1] Stockmann, M. *et al.* (2017) *Chemosphere* **187**, 277–285.
- [2] Jang, E. *et al.* (2018) *OpenGeoSys Tutorial III*, 103.
- [3] Kolditz, O. *et al.* (2012) *Environ. Earth Sciences*. **67**, 589–599.
- [4] Schneider, A. *et al.* (2016) *Report GRS-392*.
- [5] Parkhurst, D. L. *et al.* (2010) *U.S.G.S. Report 6-A35*.
- [6] Noseck, U. *et al.* (2018) *Report GRS-500*.

Effective diffusivity prediction of radionuclides in clay formations using an integrated upscaling workflow

T. Yuan, C. Fischer

The effective diffusivity is a key parameter in the diffusive transport calculations, thus decisive for predicting the radionuclide migration in low-permeable clay-rich formations. The effective diffusivity can be obtained from experimental diffusion studies assuming homogeneous transport conditions.^[1,2] This prevents to model the heterogeneous diffusion patterns in the sandy facies of the Opalinus Clay (SF-OPA) as revealed by positron emission tomography (PET) measurements.^[3] Numerical modeling of such patterns critically depends on accurate quantification of effective diffusivities based on the underlying pore network geometries and mineralogical composition analysis. In this study, we propose an upscaling workflow that integrates nm- and μm -scale simulations based on the pore network geometries from experiments to calculate the effective diffusivities in clay-rich laminae, clayey and sandy laminae, and carbonate lenses.^[4] Finally, the heterogeneous effective diffusivities are applied to a structural model based on micro-computed tomography ($\mu\text{-CT}$) data to simulate heterogeneous diffusion patterns in SF-OPA at the core scale.

NUMERICAL METHOD. The diffusive transport of a solute in a porous medium is described using the diffusion-sorption equation:

$$\frac{\partial C_{tot}}{\partial t} = \nabla \cdot J, \quad (1)$$

where C_{tot} is the total aqueous solute concentration, defined as $C_{tot} = \alpha C$, C is the aqueous solute concentration, and J is the flux through the entire domain. The constant rock capacity factor α can be calculated by $\alpha = \phi + \rho_{bd} K_d$ with the porosity ϕ , bulk dry density ρ_{bd} , and sorption distribution coefficient K_d .

The three-dimensional (3D) diffusion-sorption equation is solved numerically using a previously developed numerical simulator.^[5] Considering the diffusion in x-direction of a cubic computational domain in 3D Cartesian coordinates, the overall effective diffusion coefficient D_{oe} is calculated using Fick's law:

$$D_{oe} = \frac{J \cdot L}{(C_{in} - C_{out})}, \quad (2)$$

where C_{in} and C_{out} are the prescribed concentrations at inlet and outlet, respectively. L is the length of the domain.

We estimate the effective diffusion coefficient using digital rock physics combined with an integrated upscaling workflow from the nm to the μm scale for transport simulation.^[4] At the nm scale, the digital rock geometries include pore space and pore network in the clay mineral aggregates. We consider electrostatic diffusion for the cations and anions within the diffuse layer, and the surface electrostatic potential is calculated using the Donnan approach.^[2,4] The effective diffusion coefficients obtained at this scale are used as simulation inputs for the μm -scale digital rock simulation. At the μm scale, the digital rocks provide the mineral composition variability in the shales. For simplicity, we assume that the shales are composed of permeable clay mineral aggregates and impermeable non-clay mineral grains such as quartz, calcite, and pyrite. Finally, we estimate the effective diffusion coefficient of the radionuclides at the μm scale by solving equations (1) and (2) with the calculated effective

diffusivities at the nm scale. Next, we apply the heterogeneous effective diffusivities calculated based on the pore network geometries from the experiment as explained above to a structural model from $\mu\text{-CT}$ (Fig. 1A) to simulate heterogeneous diffusion in SF-OPA at the core scale.

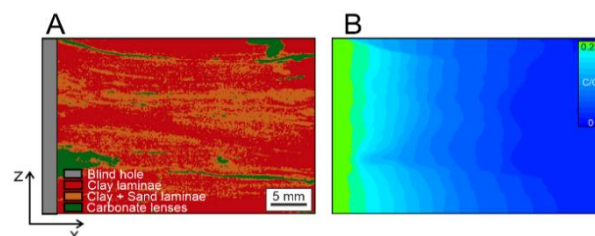


Figure 1. μCT facies combined with the upscaled pore geometries as the basis of a transport simulation at the drill core scale (A). Simulation results of diffusive transport (from left, reservoir) to right are shown as normalized concentration (B).

RESULTS. We first use sodium ($^{22}\text{Na}^+$) as the cation, HTO as the neutral species, and iodide (I^-) as the anion and compare the predicted effective diffusivities with the experimental data in the literature, which are listed in Tab. 1. Good agreement between the diffusivity from the literature^[6] and our proposed upscaling workflow shows that our suggested method is capable of predicting the diffusivity of the shales. Next, the digital rock models are reconstructed based on the pore network geometries in SF-OPA from the experiment. The results show that the diffusivity of the clay-rich laminae ($D_e > 10^{-11} \text{m}^2/\text{s}$) is up to two orders of magnitude higher than in the other subfacies components (clay and sandy laminae: $D_e = 10^{-12} \text{m}^2/\text{s}$, carbonate and sulfide lenses: $D_e < 10^{-12} \text{m}^2/\text{s}$). The transport simulation results illustrate the effects of sedimentary and diagenetic heterogeneity (Fig. 1B). This demonstrates that our numerical method is capable of modeling heterogeneous diffusion patterns in SF-OPA at the core scale, thus contributing to enhanced predictability of radionuclide migration.

Table 1. Effective diffusion coefficients of $^{22}\text{Na}^+$, HTO, and I^- in shale from experimental data in the literature compared to the predicted mean values from the model results.^[6]

Tracer	Diffusivity of shale ($\times 10^{-11} \text{m}^2/\text{s}$)	
	Experimental data ^[6]	Model results
$^{22}\text{Na}^+$	7.2–9.4	7.73
HTO	5.4–6.5	6.23
I^-	1.2–2.0	2.08

ACKNOWLEDGEMENTS. We gratefully acknowledge funding by the German Federal Ministry of Education and Research (BMBF), grant 02NUK053B and the Helmholtz Association, grant SO-093 (iCross).

- [1] Van Loon, L. R. *et al.* (2005) *Appl. Geochemistry* **20**, 2351–2363.
- [2] Appelo, C. A. *et al.* (2010) *Geochim. Cosmochim. Acta* **74**, 1201–1219.
- [3] Kulenkampff, J. *et al.* (2015) *Clay Miner.* **50**, 369–375.
- [4] Yuan, T. and Fischer, C. (2021) *Tansp. Porous Med.* **138**, 245–264.
- [5] Yuan, T. *et al.* (2019) *water* **11**, 1957.
- [6] Leupin, O. X. *et al.* (2017) *Swiss J. Geosci.* **110**, 391–403.

Heterogeneous sorption of radionuclides predicted by crystal surface nanoroughness

T. Yuan, S. Schymura, T. Bollermann, K. Molodtsov, P. Chekhonin, M. Schmidt, T. Stumpf, C. Fischer

Reactive transport modeling (RTM) is an essential tool for the prediction of contaminants' behavior in the bio- and geosphere. However, RTM of sorption reactions is constrained by the reactive surface site assessment. From an energetic point of view, a dominant factor of surface reactivity variability is the kink site density (KSD) of the crystal surface (Fig. 1).^[1] Such variability in reactive site density of the crystal surface nanotopography is responsible for heterogeneous sorption efficiency, not captured by current RTM approaches. Here, we investigate the sorption of Eu(III) at the calcite surface and study the influence of surface topography on sorption efficiency using single-crystal samples that allow for studying specific structural endmembers, *i.e.*, very low KSD *vs.* very high KSD, although the exact KSDs are not accessible for measurements. Based on experimental data of Eu(III) sorption on a polycrystalline calcite surface from micro-focus time-resolved laser-induced luminescence spectroscopy (μ TRLFS), vertical scanning interferometry, and electron back-scattering diffraction (EBSD), we parameterize a surface complexation model (SCM) and quantify the sorption efficiency as a function of surface nanoroughness.^[2] The validation of the quantitatively predicted spatial sorption heterogeneity suggests that retention reactions can be considerably influenced by nanotopographic surface features. Our study presents a way to implement heterogeneous surface reactivity into a predictive SCM for enhanced prediction of radionuclide retention.

CALCITE NANOTOPOGRAPHY EFFECTS ON EU(III) SORPTION. Figure 1 shows the different absolute concentrations of sorbed Eu(III) in a cleaved edge, a cleaved terrace, and a polished surface, as quantified by autoradiography techniques. The polished crystal surface exhibits an elevated nanoroughness that is formed by a high number of kink sites due to polishing (cf. Fig. 2, surface 4), resulting in a kink site density similar to that of a powder sample. Two dominating structural features are observed on the surface of the cleaved sample: multiple surface steps (cf. Fig. 2, surface 3) and flat terraces between the steps showing a low percentage of kinks, steps, and point defects (cf. Fig. 2, surface 1). As shown in Fig. 1, the highest amount of sorbed Eu(III) was

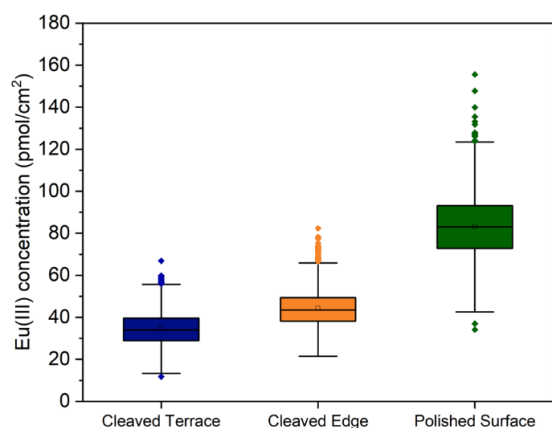


Figure 1. Box-Whisker plots of the measured absolute concentrations of sorbed Eu(III) among the cleaved terrace, cleaved edge, and polished surface. The quantitative concentration trend suggests the effect of crystal surface nanotopography (cf. Fig. 2) on sorption efficiency.

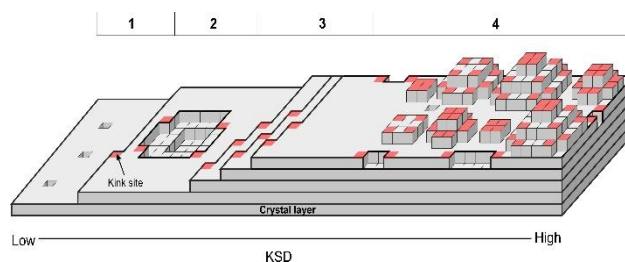


Figure 2. Schematic representation of nanotopographic characteristics of a crystal surface, showing an atomically flat terrace with point defects (1), an etch pit wall with steps and kinks (2), surface steps with kinks due to crystal cleavage (3), and a very rough surface due to mechanical treatment such as polishing (4). Surface kink sites are marked in red, and the kink site density increases from left to right in this scheme.

found on the polished surface, while the cleaved surface with an almost flat surface free of surface steps has the lowest concentrations, with step structures in between.

SURFACE NANOROUGHNESS PARAMETRIZATION.

The observed heterogeneous sorption behavior is mechanistically linked *via* differences in surface site availability. At the nanometer scale, the spatial configuration of surface building blocks defines the surface reactivity and, thus, the sorption efficiency.^[3] Nanoroughness can be considered as a proxy to quantify the occurrence of such surface building blocks. For modeling purposes, we implement it mathematically *via* the variability of specific surface area (SSA).^[2] To evaluate the general applicability of the concept, we compare and discuss published data from other laboratories on the variability of sorption site density of single-crystal surfaces, beyond Eu(III) sorption reactions. The sorption efficiencies of Np(V) on calcite surface from Zavarin *et al.* and Heberling *et al.* are distinctly different, with 25 and 70%, respectively.^[4,5] This discrepancy is related to a significant difference in the BET-SSAs of powdered calcite (0.262 m² g⁻¹ *vs.* 1.3 m² g⁻¹).^[4,5] The larger BET-SSA reflects a higher step and kink site density, thus supporting the controlling effect of nanotopographic surface building blocks. Therefore, SSA parameterization *via* surface nanoroughness allows us to implement the quantitative variability of the reactive surface sites of crystal surface into SCMs and paves the way for better predictions of radionuclide retention in the future.

ACKNOWLEDGEMENTS. We gratefully acknowledge funding by the German Federal Ministry of Education and Research (BMBF), grant 02NUK053B and the Helmholtz Association, grant SO-093 (iCross).

- [1] Bollermann, T. and Fischer, C. (2020) *Am. J. Sci.* **320**, 53–71.
- [2] Yuan, T. *et al.* (2021) *Environ. Sci. Technol.* **55**, 15797–15809.
- [3] Mehmood, F. *et al.* (2009) *Phys. Rev. B.* **79**, No. 075422.
- [4] Zavarin, M. *et al.* (2005) *Radiochim. Acta* **93**, 93–102.
- [5] Heberling, F. *et al.* (2008) *J. Contam. Hydrol.* **102**, 246–252.

Observation of fluid injection into tight barrier material with GeOPET

J. Kulenkampff, S. Gruhne, D. Lösel

Observation and understanding of transport processes in the tight materials of geological and geotechnical barriers is challenging: Representativeness of the sample, the impact of its internal structure, as well as the predominant transport process are often obscured by experimental prerequisites. In order better to elucidate these processes, we developed a surface-mounted “guard-ring” injection system that enables to observe transport of radiolabeled fluids into tight materials with positron-emission-tomography (PET). It was demonstrated that this system allows to monitor over long periods the fluid propagation along porous structures that were characterized before with X-ray tomography (μ CT). We conclude from this GeOPET- μ CT study that preferential transport pathways can substantially increase transport distances compared to the common presupposition of homogeneous porosity and permeability.

EXPERIMENTAL. The material is a drill core from a MgO-shotcrete dam that was constructed in the Teutschenthal salt mine in 2008.^[1] It is an open question if the contact zone between the shotcrete layers is more permeable than the solid material, although in-situ pressure tests on boreholes suggest extremely low permeability in the order of 10^{-20} m². Because the brittle material is hard to machine, we decided to install a surface injection cell on a saw-cut plane across such a contact zone. To ensure safe application of the radionuclide, we designed the injection cell as a guard-ring cell with a ring-shaped reservoir of unlabeled brine (saturated NaCl) protecting against spillage of the labelled fluid ($[^{22}\text{Na}]\text{NaCl}_{\text{sat}}$) in the inner chamber (Fig. 1). Both chambers were pressurized with He-cushion-gas from a gas bottle with a pressure of 200 kPa. It was possible to maintain this pressure for eight months, even through the closure of the laboratory during lock-down periods. The experiment was terminated due to a gas breakthrough through the outer chamber during such an unsupervised period. However, this was proving the safety concept of the system, because this

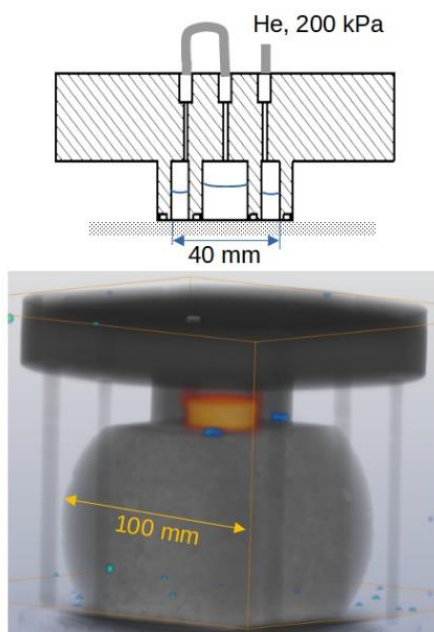


Figure 1. Guard-ring injection cell for observation of fluid penetration into low-permeable material.

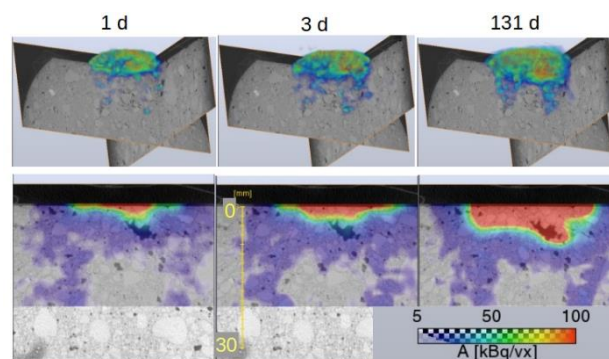


Figure 2. Three out of 28 PET-frames acquired during injection of $[^{22}\text{Na}]\text{NaCl}_{\text{sat}}$ into a MgO-shotcrete drill core over a period of 260 d, showing superposition of preferential flow and slow diffuse propagation.

unintentional pressure release stopped the injection and prevented the release of activity from the inner chamber. When the laboratory was open, PET measurements were taken periodically, showing the penetration of the labeled brine into the sample. μ CT-measurements were taken before and after this study. Also, μ CT-radiography was used for fluid level monitoring in the reservoirs. Unfortunately, these measurements had to be interrupted during lockdown periods and later stopped due to a scanner defect that could not be repaired under pandemic conditions.

RESULTS. We observed initial fast penetration of the labelled fluid into superficial voids. During the period of eight months, we observed a volume loss of 2.8 mL in the reservoir and a corresponding increase of activity in the sample. The shape of the fluid propagation is characterized by a slowly spreading diffuse pattern that reached a depth of only a few millimeters, and pointwise deeper reaching pathways that are distinguishable down to a depth of ca. 30 mm, with faint extensions down to 50 mm (Fig. 2). These pathways follow porous structures at aggregate-grain surfaces, although these appear unconnected in the μ CT data. Therefore, transport occurs along porous zones below the resolution of the μ CT and possibly by dissolution of obstructions. It is not possible to correlate these zones with shotcrete layer contacts, because the contact zone is hardly identifiable. Prognosis of the further evolution is still uncertain. It was observed a slight decrease of the injection rate that could indicate self-sealing processes by reaction between brine and solid.

ACKNOWLEDGEMENTS. This study was supported by the Federal Ministry for Economic Affairs and Climate Action (BMWK; project no. 02E11769B). The author thanks the partners of the Joint Research Project “MgO-Spritzbeton für Streckenverschlüsse für HAW-Endlager im Steinsalz (MgO-S3)”, coordinated by the TU Bergakademie Freiberg, Institut für Bergbau und Spezialtiefbau, in particular IfG Leipzig for sample preparation.

- [1] Popp, T. *et al.* (2018) The Mechanical Behavior of Salt; Proc. 9th Conference, Hannover, 305–320.
- [2] Kulenkampff, J. (2022) The Mechanical Behavior of Salt; Proc. 10th Conference, Utrecht, in press.

Heterogeneous surface retreat during enzymatic PET degradation as revealed by Vertical Scanning Interferometry

H. Lippold, C. Sonnendecker,¹ C. Fischer

¹Institute of Analytical Chemistry, University of Leipzig, Leipzig, Germany

Enzyme-based degradation is an emerging strategy for closed-loop recycling of polyethylene terephthalate (PET), accounting for 10% of total plastics production worldwide. A polyester hydrolase isolated from a compost metagenome was found to exceed the performance of previously tested enzymes considerably, shown here on the basis of surface retreat rate measurements by Vertical Scanning Interferometry (VSI). This method, applied to such kind of surface process for the first time, furthermore revealed a pronounced lateral heterogeneity in the progression of degradation, with different topographic features at initial and later stages.^[1]

EXPERIMENTAL. Amorphous PET film pieces with a thickness of 0.25 mm were fixed on a glass support with epoxy resin, partially masked with PTFE tape and reacted with the enzyme in potassium phosphate buffer solution, shaking at 70 °C for 1 h or 16 h. After quick-freezing, the samples were rinsed with ethanol and SDS solution, followed by air-drying at room temperature.

Surface topographies were analyzed by means of an S neox 3D optical profiler (Sensofar Metrology) in both VSI white-light mode using Mirau objectives (20×, 100×; Nikon) and in the mode of scanning microdisplay confocal microscopy using a confocal objective (150×; Nikon). For the construction of rate maps and rate spectra, datasets for a given surface section before and after treatment were correlated and subtracted from each other, using the masked area as a reference. Data processing was performed by means of the software SPIP, version 6.7.3 (Image Metrology A/S).

RESULTS. In Fig. 1A and B, surface retreat after equal reaction times is shown for the enzymes LCC (hitherto considered most promising in its hydrolytic activity)^[2,3] and PHL7 (recently isolated and characterized by cooperation partners, University of Leipzig).^[1] The superior efficiency of the newly discovered enzyme is evident.

As can be seen in the 3D images of the sections (C–F), the

degradation process is characterized by a pronounced heterogeneity. At later stages, it is dominated by the formation of circular pits. Examining the topographies before and after exposure, the cratering cannot be traced back to defects or irregularities on the pristine surfaces. One may hypothesize that the pit formation is caused by the presence of small domains with a highly disordered polymer chain structure (particularly amorphous and thus attacked more easily). The heterogeneity of surface retreat at the initial stage, when pits are not yet formed, is analyzed in Fig. 2. The rate maps show diffuse lateral variations without any circular contours. The corresponding rate spectra (histograms) exhibit an asymmetric distribution, with a greater variability in the range of low rates. Note the larger distribution range for PHL7 (B) compared to LCC (A). While both rate histograms are moderately skewed left, the rate distribution (B) shows a larger variability of the lower rate portions, exemplified for the sections B.1 and B.2.

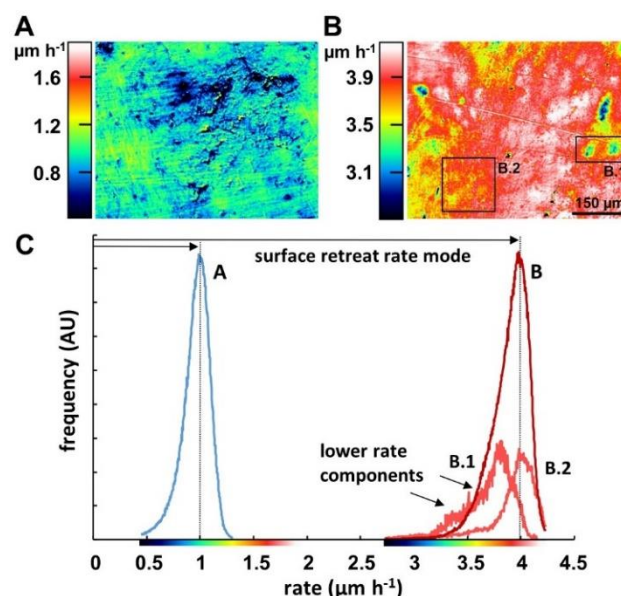


Figure 2. Degradation rate maps and histograms referring to a reaction time of 1 h with the enzymes LCC (A) and PHL7 (B). The histograms for sections B.1 and B.2 are vertically exaggerated for better visibility.

OUTLOOK. A follow-up study is in progress where exposure times are varied at denser intervals, which will allow for a correlation of retreat rates with topographic features evolving over time. This may provide the basis for prospective strategies to accelerate the degradation process through targeted surface modification.

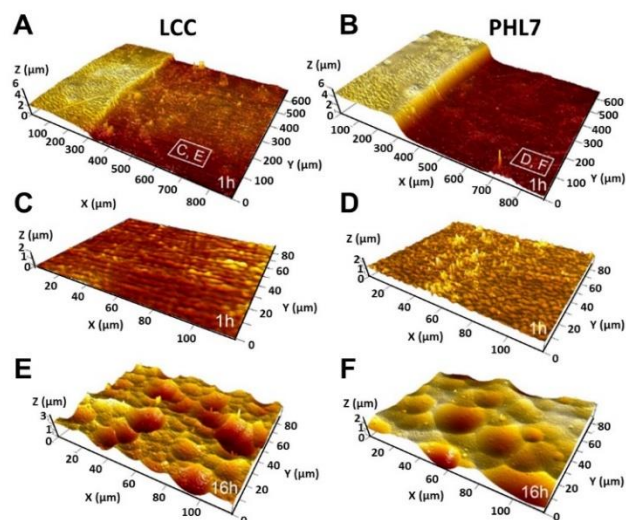


Figure 1. Surface topography of PET films exposed to LCC and PHL7 enzymes. Surface retreat after 1 h of exposure (masked area on the left) (A, B). Topographic details of exposed surface sections after 1 h and 16 h (C–F).

- [1] Sonnendecker, C. et al. (2022) *ChemSusChem* **2022**, e202101062.
- [2] Tournier, V. et al. (2020) *Nature* **580**, 216–219.
- [3] Ronkvist, Å. M. et al. (2009) *Macromolecules* **42**, 5128–5138.

Estimating uncertainties of radionuclide migration in crystalline host rock – An interdisciplinary approach

S. Pospiech, V. Brendler

Distribution coefficients (K_d -values) in rocks are uncertain by nature, but confidence in respective prognostic models can considerably increase if the uncertainty in thermodynamic data and field parameters such as the average mineralogy of potential host rocks are considered together. Namely the heterogeneity of these rocks and the preferred pathways of fluids through rocks should be included to capture the overall uncertainty as realistic as possible. In the EU project DONUT, we propose to use an interdisciplinary approach combining geology, geostatistics, geochemistry and thermodynamic modelling, to test work flows how the uncertainty of radionuclide migration through crystalline rocks could be better estimated.

(Smart)- K_d -values of natural rock samples of a representative volume element (RVE) are normally calculated based on thermodynamic parameters as well as field data such as the mineralogical composition, pH, ionic strength, or temperature.^[1] By varying all these parameters within their uncertainty boundaries, following their probability density functions (pdfs), a huge set of K_d -values can be computed, eventually forming multi-dimensional look-up tables to implement the smart- K_d concept into reactive transport codes. However, this approach does not include the uncertainties resulting from the heterogeneity of the natural rock samples, although they can influence the uncertainty of the K_d -value two-fold: Firstly, heterogeneous spatial distributions and varying grain sizes of the minerals between different RVEs may lead to different K_d -values, even if the mean composition of the minerals stays constant for the respective RVEs. Secondly, and probably even more important, the fluid migration paths through the RVE could lead to a significant offset between the average mineral composition of the RVE and the average composition of the mineral surfaces being in contact with migrating fluids, the “exposed mineral surfaces”.

METHOD. An interdisciplinary approach is followed to derive more realistic pdfs for K_d -values: Geological and geochemical knowledge is applied to characterize rock samples with respect to mineral composition, spatial distribution of minerals and preferred fluid pathways, e.g. mapping fractures, joints or micro-fissures, and estimating if they would potentially allow fluids to migrate. Methods of geostatistics are used to capture the information from the images, e.g. generated by μ CT-scans or Mineral Liberation Analysis (MLA). Results are then processed in models to predict the change of mineral composition in space, respectively the change of exposed mineral surface. Multipoint statistics (MPS) are used to simulate the variability of mineral composition and void-space based on training images. (Geo)chemistry is then applied to calculate the (smart) K_d -values for a variety of simulations of rock samples, e.g. covering extremes of mineral distributions to estimate the maximal possible uncertainty of K_d -values.

RESULTS. MLA was identified to be the preferred tool for mapping mineral composition and fractures/fissures in crystalline rocks. It provides the necessary combination of high selectivity of mineral phase distribution, allows to allocate alteration phases, and has a high spatial resolution at the

μ m-scale. μ CT-scans would allow for 3D-data, if larger fractures ($> 20 \mu\text{m}$) are to be expected. To test the workflow simulations of gneissic rocks had been generated using the turning band algorithm (Fig. 1).^[2,3] First results of MPS applied on these simulated rocks show that mean and variance of the modal mineralogy depends on the number of realizations (cycles within MPS) and simulations, but converge to the mean and variance of the training image. If several training images are combined, the variability of the host rock seems to increase beyond the variability of the single images.

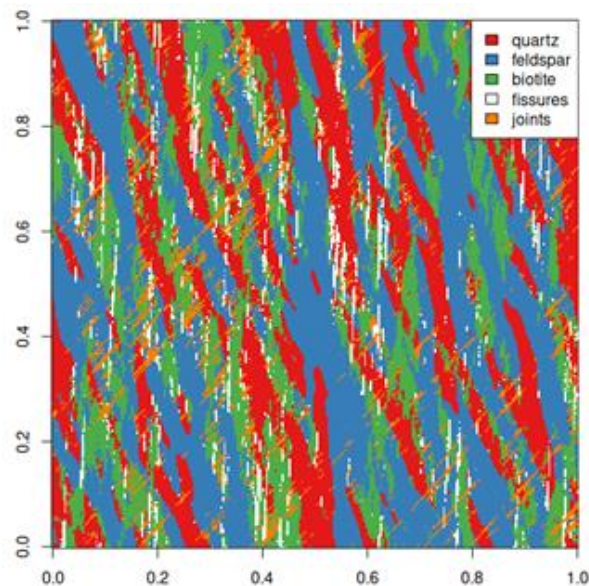


Figure 1. Example for simulated gneiss with fissures loosely following the biotite foliation: The modal mineralogy is 27% quartz (qz), 40% feldspar (fsp), 21% biotite (bi), 6% (healed) joints and 5% (open) fissures. The mineral composition exposed to the fissures is 29% qu, 25% fsp, 32% bi and 14% joints.

OUTLOOK. Larger training data sets are needed to confirm preliminary results. As “real data” extensive MLA data sets from granitic and gneissic units of the Habach series (Austrian Alps, Tauern Window) and μ CT data of the Bebertal sandstone (Thuringia) are going to be used.^[4]

ACKNOWLEDGEMENTS. This work was funded by the European Union’s Horizon 2020 research and innovation programme (DONUT WP within EURAD, no. 847593). We thank G.vandenBoogaart (HIF), R.Tolosana-Delgado (HIF) and P.Menzel (TUBAF) for their great support in consolidating the geostatistical method and providing code. We also greatly thank K.Bachmann (HIF) and C.Fischer (IRE) for helping us with providing real experimental data sets.

- [1] Stockmann, M. et al. (2017) *Chemosphere* **187**, 277–285.
- [2] Matheron, G. (1973) *Adv. Appl. Probab.* **5**, 439–468.
- [3] Tolosana-Delgado, R. et al. (2021) CRAN, gmGeostats v. 0.11.0
- [4] Thalhammer, O. et al. (1989) *Economic Geol.* **84**, 1153–1171.
- [5] Heidsiek, M. et al. (2020) *Env. Earth Sci.* **79**, 425.

Cm(III) sorption on single crystal orthoclase surfaces

M. Demnitz, S. Schymura, J. Neumann, M. Schmidt, K. Müller

Surface properties influence the retention of radionuclides such as Cm(III) on minerals. At pH 5.5 and 6.9, Cm(III) sorption was investigated on single crystal orthoclase surfaces using correlative spatially resolved investigation techniques. Sorption uptake and speciation on the surface are dependent of both pH and inherent surface roughness.

EXPERIMENTAL. An orthoclase single crystal was cleaved, exposing the [001] crystallographic plane generating two separate crystal sample surfaces for the sorption experiments. Cm(III) was sorbed onto the samples using a solution containing $[Cm(III)] = 10^{-6}M$ and $I = 0.1M$ NaCl at pH 5.5 and 6.9. The topography of the surfaces was measured using interferometry, from which the surface roughness was calculated as the root mean square of the surface roughness parameter S_q for every pixel using a 7×7 px sliding window. The sorption uptake and Cm(III) surface speciation was determined by quantitative autoradiography and μ TRLFS as has been described in detail in previous studies.^[1–3]

RESULTS. The cleaved surfaces of both crystals contain mainly terraces which are separated by surface steps with considerable surface roughness expressed by high S_q values. On the terraces themselves streaks and cracks are located, which increase the local surface roughness (Fig. 1a).

At pH 5.5, the Cm(III) uptake on the orthoclase surface is low, only accumulating to around 100 pmol/cm^2 , showing that saturation of the orthoclase surface with Cm(III) has not been reached. Two ROIs measured by μ TRLFS show that Cm(III) sorbs heterogeneously on the surface, with higher sorption uptakes in regions exhibiting a higher roughness. The Cm(III) peak maxima determined by Gaussian fitting show values between 601 and 603 nm, indicating that also the speciation on a single crystal surface is dependent on the surface roughness. In low roughness regions the peak maxima are located generally at higher wavelengths. This points towards primarily sorption on strong sorption sites. In contrast, in rougher areas the peak maxima are found in the whole range from 601–603 nm, showing that not only strong sorption sites but also weaker sorption sites are occupied. From the peak shift we can assess that mainly inner-sphere sorption (ISS) species form on both smooth and rough surfaces.^[3]

Performing luminescence lifetime analysis showed that speciation between rough and smooth surface sites did not differ significantly, likely because not all the sorption sites available on the surface have been occupied. However, since strong sorption sites are more numerous in rougher regions the uptake is higher.^[4] The main species formed on both smooth and rough surfaces are weak ISS complexes.^[3]

At pH 6.9, the sorption uptake on the crystal was higher reaching values of $125\text{--}200 \text{ pmol/cm}^2$ and $290\text{--}575 \text{ pmol/cm}^2$ in low and high roughness regions, respectively. This indicates that the saturation of the surface with Cm(III) might have been reached in some areas. Again, two ROIs were measured using μ TRLFS one of which is shown in Fig. 1. Similar to pH 5.5, heterogeneous sorption is observed (Fig. 1b). Higher uptakes are observed in rougher regions, while lower uptakes are seen in areas of lower roughness. The Cm(III) peak maxima in smoother, low-uptake regions are found between 602–603 nm (Fig. 1c). In rougher, high-uptake regions their value ranges from 601–603 nm. This

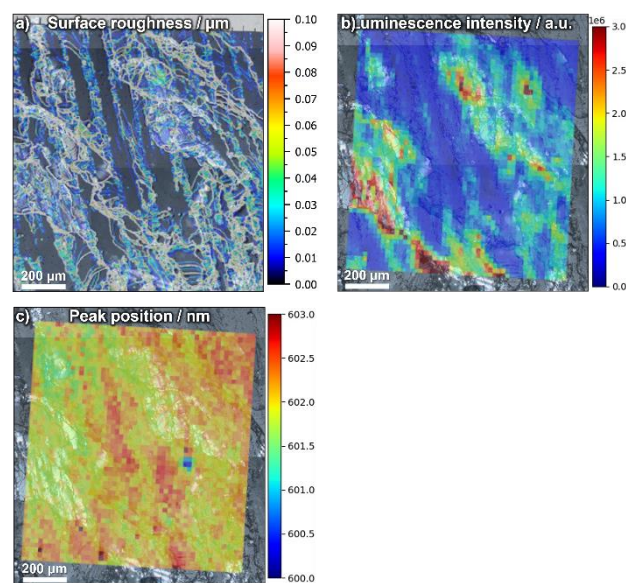


Figure 1. Surface roughness as determined by vertical scanning interferometry (a), integral Cm(III) luminescence intensity as determined by μ TRLFS (b) and Cm(III) peak maxima as determined by μ TRLFS (c).

implies that in smoother regions only one ISS complex is dominant, while in rougher regions the formed ISS complex species are more diverse.

Luminescence lifetime analysis revealed that the speciation differed significantly between rough and smooth regions, with a trend towards stronger complexation in rougher regions, where both strong and weak sorption sites are occupied. On smoother surfaces mainly weak ISS complexes form, while on rougher surface the main species are surface incorporated Cm(III) complexes.^[3]

The difference in speciation at pH 5.5 and 6.9 likely results as a consequence of the different sorption uptakes. In smoother regions the sorption uptake reaches its maximum, with mainly stronger sorption sites getting occupied. In high surface roughness regions, the uptake increases even further by also involving weaker sorption sites.

The study implies that even on single crystal surfaces sorption uptake and speciation is influenced by the surface roughness. The pH is controlling the overall amount of retained Cm(III), which in turn affects the surface speciation by the amount and type of occupied surface sorption sites.

ACKNOWLEDGEMENTS. We gratefully acknowledge the funding provided by the German Federal Ministry of Education and Research (BMBF) (Grant 02NUK053B) and the Helmholtz Association (Grant SO-093).

[1] Molodtsov, K. *et al.* (2018) *Sci. Rep.* **9**, 6287.

[2] Molodtsov, K. *et al.* (2021) *Environ. Sci. Technol.* **55**, 4871–4879.

[3] Demnitz, M. *et al.* (2022) *J. Hazard. Mat.* **423 A**, 127006.

[4] Yuan, T. *et al.* (2021) *Environ. Sci. Technol.* **55**, 15797–15809.

New insights into U(VI) sorption onto montmorillonite from batch sorption and spectroscopic studies at increased ionic strength

M. Stockmann, K. Fritsch, F. Bok, M. Marques Fernandes,¹ B. Baeyens,¹ R. Steudtner, K. Müller, C. Nebelung, V. Brendler, T. Stumpf, K. Schmeide

¹Paul Scherrer Institute, Laboratory for Waste Management, Villigen, Switzerland

The U(VI) sorption on the clay mineral montmorillonite was studied at increased ionic strength. A multi-method approach combining batch sorption experiments with spectroscopic methods (TRLFS, ATR FT-IR) as well as surface complexation modeling (SCM) was used to determine surface complexation constants. Based on a large number of experimental sorption data, a robust and comprehensive sorption model has been developed for a broad variety of geochemical settings.^[1]

Montmorillonite is a component of argillaceous rock, a potential host rock for deep geological repositories. Moreover, it is the main component of bentonite, a possible buffer and backfill material. Increased ionic strengths are observed in pore waters of North German clay deposits. Therefore, it is necessary to study the impact of increased ionic strength on radionuclide sorption, also taking the effect of calcium as competitive cation into account.

METHODS. The sorption experiments focused on a wide range of experimental conditions: variation of pH_c (4–10), background electrolytes (NaCl, CaCl₂) and ionic strength (0.1–3 mol kg⁻¹) with a solid liquid ratio of 4 g L⁻¹, $c_{m,U(VI)} = 1 \times 10^{-6}$ mol kg⁻¹, and in presence and absence of atmospheric CO₂.^[2]

Using these sorption data as well as other published U(VI) sorption studies on montmorillonite, a robust surface complexation model was developed based on the two site protolysis non-electrostatic surface complexation and cation exchange model (2SPNE SC/CE).^[3–6] The surface complexation constants were fitted with the geochemical speciation code PHREEQC v3.5.2 coupled with the parameter estimation program UCODE 2014. Thermodynamic data were taken from the PSI/Nagra thermodynamic database version 12/07 and were updated if necessary from either the THEREDA Release 2020 (www.thereda.de) or the NEA Second Update, Vol. 14. The formation of crystalline U(VI) phases was excluded due to the relatively short duration of the sorption experiments. However, the precipitation of calcite was expected and considered in the CaCl₂ model.

Surface site density and protolysis constants for the surface sites as well as cation exchange reactions were taken from literature.^[6] Due to the high ionic strengths, the Specific Ion Interaction Theory (SIT) approach was used.

RESULTS. A robust U(VI) sorption model was developed with a reduced set of surface complexes (Tab. 1). Three binary surface complexes ($\equiv S^sOUO_2^+$, $\equiv S^sOUO_2OH$, and $\equiv S^sOUO_2(OH)_3^{2-}$ and the CE reactions are sufficient to model the U(VI) sorption edges (at trace U concentrations) for different geochemical conditions.^[6] As can be seen in Fig. 1, this derived sorption model successfully describes the experimental data at various ionic strengths in the absence (not shown here) and presence of carbonates by considering only strong sorption sites. Ternary uranyl carbonate surface complexes were not required to describe the data.

In the absence of carbonate, U(VI) was nearly 99% sorbed on montmorillonite above pH_c 6 in both NaCl and CaCl₂ and no significant ionic strength effect was observed. In the pres-

Table 1. Surface complexation reactions and log K° values derived in this work for U(VI) sorption onto montmorillonite, errors correspond to $\pm 2\sigma$. Abbreviations refer to the respective surface complexes (SC).

	Surface complexation reactions	log K°
SC-1	$\equiv S^sOH + UO_2^{2+} \rightleftharpoons \equiv S^sOUO_2^+ + H^+$	2.42 \pm 0.04
SC-2	$\equiv S^sOH + UO_2^{2+} + H_2O \rightleftharpoons \equiv S^sOUO_2OH + 2 H^+$	-4.49 \pm 0.7
SC-3	$\equiv S^sOH + UO_2^{2+} + 3 H_2O \rightleftharpoons \equiv S^sOUO_2(OH)_3^{2-} + 4 H^+$	-20.5 \pm 0.4

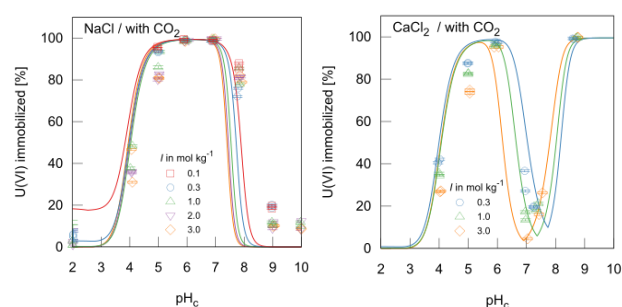


Figure 1. U(VI) experimental batch sorption data for montmorillonite (symbols) and simulated results using the final SCM model (lines) for NaCl (left) and CaCl₂ (right) as a function of pH_c and ionic strength in presence of CO₂.

ence of carbonate, U(VI) sorption was strongly reduced above pH_c 7.5 in NaCl and pH_c 6 in CaCl₂ system due to the formation of aqueous $UO_2(CO_3)_x^{(2-2x)}$ and $Ca_2UO_2(CO_3)_3$ complexes, respectively, as verified by TRLFS. A significant ionic strength effect was observed caused by the neutral $Ca_2UO_2(CO_3)_3(aq)$ complex, which strongly decreases U(VI) sorption with increasing ionic strength.

To validate the robustness of the derived sorption model, a blind prediction of independent sorption data was performed providing an excellent agreement.^[1,7] With respect to the long-term safety assessment of a radioactive waste repository in host rocks with higher salinity, the results demonstrate that increased ionic strengths must be considered for realistic predictions of U(VI) retardation in complex calcium rich natural environments.

ACKNOWLEDGEMENTS. This work was funded by the BMWK through the GRaZ II project (02E10971 and 02E11860B) and by the BMBF (02NUK053B) and the Helmholtz Association (SO-093) through the iCross project.

- [1] Stockmann, M. et al. (2022) *Sci. Total Environ.* **806**, 150653.
- [2] Fritsch, K. (2018) *PhD Thesis*, TU Dresden.
- [3] Marques Fernandes, M. et al. (2012) *Geochim. Cosmochim. Acta* **93**, 262–277.
- [4] Bradbury, M.H. and Baeyens, B. (2005) *Geochim. Cosmochim. Acta* **69**, 875–892.
- [5] Nebelung, C. et al. (2007) *NF-PRO Report*.
- [6] Bradbury, M.H. and Baeyens, B. (1997) *J. Contam. Hydrol.* **27**, 223–248.
- [7] Pabalan, R.T. et al. (1998) *Academic Press, San Diego*.

Impact of sulfate on the sorption of trivalent actinides and rare earth elements (Am, Eu, Y) on the muscovite (001) basal plane

J. Neumann, S. S. Lee,¹ H. Brinkmann, P. J. Eng,² J. E. Stubbs,² T. Stumpf, M. Schmidt

¹Argonne National Laboratory, Lemont, U.S.A.; ²The University of Chicago, Chicago, U.S.A.

Here, we study the impact of the natural inorganic ligand and sulfate on the adsorption of trivalent metal ions (Am, Eu, Y) on mica (001). Combination of *in situ* surface X-ray diffraction (SXRD) and *ex situ* alpha spectrometry is used to determine interfacial structures at the molecular level as well as M(III) coverages. M(III) is found to form two surface complexes – an adsorbed outer-sphere and an extended outer-sphere species. At low $[\text{SO}_4^{2-}]$, an up to 3x increase in coverage is observed, which corresponds to higher amounts of adsorbed M(III) than needed for surface charge compensation. This overcompensation is likely caused by ion-ion correlations at the mineral/water interface. At high $[\text{SO}_4^{2-}]$, the mono- and bisulfate complexes of M(III) dominate solution speciation. Their lower charge cause a lower sorption affinity and weaker ion-ion correlations, which leads to a strong decrease in M(III) coverage and eventually to a suppression of adsorption of M(III).

Mobility of contaminants in the environment depends strongly on their interactions with charged mineral phases and is strongly influenced by reactions with organic and inorganic ligands. Relevant contaminants in the context of a deep geological repository for radioactive waste are trivalent actinides (Am, Cm, Pu) due to their high radiotoxicity. As their inactive analogues, rare earth elements (REE) are often used in scientific studies.

Previously, the retention of REEs by muscovite mica, a main component of a crystalline rock, has been investigated and an impact of the 1:1 electrolyte NaCl beyond simple aqueous complexation was reported.^[1] Hence, it is interesting to explore also the effect of other, multivalent ligands such as the natural inorganic ligand sulfate. Therefore, we applied surface X-ray diffraction (SXRD) and alpha spectrometry to investigate the impact of sulfate on the sorption of M(III) (M = Am, Eu, Y).

EXPERIMENTAL. For sorption experiments, several solutions of 0.1 mM YCl_3 (SXRD) or 0.1 mM EuCl_3 (spiked with $^{243}\text{Am}^{3+}$ = 3.8×10^{-4} mM, for alpha spectrometry) were prepared at different $[\text{SO}_4^{2-}]$ = 0.2–4 mM and pH = 5.5. A freshly cleaved muscovite was dropped in the sample solution and reacted overnight.

SXRD measurements were conducted *in situ* at beamline 13-ID-C at the Advanced Photon Source (APS). Experimental details can be found elsewhere.^[2] For sample preparation of *ex situ* alpha spectrometry measurements, the crystals were taken out of the solution and dipped into deionized water ($10\times$) to remove non-adsorbed solution. Afterwards the crystals were covered with a stainless steel aperture to expose a defined surface area to the detector.

RESULTS. The interfacial structures of the investigated samples show generally a great similarity. Their total electron density profiles consist of three peaks with similar heights and widths, located at a distance of 1.3, ~2.4, and 4.1 Å from the surface. These values are in good agreement with the interfacial structure of muscovite in deionized water,^[3] where a peak at 1.3 Å is reported to correspond to adsorbed water in the ditrigonal cavity of the muscovite basal

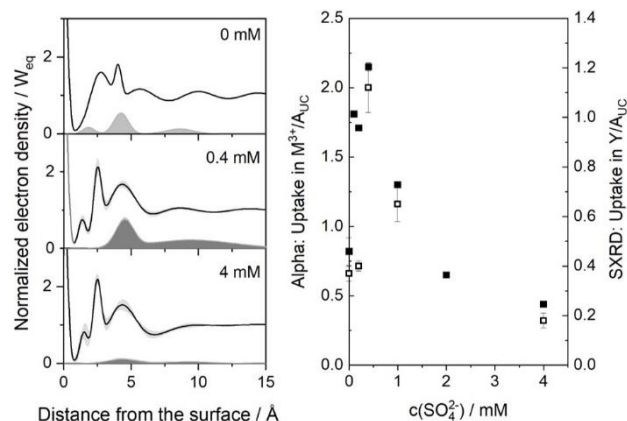


Figure 1. Interfacial structures of 0.1 mM YCl_3 adsorbed at the muscovite basal plane obtained by SXRD for two selected $[\text{SO}_4^{2-}]$ (0.4 and 4 mM) and comparison to the sulfate-free reference (left).^[1] Uptake as a function of $[\text{SO}_4^{2-}]$ obtained by *ex situ* alpha spectrometry (filled symbols, $[\text{Eu}^{3+}] = 0.1 \text{ mM}$, $^{243}\text{Am}^{3+} = 3.8 \cdot 10^{-4} \text{ mM}$) and SXRD (open symbols, $[\text{Y}^{3+}] = 0.1 \text{ mM}$) (right).

hydration layer of the surface. These observations indicate a weak interaction between M(III) and the mineral surface. Element-specific SXRD identifies two distinct outer-sphere (OS) sorption species. One adsorbed OS_{ads} at ~4.5 Å and an extended OS_{ext} at a distance of ~9.0 Å from the mineral surface.

Sorption quantity (“coverage”, in Y atoms per A_{UC} ; A_{UC} : area of the muscovite unit cell = 46.72 \AA^2) shows strong non-linear variations of OS_{ads} and OS_{ext} as a function of sulfate concentration. At low $[\text{SO}_4^{2-}]$ (~0.4 mM), total coverage increases to ~1 $\text{M(III)}/\text{A}_{UC}$ (Fig. 1), which is three times more than the amount needed for compensation of the muscovite surface charge ($1e^-/\text{A}_{UC}$). The study shows that the formation of MSO_4^+ and its adsorption is not responsible for the observed strong increase in coverage. Instead, electrostatic ion-ion correlations between adsorbed Y^{3+} are suggested to be the reason for the observed overcompensation of the surface charge. Ion-ion correlations are complex, electrostatic interactions, which are particularly strong for highly charged ions, such as M^{3+} and SO_4^{2-} .

At higher sulfate concentrations (> 0.4 mM), coverage decreases significantly, which could be attributed to the decrease in $[\text{M}^{3+}]$ due to the formation of MSO_4^+ and $\text{M}(\text{SO}_4)_2^-$, which have a lower or even negative charge. Hence, they have a lower sorption affinity and show weaker ion-ion correlations than M^{3+} .

These results demonstrate that the natural inorganic ligand sulfate may have a strong impact on the sorption of trivalent actinides and REE at charged mineral phases. This impact goes beyond simple aqueous speciation, but involves complicated electrostatic interactions within the mineral/water interface. These interactions need to be considered for a reliable safety assessment of a repository for radioactive waste.

ACKNOWLEDGEMENTS. Funding from the Federal Ministry for Economic Affairs and Climate Action (BMWK) for SMILE (02E11668B) is acknowledged.

[1] Lee, S. S. *et al.* (2013) *J. Phys. Chem. C*, **117**, 23738–23749.

[2] Neumann, J. *et al.* (2022) *J. Phys. Chem. C*, *in press*.

[3] Cheng, L. *et al.* (2001), *Phys. Rev. Lett.*, **87**, 156103.

Batch sorption studies of Np(V) onto ZrO₂

I. Jessat, H. Foerstendorf, N. Jordan

Batch sorption experiments showed an increased sorption of Np(V) onto zirconia (ZrO₂) upon raising pH. The impact of ionic strength, Np(V) concentration, and the solid-to-liquid ratio of ZrO₂ on the Np(V) sorption was investigated. Results suggested the predominant formation of inner-sphere Np(V) surface complexes. Electrophoretic mobility measurements supported these findings. However, the sorption isotherm obtained at pH6 indicated the presence of different sorption sites on the zirconia surface.

The interactions of actinides such as neptunium, a long-lived transuranium element, with corrosion products in the near-field of a geological repository are of concern regarding its safety assessment. The main corrosion product of the zirconium alloy cladding material is ZrO₂, which represents one of the first barriers for interactions with radionuclides.^[1]

EXPERIMENTAL. All experiments were conducted at room temperature under N₂ atmosphere to exclude carbonate and at an ionic strength of 0.1 or 0.01 mol L⁻¹ NaCl (Tab. 1). The equilibration time for the samples of the pH dependent and the isotherm series was 3 and 2–9 days, respectively. After pH measurements, samples containing 0.5 g L⁻¹ monoclinic ZrO₂ (US Research Nanomaterials, Inc.) were subsequently centrifuged (1 h, 4,020 × g), whereas those containing 4 g L⁻¹ ZrO₂ were ultracentrifuged (45 min, 174,900 × g). All concentrations of Np-237 in the supernatants were determined by liquid scintillation counting or ICP-MS.

Table 1. Experimental parameters of the Np(V) pH-dependent and isotherm batch sorption experiments onto ZrO₂.

Experiment (m/V ratio)	pH	Time (d)	[Np(V)] (mol L ⁻¹)	I (NaCl) (mol L ⁻¹)
pH-dependent (0.5 g·L ⁻¹)	3–10	3	10 ⁻⁶	0.01 or 0.1
			6 × 10 ⁻⁶	0.01
pH-dependent (4 g·L ⁻¹)	3–10	3	10 ⁻⁶	0.01
Isotherm (0.5 g·L ⁻¹)	6	2–9	10 ⁻⁹ –6 × 10 ⁻⁵	0.01

The pH of the isoelectric point (pH_{IEP}) of the neat ZrO₂ was determined by zeta potential measurements of samples containing 0.5 g L⁻¹ ZrO₂ at I = 0.01 mol L⁻¹ NaCl after three days of equilibration. Additionally, zeta potential measurements were conducted for pH-dependent batch sorption samples containing 6 × 10⁻⁶ mol L⁻¹ Np(V) (before centrifugation).

RESULTS. The sorption of the positively charged neptunylion (NpO₂⁺) generally started around pH 3 and reached its maximum above pH 7 (Fig. 1), which is ascribed to the increasing negatively charged zirconia surface upon raising pH. Np(V) hydrolysis species and chloro species like NpO₂Cl(aq.) can be neglected under the investigated conditions.^[2,3] The change of the ionic strength from 0.01 to 0.1 mol L⁻¹ did not impact the Np(V) sorption (Fig. 1, open and filled squared symbols), indicating the formation of inner-sphere Np(V) surface complexes.

At a higher Np(V) concentration (6 × 10⁻⁶ mol L⁻¹), the sorption edge was slightly shifted towards higher pH as a result

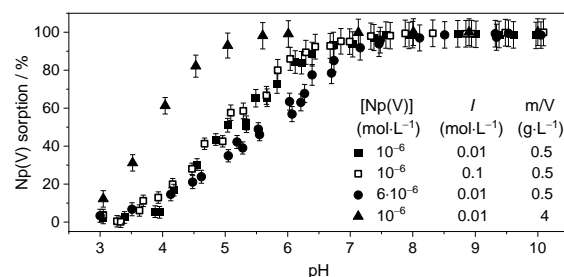


Figure 1. Sorption pH edges of Np(V) onto ZrO₂ at different conditions. [Np(V)] = 10⁻⁶ or 6 × 10⁻⁶ mol L⁻¹, I = 0.1 or 0.01 mol L⁻¹ (NaCl), m/V = 0.5 or 4 g L⁻¹ ZrO₂.

of increased competition of Np(V) for sorption sites (Fig. 1, filled circles).

A shift of the pH_{IEP} of the neat zirconia from 8.3 to 8.8 was observed in the presence of Np(V) (data not shown). The impact of the NpO₂⁺ sorption on the pH_{IEP} of ZrO₂ also hints towards the presence of inner-sphere Np(V) complexes on the ZrO₂ surface.

At an increased solid-to-liquid ratio a considerable shift of the sorption edge towards lower pH values was observed (Fig. 1, filled triangles), which might indicate the presence of different kinds of sorption sites. This can also be assumed from the sorption isotherm (Fig. 2) showing a linear slope over a broad concentration range and a steeper slope at very low Np(V) concentrations. The lower slope observed at increased Np concentrations (> 10⁻⁶ mol L⁻¹) is assigned to the saturation of the binding sites on the zirconia surface.

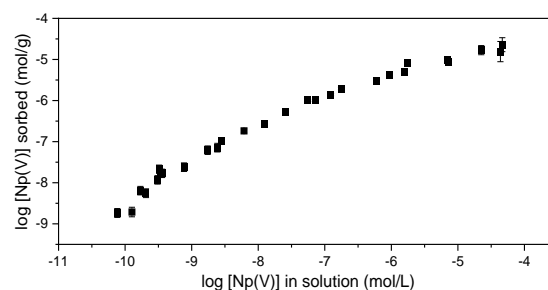


Figure 2. Sorption isotherm with m/V = 0.5 g L⁻¹ ZrO₂, 0.01 mol L⁻¹ NaCl and 10⁻⁹–6 × 10⁻⁵ mol L⁻¹ Np(V) at pH 6.

Spectroscopic investigations, namely X-ray absorption spectroscopy and *in situ* ATR FT-IR experiments, will provide further information about the structure of the Np(V) surface species. Surface complexation modelling will then be used to derive thermodynamic surface complexation constants. The gained information will help to better predict the environmental fate of pentavalent actinides and will thus contribute to a reliable safety assessment of a nuclear waste repository.

ACKNOWLEDGEMENTS. The authors thank A. Dietze for the preparation of the isotherm samples and S. Beutner for the ICP-MS measurements.

- [1] Motta, A. T. *et al.* (2015) *Annu. Rev. Mater. Res.* **45**, 311–343.
- [2] Neck, V. *et al.* (1992) *Radiochim. Acta* **56**, 25–30.
- [3] Müller, K. *et al.* (2015) *Environ. Sci. Technol.* **49**, 2560–2567.

Uranium carbonates removal by layered double hydroxides

N. Mayordomo, G. Padberg, D. M. Rodriguez, K. Müller

Two layered double hydroxides (LDH) with different redox properties have shown great Uranium (U) carbonate removal efficiency, regardless on pH, ionic strength, and U or carbonate concentration.

Uranium carbonate species represent an environmental problem since their negative charge in solution hinders their immobilization by most of the widely distributed minerals such as clays or iron and aluminum oxides.^[1] Layered double hydroxides (LDH), present in many natural and engineered environments could diminish this problematic, because of their permanent positive charge.^[2] In this work, we have used two LDH phases with different redox properties to study uranium immobilization: (i) Ca(II)-Al(III)-Cl LDH that is redox inactive, and (ii) Fe(II)-Al(III)-Cl LDH that presents reductive potential due to the presence of Fe(II) (hereafter simplified as Ca-LDH and Fe-LDH, respectively). Contact experiments as a function of pH value, ionic strength and carbonate concentration have been carried out to determine the uranium removal yield.

EXPERIMENTAL. All the experiments were performed in a N₂ glove box (O₂ < 5 ppm). The LDH were synthesized by coprecipitation of M(II)Cl₂ (with M = Ca, Fe) and AlCl₃ at alkaline pH. The resulting solid phase was washed thrice and its identity was confirmed by X-ray diffraction.

Contact experiments were carried out using 0.5 g L⁻¹ suspensions of Ca-LDH or Fe-LDH in presence of 0.5 μM U(VI)O₂Cl₂ and at increasing Na₂CO₃ concentrations (from 0 to 2 mM). The pH was adjusted to the desired value (pH 6–12) and the suspensions were shaken for two days. Afterwards, the pH values were measured, the samples were centrifuged at 14,000 × g for 45 minutes and the supernatant was sampled for uranium concentration in solution using ICP-MS.

The U sorption yield was calculated as a distribution coefficient (K_d) using the equation:

$$K_d = \frac{([U]_0) - ([U]_t)}{[U]_t} \cdot \frac{V}{m} \quad (1)$$

where V is the volume of suspension in L, m is the mass in g, and [U]₀ and [U]_t are the initial and final molar concentration of U, respectively.

RESULTS. Uranium removal by Ca-LDH or Fe-LDH at pH 9.0 as a function of NaCl and CO₃²⁻ concentration is shown in Fig. 1. It is observed that U removal by Fe-LDH is maximum (log K_d = 5.3 represents ≈100% removal) and the U uptake is not influenced by neither an increase in ionic strength (Fig. 1A) nor in carbonate concentration (Fig. 1B). On the contrary, the U immobilization by Ca-LDH slightly decreases with an increase in NaCl and CO₃²⁻ concentration. The lowest U uptake measured by Ca-LDH represents log K_d = 4.1 represents (85% removal) at 0.1 M NaCl and log K_d = 4.8 (97% removal) at 2 mM Na₂CO₃. This is an indication that outer-sphere complexation or anionic exchange mechanism may contribute to the processes occurring at Ca-LDH surface responsible of U immobilization.

The lowest uranium yield values observed in Ca-LDH are in any case, higher than other reported U removal values by redox-inactive minerals, e.g., clays.^[3] Other uranium contact experiments performed in water in a wider range of pH

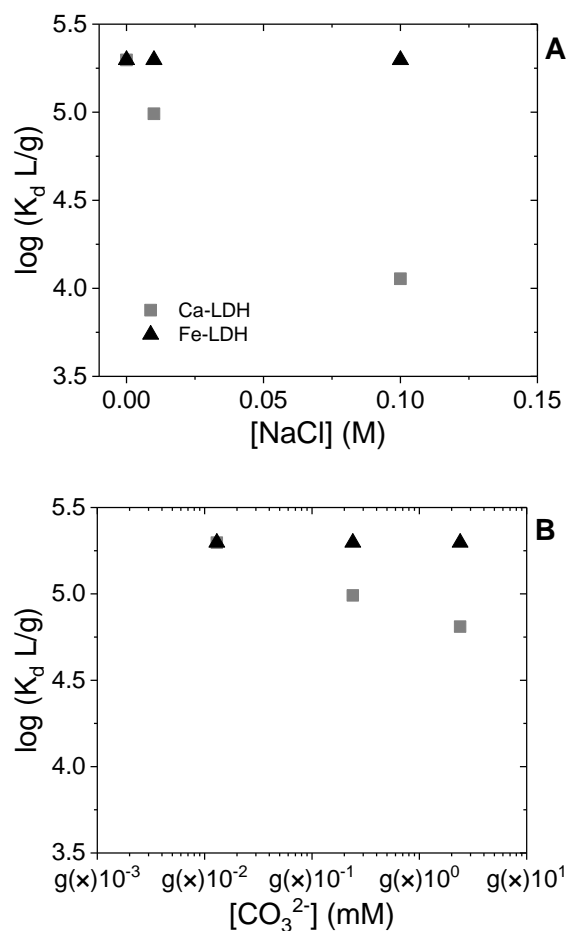


Figure 1. Uranium removal ([U(VI)]₀ = 0.5 μM) (in K_d) by Ca-LDH and Fe-LDH (0.5 g L⁻¹) at pH 9.0 as a function of NaCl concentration at 0.013 mM [CO₃²⁻] (A), and carbonate concentration in H₂O (I = 0) (B).

(from 6 to 12) at fixed U concentration (0.5 μM), showed that both LDH phases sorbed U with a yield of ≈ 100% throughout the entire range of pH values evaluated.

The results confirm the high efficiency of the studied LDH phases towards U immobilization under a broad variation of experimental parameters. However, the observed difference on the uranium removal trend indicates that both LDH remove U by different mechanisms and further investigations by infrared, luminescence, and X-ray absorption and photoelectron spectroscopy will be essential to identify them.

ACKNOWLEDGEMENTS. The authors acknowledge S. Beutner and S. Shams Aldin Azzam for performing ICP-MS and XRD measurements, respectively. Funding from the Federal Ministry for Economic Affairs and Climate Action (BMWK) for VESPA II (02E11607B) is acknowledged.

- [1] Grenthe, I. et al. (2020) *Second update on the Chemical Thermodynamics of U, Np, Pu, Am and Tc*. OECD-NEA.
- [2] Forano, C. et al. (2013) in: *Development in Clay Science*. 745–782, Elsevier, Amsterdam.
- [3] Marques Fernandes, M. et al. (2012) *Geochim. Cosmochim. Acta* **93**, 262–277.

Retention of trivalent lanthanides (Eu, La) and actinides (Am, Cm) by natural and synthetic Ca-feldspars

J. Lessing, J. Neumann, F. Bok, J. Bezzina, J. Lützenkirchen,¹ V. Brendler, T. Stumpf, M. Schmidt

¹Karlsruhe Institute of Technology (KIT), Institute for Nuclear Waste Disposal, Karlsruhe, Germany

Crystalline rock is a possible host rock for deep geological repositories for radioactive waste. One of its main components are feldspars. Therefore, the retention of trivalent actinides (Cm, Am) as well as their less toxic homologue Eu(III) with Ca-feldspar were investigated. Zeta potential measurements, batch experiments, and time-resolved laser-induced fluorescence spectroscopy (TRLFS) were used to analyze the sorption of these trivalent metal ions by Ca-feldspar on the molecular level. With these data a generic, robust surface complexation model (SCM) that satisfactorily describes sorption of Ln(III) and An(III) on all feldspars was developed.

Trivalent minor actinides (Cm, Am) dominate the radiotoxicity of spent nuclear fuel over thousands of years. Feldspars together with quartz and micas are the main components of crystalline rock, which is considered as a possible host rock for a deep geological repository for radioactive waste, due to its ability to isolate toxic components from the biosphere. So far, the retention of radioactive trivalent metals has only been investigated for K- and Na-feldspar.^[1] Here, we investigate the impact of Ca(II) content of the feldspar on its retention potential towards M(III). We study two natural plagioclase materials containing 23 % and 79 % Ca, respectively, as well as a pure synthetic Ca-feldspar (99 % Ca), and compare our findings to previously published data for K-feldspar.^[1]

EXPERIMENTAL. First, Ca-feldspar was synthesized following the synthesis route of Chihara *et al.*^[2] The composition of the two natural feldspars was measured by X-ray fluorescence analysis and the phase purity was confirmed by powder-XRD. For all materials a zeta potential was determined at a solid-liquid ratio = 0.2 g L⁻¹. Subsequently, batch sorption experiments under different geochemical conditions ([M³⁺ = 52 nM–10 μM; solid-liquid ratio = 1–3 g L⁻¹, I = 0,1 M NaCl, pH = 3–9) were carried out.

To gain structural information of the sorption complexes on the molecular level, time-resolved laser-induced spectroscopy (TRLFS) using Cm(III) was applied. Finally, the obtained quantitative and structural data were combined to develop a surface complexation model (SCM) with the corresponding surface complexation parameters for the spectroscopically identified surfaces complexes.

RESULTS. Zeta potential measurements of the different feldspars show an unusual increase of the zeta potential for pH 4–7, which becomes more pronounced with increasing Ca(II) amount in the mineral (Fig. 1). Experiments with K-feldspar in the presence of Ca(II) and Al(III) show that the increase is mainly caused by sorption of Al(III) and/or precipitation of an Al phase, while Ca(II) sorption plays only a minor role. For Ca-feldspar Al(III) is released during the experiments due to mineral dissolution.

Batch sorption experiments show an analogous retention behavior for K- and Ca-feldspar at low [M(III)].^[1,3] However, at higher [M(III)] the sorption edge for Ca-feldspar is steeper than for K-feldspar and again the effect becomes stronger with increasing Ca amount. This indicates a slightly higher

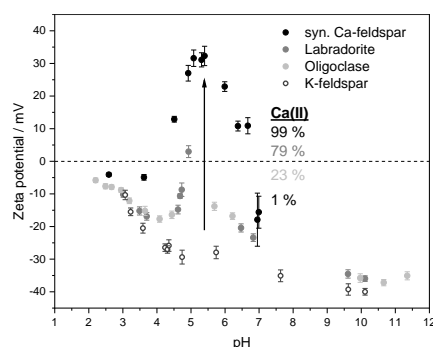


Figure 1. Zeta potential of feldspars at S/L = 0.2 g L⁻¹.

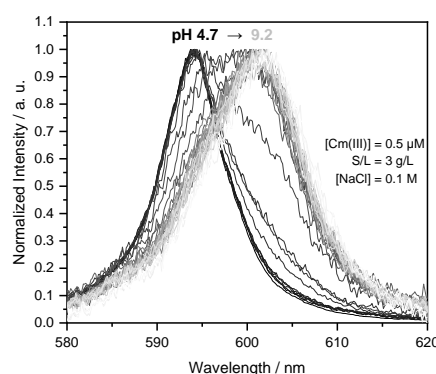


Figure 2. Emission spectra of Cm(III) adsorbed on synthetic Ca-feldspar.

retention potential towards M(III) for Ca- compared to K-feldspar.^[1,3]

Spectroscopic investigations (Fig. 2) show the formation of an inner sphere (IS) species and its two hydrolysis forms. These are the same species previously identified on K-feldspar, but hydrolysis of the IS complex begins at lower pH for Ca-feldspar.^[1,3]

The identified species were used in the formulation of a surface complexation model based on the diffuse double layer approach. The derived log K values of surfaces complexes for Ca-feldspar are shown in Tab. 1.^[3] They are generally in good agreement with those determined by a similar approach for K-feldspar, sometimes even identical within the margins-of-error. The largest deviation is found for the first hydrolyzed surface complex, as expected from the spectroscopic investigation.

Table 1. Stability constants of spectroscopically identified surface species.

Log K	Ca-feldspar	K-feldspar ^[1]
(=S-O) ₂ M ⁺	-8.4 ± 0.9	-8.0 ± 0.3
(=S-O) ₂ M(OH)	-10.8 ± 0.2	-11.6 ± 0.3
(=S-O) ₂ M(OH) ₂	-16.4 ± 0.6	-16.6 ± 0.4

ACKNOWLEDGEMENTS. Funding from the Federal Ministry for Economic Affairs and Climate Action (BMWK) for SMILE (02E11668B) is acknowledged.

[1] Neumann, J. *et al.* (2021) *J. Colloid Interface Sci.* **591**, 490–499.

[2] Chihara, H. *et al.* (2017) *Planet. Space Sci.* **149**, 94–99.

[3] Neumann, J. *et al.* (2022) in preparation.

Structural modelling of Tc(IV) complexes with green rust: application of Fourier filtering algorithm combined with target factor analysis

A. Rossberg, N. Mayordomo

Tc, a fission product of ^{235}U and ^{239}Pu , must be considered in the nuclear waste management over geological time scales due to its long half-life; especially the high ground water mobility of Tc(VII) is of great concern. Green rust (GR), a naturally occurring Fe(II)/Fe(III) layered double hydroxide forming after iron or steel corrosion can immobilize Tc(VII) by sorption and reduction to less soluble Tc(IV). The complexity of the system, with GR transformation to secondary mineral phases like hematite and magnetite, Tc(IV)O₂·H₂O precipitation, and the sorption and incorporation of mononuclear and/or polynuclear Tc(VI) species, makes the analysis of the manifold molecular mechanisms by EXAFS shell fitting impossible. Here, we propose a problem-adapted analysis of TcK-edge spectra of the Tc-GR system at different pH and Tc loads, which consists of a newly developed Fourier filtering algorithm combined with target factor analysis.

EXPERIMENTAL. The TcK-edge of nine samples with pH 4.5, 7.5 and 10.5 and Tc loads of 400, 600 and 1,000 ppm were measured at the ROBL beamline by using a closed-cycle He-cryostat and an 18 element Ge-detector^[1]. Boundary conditions considering the occurrence of spectral mixtures, of several Fe phases, of mono- and polynuclear Tc species, and of simultaneous sorption and incorporation processes as well as the fact that the local structural environment of Tc(IV) is similar to that of Fe(III), the following ansatz for the EXAFS analysis was implemented:

(i) Performance of a shell fit in order to determine ΔE_0 and to measure the most common Tc–O, Tc–Tc and Tc–Fe radial distances. (ii) Application of ITFA for the spectral decomposition of the EXAFS spectral mixtures into the eigenvectors.^[2] (iii) Performance of a target test (TT) with theoretical spectra gained by FEFF calculations based on structural models and ΔE_0 .^[3] (iv) Storage of the best matching theoretical spectra and corresponding model structures.

For step (iii) and in order to supply a broad structural variability of Fe, several Fe minerals like fougérite (carbonate GR), two models of ferrihydrite (Fh), magnetite, hematite, goethite and four XRD structures of maghemite were selected. For each Fe site and for each Fe mineral a theoretical TcK-edge spectrum was calculated by substituting Fe(III) with Tc(IV). For each theoretical spectrum, *i.e.* target spectrum, the TT predicts a spectrum, as a linear combination of the eigenvectors, which matches best the target spectrum where the SPOIL value measures the quality of the fit.^[3] However, since for the calculation of the target spectra the Debye-Waller damping terms are unknown we applied the recently published Fourier filtering algorithm (FFA) in step 3.^[4] Furthermore, we assumed that the radial distances of the Tc surrounding atoms may not necessarily match those of the replaced Fe atoms. Therefore, only Fe sites for which the radial Fe–O and Fe–Fe distances match the fitted Tc–O and Tc–Fe distances within a maximum deviation of $\pm 0.2 \text{ \AA}$ were selected, while shifting the surrounding O and Fe atoms to the fitted distance before calculating the target spectrum.

RESULTS. ITFA yielded two components. The structural models and target spectra with the lowest SPOIL value are shown in Figs. 1 and 2, respectively. In the case of compo-

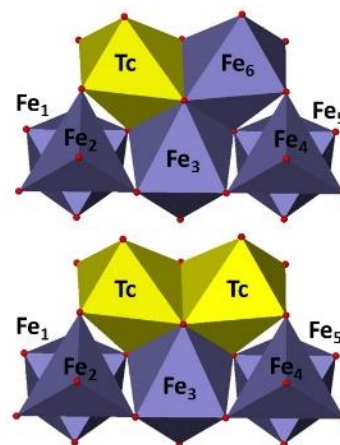


Figure 1. Best structural models for spectral component 1 (top) and 2 (bottom) gained by the TT of FEFF calculated theoretical spectra based on Fe mineral structures.

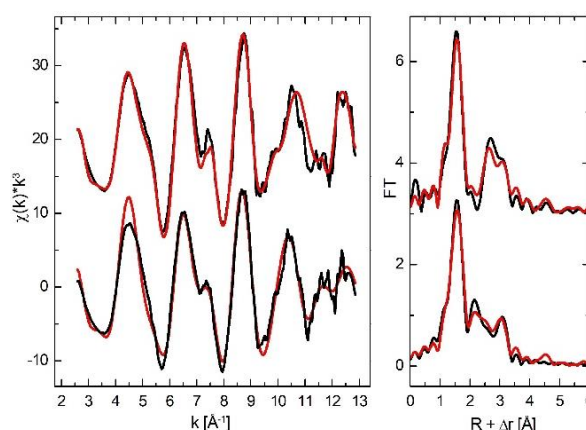


Figure 2. Best matching target spectra (red) and their corresponding TT predictions (black) of component 1 (top) and 2 (bottom). Corresponding Fourier transforms (right).

nent 1 (prevalent at low pH), a mononuclear edge (Fe_{3,6}) and corner sharing (Fe_{1,2}) complex is formed, with the radial distances Tc–Fe_{3,6} of 3.09 Å and Tc–Fe_{1,2} of 3.52 Å. Component 2 is different from component 1 only by an additional Tc cation at position Fe₆ (Fig. 1 bottom). The distances are Tc–Tc@2.55 Å, Tc–Fe₃@3.08 Å and Tc–Fe_{1,2}@3.52 Å, while both Tc are equivalent due to the symmetry. This species is prevalent at high pH. Both arrangements are found in the structure of Fh, which does not necessarily mean that Fh is indeed the Tc-trapping mineral phase. The resulting structural arrangements are just models which reflect only the local molecular environment of Tc(IV), while they are based on XRD validated structural arrangements of Fe sites.

ACKNOWLEDGEMENTS. Funding from the Federal Ministry for Economic Affairs and Climate Action (BMWK) for VESPA II (02E11607B) is acknowledged.

- [1] Scheinost, A. et al. (2021) *J. Synchrotron Rad.* **28**, 333–349.
- [2] Rossberg, A. et al. (2003) *Anal. Bioanal. Chem.* **376**, 631–638.
- [3] Malinowski, E. R. (1991) in: *Factor Analysis in Chemistry*, John Wiley & Sons, New York.
- [4] Taube, F. et al. (2019) *Inorg. Chem.* **58**, 368–381.

Neural network analysis of EXAFS spectra to identify technetium chukanovite species

K. Schmeide, A. Rossberg, F. Bok, S. Shams Aldin Azzam, S. Weiss, A. C. Scheinost

Chukanovite ($\text{Fe}_2(\text{OH})_2\text{CO}_3$), a relevant corrosion product of steel and cast iron under nuclear waste repository conditions, was identified as efficient reductant and immobilization agent for technetium (Tc) under a wide pH range (7.8–12.6). Self-organizing (Kohonen) mapping (SOM), a biologically inspired neural network-based approach of machine learning, was applied to analyze 37 extended X-ray absorption fine-structure (EXAFS) spectra to derive spectral endmembers and their dependence on geochemical parameters.^[1]

The fission product ^{99}Tc plays a crucial role in release scenarios for safety assessments of repositories for high-level radioactive waste. Tc can occur in oxidation states ranging from $-I$ to $+VII$.^[2] Its environmental mobility is mainly determined by redox conditions. Under oxic conditions, the very mobile $\text{Tc(VII)}\text{O}_4^-$ is predominant. Under anoxic conditions, however, interaction with Fe(II) -bearing solids commonly present as iron corrosion products but also as natural minerals, leads to formation of Tc(IV) , which is efficiently immobilized by sorption to and/or incorporation by primary and secondary mineral phases.^[3,4]

EXPERIMENTAL. Two series of samples, Tc chukanovite sorption samples and coprecipitates, were prepared under inert gas conditions (N_2) at RT under varying geochemical conditions (Tc loading: 720–6,650 ppm, $S/L = 7.5 \text{ g L}^{-1}$, $I = 0.1\text{--}1 \text{ M}$ (NaCl), $\text{pH } 7.8\text{--}12.6$, [carbonate]: 0–0.6 M, contact time: 2–235 d) and investigated by using Tc K -edge EXAFS spectroscopy.

RESULTS. The retention capability of chukanovite towards Tc(VII) was found to be high in the pH range 7.8 to 12.6, evidenced by high solid-water distribution coefficients, $\log R_d \sim 6$, and independent of ionic strength (up to 1 M NaCl).

From a total of 37 EXAFS spectra, the spectral endmembers and their dependence on geochemical parameters were derived using SOM.^[5] SOM is used to explore the hidden structure of data by reducing the high dimensional input space, given by EXAFS spectral mixtures, into a two-dimensional space. Thus, SOM enables an easier interpretation of the relationship between spectra and geochemical parameters, like pH, concentration, and temperature of samples. We generalized the fusion approach, as proposed by Melssen *et al.*,^[6] to be able to combine more than two SOM, *i.e.* to implement several geochemical parameters simultaneously. For this, we combined seven rectangular-shaped SOM with 900 nodes per SOM (*i.e.* neurons). The first SOM (X-map) contains the EXAFS spectra, the second and following SOM (Y-maps) contain for each spectrum in the X-map the fractions of the Tc-species (Y_1 -map) and geochemical parameters like pH, E_h , Tc(VII) initial, Tc loading, carbonate and contact time ($Y_{2,\dots,7}$ -map). Moreover, our supervised trained XY-SOM allows a quantification of the coexisting Tc-species and the isolation of their EXAFS spectra from the spectral mixtures.^[7] The architecture for a three fused XY-SOM is shown in Fig. 1 as an example.

X-ray absorption near-edge structure (XANES) data confirmed the complete reduction of Tc(VII) to Tc(IV) by chukanovite under all experimental conditions. Consistent with mineral phases identified by X-ray diffraction, SOM analysis of the EXAFS spectra revealed the presence of three species

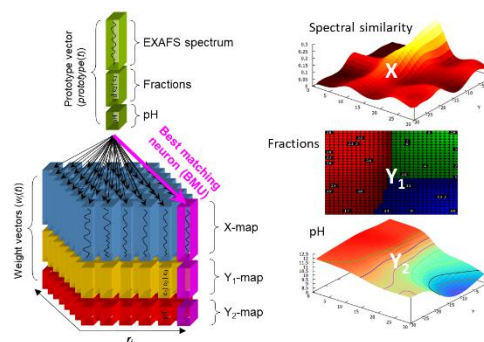


Figure 1. Schematic presentation of three fused self-organizing maps (SOM) (X , Y_1 , and Y_2 -maps). The node which matches best a randomly chosen prototype vector is determined.

in the sorption samples (Fig. 2): Between $\text{pH } 7.8$ and 11.8 , TcO_2 -dimers form inner-sphere sorption complexes both at the surface of the initial chukanovite as well as on the surface of magnetite formed due to redox reaction. At $\text{pH } \geq 11.9$, Tc(IV) is incorporated in a mixed, chukanovite-like, Fe/Tc hydroxy carbonate precipitate. These species also formed in coprecipitates.

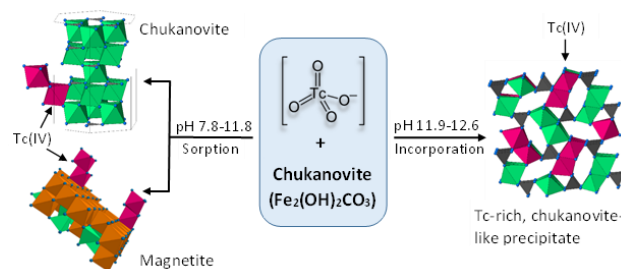


Figure 2. Tc chukanovite reaction pathways: Two sorption and one incorporation species determined by SOM as endmember components as a function of pH value.

Re-oxidation experiments showed the instability of chukanovite under aerobic conditions. Instead of re-oxidizing to soluble Tc(VII) , however, Tc remained in its tetravalent oxidation state, and was firmly retained by environmentally more stable minerals, magnetite and/or goethite, which formed due to the oxygen ingress. Tc(IV) incorporation into octahedral sites of these iron minerals prevents or impedes Tc re-oxidation.

Generally, it can be concluded that the corrosion products chukanovite, magnetite and goethite contribute over a wide pH range to the overall *in situ* Tc retention capacity expected for subsurface nuclear waste repositories as well as for contaminated sites, thus mitigating its environmental mobility.

ACKNOWLEDGEMENTS. This work was partially funded by the BMWK within the project no. 02E10971. We thank K. Kvashnina and N. Baumann from the ROBL team as well as C. Müller for support during XAS measurements.

[1] Schmeide, K. *et al.* (2021) *Sci. Total Environ.* **770**, 145334.
 [2] Bauters, S. *et al.* (2020) *Chem. Commun.* **56**, 9608–9611.
 [3] Yalcintas, E. *et al.* (2016) *Dalton Trans.* **45**, 17874–17885.
 [4] Pearce, C. I. *et al.* (2020) *Sci. Total Environ.* **716**, 132849.
 [5] Kohonen, T. (1982) *Biol. Cybern.* **43**, 59–69.
 [6] Melssen, W. *et al.* (2006) *Chemometr. Intell. Lab. Systems* **83**, 99–113.
 [7] Domaschke, K. *et al.* (2014) in: *ESANN Proceedings*, p. 277–282, Bruges, Belgium.

Spectro-electrochemical cell development for the investigation of redox mechanisms

D. M. Rodriguez, N. Mayordomo, V. Brendler, K. Müller

To gain mechanistic understanding of redox processes, UV-vis spectroscopy was coupled into an electrochemical cell. A potential staircase (chronoamperometry) triggers the redox process while UV-vis spectra are recorded in parallel, thus allowing an *in situ* monitoring of the reaction progress.

The determination of reaction mechanisms is very relevant not only from a fundamental chemistry point of view but also for interesting applications in fields like catalysis or remediation. In particular, in radioecology or the safety assessment of nuclear waste repositories, it is key to understand the speciation of the radionuclides for modeling their environmental behavior. Electrochemistry offers a wide range of techniques that can be used to propose redox reaction mechanisms. However, such proposals are often difficult to prove with spectroscopy since the intermediate species only appear at specific potential ranges and rapidly become more stable species once the potential application stops. In consequence, we have coupled UV-vis spectroscopy with chronoamperometry in order to monitor the redox reactions *in situ*, thus proving electrochemical hypotheses of the reaction mechanism and electrons involved.

EXPERIMENTAL. The spectro-electrochemical cell is presented in Fig. 1. It was built inside a mobile glovebox (SICCO) in order to maintain an inert N₂ atmosphere and for radiation protection. The cell holder (made of polyethylene terephthalate glycol, PETG) was fabricated with a 3D printer (3DWOX 1, Sindoh) and the quartz cell dimensions were also customized (width × depth × height: 20 × 10 × 30 mm and an optical path length of 5 mm). For the chronoamperometry, a potentiostat (PGSTAT 101, Metrohm) placed outside the glovebox was connected to three electrodes (all ALS Japan): glassy carbon rod as working electrode, Pt wire as counter electrode and Ag/AgCl (3 M KCl) as reference electrode. The UV-vis spectrometer (AvaSpec-ULS2048 StarLine, Avantes) and the lamp (AvaLight-DH-S-BAL, Avantes) were located outside the glovebox and connected to the cell holder *via* optical fiber.

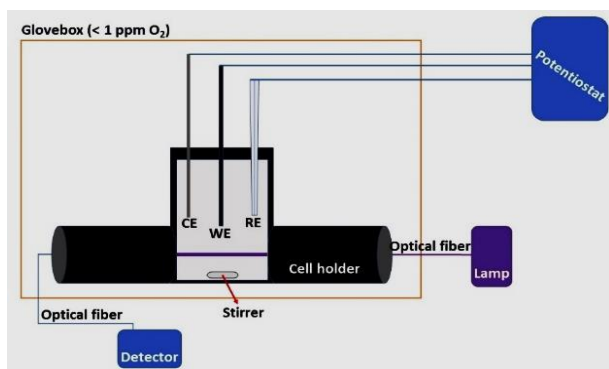


Figure 1. Schematic representation of the spectro-electrochemical cell.

The working temperature was 21 °C. A general procedure for the spectro-electrochemical experiments is as follows: 1.5 mL of sample, consisting on the analyte of interest – that undergoes redox reaction – and a background electrolyte, are placed in the quartz cell. The sample is agitated throughout the entire experiment using a 5 mm magnetic stirrer.

The potential staircase can be customized depending on the sample. It is recommended to perform a cyclic voltammetry to determine the potential range of the staircase as well as the height of the step. The duration of the step can be adapted, too. Example: staircase varying the potential 10 mV every four minutes; thus, 480 mV for four minutes, then 490 mV for four minutes and so forth until the potential range is covered.

In parallel to the chronoamperometry, the UV-vis spectra are continuously recorded. Depending on the experiment, the time interval between each spectrum can be varied accordingly. Continuing with the staircase example, if one spectrum is recorded every 30 seconds, eight spectra per potential step will be obtained, subsequently averaged to reduce noise.

RESULTS. Recently, this spectro-electrochemical cell (Fig. 2) has been used to study the reduction from Tc(VII) to Tc(IV).^[1] That is of high concern from an environmental point of view as Tc migration and bioavailability depend on its redox speciation.^[2] It was found that the reduction mechanism depends on the pH. At pH 2, Tc(VII) gains two electrons and becomes Tc(V) that rapidly reduces to Tc(IV). At pH ≥ 4 the reduction occurs in one step with the transfer of three electrons.^[3]

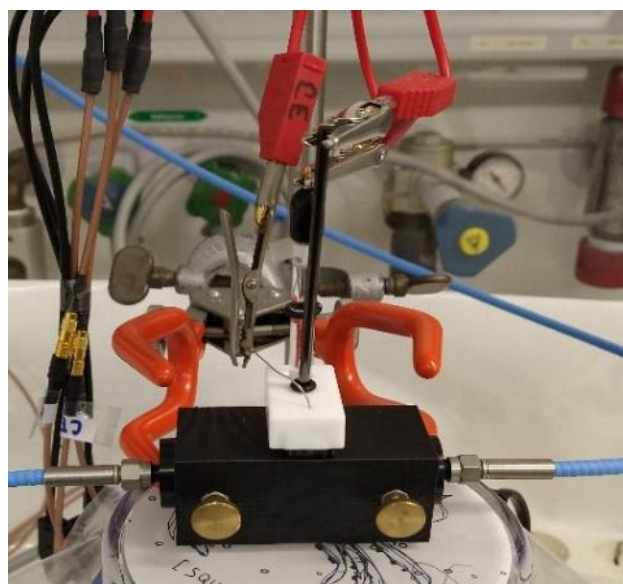


Figure 2. Picture of the spectro-electrochemical cell.

This cell can be used to study the redox behavior of any redox sensitive species. Fundamental information on the speciation and the underlying redox reactions will increase the reliability of modelling these complex systems.

ACKNOWLEDGEMENTS. Funding from the Federal Ministry for Economic Affairs and Climate Action (BMWK) is acknowledged (02E11607B).

- [1] Rodriguez, D.M. (2021) Ph. D. Thesis, Technische Universität Dresden, Germany.
- [2] Meena, A.H. *et al.* (2017) *Environ. Chem. Lett.* **15**, 241–263.
- [3] Rodriguez, D.M. *et al.* (2022) in preparation for *ES&T Engineering*.

Isothermal Titration Calorimetry (ITC) for surface processes – Thermograms correlate with classical batch experiments

H. Foerstendorf, N. Jordan

The applicability of micro-calorimetry for sorption processes in mineral phases was exemplarily evidenced for the Se(IV)/maghemite system. It was found that thermograms recorded at different pH reflected the different extent of Se(IV) uptake derived from batch sorption studies. Additionally, the thermogram signal followed the amount of Se sorbed onto maghemite during an ITC experiment.

As a consequence of nuclear waste disintegration heat, elevated temperatures in the near field of a repository may influence radionuclide retention significantly. However, the experimental data base providing values of free Gibbs energy ($\Delta_r G$), enthalpy ($\Delta_r H$) and entropy ($\Delta_r S$) of sorption reactions of radionuclides onto minerals is still sparse.

Isothermal Titration Calorimetry (ITC) potentially provides direct access to such thermodynamic functions of adsorption reactions. In the past, the vast majority of ITC studies focused on complexation reactions in homogeneous phases. In this approach, we extend the applicability of ITC to reaction occurring on the water-solid interface of minerals.

EXPERIMENTAL. The detection of the heat of the sorption reaction of Se(IV) onto maghemite was accomplished by microcalorimetric titrations experiments at 25 °C using a TAM Instrument. A maghemite suspension (2.4 mL, 3 g L⁻¹, at pH 4, 6, or 8) was introduced into the titration ampoule and permanently stirred using a turbine. After thermal equilibration, 25 successive injections of 10 μ L of 0.01 mol L⁻¹ Se(IV) (at pH 4, 6, or 8) were performed. Between each injection, 30 minutes were found sufficient for the system to return to thermal equilibrium. All experiments were carried out at 25 °C. Details about maghemite and the performance of Se(IV) batch experiments can be found elsewhere.^[1]

RESULTS. The thermograms represent the heat flow recorded as a function of time during the titrations. For sorption processes, it is expected that the signal continuously decreases as the number of injections increases because the binding sites of maghemite are being gradually saturated by Se(IV), and the thermal effect gets consequently reduced (Fig. 1, top). The verification of this assumption can be accomplished by classical batch sorption experiments applying parameter that correspond to those of the titration steps of the ITC experiments. A decrease of the amount of Se(IV) adsorbed onto maghemite, exemplarily shown for the first four titration steps was observed (Fig. 1, bottom), and nicely correlates with the amplitude of the thermogram (Fig. 1, top). Furthermore, the thermograms are expected to represent the different extent of sorption depending on the prevailing pH. This was confirmed by the cumulative heat of reaction derived from the thermograms – recorded at different pH values – by summing up the single heat values of each titration step (ΣJ ; Fig. 2). The curves clearly showed that sorption is preferred at lower pH (Fig. 2) in accordance with to the batch sorption series obtained earlier.^[1]

The accurate evaluation of the thermograms/heat of reaction for the determination of enthalpy values by sound routines is under development and will represent the next step of this work in progress. A combined approach with spectroscopic techniques evidencing the nature of the adsorption process

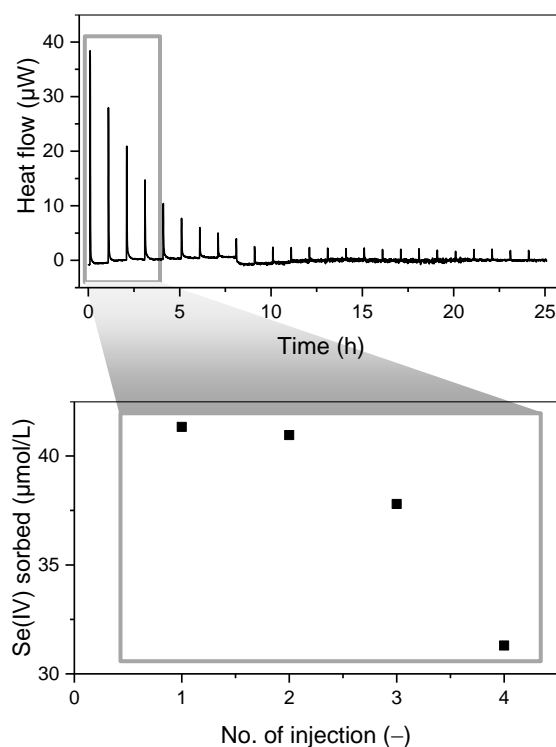


Figure 1. ITC thermogram of the Se(IV) sorption reaction on maghemite at pH 4 (top). Results from batch sorption experiments applying corresponding parameter (m/V ratio, pH, I, [Se(IV)]) to the first four titration steps of the ITC experiment (bottom).

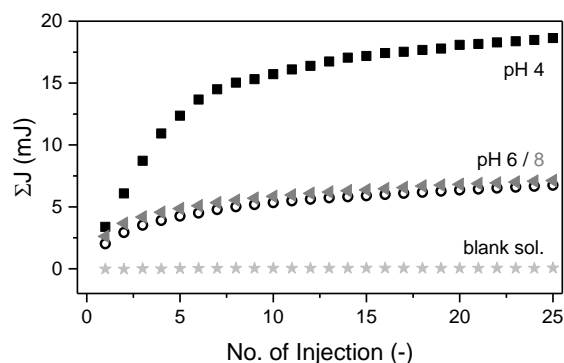


Figure 2. Isotherms derived from ITC thermograms of the Se(IV) sorption reaction on maghemite at different pH.

and the number of relevant species at the surface will then provide a comprehensive thermodynamic description of the mobility of contaminants including radionuclides (e.g. U, Np, etc.) in natural systems leading to a much more confident safety assessment.

ACKNOWLEDGEMENTS. This work was supported by the Helmholtz Association, grant SO-093 (iCross) and by the German Federal Ministry of Education and Research (BMBF), grant 02NUK053B.

[1] Jordan, N. et al. (2014) *Environ. Sci. Technol.* **48**, 1656–1674.

Phase transformations in cerium-doped zirconia

L. B. F. dos Santos, N. Huittinen, V. Svitlyk, C. Hennig

A series of cerium doped zirconia samples with varying Ce concentrations (14–58 mol-%) was synthesized *via* the co-precipitation route. Diverse crystal structures have been reported for $Zr_xCe_{1-x}O_2$ solid solutions: three stable structures, namely, monoclinic (m), tetragonal (t), and cubic (c), as well as several metastable ones (t' , t'' , κ , and t^*).^[1] The obtained phase composition highly depends on the synthesis conditions. In the current work, the solid phases were investigated by combined Raman and PXRD analyses. None of the investigated solid phases showed the presence of one crystal structure only, but the samples were mixtures of two to three different ZrO_2 modifications. Along with the stable m, t, and c phases, the metastable t' phase was identified, depending on the Ce concentration in the sample.

Zirconia (ZrO_2) is a product derived from Zircaloy corrosion and it has the capacity to incorporate lanthanides and actinides in its crystal structure.^[2] This is why ZrO_2 has been extensively studied for several applications, such as for the immobilization of actinides present in High-Level Radioactive Waste streams (HLW), in special the radioactive isotope ^{239}Pu .^[2] The lanthanide cerium is often used as a surrogate for plutonium due to its similar ionic radius, comparable chemical properties in the oxidation states +III and +IV, and its easier handling.^[4]

EXPERIMENTAL. To understand the behavior of cerium in the zirconia structure, six solid solutions with Ce^{4+} concentrations from 14 to 58 mol-% were synthesized. A pure CeO_2 solid was also synthesized to serve as a reference, facilitating the detection of CeO_2 in the zirconia samples, in case of phase separation. 400 mg $ZrOCl_2$ was dissolved in a 0.01 M hydrochloric acid solution. An adequate amount of Ce-stock solution, (2.763 M $CeCl_3 \cdot 7H_2O$), to reach the desired doping concentrations, was added to the acidic Zr^{4+} solution. The solution was thereafter slowly added to 12.5% NH_4OH under constant stirring, resulting in an instantaneous formation of a hydrous zirconia precipitate. The CeO_2 precursor was synthesized using the same syntheses conditions, but without the zirconia reagent. The resulting suspensions were kept at room temperature for around 20 h for complete precipitation. Afterward, the solid phases were separated *via* centrifugation and the precipitates were washed 6 times with water, to remove all ammonia residue. The samples were dried and thereafter sintered at 1,500 °C for 48 h to ob-

tain a crystalline solid, which was mortared into a fine powder. Raman spectroscopy was performed on a HORIBA Jobin Yvon LabRAM Aramis Vis Raman microscope; synchrotron Powder X-Ray Diffraction (PXRD) measurements were done at ROBL beamline at the European Synchrotron Radiation Facility in Grenoble. The Rietveld Refinement was done by FullProf and/or PDXL2 programs.

RESULTS. The Raman spectra (Fig. 1a) show clear bands for the monoclinic phase only in the sample with 14 mol-% Ce doping. The cubic CeO_2 phase has a unique band at $\sim 450\text{ cm}^{-1}$. The intermediate compositions show the same band, indicating that these compounds have the same or very similar solid structures. By Rietveld refinement of the PXRD data, the cubic phase is confirmed to be 100 mol-% Ce with a Goodness of fit equal to 0.5441. As the diffraction peaks from this sample do not match the others, no solid-phase separation ($CeO_2 + ZrO_2$) was detected in the investigated dopant range. The t' and c phases are not easily distinguished. Owing to the high-resolution PXRD data (Fig. 1b), however, the two diffraction peaks between 24.2° and 24.6° are from the tetragonal phase, the three peaks around 24.3° belong to the monoclinic phase with 14 mol-% Ce. The peak around 24.1° could be attributed to the t' phase and the peak at 23.9° to the cubic one. Both peaks could be identified in the compounds with more than 22 mol-% of Ce. The metastable phase increases up to 42 mol-% Ce, after this concentration this phase is replaced by the cubic phase. In addition, the compound with 58 mol-% Ce has a larger peak at 23.9° , suggesting that the solid phase separation is about to begin. As a result, the samples with 30, 42, and 50 mol-% have three phases: t, t' , and c.

ACKNOWLEDGEMENTS. This work was supported by the German Federal Ministry of Education and Research (BMBF) under the ACE project (02NUK060A).

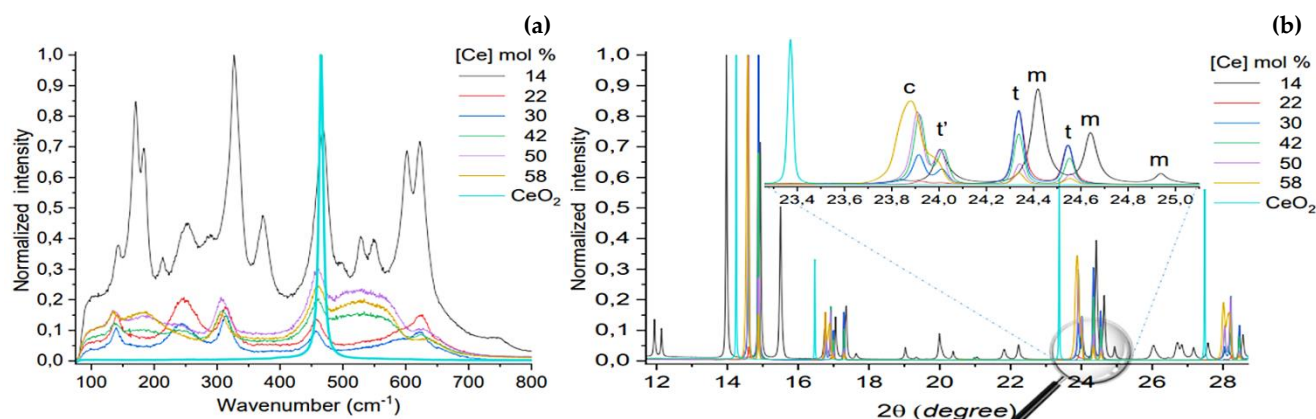


Figure 1. Zirconia doped with 14–58 mol-% of cerium and dioxide of cerium (CeO_2): Raman spectra (a) and X-Ray Diffraction pattern (b).

Production of monazite targets for heavy ion irradiation experiments

S. E. Gilson, A. A. Bukaemskiy,¹ M. K. Henkes,¹ G. L. Murphy,¹ N. Huittinen

¹Institute of Climate and Energy Research – 6, Forschungszentrum Jülich, Jülich, Germany

A method for the preparation of monazite targets in the form of polycrystalline pellets with high percent theoretical densities was established. Targets were prepared for ion irradiation experiments. At least two parallel pellets of nine compositions of monazite endmembers LnPO_4 and solid solutions $\text{La}_{0.5}\text{Ln}_{0.5}\text{PO}_4$ ($\text{Ln} = \text{Ce}, \text{La}, \text{Nd}, \text{Pr},$ and Sm) were manufactured. Precursor rhabdophane powders doped with Eu^{III} as a luminescent probe were pressed into 10 mm diameter pellets using a uniaxial cold pressing method, then sintered at 1,400 °C. Archimedean and modified Archimedean methods were used to determine the density and total porosity of the targets. Results indicate the targets have percent theoretical densities (> 93 %) and percent porosities (< 7 %) that are suitable for irradiation.

Monazites are candidate materials for the immobilization of trivalent ions present in certain nuclear waste streams. Hence, detailed knowledge about the radiation tolerance of their structure is important.^[1,2] Irradiation with heavy ions is often used to simulate and investigate radiation damages in crystalline materials. For this purpose, powder samples are typically manufactured to dense pellets with low porosity and high density. Although previous studies have described the target production process for LaPO_4 , process optimization was needed.^[3]

EXPERIMENTAL. Precursor rhabdophane powders ($\text{LnPO}_4 \cdot 0.67\text{H}_2\text{O}$) were prepared according to methods described in the literature.^[4] Powders were washed with Milli-Q water and dilute acid to remove impurities that could affect density of the targets. Thereafter, the amorphous samples were pressed using an Oehlglass, Hahn, and Kolb uniaxial cold press by applying a force of 38 kN ($P = 450 \text{ MPa}$) to approximately 500 mg of material as reported previously.^[3] The obtained pellets were weighed geometrically so green density could be calculated. Pellets were then sintered in a tube furnace in air at 1,400 °C for five hours. Densities of the crystalline targets were calculated through geometric and hydrostatic weighing as dictated by Archimedean and modified Archimedean methods.^[3] As a final step, targets were polished using abrasive silicon carbide paper and 1 μm diamond paste on an automatic polishing table for approximately 15 minutes.

RESULTS. About sixteen grams of Eu^{III} -doped lanthanum rhabdophane, $\text{LaPO}_4 \cdot 0.67\text{H}_2\text{O}$, was precipitated. The first set of pellets that were pressed had low green densities of less than 60 %. Although density did increase upon sintering, many of the pellets were brittle, and broke during hydrostatic weighing. It was hypothesized that an impurity in the powder was not removed through multiple washes with Milli-Q-grade water. To determine if the impurity could be removed with acid, the remaining powder was washed once with dilute HNO_3 .^[3]

A second set of pellets prepared with the acid-washed powder had green densities above 60 %. Sintering also improved the density of these targets. An average density of approximately 95 % of the theoretical value was calculated for this second set of targets.^[5] All those pellets survived the hydrostatic weighing needed for density calculations. Because of

the improvement in density of the targets upon acid-washing, this step was conducted for the remaining monazite endmembers and solid solutions. After establishing this method, the same process for pressing, sintering, and weighing was followed for each of these compositions. Representative percent theoretical densities and percent total porosities for the monazite endmembers are given in Tab. 1. The open porosity represents the percentage of the pores that are on the surface of the pellet that are accessible to liquids, such as water. Closed porosity represents the pores that are inside the pellet that are not accessible to liquids.

Table 1. Calculated density and porosities of selected monazite compositions.

Composition	Density (% TD*)	Porosity (%)	
		Open	Closed
LaPO_4	93.6	1.6	4.8
CePO_4	95.5	1.6	2.8
PrPO_4	93.9	1.5	4.5
NdPO_4	94.1	2.5	3.5
SmPO_4	94.3	1.3	4.1

*TD = theoretical densities taken from Ni *et al.*^[5]

The final step of pellet preparation was polishing. A transmitted light image of the surface of a CePO_4 pellet after polishing is given in Fig. 1. Eleven LaPO_4 targets were produced, whereas two to three targets of the remaining compositions were fabricated. In an incoming irradiation experiment at the Ion Beam Center (IBC), these targets will be subjected to irradiation with 14 MeV Au ions at varying fluences.

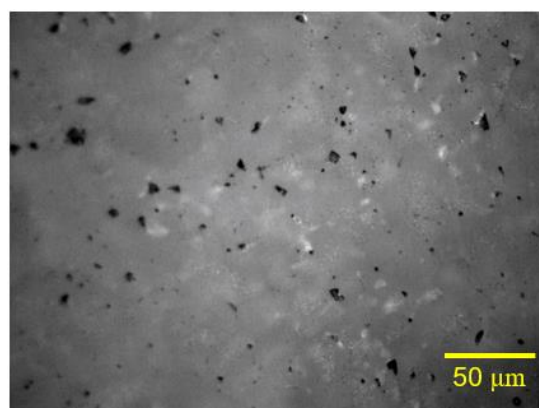


Figure 1. Transmitted light image of the polished CePO_4 target surface.

ACKNOWLEDGEMENTS. BMBF for funding of the AcE project (02NUK060A).

- [1] Neumeier, S. *et al.* (2017) *Radiochim. Acta* **105**, 961–984.
- [2] Ewing, R. (1999) *Proc. Natl. Acad. Sci. U.S.A.* **96**, 3432–3439.
- [3] Babelot, C. (2017) *J. Eur. Ceram. Soc.* **37**, 1681–1688.
- [4] Huittinen, N. *et al.* (2016) *J. Colloid Interface Sci.* **483**, 139–145.
- [5] Ni, Y. *et al.* (1995) *Am. Mineral.* **80**, 21–26.

Thermodynamic reference database THEREDA: 11. News in the 2021 data release and major developments

F. Bok, H. C. Moog,¹ A. Richter, S. Zechel

¹Gesellschaft für Anlagen- und Reaktorsicherheit (GRS)mbH, Braunschweig, Germany

THEREDA is a joined database project to assess potential radionuclide retardation due to solubility limits, thus contributing to the long-term safety assessment of nuclear waste repositories.^[1,2]

THEREDA provides thermodynamic data to calculate the solubility of actinides, fission products as well as matrix and building materials using the Pitzer ion interaction model for high saline solutions (ionic strength up to at least 7 molal) in the temperature range 0–100 °C.^[3]

THEREDA has gained a great international reputation; users from 40 countries are currently registered. In the fourth phase of the THEREDA project, the following relevant changes and new features have been introduced so far:

THE 2021 DATA RELEASE. Thermodynamic data and Pitzer interaction parameters for the element lead were added to the data set. The data were taken from Hagemann^[4,5] and allow for the calculation of solubility of the following lead phases: Lithargite (red PbO), Massicot (yellow PbO), Cerussite (PbCO₃), Plumbonacrite (3PbCO₃·2PbO·H₂O), Hydrocerussite (PbCO₃·2Pb(OH)₂), Phosgenite (PbCl₂·PbCO₃), Cotunnite (PbCl₂), Blixite (3PbO·PbCl₂·H₂O), Laurionite (Pb(OH)Cl), 6PbO·PbCl₂·2H₂O, Challaolite (KCl·2PbCl₂), 3KCl·3PbCl₂·H₂O, 3MgCl₂·PbCl₂·19H₂O, Anglesite (PbSO₄), Lanarkite (PbO·PbSO₄), 3PbO·PbSO₄·H₂O, Leadhillite (PbSO₄·2PbCO₃·Pb(OH)₂), Palmierite (K₂SO₄·PbSO₄), PbCl₂·2PbSO₄·2Na₂SO₄·5H₂O. In addition, thermodynamic data were added for phosphate-bearing plumbous minerals Chloropyromorphite (Pb₅(PO₄)₃Cl) and Plumbogummite (PbAl₃(PO₄)₂(OH)₅·H₂O).

DATABASE DEVELOPMENTS. Due to the further development of the geochemical codes supported by THEREDA (e.g. Geochemist's Workbench,^[6] PHREEQC^[7]) the output parsers were adapted to code-specific changes. During this adjustment, efforts were also made to display the additional information compiled for the users in a more compact and comprehensible way.

APPLICATION CASES. THEREDA's capabilities are demonstrated using application case calculations, whose results were compared with experimental values published in literature. In 2021, 56 such cases were added, yielding a total of 436 application calculations right now. Of these, 198 were performed at HZDR-IRE. All demo calculations can be browsed on a new section of the website (www.thereda.de). Examples are shown in Figs. 1 and 2. After a free registration on the website, users also have access to all data and ready-to-use parameter files in the code-specific formats of the common geochemical calculation programs.

ACKNOWLEDGEMENTS. This kind of database work can only be managed in a great team. The authors thank all members of the great THEREDA team at GRS, KIT-INE, TUBAF and CSD. THEREDA is funded by the Federal Company for Radioactive Waste Disposal (BGE) with the contract number 45181017.

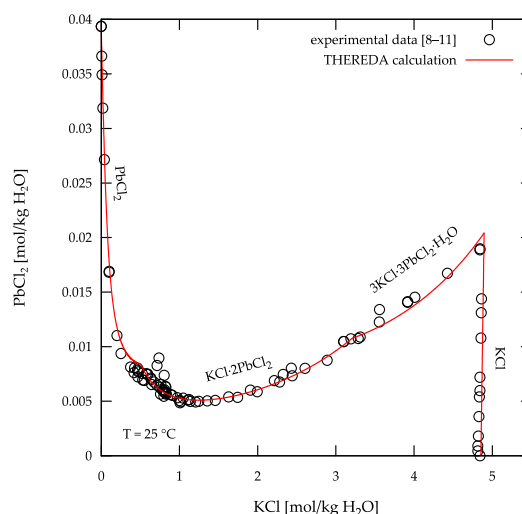


Figure 1. Solubility diagram of the system KCl-PbCl₂-H₂O(l) at T = 25 °C, Symbols: experimental data from literature^[8–11], Line: calculation using THEREDA.

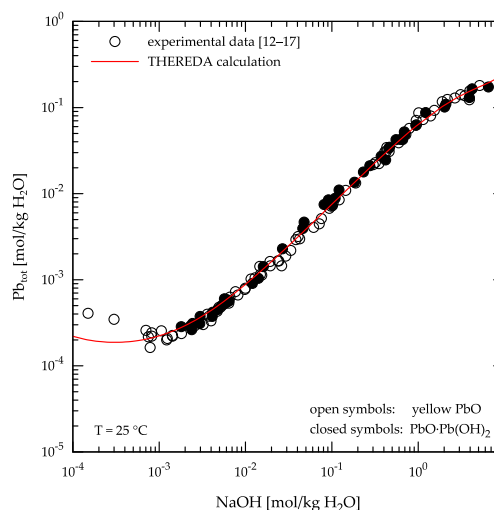


Figure 2. Solubility of yellow PbO in NaOH solution at T = 25 °C, Symbols: experimental data from literature^[12–17], Line: calculation using THEREDA.

- [1] Altmaier, M. et al. (2008) *atw Int. J. Nucl. Power*, **53**, 249–253.
- [2] Moog, H. C. et al. (2015) *Appl. Geochem.* **55**, 72–84.
- [3] Pitzer, K. S. (1991) *Activity Coefficients in Electrolyte Solutions*, 2nd Ed., CRC Press, Boca Raton.
- [4] Hagemann, S. (1999) Ph.D. Thesis, Technische Universität Braunschweig, Brunswick, Germany.
- [5] Hagemann, S. (2022) *Development of a thermodynamic model for zinc, lead and cadmium in saline solutions*, Revised edition. Report GRS-653.
- [6] <https://www.gwb.com>.
- [7] <https://www.usgs.gov/software/phreeqc-version-3>.
- [8] Kendall, J. et al. (1925) *J. Am. Chem. Soc.* **47**, 2306–2317.
- [9] Burrage, L. J. (1926) *J. Chem. Soc. Res.* **129**, 1703–1709.
- [10] Allmand, A. J. et al. (1933) *Trans. Faraday Soc.* **29**, 679–689.
- [11] Parton, H. N. et al. (1939) *Trans. Faraday Soc.* **35**, 402–412.
- [12] Brujle, E. S. et al. (1959) *Zh. Neorg. Khim.* **4**, 2091–2099.
- [13] Garrett, A. B. et al. (1939) *J. Am. Chem. Soc.* **61**, 367–373.
- [14] Töpelmann, H. (1929) *J. Prakt. Chem.* **121**, 320–363.
- [15] Glasstone, S. (1922) *J. Chem. Soc.* **121**, 58–66.
- [16] Kulba, F. J. et al. (1961) *Zh. Neorg. Khim.* **6**, 2814–2815.
- [17] Müller, E. (1925) *Z. Phys. Chem.* **114**, 129–156.

SCIENTIFIC CONTRIBUTIONS (PART III)

Biological Systems

Long-Lived Radionuclides in
**BIOLOGICAL
SYSTEMS**

Binding of U(VI) to plant cells of *Brassica napus*

J. Jessat, R. Hübner,¹ W. A. John, A. Rossberg, D. Prieur, S. Sachs

¹Institute of Ion Beam Physics and Materials Research, HZDR, Dresden, Germany

Uranium (U) is immobilized by interaction with organisms such as plant cells. Localization of U in *Brassica napus* (canola) cells showed an abundant occurrence of U in physiologically intact cells providing visual evidence for (active) uptake of U by plant cells. A co-localization of U and phosphorous (P) at bio-membranes was found. This observation is supported by X-ray spectroscopic measurements, which indicate the occurrence of cell-associated U(VI) bound to organic phosphate groups.

Risk assessments for the health of humans and environment are required in case of a possible release of radionuclides (RNs) from a nuclear waste repository into the environment. U as the major component of spent nuclear fuel rods is investigated with regard to its interaction with the biosphere in case of its possible release and transport in groundwater and soil up to the food chain.^[1] It is known that U is immobilized by interaction with plant cells, but re-mobilization processes can also occur.^[2] For a more detailed understanding of the immobilization of U by *Brassica napus* suspension cells, EXAFS (extended X-ray absorption fine structure) spectroscopy was performed to obtain information on the binding environment of U that was localized in the cells using STEM-EDX (scanning transmission electron microscopy coupled with energy-dispersive X-ray spectroscopy).

EXPERIMENTAL. *B. napus* cells (1.5 g) were incubated with 20, 100, and 200 μM U(VI) containing P-reduced medium R (10 mL). After 1, 24, 48, and 72 h cells were separated from the supernatants and washed. For EXAFS measurements, the biomass was transferred into a 3 mm thick polyethylene double confined sample holder. Data were collected on samples under cryogenic conditions. For STEM-EDX measurements, cells exposed to 200 μM U(VI) for 24 h were used. Preparation of thin sections and STEM-EDX measurements were performed as described in the literature.^[2]

RESULTS. EDX-based element mapping showed a co-localization of U, P and osmium (Os) in *B. napus* cells (Fig. 1). Os was added to the TEM samples for an enhanced contrast as it particularly attaches to lipid structures, *i.e.*, bio-membranes. The co-localization of U, P, and Os suggests the binding of U to P-containing membrane components, such as phospholipids. EXAFS measurements were carried out to support these results. In particular, EXAFS shell fit parameters were determined. Reference spectra for the U(VI) interaction with various biological systems, *e.g.*, adenosine monophosphate (AMP) and adenosine triphosphate (ATP), fructose-1,6-bisphosphate, meta-autunite, as well as structural data for bacteria and plants (root), were used for structure assignment.^[3–6] An unequivocal structural assignment was not possible. The best matches were found with reference spectra for the binding of U(VI) to AMP and lupine roots.^[3,7] It is therefore suggested that the binding of U(VI) to *B. napus* cells occurs *via* organic phosphate binding motifs. This is in agreement with results obtained from STEM-EDX showing a co-localization of U with P in membranes and with TRLS data revealing a dominant binding of U(VI) to organic and/or inorganic phosphate groups of *B. napus* cells.^[8]

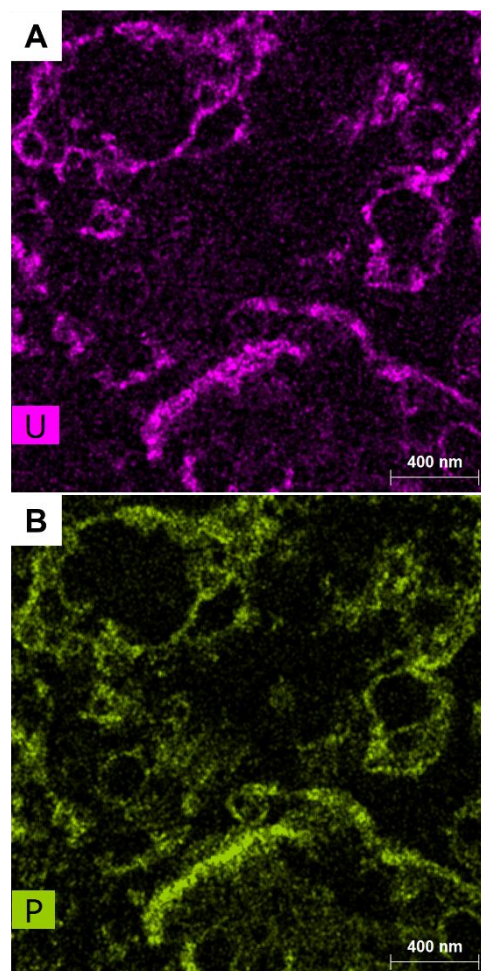


Figure 1. EDX-based elemental mapping corresponding to a dark field STEM image of U-containing membranal compartments for uranium (A) and phosphorous (B). Co-localization with osmium was also observed (data not shown), demonstrating that uranium binding occurs to lipid structures.

ACKNOWLEDGEMENTS. The authors thank J. Seibt for experimental support. This work was funded by the Federal Ministry of Education and Research (BMBF) under contract number 02NUK051B. Furthermore, we acknowledge the use of the HZDR Ion Beam Center TEM facilities and the funding of TEM Talos by the BMBF (grant No. 03SF0451) in the framework of HEMCP.

- [1] Salvatore, M. *et al.* (2006) Physics and Safety of Transmutation Systems – A Status report. 1–120.
- [2] Jessat, J. *et al.* (2021) *Environ. Sci. Technol.* **55**, 6718–6728.
- [3] Hennig, C. *et al.* (2003) *Report FZR-373*, p. 44.
- [4] Rossberg, A. *et al.* (2019) *Chem. Commun.* **55**, 2015–2018.
- [5] Hennig, C. *et al.* (2001) *Radiochim. Acta* **89**, 625–632.
- [6] Hennig, C. *et al.* (2003) *Z. Kristallogr. Cryst. Mater.* **218**, 37–45.
- [7] Günther, A. *et al.* (2003) *Radiochim. Acta* **91**, 319–328.
- [8] Moll, H. *et al.* (2020) *Environ. Sci. Pollut. Res.* **27**, 32048–32061.

Curium speciation studies in the presence of plant cells (*Brassica napus*)

H. Moll, M. Schmidt, S. Sachs

A rapid biosorption process could be identified as soon as 5 h post-exposure with 73 ± 4 % of the Cm(III) bioassociated, 1.82 μmol Cm/g_{fresh cells} at 0.68 μM Cm(III). Luminescence spectroscopy results based on UV and site-selective excitation confirmed the existence of three Cm(III) species in both the supernatants and cells. The findings detailed herein support that Cm(III) coordinates to two kinds of carboxyl groups and phosphate groups.

For this study we expanded our recently published approach with a focus on Cm(III) as a representative of the trivalent actinides.^[1,2] We utilized spectroscopic analysis, both in suspension and for the first time by applying site-selective TRLFS, to identify the functional groups responsible for trivalent metal (Cm(III)/Eu(III)) binding in a biological system. For the first time, we report Cm(III) luminescence data in the presence of plant cells with subsequent Cm(III) speciation analyses.

EXPERIMENTAL. For experiments with Cm(III), 265 ± 20 mg *B. napus* callus cells were transferred into 15 mL Greiner tubes. The cells were suspended in 4 mL 0.154 M NaCl at pH 5.8. The Cm(III) concentration in the reaction tubes was adjusted to 0.685 μM and 2.0 μM for site-selective TRLFS. All details concerning cell cultivation, analytical details, statistical analyses, and laser-induced luminescence spectroscopy experiments can be found in our publication.^[3]

RESULTS. *B. napus* cells had a strong capacity to bioassociate Cm(III), 1.82 μmol Cm/g_{fresh cells} in the presence of 0.68 μM Cm(III). We observed a rapid biosorption process for Cm(III); specifically, after only 5 h of incubation the bioassociation level approached an equilibrium. Our findings indicate that near-metabolically inactive cells also associated Cm(III), but that significantly higher amounts are associated compared with active cells for Eu(III).^[3]

The rapid Cm(III) biosorption process to the cells induced a red shift in the emission spectra from 593.7 to 600.4 nm after 5 h of exposure (Fig. 1). The intensity at ~600 nm initially decreased, but then increased at 603.5 nm as a function of exposure time. The spectra of all Cm(III)-loaded cells as a function of exposure time featured one isosbestic point at 601.7 nm. A bi-exponential luminescence decay was observed. One Cm(III) cell species featured a lifetime of

133 ± 17 μs (N_{H₂O} = 4.0), whereas the second Cm(III)-species displayed a lifetime of 366 ± 28 μs (N_{H₂O} = 0.9). For the supernatants a strong red shift in the emission maximum to 602.4 nm was observed after a short exposure time of just 5 h (data not shown). An unsystematic shift of the emission maximum was observed: first to 602.4 nm then back to 599.7 nm and finally to 604.2 nm after 168 h. A bi-exponential luminescence decay was measured: 108 ± 9 μs (N_{H₂O} = 5.1) and 260 ± 29 μs (N_{H₂O} = 1.6). These results indicate the occurrence of at least two Cm(III)-supernatant species with a structure different from the Cm(III) aquo ion.

The deconvolution of the Cm(III) cell spectra using the ITFA algorithm^[4] yielded a spectrum of species 1 depicting an emission maximum at 600.5 nm and a shoulder at 606.7 nm (cf. Fig. 2), which is quite unusual for a single-component spectrum of Cm(III). Hence, the manual deconvolution of the sum spectra showed the dominance of two Cm(III)-*B. napus* species (Fig. 2). Species 1 is comprised of species 1a and 1b. We observed the very rapid formation of Cm(III)-*B. napus* species 1 with an equilibrium between species 1a and 1b (Fig. 2B). Finally, Cm(III)-*B. napus* species 2 dominates the Cm(III) speciation at an exposure time of 168 h. Species 2 was further characterized by site-selective TRLFS.^[3] In conclusion, species 2 is characterized by a main emission band at 602 nm and a hot band of this transition at 594 nm.

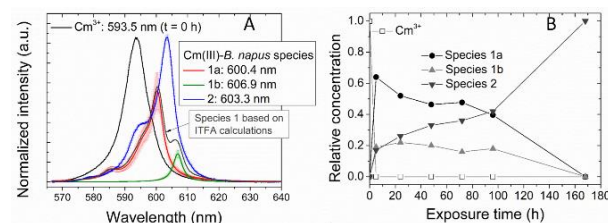


Figure 2. Deconvolution of the sum spectra of Cm(III)-loaded *B. napus* cells. Extracted single component spectra (A). Spectroscopic Cm(III) species distribution (B).

Based on the individual luminescence parameter, Cm(III)-*B. napus* species 1a can be interpreted by an interaction of Cm(III) with organic phosphate groups. The most red-shifted emission maximum for species 1b may indicate Cm(III) binding to proteins. Species 2 could be assigned to an interaction with carboxyl groups.

MISCELLANEOUS. This work is licensed under Journal of Hazardous Materials <https://doi.org/10.1016/j.jhazmat.2021.125251>.

ACKNOWLEDGEMENTS. This work was partly funded by the Federal Ministry of Education and Research under contract number 02NUK051B.

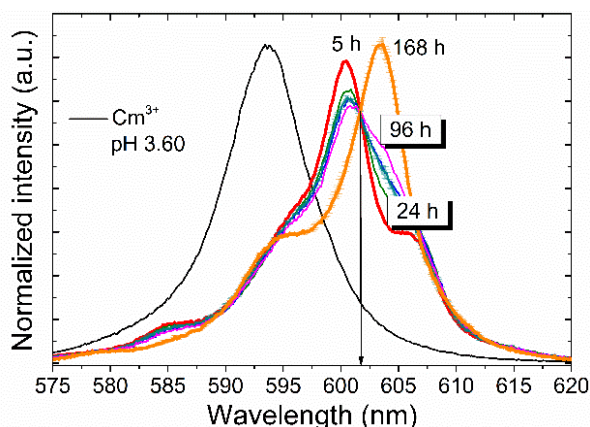


Figure 1. Cm(III) luminescence spectra in the presence of *B. napus* cells at pH = 5.5.

- [1] Moll, H. et al. (2020) *Environ. Sci. Pollut. Res.* **27**, 32048–32061.
- [2] Moll, H. et al. (2021) *Report HZDR-113*, p. 60.
- [3] Moll, H. et al. (2021) *J. Hazard. Mater.* **412**, 125251.
- [4] Rossberg, A. et al. (2003) *Anal. Bioanal. Chem.* **376**, 631.

Evidence of efficient uranium sorption by *Magnetospirillum magneticum* AMB-1 cells

E. Krawczyk-Bärsch, J. Ramtke, B. Drobot, R. Steudtner, J. Raff

The use of bacteria that bind uranium very effectively may open up new options for the remediation of uranium-contaminated water. Magnetotactic bacteria are particularly interesting for this. In sorption experiments and subsequent spectroscopic investigation by means of TRLFS combined with PARAFAC, the α -proteobacterium *Magnetospirillum magneticum* AMB-1 which is known as a motile, facultative anaerobe bacteria, proved to be a promising sorbent. By PARAFAC it was possible to extract the single component spectra of five species. The comparison of the detected species with important ligands of alpha-Protobacteria showed that peptidoglycan from the cell wall is the dominant ligand and binding site of uranium to the cells of *Magnetospirillum magneticum* AMB-1 at pH 4.5 and 5.5.

EXPERIMENTAL. Cells of *Magnetospirillum magneticum* AMB-1 were cultivated at 30 °C in 1.5 mM MagMin medium, modified by CEA Cardarache with the addition of iron malate (1:2,000) and vitamin elixir (1:2,000).^[1] For uranium batch experiments, cell suspensions with an OD_{600nm} of 0.3–0.4 were washed, centrifuged and transferred in sterilized tap water adjusted to pH of 3.5, 4.5, 5.5, 6.5 and 7.5. To each suspension a 0.1 M stock solution of UO₂(NO₃)₂ was added to finally reach a uranium concentration of 0.1 mM. After 0.5 h, 2 h, 5 h and 24 h of inoculation, samples were taken. They were centrifuged and each of the biomass pellets were washed three times with tap water adjusted to the appropriate pH. The biomass samples were transferred in specially designed Cu-holders for solid-phase *cryo*-TRLFS. The measurements were performed at 153 K with laser pulses at 266 nm (Minilite high-energy solid-state laser; Continuum) and average pulse energy of 300 μ J. The luminescence light emitted by the laser-induced biomass samples was recorded using an iHR550 spectrograph and an ICCD camera (both from HORIBA Jobin Yvon) in a wavelength range of 370–670 nm by averaging 100 laser pulses and with a time gate of 20 μ s. The achieved data were analyzed by OriginLab2020, version 9.0 (OriginLab Corporation), including the Peak Fitmodule, version 4.0. Single component spectra were extracted from data sets of the total emission spectra by parallel factor (PARAFAC) analysis. In addition, peptidoglycan (PGN) from *Bacillus subtilis* (Sigma Aldrich) as a reference ligand was dissolved in 2 mL of sterile tap water at pH 3.5, 4.5, 5.5, 6.5 and 7.5 with a ligand excess of 1:20. A stock solution of 0.1 M UO₂(NO₃)₂ was added to a final uranium concentration of 0.1 mM. The samples were transferred into a UV cuvette and used for *cryo*-TRLFS measurements as reference samples.

RESULTS. By analyzing the TRLFS data sets of the total emission spectra by PARAFAC, it was possible to extract the single component spectra of five uranyl species that were formed during the incubation of *Magnetospirillum magneticum* AMB-1 cells. In Fig. 1, the luminescence intensity distributions of the extracted species *versus* the pH range from 3.5 to 7.5 are shown indicating a pH dependent formation of the species. The comparison with important reference ligands identified three U peptidoglycan species, whose spectra coincide with the spectra of the species (1, 2, and 3), which are dominant in the pH range from 4.5 to 5.5. At pH 3.5, according to literature the emission bands of the spectrum of species (4) suggests the presence of fully hydrated UO₂²⁺ due to

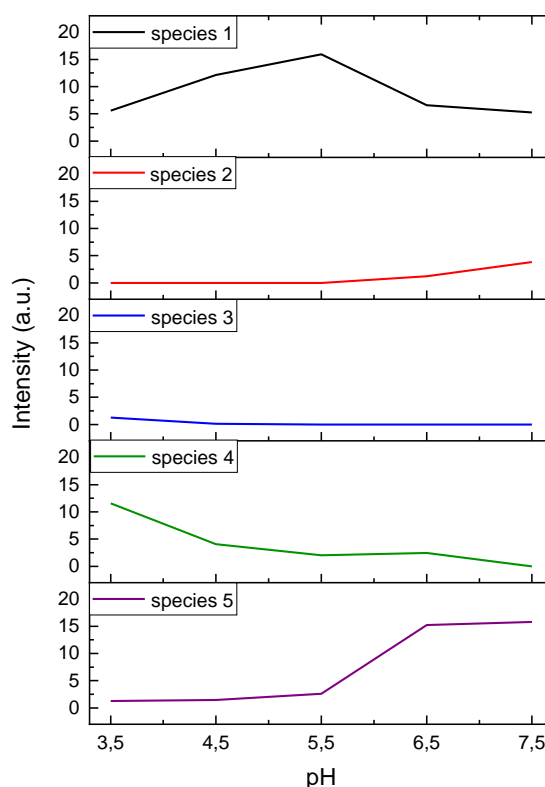


Figure 1. Luminescence intensity distribution of five uranium species, extracted by PARAFAC from the total emission spectra of *Magnetospirillum magneticum* AMB-1 cells, which were incubated with 0.1 mM U at different pH values during 24 h.

the very acidic pH.^[2] The spectrum of species (5) shows the loss of the fine structure of the bands characteristic for the formation of polynuclear species such as the 3:5 U(VI) hydroxocomplex.^[3]

ACKNOWLEDGEMENTS. We would like to thank S. Beutner for ICP-MS measurements and S. Kluge for the cultivation of *Magnetospirillum magneticum* AMB-1.

[1] Komeili, A. *et al.* (2004) *Proc. Natl. Acad. Sci. U.S.A.* **101**, 3839–3844.

[2] Drobot, B. *et al.* (2015) *Chem. Sci.* **6**, 964.

[3] Wollenberg, A. *et al.* (2021) *J. Hazard. Mater.* **411**, 125068.

Interaction of U(VI) with *Nicotiana tabacum* cells – Role of Ca ion channels in U uptake into plant cells

F. Rajabi, S. Sachs

The role of mechanosensitive calcium (Ca) channels for the uptake of uranium (U) in tobacco BY-2 cells was studied. The blocking of the Ca channels with gadolinium chloride caused a decrease in the U content of U-exposed cells, suggesting that Ca channels represent a possible transport route for U uptake into BY-2 cells.

Since radionuclides, e.g., uranium (U), are non-essential elements for plants, they likely have no specific pathway for transportation into plant cells. Disturbing the homeostasis of essential micro- and macronutrients and utilizing their transport systems are plausible ways for the access of radionuclides into plant cells.^[1] As an example, for tobacco BY-2 cells we found experimental proof that U interferes with the homeostasis of essential micro- and macronutrients, such as phosphorous, potassium, calcium, magnesium, iron, manganese, and zinc.^[1] To obtain a deeper understanding of the mechanisms involved in the U uptake into plants, we elucidated the role of mechanosensitive calcium (Ca) channels in the uptake of U into tobacco BY-2 cells. For this purpose, the Ca influx into the cells was blocked by gadolinium chloride (GdCl₃) that is used as an inhibitor of Ca influx channels.^[2,3] The bioassociation of U with Gd-treated plant cells was studied and compared to those of untreated control cells.^[1]

EXPERIMENTAL. *Nicotiana tabacum* (BY-2) cells were cultivated in medium MS as described in the literature.^[1] For U exposure experiments, 1.5 mL cell suspension were cultivated in medium MS_{red} with a reduced phosphate concentration of 1.25×10^{-5} M to limit the formation of hardly soluble U(VI) phosphate complexes. Three days after subcultivation, cells were first treated for 30 min with 0.15 mM GdCl₃ solution (Sigma-Aldrich) before the addition of 20 μM U(VI) in form of a sterile aqueous UO₂(NO₃)₂ stock solution. Simultaneously, control cells were treated only with 20 μM U(VI). After 1 h of U exposure, the cell viability was measured by the Evans Blue dye exclusion test and the cell associated concentrations of Ca and U were quantified by inductively coupled mass spectrometry (ICP-MS) after digestion of the cells with HNO₃ (p.a., ≥ 65%; Roth) and H₂O₂ (30%; Roth).^[1]

RESULTS. A number of rare earth elements are capable of inhibiting Ca influx into cells. Because of its ionic radius close to that of the Ca²⁺ ion, Gd³⁺ was found among those that showed the highest inhibitory effects of Ca influx.^[4] The successful inhibition of the Ca influx into BY-2 cells by treatment with GdCl₃ and thus, the blocking of Ca ion channels is shown in Fig. 1. GdCl₃-treated cells showed a significantly lower Ca content than non-treated cells. Interestingly, lower U concentrations were detected in BY-2 cells treated with 20 μM U, in which the mechanosensitive Ca channels in the plasma membrane were blocked by 0.15 mM GdCl₃ (Fig. 1). The U level in the cells with inhibited Ca influx was about 60 % of those detected in control cells with non-treated Ca channels. This result suggests that Ca channels serve as one possible transport route for U uptake into BY-2 cells. The cell viability for BY-2 cells with blocked Ca ion channels was found to be $94 \pm 1\%$ compared to $88 \pm 2\%$ determined for untreated cells. The higher viability of BY-2 cells treated with GdCl₃ compared to the control cells excludes the sce-

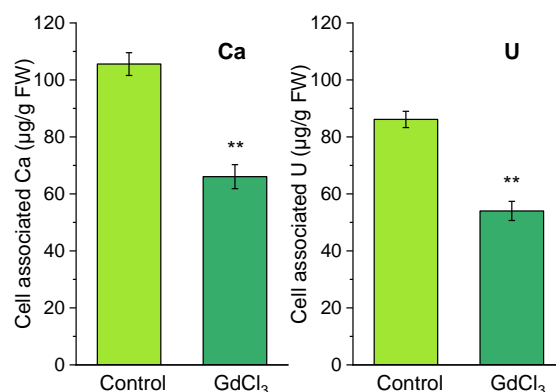


Figure 1. Effect of the blocking of Ca channels of BY-2 cells by GdCl₃ on the cell-associated Ca and U content. Data represent mean values and standard errors of the mean from three independent experiments. Compared to the non-GdCl₃ treated cells, significant differences in the amount of cell-associated metal were confirmed using Student's t-test. Two asterisks (**) indicate a very significant difference ($p < 0.01$).^[1]

nario that the lower U content in these cells is caused by cell death and the release of U into the cell culture medium.

Our results are in agreement with recently published data of Sarthou *et al.* who reported the involvement of Ca-permeable cation channels in the U uptake in *Arabidopsis thaliana* plants. They showed first that deprivation of Arabidopsis plants with Ca induces an increase of the root capacity to accumulate U, suggesting that Ca deficiency promotes the U uptake pathway. Second, they observed that external Ca inhibits U accumulation in roots. Similar to our findings, they identified an inhibited U absorption after blocking Ca ion channels with gadolinium.^[5]

This study contributes to a deeper understanding of the uptake routes for U into plant cells. In combination with further studies regarding the U uptake pathways in conjunction with proteomics and chemical microscopy this will help to describe the U uptake in plants on a molecular level. This knowledge is required to reliably assess the radionuclide uptake in the food chain as well as to develop sophisticated phytoremediation strategies.

MISCELLANEOUS. This work is part of a publication licensed under Ecotoxicology and Environmental Safety, <https://doi.org/10.1016/j.ecoenv.2020.111883>.

ACKNOWLEDGEMENTS. The authors thank Prof. P. Nick (Botanical Institute, KIT) for providing the first batch of BY-2 cells, J. Seibt for experimental support and S. Beutner for ICP-MS analyses. This work was funded by the Federal Ministry of Education and Research under contract number 02NUK051B.

- [1] Rajabi, F. *et al.* (2021) *Ecotoxicol. Environ. Saf.* **211**, 111883.
- [2] Allen, G. J. *et al.* (1994) *Plant Cell* **6**, 685–694.
- [3] Klüsener, B. *et al.* (1995) *EMBO J.* **14**, 2708–2714.
- [4] Lin, C. *et al.* (2006) *Z. Naturforsch.* **61**, 74–80.
- [5] Sarthou, M. C. M. *et al.* (2022) *J. Hazard. Mater.* **424**, 127436.

Elucidation of metal-reducing proteins in plant cells using tobacco BY-2 suspension cultures

W. A. John, S. Matschi,¹ S. Sachs

¹Leibniz Institut für Pflanzenbiochemie, Halle, Germany

Plants are known to have several mechanisms of reducing metals, which could potentially be used to mitigate heavy metal toxicity. A screening was done to investigate proteins in tobacco cells with Fe(III) reductase activity.

Bioreduction of heavy metals such as uranium (U) is one way of mitigating toxicity in organisms, which has been widely studied in bacteria.^[1] Plants are also known to possess several mechanisms for reducing metals. Iron (Fe), for instance, is an essential element, which is first reduced in soil from Fe(III) to Fe(II) by membrane bound enzymes such as ferric chelate reductase 2 and then transported into the roots *via* broad-spectrum ion channels such as iron regulated transporter 1 (IRT1).^[2]

We therefore postulate that such enzymes capable of reducing metals such as Fe are able to reduce certain other heavy metals such as U. Proteins from tobacco (*Nicotiana tabacum*) BY-2 suspension cells exposed to U were therefore resolved with native polyacrylamide gels and Fe(III) reductase activity was screened for using an in-gel Ferrozine assay, with the aim of identifying any such protein.^[3]

EXPERIMENTAL. In triplicate, tobacco BY-2 cells were cultured in MS_{red} medium, supplemented with 0, 20 and 200 μ M uranyl(VI) nitrate for 24 h at 25 °C in the dark on an orbital shaker.^[4] Protein was extracted from the whole culture as done before only without the use of dithiothreitol.^[4] 30 μ g of protein extract was then resolved in 12.5 % non-denaturing, non-reducing polyacrylamide gels. Electrophoresis was done in tris-borate buffer (50 mM Tris, 25 mM boric acid, pH 8.7) at 4 °C at a maximum voltage of 120 V and a current of 10 mA for 7 h. NADH-dependent Fe(III) reductase activity was assessed using an in-gel Ferrozine assay as described in other research and total protein content was visualized by staining with CoomassieTM G250.^[3]

The respective bands that were stained pink by Ferrozine, indicative of Fe(III) reduction to Fe(II), were excised from the gel and digested with 43 % HNO₃ and 10 % H₂O₂. U content of the resulting solutions was quantified using inductively coupled plasma mass spectrometry (ICP-MS) to detect any U that binds to these Fe(III) reducing proteins.

The corresponding band on the Coomassie-stained gel was excised for protein identification, where the protein was in-gel digested with trypsin and desalted as described in previous work.^[5] Dried peptides were dissolved in 5 % acetonitrile, 0.1 % trifluoroacetic acid and resolved with C18 reverse phase liquid chromatography. Eluted peptides were electrosprayed on-line into a QExactive Plus mass spectrometer (Thermo Scientific). Protein identification was done using the Mascot software v2.5.0 linked to Proteome Discoverer v2.4. *q*-values below the significance threshold $\alpha = 0.01$ for peptide spectrum matches and peptide groups, and 0.05 for proteins were considered identified.

RESULTS. There was an intense Ferrozine-stained gel band at around 146 kDa in all three testing conditions, indicative of NADH-dependent Fe(III) reductase activity (Fig. 1). This band did not visually show a major change in intensity, irrespective of U exposure. ICP-MS analysis of this digested Ferrozine-stained protein band showed that with cells exposed to 0, 20 and 200 μ M U, there were 0.2 ± 0.2 , 0.79 ± 0.4 and

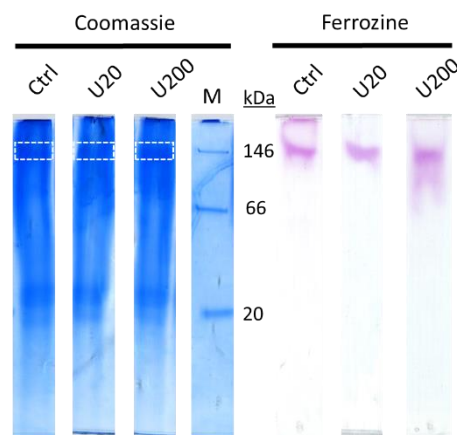


Figure 1. Natively resolved protein extracts of tobacco BY-2 cells exposed to 0 (Ctrl), 20 (U20) and 200 (U200) μ M uranyl(VI) nitrate for 24 h. Coomassie stain shows total protein and Ferrozine stain shows proteins with NADH-dependent Fe(III) reductase activity. White dashed lines shows excised gel section. M: NativeMarkTM protein ladder.

16.3 ± 3.3 ng, respectively, of bound U after subtracting background values. This indicates that at least one protein in this gel band strongly immobilizes U.

LC-MS-based protein identification of the excised gel band yielded a total of around 8,000 unique proteins from duplicates of the three testing conditions (*i.e.* six samples), of which, 1,759 proteins were observed in all samples. To further shorten the list, proteins were screened for oxidoreductase activity, yielding 130 viable candidates. Glyceraldehyde-3-phosphate dehydrogenase (GAPDH) ranked the highest among the top five candidates based on the peptide spectrum matches, whilst also showing the highest protein sequence coverage. Other high-ranking proteins included aldehyde, malate and isocitrate dehydrogenases. GAPDH is one of the most abundant proteins in the cell, known to exist as a homotetramer of 37-kDa subunits with activity being highest in the tetramer complex.^[6] This would fit the appearance of a prominent band at around 146 kDa. Furthermore, while GAPDH has never previously been reported to show Fe(III) reductase activity, it is known to be able to reduce arsenate in erythrocytes, thus making Fe(III) or U(VI) reduction in plants a likely possibility.^[7]

In conclusion, we are a step closer to ascertaining a cellular protein able to reduce heavy metals such as U and investigating the reductase potential of GAPDH would be a good starting point.

ACKNOWLEDGEMENTS. The authors thank Prof. P. Nick (Botanical Institute, KIT) for providing the first batch of BY-2 cells, J. Seibt for support with cell cultures and S. Beutner for ICP-MS measurements. This work was funded by the Federal Ministry of Education and Research (contract number 02NUK051B).

- [1] Wall, J. *et al.* (2006) *Annu. Rev. Microbiol.* **60**, 149–166.
- [2] Berthet, S. *et al.* (2018) *New Phytol.* **217**, 657–670.
- [3] Meisrimler, C. *et al.* (2015) *Front. Plant Sci.* **6**, 230.
- [4] John, W. A. *et al.* (2020) *Report HZDR-113*, p. 55.
- [5] Majovsky, P. *et al.* (2014) *J. Proteome Res.* **13**, 4246–4258.
- [6] Hoagland, V. *et al.* (1969) *Biochemistry* **8**, 694–602.
- [7] Gregus, Z. *et al.* (2005) *Toxicol. Sci.* **85**, 859–869.

Geochemical and microbiological characterization of mine water from two former uranium mines in Saxony/Germany

A. M. Newman-Portela,¹ E. Krawczyk-Bärsch, M. Lopez-Fernandez,¹ B. Drobot, A. Kassahun,² J. Raff, M. L. Merroun¹

¹Department of Microbiology, University of Granada, Spain; ²WISMUT GmbH, Chemnitz, Germany

Mine water contaminated by Uranium (U) and other heavy metals remain a major environmental and human health concern. The aim of this study was firstly the geochemical characterization of mine waters from two former German mines (Schlema-Alberoda and Pöhla) and secondly the determination of the microbial diversity in both samples. The mine water from Schlema-Alberoda is characterized by a higher ionic strength and a higher U concentration (1.01 vs. 0.11 mg U L⁻¹) compared to the water from Pöhla, which might be due to different microbial diversity and activity. 16S rRNA and ITS1 gene analyses identified a heterogeneous native community of microorganisms consisting of U reducing bacteria and U tolerant fungi, which could be involved in the reduction of low U contaminated mine waters.

EXPERIMENTAL. Two sampling campaigns were carried out at the Schlema-Alberoda and Pöhla mine. A total of 13 L were collected per mine. The pH and E_h were determined immediately upon arrival in the laboratory. Aliquots of 15 and 50 mL were taken from both mine waters to analyze the concentration of cations and anions by Inductively Coupled Plasma-Mass spectrometry (ICP-MS) and Ionic Chromatography (IC) measurements, respectively. From aliquots (2 mL), aqueous U(VI) species were determined from both U mines by cryo-Time-Resolved Laser Fluorescence spectroscopy (cryo-TRLFS). The spectra were analyzed by parallel factor (PARAFAC) analysis. 800 mL of mine water were filtered through 0.44 and 0.22 μm pore size membrane. Subsequently, filters were frozen at -20 °C up to DNA extraction. Three technical replicates per mine water sample were analyzed. Each filter (divided into two pieces) was used to extract bacterial DNA by a commercial extraction kit (QIAGEN, Germany), according to the manufacturer's protocol and modifying the cell lysis temperature for the extraction of fungi DNA. The obtained DNA was then used for PCR amplification to detect the V3-V4 region of bacterial 16S rRNA gene and the fungal ITS1 rRNA gene by using the primers 341F-785R and ITS1F-ITS2R, respectively. PCR amplification and Illumina libraries were constructed and sequenced at STAB-VIDA laboratories (Caparica, Portugal). Raw sequences obtained by Illumina MiSeq were analyzed by the software QIIME2 v2020.8.

RESULTS. Water samples from the mine indicated a neutral pH ranging from 6.8 to 7.4 and a E_h of 357 mV in Schlema-Alberoda and 117 mV in Pöhla. The highest concentrations of U, Fe, Mn, SO₄²⁻ were found in the Schlema-Alberoda mine water compared to Pöhla (U: 1.01 and 0.11 mg L⁻¹, SO₄²⁻: 335 and 0.26 mg L⁻¹, Fe: 0.99 and 0.13 mg L⁻¹ and Mn: 1.44 and 0.16 mg L⁻¹, respectively). U speciation studies in mine waters determined by cryo-TRLFS and PARAFAC the aqueous species UO₂(CO₃)₃⁴⁻ as the main species in Schlema-Alberoda. The 16S and ITS1 rRNA gene analyses of both mine waters revealed a high microbial diversity. The microbial community was mainly dominated by a high relative abundance of bacteria and fungi (Fig. 1). The bacterial community contained anaerobic or facultative anaerobic, neutrophilic, chemolithoautotrophic bacteria with a wide metabolic range. The fungi community is characterized by wood-



Figure 1. Relative abundance and diversity of microorganisms at kingdom level in Schlema-Alberoda and Pöhla mine water.

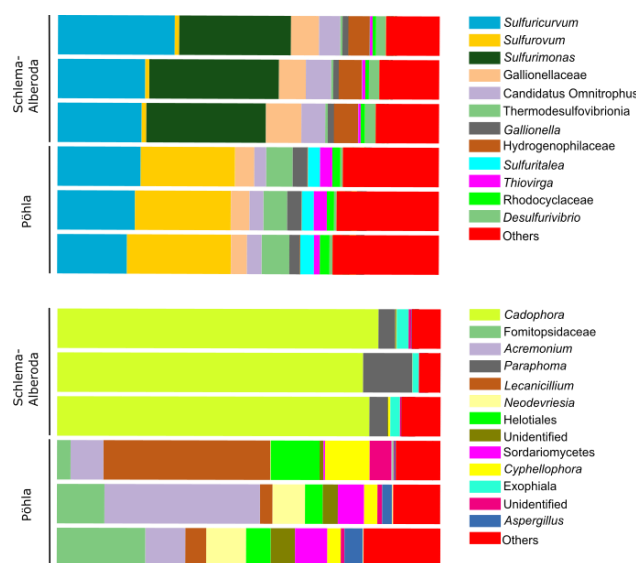


Figure 2. Relative abundance and diversity of bacteria (top) and fungi (below) in Schlema-Alberoda and Pöhla.

degrading fungi adapted to extreme environments. In Schlema-Alberoda mine water, the more representative bacterial genus was *Sulfuricurvum*, *Sulfurimonas*, *Desulfurovibrio*, "Candidatus Omnitrophus" and an uncultured genus of the Hydrogenophilaceae family, among others with an occurrence of below 1.5%. Instead, the fungal community was represented by the genus *Exophiala*, *Cadophora* and *Cystobasidium*. On the other hand, the results at bacterial genus level showed at Pöhla mine water a higher relative abundance of *Sulfuricurvum*, "Candidatus Omnitrophus", *Sulfurovum*, *Gallionella*, *Sulfuritalea*, *Thiovirga* and uncultured *Thermodesulfobionia*. In addition, the fungal community was characterized by *Neodevriesia*, *Cyphellophora*, *Aspergillus*, *Lecanicillium*, *Acremonium* and unidentified genus of the family Fomitopsidaceae (Fig.2).

ACKNOWLEDGEMENTS. The authors are grateful to T.-S. Wei, R. Steudtner, M. Vogel, S. Kluge, S. Jiménez, S. Weiss, R. Bertheau, S. Beutner, and S. Gürtler (HZDR, Germany).

Spatially resolved Eu(III) environments by chemical microscopy

R. Steudtner, M. Vogel,¹ T. Fankhänel, J. Raff, B. Drobot

¹VKTA – Strahlenschutz, Analytik & Entsorgung Rossendorf e. V., Dresden, Germany

Linking microscopy and spectroscopy based on the correlative application of state of the art spectroscopic, microscopic and biochemical methods and equipment is inevitable in the modern time of f-element biochemistry. The aim of this work was the direct visualization and localization in combination with the chemical identification and characterization of f-elements, here Eu(III), interacting with biostructures, here *Shewanella oneidensis* MR-1 sorbed on calcite.

EXPERIMENTAL. For linking the microscopy and spectroscopy we carried out a luminescence spectroscopic mapping of Eu(III) species with a Raman microscope (LabRAM system, HORIBA Jobin Yvon, Lyon, France) using a 532 nm external Nd-YAG laser (Sacher Lasertechnik, Marburg, Germany). The laser beam is coupled into an Olympus BX-40 microscope (Olympus, Hamburg, Germany). Eu(III) luminescence was collected with the same objective and directed through a pinhole (200 μm) to a spectrometer (200 μm entrance slit, 300 l/mm grating) that disperses the light before reaching the Peltier cooled CCD detector (-70°C). The sample is fixed on a piezo-electrically driven microscope scanning stage. The analyzed sample areas were pinpointed by using a camera. Further experimental details concerning chemicals, synthesis of Eu(III) compounds, preparation of *Shewanella oneidensis* MR-1 cells and biofilm on calcite, time-resolved laser-induced fluorescence spectroscopy of the Eu(III)-RNA system and X-Ray Diffraction data are reported in Vogel *et al.*^[1]

RESULTS. Chemical microscopy is a combination of microscopy with high resolution luminescence spectroscopy to study inhomogeneous samples at the (sub-)micronscale. Firstly, we benchmarked our micro-spectroscopic setup for luminescence mapping analysis with a mixture of four distinct Eu(III)-containing compounds – Eu_2O_3 , $\text{Eu}_2(\text{oxalate})_3$, $\text{NaEu}(\text{SO}_4)_2 \cdot \text{H}_2\text{O}$ and EuPO_4 . A Raman microscope using a 532 nm laser for excitation was used for the luminescence spectroscopic mapping of these Eu(III) mixture. After successful data acquisition a new two-step data analysis algorithm was developed and verified with this initial mixture sample. By a ‘rolling ball’ algorithm, all spectra were background corrected and data deconvolution was performed by a non-negative iterative factor analysis (NIFA).^[2,3] Based on the special spectral characteristics of the four spectra derived from NIFA, we were able to achieve unambiguous assignment to the spectra of the pure components using this proof of concept. Both spectra, pure and deconvoluted, are almost identical. These results clearly demonstrate the applicability of the employed microscopic system for the chemical microscopy analysis of environmental samples.

After successful setup validation of the artificial system, a ternary system consisting of Eu(III), calcite, and *Shewanella oneidensis* MR-1 was investigated. Figure 1 shows the successful colonization of calcite by the rod-shaped bacteria. In the next step, a specific region of interest was mapped spectroscopically in both horizontal and vertical orientations. After the luminescence mapping the corresponding local species distribution for the region of interest was derived using NIFA. Figures 2 A and B provide the luminescence characteristic results for the deconvoluted individual Eu(III) com-

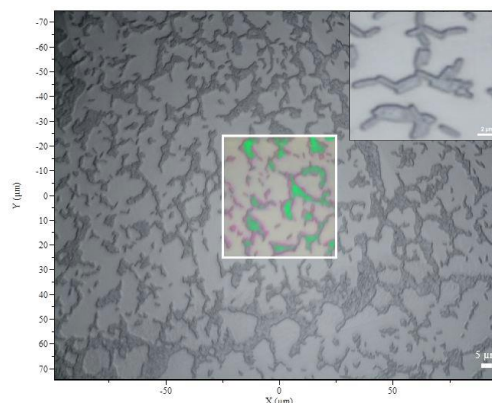


Figure 1. Microscopic image of Eu(III)-calcite-*Shewanella oneidensis* MR-1 sample with the region of interest (white square) and overlay of the spectroscopic mapping analyses. Additionally, a zoom-in of microscopic image of single *Shewanella oneidensis* MR-1 cells. Objective: 50-fold magnification (laser spot size of ca. 0.9 μm), $\lambda_{\text{exc.}} = 532 \text{ nm}$, exposure time 10 s, ROI $25 \times 25 \mu\text{m}$, step size of 2 μm in horizontal and vertical orientation.

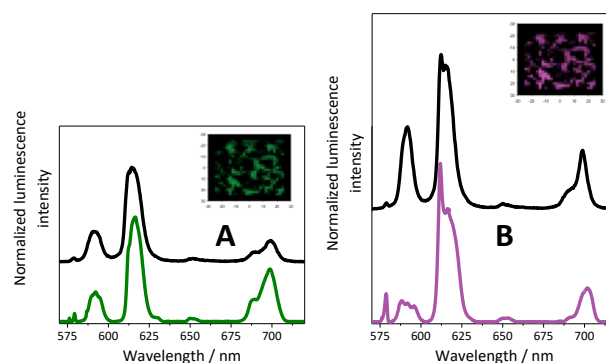


Figure 2. Deconvoluted luminescence spectra obtained by TRLFS (black) and by mapping (coloured) for Eu(III) bound to protein-like structures (A) and Eu(III) complexed with biofilm eDNA (B).

pounds, which were overlaid in the region of interest in the light-microscopic image (Fig. 1). Based on their spectral characteristics, the two deconvoluted TRLFS Eu(III) species (black spectra in Figs. 2A and B) were assigned to Eu(III) bound to protein-like structures (A) and Eu(III) complexed with biofilm eDNA (B).

Overall, this chemical microscopy study demonstrates the high potential of non-functionalized Eu(III) as a molecular probe for

- visualization (biomass sorbed on Calcite),
- localization (Eu(III) detected on Biomass),
- identification (two different Eu(III) species), and
- characterization (Eu(III) protein-like structures, Eu(III) biofilm eDNA),

which ultimately contributes to a comprehensive understanding of lanthanide/actinide interaction pathways and their migration in our environment.

[1] Vogel, M. *et al.* (2021) *Analyst* **146**, 22–27.

[2] Sternberg, S. R. (1982) in: *Cellular computers and biomedical image processing*, Berlin, Heidelberg.

[3] Andersson, C. A. *et al.* (2000) *Chemom. Intell. Lab. Syst.* **52**, 1–4.

Nanoscale membrane mimetics for structural investigations of membrane proteins

M. Subramanian, C. Kielar, S. Tsushima, K. Fahmy, J. Oertel

Membrane-scaffolding proteins (MSPs) serve to generate nano-sized discoidal membrane mimetics (nanodiscs) for membrane protein research. The arrangement of membrane proteins in regular supramolecular structures of nanodiscs is attractive for diffraction studies. Thereby, crystallization as the limiting factor in structure determination of membrane proteins would be circumvented. We describe here the formation of multimers of membrane-scaffolding protein MSP1D1-bounded nanodiscs using the thiol reactivity of engineered cysteines. The mutated positions N42 and K163 in MSP1D1 were chosen to support chemical modification. Disulphide bond formation of nanodiscs formed by the MSP1D1_N42C variant led to dimers and trimers. In contrast, transmission electron microscopy revealed that the attachment of oligonucleotides to the engineered cysteines of MSP1D1 allowed the growth of submicron-sized tracts of stacked nanodiscs by hybridization of nanodiscs carrying complementary DNA strands and a flexible spacer.^[1]

EXPERIMENTAL. Cysteines were introduced in MSP1D1 using the QuikChange Lightning Multi Site-Directed Mutagenesis Kit (Agilent) according to the manual. The MSP1D1 variants were expressed and purified for lipid nanodisc assembly followed by circular dichroism (CD) and dynamic light scattering (DLS) measurements to verify correct secondary structure and particle size of the resulting nanodiscs. These were used for the linkage with maleimide-modified oligonucleotides to induce nanodisc multimer formation, which were observed by atomic force microscopy (AFM) and transmission electron microscopy (TEM). The structures of MSP1D1 nanodiscs was generated with CHARMM-GUI Nanodisc Builder.^[2] Cysteine replacements were introduced using Pymol.^[3] Short Molecular Dynamics (MD) simulations (5 ns) were performed on the oligo using the AMBER15 program package.^[4] All experiments are explained in detail by Subramanian *et al.*^[1]

RESULTS. To enable the assembly of individual nanodiscs into multimeric structures, we introduced cysteines into MSP1D1 (to induce direct site-specific disulfide bond formation or exploit their thiol reactivity for the attachment of maleimide-conjugated oligonucleotides). The purified two single amino acid replacement variants MSP1D1_N42C and MSP1D1_K163C generated bands at the monomer molecular weight of 25 kDa, whereas the doubly mutated variant MSP1D1_N42C/K163C exhibited an additional fraction of dimers at 50 kDa. The subsequent nanodisc assembly showed that all MSP1D1 cysteine variants self-assembled with lipids into particles covering the expected size range of MSP1D1 nanodiscs. CD and DLS measurements revealed that neither the protein structure nor the self-assembly process of the nanodisc formation were affected by the cysteine mutations in any of the MSP1D1 variants. For nanodisc multimer formation, the variants MSP1D1_N42C and MSP1D1_N42C/K163C were subjected to copper catalyzed disulphide bond formation between the solvent-accessible cysteines of multiple nanodiscs. Dimer and trimer formation was evidenced by AFM (Fig. 1A/B) but unfortunately, the yield of oxidative multimer formation was low. Steric hindrance between adjacent nanodiscs is probably the main reason for the low yield. To allow more

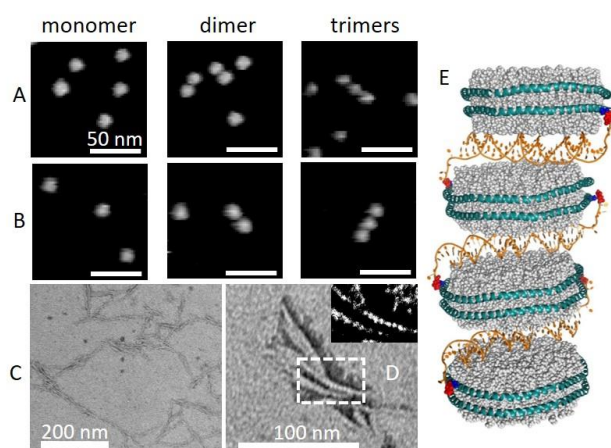


Figure 1. Imaging of nanodisc multimers. AFM images of disulphide-bond linked nanodisc multimers formed by copper-catalyzed disulphide bond formation between individual MSP1D1_N42C nanodiscs (A). The corresponding multimers formed by MSP1D1_N42C/K163C nanodiscs (B). Left panel: representative TEM image of > 200 nm long threads of DNA-linked MSP1D1_N42C nanodiscs (C). Right panel: close-up TEM image of a short multimeric assembly of the same nanodisc preparation (D). Putative molecular model of the multimeric nanodisc assembly (E). Cys-mutated MSP1D1 and maleimide-modified oligos were alternately arranged to constitute a multimeric structure in accordance with the TEM images.

freedom in the design of multimeric structures with longer and variable linkers, we used oligonucleotides connected to nanodisc cysteines through a maleimide-thiol reaction. Furthermore, the flexibility of the adduct was purposefully increased by a 50 linker of four thymines preceding 30 bases for nanodisc hybridization, which correspond to three helical turns of dsDNA. The actual arrangement of dsDNA-linked nanodiscs was investigated by TEM (Fig. 1C/D). Typically, the multimers showed a tendency to branch and run in roughly parallel bundles. The nanodisc multimers appeared densely packed with very little space between them and with a contrast periodicity of ~4 nm along the stacking axis, indicative of the linking dsDNA being sandwiched between nanodiscs, as proposed in the structural model of the assembly shown in Fig. 1E.

Taken together, we demonstrated an alternative way to induce dsDNA-mediated stacking of nanodiscs that exploits chemical modification of the MSP. Thereby, interference with lipid protein interactions can be prevented in applications that require native membrane protein structures within stacked nanodiscs as, for example, in single particle X-ray diffraction.

- [1] Subramanian, M. *et al.* (2021) *Molecules*. **26**, 1647.
- [2] Jo, S. *et al.* (2008) *J. Comput. Chem.* **29**, 1859–1865.
- [3] The PyMOL Molecular Graphics System, Version 1.8 (2015) Schrodinger Inc., New York, NY, U.S.A.
- [4] Case, D. A. *et al.* AMBER15, University of California, San Francisco, CA, U.S.A.

Development of an in-house preparation route for vesicles

T. Fankhänel, R. Steudtner, L. Nucke, B. Drobot

Liposomes are small amphiphilic vesicles and consist of a lipid bilayer which is typically known from biological membranes and is in contrast to micelles. They can be used for a wide spectrum of tasks in biophysics, medicine, pharmaceuticals and various technical applications. The focus of the covered work is an extrusion approach for preparing such liposomes that can be used, e.g. for further biophysical experiments. The characteristics of obtained liposomes can be investigated by means of DLS, AFM or microscopy. The tightness of the vesicles can be checked with a fluorescence leakage assay using static fluorimetry.

Liposomes have been proposed for the application of lanthanide accumulation.^[1] They can be prepared artificially and by customizing relevant properties during the synthesis, they are used in a wide field of appliances, e.g. in cosmetics, pharmaceuticals for drug delivery purposes and for model systems of artificial cells and cell membranes.^[2-4] The goal of this work was to establish a preparation protocol for the synthesis of vesicles in GUVs (*Giant Unilamellar Vesicles*) or LUVs/ LUVETs (*Large Unilamellar Vesicles/ by Extrusion*) and to characterize them in connection with loading the enclosed vesicle volume with chelating substances, e.g. EDTA, so that they can be used for lanthanide extraction.

EXPERIMENTAL. 120 mM of calcein disodium salt (Standard Fluka, Honeywell, U.S.A.) was used with the HEPES liposome buffer (HLB buffer) consisting of 150 mM sodium chloride and 25 mM HEPES solution (Carl Roth, Karlsruhe, Germany) in Milli-Q water; pH values of all prepared solutions were adjusted to 5.8; the complexing agent to be loaded inside of the vesicles was 120 mM of EDTA (Roth). The lipid solution with an overall lipid concentration of 4 mM consists of 75 mol-% 1,2-dioleoylsn-glycero-3-phosphocholine (DOPC, 18:1 (Δ^9 -Cis) PC) and 25 mol-% cholesterol (Avanti Polar Lipids, Alabaster, AL, U.S.A.) that are to be pipetted and dosed with glass syringes.

The lipid mixture in the glass vessel is to be dried under a nitrogen flow for 10 min, solvent remnants are removed under vacuum for at least two hours before the dried lipid film can be hydrated for at least 30 min with the prepared buffer containing the fluorescent dye and complexing agent, using a shaker (600 rpm). The lipid suspension must always be kept above the lipid's phase transition temperature which is true for the whole procedure covering the extrusion, too. The mixture can now be transferred in a plastic micro centrifuge tube. To improve the efficiency of the encapsulation of the aqueous components inside of the vesicles, the suspensions are exposed to freeze-thaw cycle (10 ×) utilizing liquid nitrogen and a thermocycler. The actual extrusion is done with a Mini Extruder (Avanti) using two 0.5 mL *Hamilton* glass syringes and a 100 nm polycarbonate membrane filter (Whatman Nuclepore, Cytiva, Marlborough, MA, U.S.A.). After prewashing the equipment with ethanol, water and buffer (3×), one syringe of buffer should be extruded through the fully assembled device to minimize the dead volume. Finally, 0.5 mL of lipid suspension are extruded 20 times through the Mini Extruder. The maximum temperature must not exceed 80 °C to prevent the syringes from taking damage. During the process, the syringes should be free from air bubbles. Afterwards, a purification process using a PD-10 desalting column (> 5,000M_r) took place, collecting 6 fractions. Pre-

pared liposomes in aqueous solution are stable for at least 4 days when stored at 4 °C.

DLS measurements were performed with a Malvern Zetasizer Nano ZS Helix device (Malvern Instruments/ Malvern Panalytical, UK) and 20 μ L Helix cuvettes. For the results, we focused on the Intensity Particle Size Distribution, Intensity PSD. To check for vesicle tightness, the self-quenching effect of the calcein fluorescent dye is utilized: Due to the high concentration in the small volume inside of the vesicles, there is a reduced fluorescence intensity because of self-quenching while in contrast, intensities increase in case of leakages because of a dilution of the calcein and subsequent dequenching. This effect was monitored for three hours using fluorimetry adjusted to the relevant wavelengths of calcein ($\lambda_{\text{ex}} = 494 \text{ nm}$, $\lambda_{\text{em}} = 517 \text{ nm}$) after which an intentional complete leak of the vesicles can be caused by adding 0.01 % Triton X-100 (Alfa Aesar, Thermo Fischer Scientific, Waltham, MA, U.S.A.), a strong detergent.

RESULTS. The extrusion process yields a suspension completely transparent and almost clear in contrast to the opaque and turbid appearance before extrusion. DLS results indicate that across all six collected fractions, there were particles with 100–250 nm in diameter which fits in the LUV/ LUVET dimension, cf. Fig. 1. The fluorescence leakage assay showed a slight increase (30–40 %) of fluorescence intensity pointing at a somewhat compromised vesicle tightness which could be attributed to the limited storage stability of the liposomes.

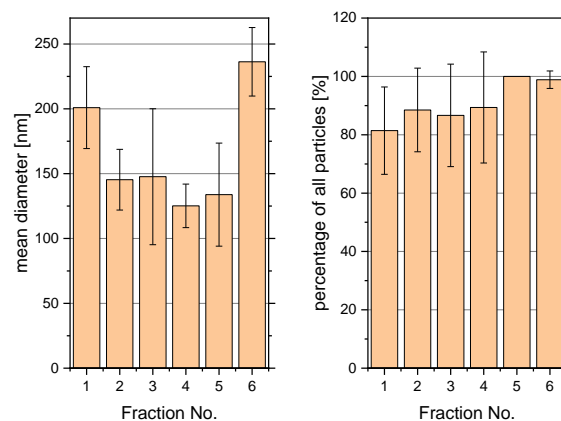


Figure 1. Results of DLS measurements and statistics of particle sizes (diameters of intensity PSD (l.) and percentage of all particles (r.)).

ACKNOWLEDGEMENTS. The authors thank Dr. M. Vogel for her support during this work.

- [1] Sofroniou, M. C. et al. (2019) *J. Colloid Interface Sci.* **557**, 568–579.
- [2] Figueroa-Robles, A. et al. (2021) *Int. J. Pharm.* **593**, 120125.
- [3] Sercombe, L. et al. (2015) *Front. Pharmacol.* **6**, 286.
- [4] Jørgensen, I. L. et al. (2017) *Eur. Biophys. J.* **46**, 103–119.

Selectivity of the natural lanthanide binding protein lanmodulin

B. Drobot, H. Singer,¹ C. Zeymer,¹ L. J. Daumann,¹ R. Steudtner

¹Ludwig Maximilian University, Munich, Germany

Lanmodulin is a protein of the methylotroph *Methylobacterium extorquens* and was discovered in 2018.^[1] It has been shown that this protein can bind lanthanides with extremely high affinity. Depending on the lanthanide probed, the affinity is reported to be femtomolar.^[2] In the present work, we screened the entire lanthanide series and some trivalent actinides for their relative affinity to lanmodulin. We found a clear trend in the lanthanide affinities showing a maximum affinity for neodymium. Both, smaller and bigger lanthanide ions have significantly lower affinities. Interestingly, the affinity of americium and curium from the actinide series do even show a higher affinity with americium providing the strongest interaction with lanmodulin.

EXPERIMENTAL. The different relative affinities of lanthanides and actinides were determined using time-resolved laser-induced fluorescence spectroscopy (TRLFS). Since not all metals can be directly measured with TRLFS, trivalent europium (Eu(III)) and curium (Cm(III)) were used as readout in metal ion competition experiments. For those experiments lanmodulin (LanM) was preincubated with either Eu(III) or Cm(III) using a molar ratio of 1:5.5 (LanM:metal) to account for the number of binding sites of LanM. In case of Eu(III), 1 μ M LanM was incubated with 5.5 μ M Eu(III) while the higher quantum yield of Cm(III) enables us to work in lower concentrations of 18 nM LanM and 100 nM Cm. After incubation each competing metal was added to the same concentration and changes in luminescence emission were followed.

All TRLFS experiments were carried out using the NT230 laser with a 5 ns pulse. The excitation wavelength was adjusted to 394 nm for Eu(III) experiments and 396 nm for Cm(III) experiments. Samples were measured in a standard 4 mL quartz glass cuvette. Emitted light was collected from a perpendicular orientation and a light guide transferred it to a spectrograph (Andor, SR-303i-A) equipped with an intensified CCD (Andor iStar, DH320T-18U-63) for detection.

Data analysis was performed with PARAFAC using the N-way toolbox in Matlab.^[3] Thereby, the data were deconvoluted into signals from the metal aquo ions and the complexes of LanM with Eu(III) and Cm(III), respectively. The reduction of the protein-metal complex was followed until a chemical equilibrium was reached. If a metal would have the same affinity as the probed metal (Eu(III) or Cm(III)), the initially formed complex will be reduced to 50%. Metals with higher affinities should reduce these complex below 50% and metals owing lower affinities will remove less metal from the protein ending with protein metal complexes above 50% of the initial value. Full experimental details are reported elsewhere.^[4]

RESULTS. Accurate affinities of LanM to the lanthanides were complicate to measure, due to its high affinity. Previously reported values for lanthanide affinities were therefore scattering and not entirely consistent. With our approach here, we have not addressed absolute values for the metal protein affinities but their relative affinities along the lanthanide series as well as some chosen actinides. The relative affinities for the lanthanides are shown in Fig. 1. This graph shows that neodymium (Nd(III)) has the highest affinity

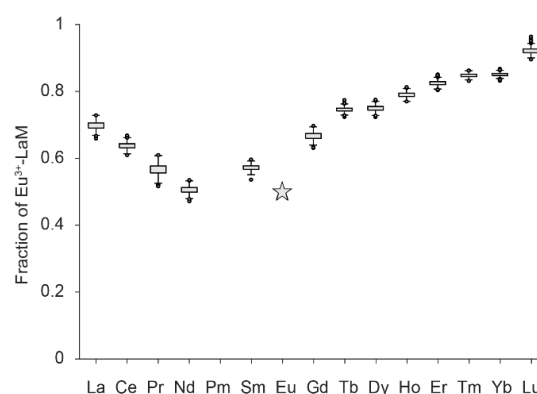


Figure 1. The relative affinities of lanmodulin to the metals of the lanthanide series showing the highest affinity (lowest Eu(III)-LanM fraction) for Nd(III).^[4]

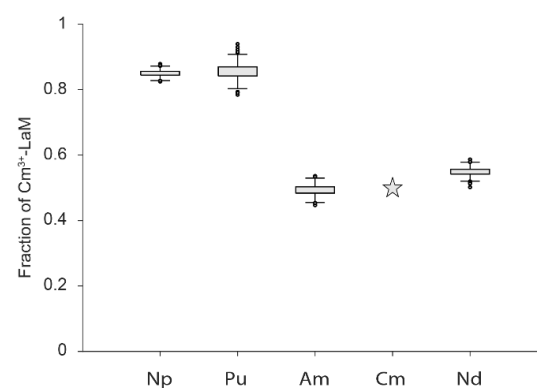


Figure 2. The relative affinities of lanmodulin to some trivalent metals of the actinide series showing the highest affinity (lowest Cm(III)-LanM fraction) for Am(III).^[4]

from the lanthanide series. The relative affinities were significantly reduced for the lighter and heavier lanthanides. Nd(III) as the best lanthanide was further used in the analysis of the trivalent actinides. These results are shown in Fig. 2. In fact, the trivalent actinides Am(III) and Cm(III) exhibit higher affinities to LanM than Nd(III).

Our study demonstrates that LanM – a protein, which is optimized by nature to bind lanthanides – even prefers Am(III). Further results and a detailed discussion are reported elsewhere.^[4]

[1] Cotruvo Jr, J.A. *et al.* (2018) *J. Am. Chem. Soc.* **140**, 15056–15061.

[2] Mattocks, J.A. *et al.* (2021) *Meth. Enzymol.* **651**, 23–61.

[3] Andersson, C.A. *et al.* (2000) *Chemometr. Intell. Lab. Syst.* **52**, 1–4.

[4] Singer, H. *et al.* (2021) *Chem. Sci.* **12**, 15581–5587.

Interaction of Ferritin with Pu⁴⁺

S. Tsushima, C. Zurita,¹ C. Den Auwer¹

¹Université Côte d'Azur, CNRS, ICN, Nice, France

Molecular dynamics (MD) simulation together with spectroscopic data suggests that Pu(IV) is complexed with ferritin mainly to aminoacid side chains of the apoprotein, rather than interacting with the ferrihydric core.^[1,2]

EXPERIMENTAL. MD simulations were performed using the AMBER 15 package with ff99SB force field applied on the protein. For Pu⁴⁺, 12-6-4 LJ-type parameters developed by the group of Prof. Kenneth Merz, Jr. have been employed. For carbonate ions, additional parameters have been employed. Protonation state of the protein was adjusted to model pH 7.4. Na⁺ ions were added to make the system electrostatically neutral. TIP3P waters were then added with minimum water layer thickness of 10 Å. Finally, 150 ns MD run was performed in a periodic boundary condition in NPT ensemble at 298 K. Simulations were terminated and restarted every 5 ns to avoid artificial convergence to a particular geometry. The SHAKE algorithm, a 2 fs time integration step, 12 Å cutoff for non-bonded interactions, and the particle mesh Ewald method were used. MD trajectory was recorded at every 50 ps. Simulations were performed for 150 ns out of which only the last 75 ns MD trajectory was used for statistical sampling to ensure the equilibrated structures.

RESULTS. Classical MD simulations on Pu⁴⁺ bound to the L chain of ferritin (hereafter F^L) were performed starting from Pu(CO₃)₅⁶⁻ in the presence of F^L. Since using an entire Ferritin molecule would be too costly for such a simulation, especially in light of the fact that our primary focus is on the local environment around Pu atoms, we selected single L-chain of horse apo-Ferritin (from cadmium-bound Ferritin) and used it as a model for Pu(IV)-bound F^L. Six Pu atoms were randomly distributed around a metal-free L-chain. Carbonate (CO₃²⁻) and Na⁺ ions were further added to mimic experimental carbonate concentrations and for the sake of charge neutralization. Simulations were performed for 150 ns. The results of MD simulations show that out of 6 Pu⁴⁺ ions in the simulation box, roughly one third binds to the protein and the rest remains unbound. In course of testing different simulation settings, it was revealed that the positions of Pu atoms in MD trajectories depends heavily on where they were initially deposited and the snapshots depicted in Fig. 1 may further develop over longer simulation scale. Therefore, this image should only be taken as conceptual. Pu(IV) positions therein should not be considered as their "final" positions. Closer look into the local environment around Pu gives clear hints about the nature of Pu-Ferritin interactions. Pu(IV) binding to the L-chain appears to be non-specific and each Pu has its own environment composed of water, carbonates and carboxylate groups derived from the amino acids of the protein. Two Pu(IV) ions are bound to the protein involving two or four carboxylic groups of Asp or Glu. The rest of Pu (which remains unbound to the protein) forms carbonate aquo complexes. However, it is possible that in the present simulation, the presence of unbound Pu is overrepresented because of the high concentration of metal in the simulation box. From the radial distribution functions (RDF) around the Pu (not shown here), the first Pu coordination sphere emerges at around 2.35 Å with main contributors being oxygens from coordinating amino acid side chains, waters and car-

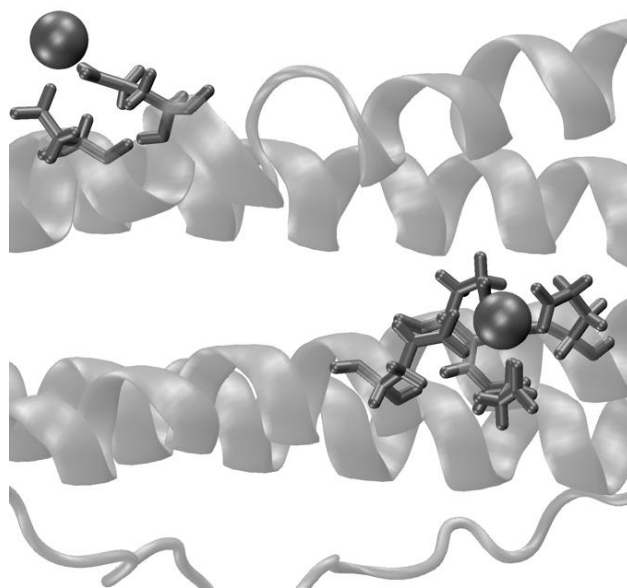


Figure 1. Representative structure from MD trajectory of Pu⁴⁺-bound L-chain. Two Pu atoms which are bound to the protein are highlighted. Protein in ribbon, Pu in large balls, residues associated with Pu in licorice. Waters and carbonate ions are omitted for clarity.

bonate. The second coordination sphere is made of C atoms. It is localized around 2.85 Å and it corresponds to atoms from carbonate anions and protein. A third coordination sphere, characteristic of only C atoms from the protein, is localized around 3.45 Å. In conclusion, C from carbonates and protein are visible in the second and third coordination spheres, respectively, when a ternary complexes form. When a binary complex occurs, C atoms from the protein in the third coordination sphere are visible only with less intensity. 6 EXAFS spectra corresponding to the 6 Pu atoms of MD simulation have been calculated (figure not shown). The average EXAFS spectrum of Pu correspond well to the average of two Pu bound to the protein in MD simulation. Qualitatively, both spectra (MD and experimental) are very similar, except for extra oscillations of the amplitude in the 9–11 Å⁻¹ region for the experimental spectrum.

ACKNOWLEDGEMENTS. MD simulations were performed at the Centre for Information Services and High-Performance Computing (ZIH) at the Dresden University of Technology, Germany, using a library program AMBER.

[1] Zurita, C. et al. (2021) *Chem. Eur. J.* **27**, 2393–2401.

[2] Zurita, C. et al. (2022) *J. Synchrotron Rad.* **29**, 45–52.

Investigation of the structure and dynamics of gallium binding to high-affinity peptides elucidated by multi-scale simulation, quantum chemistry, NMR and ITC

C. J. Taylor, N. Schönberger,¹ A. Lanikova,² M. Patzschke, B. Drobot, L. Zidek,² F. Lederer¹

¹Helmholtz Institute Freiberg for Resource Technology, Freiberg, Germany; ²Central European Institute of Technology (CEITEC), Brno, Czech Republic

Two peptides (M3 and C3.15) were selected from prior work, due to their high affinity for Ga³⁺.^[1,2] ITC was used to determine the thermodynamic parameters of peptide-Ga³⁺ reactions. A mixture of classical MD and QMMM simulation was used to determine the formation of stable Ga³⁺-peptide interactions and predict their positions. Quantum chemistry was used to analyze bonding patterns and ascertain the determinants of stable complex formation. Different NMR techniques (TOCSY, HSQC, NOESY) were used to calculate chemical shifts to determine short, medium and long-range correlations between nuclei and to observe changes in peptide structure upon Ga³⁺ binding.

Gallium (as Ga³⁺) is a Group IIIa metal and its recovery from wastewaters has become increasingly important for its reuse. The use of peptides for recycling offers a low-cost and environmentally-friendly option but the structural characteristics of peptides likely to bind Ga³⁺ are largely unknown. Multiple computational methods, coupled with experimental verification *via* NMR and Isothermal Calorimetry (ITC), were used to establish that Ga³⁺ binds with high affinity to peptide sequences and to elucidate the structural characteristics that contributed. It was demonstrated that peptide pre-organization is key to Ga³⁺ binding and that a favorable binding position is necessarily governed by the size and shape of the electrostatic environment as much as individual electrostatic interactions with peptide residues themselves. Given favorable conditions, Ga³⁺ will find a favorable binding position involving both charged and uncharged residues. This greatly increases the range of bonding possibilities with other peptide sequences and offers insights for binding other metals. The addition of a pH buffer substantially improved the affinity of Ga³⁺ and a structural role for a buffer component was demonstrated.

RESULTS. Binding affinity, expressed as dissociation constant K_d , the stoichiometry of the interaction between Ga³⁺ and the peptides as well as the thermodynamic parameters of the reactions in the presence and absence of sodium acetate buffer (ACET) were calculated (Tab. 1). A negative ΔG was determined for both peptides, indicative of spontaneous Ga³⁺ binding to both peptides in their respective reaction environment. Some differences were observed in thermodynamic parameters, whether ACET was present or not, the reaction with M3 was enthalpically-driven whereas the overall reaction with C3.15 is entropically-driven.

Classical simulation elucidated substantial peptide pre-organization in the absence of Ga³⁺. Molecular Electrostatic

Potential maps calculated from simulation snapshots revealed areas of negative potential, favorable for Ga³⁺ binding. Upon energetic convergence, QMMM simulation determined stable binding positions for Ga³⁺ in both peptides, the formation of interactions with charged residues in M3 and uncharged residues in C3.15 confirming the enthalpic and entropic-driven reactions from ITC, respectively. Quantum chemistry calculations (DFT) and Quantum Theory of Atoms In Molecules (QTAIM) analysis of calculated electronic density and its topology confirmed the largely ionic nature of non-covalent Ga³⁺-peptide interactions and the stabilizing role of ACE in each complex (Fig. 1).

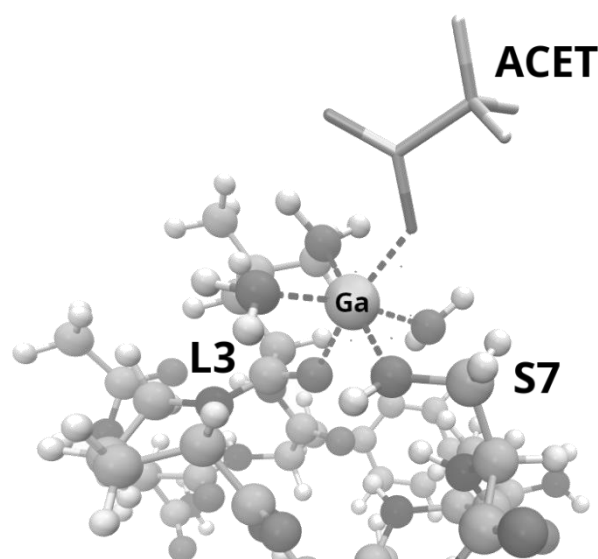


Figure 1. DFT-optimized structure of peptide C3.15 in complex with Ga³⁺ and buffer component, ACET.

NMR confirmed the structural changes observed in the QMMM simulation upon Ga³⁺ binding, particularly the formation of stabilizing helical secondary structure (*e.g.* β -I and β -II turns). Overall, differences in peptide structure upon Ga³⁺ binding, whilst observable, were minimal, confirming the importance of peptide pre-organization and its accurate prediction.

Table 1. Calculated enthalpic (ΔH) and entropic ($T\Delta S$) contributions to binding and Gibbs free energy (ΔG) for peptides M3 and C3.15. Units for all thermodynamic quantities are given in kJ mol⁻¹.

Peptide	Sequence	ΔH ($\times 10^{-2}$)	ΔG	$-T\Delta S$
M3 (-ACET)	HTCHIQSCDHLA	-4.38	-14.7	423.0
M3 (+ACET)		-34.6	-22.0	12.6
C3.15 (-ACET)	NYLPHQSSSPSRC	1.93	-25.2	-218.0
C3.15 (+ACET)		1.68	-23.0	-191.0

[1] Schönberger, N. *et al.* (2019) *J. Chromat. A* **1600**, 158–166.

[2] Schönberger, N. *et al.* (2019) *Biomimetics* **4**, 35.

In vivo capture of bacterial cells by remote guiding

I. Rybkin, S. Pinyaev,¹ O. Sindeeva,^{2,3} S. German,^{2,3} M. Koblar,⁴ N. Pyataev,¹ M. Čeh,⁴ D. Gorin,^{2,3} G. Sukhorukov,^{2,3} A. Lapanje⁴

¹National Research Ogarev Mordovia State University, Saransk, Russian Federation; ²Skolkovo Institute of Science and Technology, Skolkovo, Russian Federation; ³Saratov State University, Saratov, Russian Federation; ⁴Jožef Stefan Institute, Ljubljana, Slovenia

Fluorescently labeled polyelectrolytes (PEs) and magnetite nanoparticles (NPs) were deposited on the bacterial cell surface by a Layer-by-Layer (LbL) approach to control cell growth, distribution and detection of bacteria. According to the results obtained *in vivo*, the local concentration of the cells was increased more than five times by the magnet entrapment of the modified bacteria keeping the high concentrations even when the magnet was removed.

Recently, it has been shown that several bacterial strains can be very efficient in cancer treatment, since they possess many important properties, such as self-targeting, ease of detection, sensing and toxicity against tumors. However, there are only a few relevant “candidates” for such an approach, as targeting and detection remain the biggest challenges. We propose a solution using labeled PEs and magnetite NPs that enables surface modification of alive bacterial cells without interfering with their genetic material potentially reducing their toxic side effect.

EXPERIMENTAL. Non-motile *Escherichia coli* TOP 10 strain, was harvested at $OD_{600} = 0.2$ (measured with reduced optical path of 200 μ L well of a 96-well plate) and then washed 3 times using centrifugation (5,000 \times g, 5 min) and replacement of supernatant with sterile 0.9% NaCl. The cells were coated in layers of PEI/PSS/PEI/magnetite-NP/(PEI/PSS)₂. Firstly, a layer of positively charged PEI was deposited by adding 0.25% (w/v) solution of PEI in MQ water (pH 7) to the washed and concentrated cells with the final $OD_{600} = 1.2$ in 1:1 v/v ratio incubating for 5 min. Unattached PEI was washed out from the suspension by centrifugation (900 \times g, 2 min). The obtained pellet was washed (2 \times) by gently pouring 1 mL 0.9% NaCl not resuspending the pellet. The PEI coated cells were washed in 0.9% NaCl solution. The second negatively charged PSS layer was deposited (pH 7) using the same procedure as for PEI and cell centrifugation (1,500 \times g, 3 min). After addition of another PEI layer, magnetite NPs were added and incubated for 5 min. (1 mg mL⁻¹ particles, 1:1 v/v particles to cells). The excess of magnetite particles was washed out by centrifugation (1,500 \times g, 3 min). After magnetite, the layers of Cy-7 labeled PEI/PSS were deposited in the same way as described above. Finally, we obtained eight layers of the PEs on the bacterial cells including a paramagnetic layer. The biodistribution of the coated bacterial cells was investigated in two groups of three BALB/c female mice 6–8 weeks old with weight distribution 20–25 \times g. For all animals, the bacterial cells were injected in the right femoral artery and collected in the left paw by placing the permanent magnet NdFeB (1,400 mT remnant magnetization, $\varnothing \times$ height: 50 \times 20 mm) for 60 min, which was then removed. The control group of animals was correspondingly treated without magnetization.

RESULTS. After administration of the electrostatically functionalized bacterial cells (EFBC) into the bloodstream of mice, we observed differences in distribution of the cells that were dependent on the presence of the magnet. Under exposure to the magnetic field, spreading of the cells in the or-

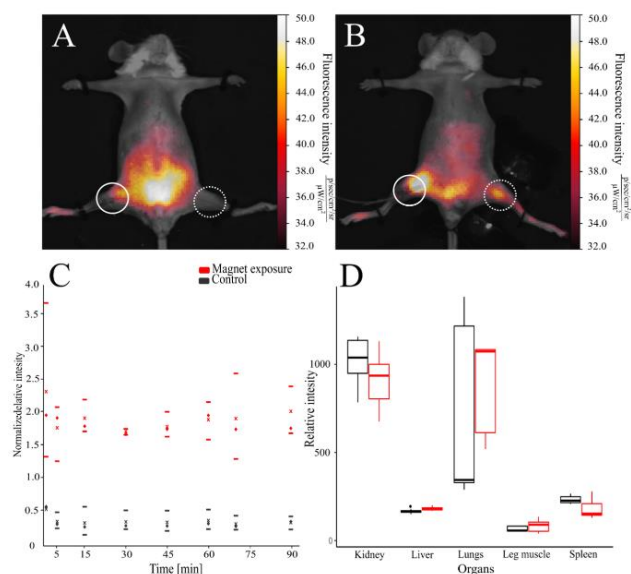


Figure 1. Distribution of the bacterial cells modified with magnetite nanoparticles and Cy-7 labeled PEI in the mice. The bacteria were detected in control mouse (A) and exposed under magnet mouse (B), respectively. Dash circles indicate place of injection, solid circles – place of cell collecting. Relative fluorescence intensity of the signal in the paw under magnet exposure and normal distribution by blood flow was chosen to compare the accumulation of cells (C), where – Median, \times average, upper and lower borders are 25th to 75th percentile, respectively. Normalized relative fluorescence was also assessed in the organs of animals (D).

ganism from the place of injection was directed toward the paw with a magnet followed by accumulation of the bacterial cells resulting in bright areas in the paw where a magnet was placed (Fig. 1A). In contrast, the signal in other parts of the body was 2.4 times on average weaker than in the paw. In control groups, the EFBC were distributed mainly in the abdomen forming dense shining areas, whereas in the intact paw the signal was 1.8 times weaker than in other parts of the body (Fig. 1B). Throughout all experiments, the animals remained alive. During the magnet entrapment, we were able to significantly increase the signal intensity by more than 5 times in the paw region than in the control group ($P < 0.001$) (Fig. 1C). However, although the magnet attracted bacterial cells, we found that only a small fraction of cells (up to 4.6% \pm 0.1%) was accumulated in the paw, while the overall distribution of free circulating cells remained the same in both groups. After the magnet was removed, we observed that the signal in the exposed paw was 5.8 times higher than in unexposed paw over the remaining half an hour ($P < 0.001$). After animals were dissected, the analysis of the fluorescence of the vital organs exposed to the magnet was 1.1 times higher just in the liver compared to the control group ($P < 0.05$, Fig. 1D).

ACKNOWLEDGEMENTS. The research was performed at Saratov State University and Jožef Stefan Institute in collaboration with HZDR. We acknowledge financial support by the Helmholtz-Association, grant PIE-0007 (CROSSING).

Dual-radiolabeling shows dissolution-based uptake pathway of CeO₂ in freshwater shrimp

S. Schymura, I. Rybkin, S. S. S. Uygan, S. Drev,¹ R. Podlipec,¹ T. Rijavec,¹ A. Mansel, A. Lapanje,¹ K. Franke, M. Strok¹

¹ Jožef Stefan Institute, Ljubljana, Slovenia

The risk assessment of nanomaterial release into the environment and consequences for organisms depend on the accurate measurement of doses and knowledge of environmental transformations along transfer pathways. This is especially important for slowly dissolving particles, such as CeO₂. Our dual-radiolabeling strategy provides answers to both dosimetric and mechanistic questions. The CeO₂ nanoparticle uptake pathways in freshwater shrimp are elucidated. The results suggest a dissolution-based translocation of cerium over the gut wall and a consequent exposure of the internal organs of the crustaceans to potentially toxic, dissolved cerium.^[1]

EXPERIMENTAL. CeO₂ nanoparticles (NPs) procured from the JRC Nano-material Repository were activated *via* neutron irradiation at the TRIGA Mark II nuclear reactor of the Jozef Stefan Institute yielding radiolabeled [Ce-141]CeO₂ NPs. A second radiolabel was introduced *via* in-diffusion of cyclotron-produced Ce-139.^[2,3] The so-produced dual-labeled [Ce-139/Ce-141]CeO₂ were introduced into a food pellet which was fed to freshwater shrimp (*Caridina pareparensis parvidentata*). The uptake and excretion of the radiotracers was monitored by gamma spectroscopy for a period of one month. The distribution of the radiotracers inside the NPs was established by controlled dissolution experiments in 1 mM HNO₃.

RESULTS. Controlled dissolution experiments in HNO₃ revealed that the Ce-139 was released preferentially upon dissolution of the particles. The different distributions of the radiotracers, surface-near for the Ce-139 *vs.* volume-based for the Ce-141, let us track dissolution effects along the uptake pathway with easily established dose measurements on the live shrimp throughout the experimental run (Tab. 1).

Table 1. CeO₂ dose and uptake at start and end of the experimental run as established by Ce-141 gamma spectroscopy.

Exp.	Dose offered	Uptake per shrimp	Uptake per dry weight	Uptake per wet weight
Start	59 µg	2.5 µg	0.41 µg mg ⁻¹	0.081 µg mg ⁻¹
End	–	380 pg	62.0 pg mg ⁻¹	12.4 pg mg ⁻¹

The shrimp were exposed to a single dose of 59 µg CeO₂ per shrimp, 4% of which was consumed. No acute toxic effects were observed during the experimental run. The excretion of CeO₂ from the shrimp follows an exponential decay curve with a half-life of 2.3 days, consistent with the feeding schedule. At the end of the 30 days experimental run only 380 ± 173 pg CeO₂ remain per shrimp, *i.e.* 99.985 ± 0.007% of the initially taken up amount was eliminated from the shrimp with only 0.015 ± 0.007% remaining.

A closer look at the elimination curves of the different cerium nuclides reveals differences between the Ce-141 and Ce-139 elimination from the shrimp (see Fig. 1). We can see that both nuclides follow the same trend for 20 days after which no further excretion of Ce-139 is seen. We conclude that after 20 days the vast majority of nanoparticles are eliminated from the organism *via* the feed stream while the remaining cerium took a dissolution-based uptake pathway into the organism and cannot be readily removed. This translates into a dissolution of about 0.15‰ of the CeO₂

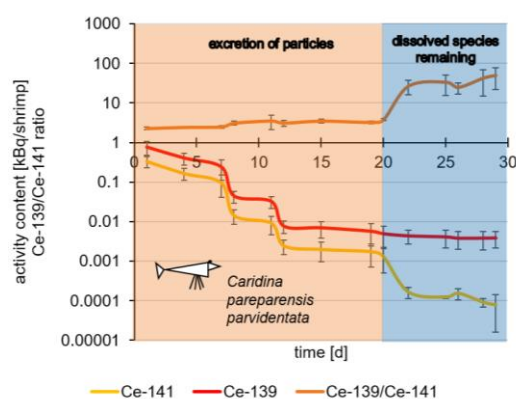


Figure 1. Development of Ce-139 and Ce-141 content of freshwater shrimp, as well as the isotope ratio over the course of one month.

within the digestive tract of the shrimp. Autoradiographic analysis of the distribution of the activity remaining in the shrimp after the experimental run reveal that the activity is primarily located in the lower cephalothorax of the shrimp (see Fig. 2). A cross-referencing with general shrimp anatomy allows us to identify the hepatopancreas as the main accumulator of the remaining cerium. The hepatopancreas is the main digestive gland of crustaceans and is considered to be the major invertebrate organ that sequesters and detoxifies dietary or water-borne metals.^[4] Our data shows that the dissolution is not only coincidental but instrumental in the uptake of CeO₂ NPs into the shrimp, *i.e.* it was a prerequisite for cerium uptake into the internal organs of the shrimp under our experimental conditions.

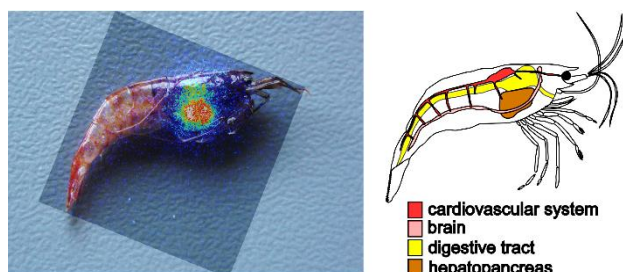


Figure 2. Distribution of the remaining activity within the shrimp after the experimental run measured by autoradiography (left), and scheme of shrimp internal organs (right).

ACKNOWLEDGEMENTS. We acknowledge financial support by the Helmholtz-Association, grant PIE-0007 (CROSSING).

- [1] Schymura, S. *et al.* (2021) *Environ. Sci. Nano.* **8**, 1934–1944.
 [2] Hildebrand, H. *et al.* (2015) *J. Nanopart. Res.* **17**, 278.
 [3] Schymura, S. *et al.* (2017) *Angew. Chem. Int. Ed.* **56**, 7411–7414.
 [4] Ahearn, G. A. *et al.* (2004) *J. Comp. Physiol. B* **174**, 439–452.

α - β -separation in liquid scintillation counting using small economical detectors

S. Stalke, R. Steudtner, K. Grossmann¹

¹VKTA, Dresden, Germany

Temporal information of scintillating pulses can be used to distinguish between α - and β -radiation. Herein, it is shown that, by using appropriate energy windows, two separated pulse width distributions can be extracted from a complex sample of nuclides. It is argued that these two distributions stem from contributions of temporally separated α - and β -nuclides.

α -emitting nuclides are known to create scintillating pulses having larger widths than pulses created by β -emitting nuclides.^[1] We used our “UltraSens” small scale liquid scintillation counter to investigate a complex sample containing three β -emitting nuclides, one electron capture nuclide and one α -emitting nuclide (Tab. 1). The setup was similar to the one described before,^[2] with the exception of using a new oscilloscope (RTB2004), a new type of silicon photomultiplier SiPM (WL3347) and a data acquisition rate closely matching the count rate of the sample.

Table 1. Composition of nuclide mixture as measured by γ -spectroscopy.

Nuclide	Activity (Bq)	Energy (keV)	Ref.
Pb-210 (β)	3.4×10^3	6.3 (mean)	[3]
Cs-137 (β)	7.8×10^2	178 (mean)	[3]
Co-60 (β)	4.8×10^2	95.8 (mean)	[3]
Cd-109 (EC)	4.5×10^2	88.0 (max. band)	[4]
Am-241 (α)	3.5×10^2	5,486 (max. band)	[5]
Other	$< 3.5 \times 10^0$	n.a.	

EXPERIMENTAL. 0.1 mL of the nuclide mixture in aqueous solution was blended with 5 mL of Ultima Gold XR to give a homogeneous solution. 0.6 mL of the solution was placed in fluorinated ethylene propylene (FEP) hosing and coupled to the SiPM. The energy window was set by setting the trigger level of the oscilloscope. The count rate of the sample at trigger levels of 30 mV and 150 mV was 45 cps and 5 cps, respectively. Background count rates of ~ 1.2 cps (30 mV) and ~ 0.3 cps (150 mV) were neglected in this first case study.

RESULTS. 1D data of the distribution of mean scintillating pulse energy at trigger levels of 30 mV and 150 mV is shown in Fig. 1, top. The mean pulse energy spectrum at 30 mV is dominated by low energy contributions probably stemming from Pb-210, Cd-109 and, more probably, lower energy parts of Cs-137 and Co-60. If the trigger level is increased to 150 mV the mean pulse energy spectrum now shows the low energies being cut out and at higher energies two additional bands can be seen.

The pulse width distribution at different trigger levels is shown in Fig. 1, bottom. At 30 mV, a broad band with a shoulder at shorter pulse widths can be seen. This broad width distribution is due to the fact, that low energy pulses cannot be analyzed with same precision as higher energy pulses. At 150 mV, the pulse width distribution shows two separated bands. The area of both bands suggests that at this trigger level the contribution of Am-241 α -nuclide and Cs-137 and Co-60 β -nuclides to the mean energy spectrum is roughly the same. This is supported by the fact that a big part of the mean energy spectrum of the β /EC emitters has been cut out by the trigger. Scintillating pulse width meas-

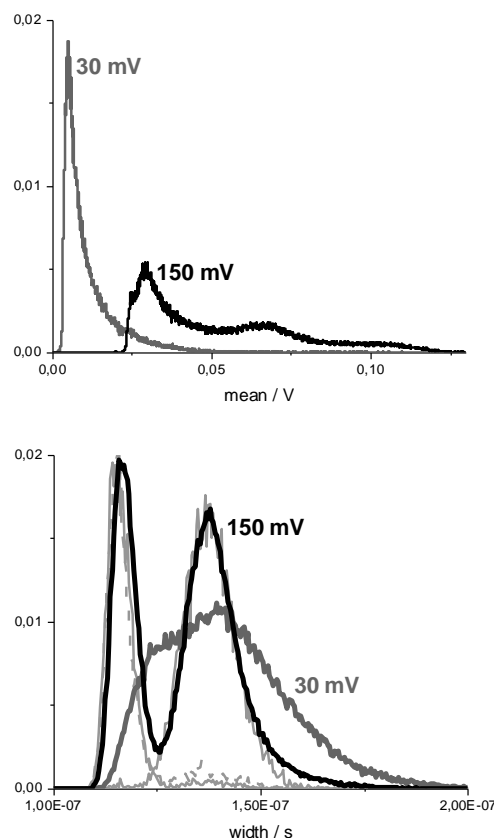


Figure 1. Scintillating pulse properties of the nuclide mixture at trigger levels of 30 mV (gray) and 150 mV (black). Top: mean pulse energy distribution. Bottom: pulse width distribution. Light gray: pulse width distributions of Am-241, Cs-137 and Co-60 (dash) external sources at 150 mV. Nuclide mixture spectra were normalized to unit area, external sources spectra were normalized arbitrarily.

urements with Am-241 (22 cps), Cs-137 (2.8 cps) and Co-60 (1.3 cps) external sources, applied to the SiPM-FEP interface at trigger level of 150 mV (see light gray lines in Fig. 1, bottom), further strengthen the hypothesis.

OUTLOOK. Despite of successfully showing two different types of pulse width distributions, a closer look at Fig. 1, bottom, reveals a certain amount of spill-over and therefore the necessity of a dual label counting which is accompanied by losing successfully counted pulses. This situation will have to be circumvented by using (a) a higher resolution analog digital conversion, *i.e.* 12–16 bit, (b) 2D data, *i.e.* pulse energy *vs.* pulse width or pulse energy *vs.* rise time, and (c) dedicated Cocktails, *i.e.* Ultima Gold LLT or Ultima Gold AB.

ACKNOWLEDGEMENTS. The project was kindly funded by Forschungszentrum Jülich (100455901) in the scope of WIPANO. Additional appreciation is given to B. Bauer and S. Bartel (both VKTA) for providing the samples and the γ -spectroscopy measurements.

[1] Edler, R. (2020) *Application Note Perkin Elmer-57*.
 [2] Stalke, S. *et al.* (2020) *Report HZDR-113*, p. 238.
 [3] Cross, W. G. *et al.* (1982) *Phys. Med. Biol.* **28**, 1251–1260.
 [4] Oliván, M. A. *et al.* (2017) *Astropart. Phys.* **93**, 86–95.
 [5] Malain, D. *et al.* (2019) *J. Phys. Conf. Ser.* **1285**, 1–5.

SCIENTIFIC CONTRIBUTIONS (PART IV)

Safety

Nuclear Reactor

**SAFETY
RESEARCH**

Research

Neutronic benchmark solution of the FFTF Loss of Flow Tests – Preliminary results

E. Nikitin, A. Ponomarev, E. Fridman

The Reactor Safety Division of HZDR is participating in the IAEA Coordinated Research Project (CRP) on the benchmark analysis of Fast Flux Test Facility (FFTF) Loss of Flow Without Scram (LOFWOS) Test #13. During the blind phase of the CRP, preliminary results of the neutronics component of the benchmark were submitted, which are presented in this report. The results were obtained with Monte Carlo code Serpent. The results were in a good agreement with the solutions provided by other CRP participants.

DESCRIPTION OF THE REACTOR. The FFTF had a small 400 MW_{th} core cooled with liquid sodium. In the Cycle 8C, the core comprised 80 driver fuel assemblies, six control and three safety rods, nine gas expansion modules, three material testing assemblies. These were surrounded by 98 reflector assemblies. The core was fueled with mixed uranium-plutonium oxide. Four different driver fuel types were used varying in plutonium content and uranium enrichment.

DESCRIPTION OF THE FFTF NEUTRONIC MODEL.

The neutronic model of the core was created with Serpent according to the detailed benchmark specification.^[1,2] The drivers were modeled using the detailed material compositions, *i.e.* each driver assembly had their own material composition with an axial variation. The assemblies were kept homogenized on pin level. The ENDF/B-VII.1 nuclear library was applied. A reference fuel temperature of 1,000 K and a reference temperature for all structure materials at 600 K was assumed. The physical dimensions of the core correspond to hot full power conditions with a core-averaged temperature of 716 K.

In order to approximate the explicit fission product (FP) content, single-assembly burnup calculations were performed using Serpent. The assembly included a diluted fuel pin containing only Pu-239 in order to obtain the burnup-dependent FP vector of this actinide. The final FP compositions used in the full core calculations were estimated by scaling the obtained Pu-239 FP vector with the corresponding atomic densities of the lumped FP provided in the benchmark.

SELECTED RESULTS. Various neutronic parameters were evaluated. Table 1 summarizes the feedback coefficients and kinetics parameters required for transient calculations. As compared to the nine other participants of the neutronic benchmark, our results remained within 2σ in all counts indicating a good quality of our models.

The nominal power production for each assembly including the fission and gamma heat is presented in Fig. 1. The power distribution was produced with Serpent in coupled neutron-photon mode with an advanced energy deposition treatment.^[3] This means that Serpent calculated local energy deposition (kinetic energy of fission products and the energy of delayed betas), direct energy deposition by neutrons due to reactions other than fission such as scattering or capture, and direct energy deposition by photons (prompt and delayed gammas). In the driver assemblies, the photons are responsible for about 9–10% of power production.

SUMMARY AND OUTLOOK. The neutronic models of the FFTF core in Cycle 8C was created and tested. The presented results were in a good agreement compared to the leading research organizations in reactor safety.

Table 1. Neutronics parameters.

Neutron Multiplication Factor	1.00003 ± 0.000053
Delayed Neutron Fraction	3.13 × 10 ⁻³
Prompt Neutron Lifetime	5.43 × 10 ⁻⁷
Axial Expansion Coefficient (pcm/K)	-0.33
Radial Expansion Coefficient (pcm/K)	-1.41
Fuel Doppler Constant (pcm)	-682
Fuel Density Coefficient (pcm/K)	-1.39
Structure Density Coefficient (pcm/K)	0.22
Sodium Density Coefficient (pcm/K)	-0.76
Control and Safety Rods (pcm)	-10864
Gas Expansion Modules (pcm)	-394

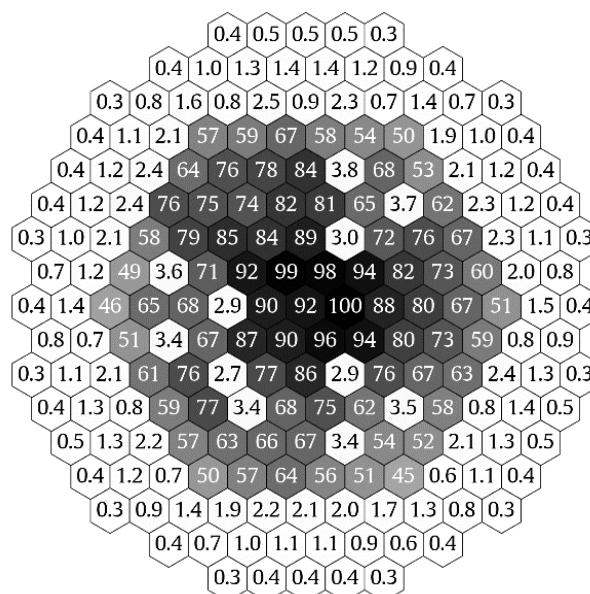


Figure 1. Radial power (fission + gamma heat) distribution in percent power peaking factor (PPF = 1.4 equivalent to 3.4 MW power). Gray-Black assemblies are fuel; white assemblies are non-fuels with no fission power.

The established neutronic models will serve as a basis for producing neutronic data and models for transient simulations of the FFTF LOFWOS Test #13. The goal will be to utilize our Serpent/DYN3D/ATHLET codes system, which was recently established for safety analyses of sodium cooled fast reactors.^[4,5]

- [1] Leppänen, J. *et al.* (2015) *Ann. Nucl. Energy* **82**, 142–150.
- [2] Sumner, T. *et al.* (2017) ANL-ART-102 (Rev 2).
- [3] Tuominen, R. *et al.* (2019) *Ann. Nucl. Energy* **129**, 224–232.
- [4] Rohde, U. *et al.* (2016) *Prog. Nucl. Energy* **89**, 170–190.
- [5] Lerchl, G. *et al.* (2012) ATHLET Mod 3.0 Cycle A. User's Manual.

Optimization of multi-group energy structures for diffusion analyses of sodium-cooled fast reactors assisted by simulated annealing

Y. Bilodid, V. A. Di Nora, E. Fridman, E. Nikitin

This study presents an approach to the selection of the optimal energy group structures for multi-group nodal diffusion analyses of Sodium-cooled Fast Reactor cores. The goal is to speed up calculations, particularly in transient simulation, while maintaining an acceptable accuracy of the results.

The nodal neutron diffusion simulation is a standard tool for nuclear reactor analysis. The neutron energy variable is subdivided into discrete intervals referred to as energy groups. The choice of a number of energy groups and their structure (EGS) affects the accuracy of the results and the computational time required for simulation.

The in-house nodal diffusion code DYN3D is successfully applied to analyses of various sodium-cooled fast reactors (SFR) utilizing 24-group EGS.^[1-4] This study proposes a new methodology for identifying an optimized EGS with a reduced number of EGs to accelerate static and transient analyses of SFRs.

OPTIMIZATION METHOD. The preliminary study have demonstrated that calculation time is proportional to the number of groups in EGS. Search for an optimal EGS was performed by condensing the reference 24-group EGS into 1–12-groups EGS, which results in $\sim 10^7$ possible combinations. To perform optimization in a large space the Monte Carlo meta-heuristic simulated annealing algorithm was applied in this study.^[5] The technique combines features of the random walk and hill-climbing procedures.

The accuracy of a generic EGS is measured by a cost function which represents the deviation of the condensed EGS solutions from the reference 24-group solution. The goal of optimization analysis is to find EGS with minimal cost function value. The cost function H (Eq. 1) chosen for this study is a combination of error in core reactivity $\Delta\rho$ (reactor core global value) with a root mean square (RMS) error in subassembly power ΔP_{RMS} (local value):

$$H = |\Delta P_{RMS}| + w_p |\Delta\rho| \quad (1)$$

The study was performed on international benchmarks on Superphénix (static states) and Phénix (transient) reactors.^[6,7]

RESULTS. The results confirmed that it is possible to noticeably improve the DYN3D performance without a significant deterioration of the accuracy. It is worth noting that the “acceptable accuracy” is a relative term, which depends on a particular application. Therefore, it is up to the code user to select a proper trade-off between the computational performance and the desired accuracy.

The optimization procedure appeared to be core-design dependent and showed clear tendency to resolve more populated energy regions and merge less populated ones.

The comparison with 24-group reference solution shows clear tendency of increasing deviation from the reference with decreasing of energy discretization. The application of the optimal 12-group EGS delivers results practically equivalent to the reference but with a half of the computational cost. Furthermore, depending on the target accuracy, reasonable results may be obtained with lower (8–6) numbers of energy groups. The use of EGS with less than six energy groups, for both the static Superphénix and transient Phénix

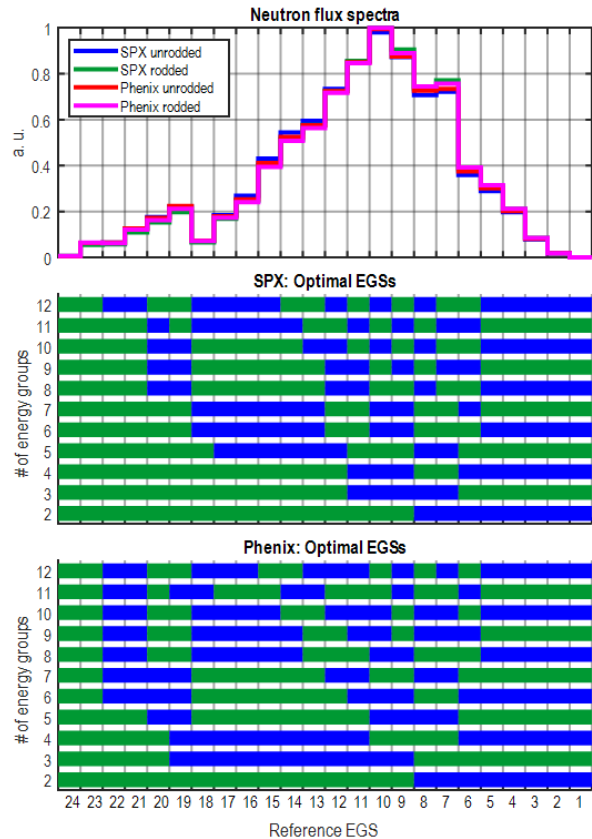


Figure 1. Optimal energy group structures.

calculations, induces greater deviation of the solutions from the reference and therefore can be only recommended for scoping studies (Fig. 1).

Obtained results were published in journal articles and included into Ph.D. thesis work of V. A. Di Nora.^[8,9]

ACKNOWLEDGEMENTS. The work has been prepared within EU Project ESFR-SMART which has received funding from the EURATOM Research and Training Program 2014-2018 under the Grant Agreement No. 754501.

- [1] Rohde, U. et al. (2016) *Prog. Nucl. Energy* **89**, 170–190.
- [2] Fridman, E. et al. (2013) *Ann. Nucl. Energy* **53**, 354–363.
- [3] Nikitin, E. et al. (2015) *Ann. Nucl. Energy* **75**, 492–497.
- [4] Nikitin, E. et al. (2018) *Ann. Nucl. Energy* **119**, 382–389.
- [5] Osman, I. H. et al. (1996) *Meta-Heuristics: Theory & Applications*, Springer U.S.A., Boston.
- [6] Ponomarev, A. et al. (2018) in *Proc. of PHYSOR*.
- [7] IAEA (2013) *IAEA-TECDOC-1703*.
- [8] Di Nora, V. A. et al. (2021) *Ann. Nucl. Energy* **155**, 108183.
- [9] Di Nora, V. A. et al. (2021) *Ann. Nucl. Energy* **163**, 108541.

Plant modelling and applied safety analyses in NuScale Small Modular Reactor (SMR) with thermal-hydraulic system code ATHLET and CFD software

E. Diaz-Pescador, A. Grahn

The SMR NuScale is modelled in the framework of the European McSAFER project.^[1] McSAFER fosters high-fidelity calculations by state-of-the-art multiscale and multi-physics techniques applied to safety analyses in SMRs. The present contribution provides an insight on multiscale vessel analysis methodologies using the thermal-hydraulic system code ATHLET and open source CFD software, including preliminary calculation results.

NUSCALE NUCLEAR POWER MODULE. NuScale is a SMR of integral pressurized water reactor (PWR) type operated with light water driven by natural circulation with reactor core, helical coil steam generators and pressurizer system located in a common reactor vessel in a cylindrical steel containment. The nominal core power accounts for 160 MWth with an electrical output of 50 MWe. It has been developed by NuScale Power LLC and is modelled in the framework of McSAFER with the system code ATHLET and a CFD software.^[1]

MODELLING APPROACH. The scope, governing equations closure relations and mesh between system and CFD codes differs significantly. So does the modelling approach and thermal-hydraulic domain between codes. The first aims at predicting overall plant dynamics at system scale, whereas the second targets representation of local processes with high accuracy. In McSAFER, ATHLET models the full-plant NuScale SMR, comprising a 3-D vessel with helically-coiled steam generator tubes and corresponding auxiliary and safety systems, as well as secondary side up to the turbine admission (Fig. 1). The vessel 3-D modelling approach pursues an enhanced representation of transport and mixing processes during transient calculation. On the other hand, the CFD model domain comprises a much finer 3-D representation of the vertical downcomer section and lower plenum regions (Fig. 2), to accurately represent transport and coolant mixing locally.

PRELIMINARY RESULTS. The boron dilution event is one of the reference scenarios for system codes. Deboratation is assumed through the make-up line of the chemical and volume control system (CVCS) at nominal operation conditions, as stated in Chapter 15 from the final safety analysis report (FSAR).^[2] Figure 3 shows the [B] decrease at the core inlet and subsequent evolution of the reactivity rates, calculated by ATHLET. Reactor SCRAM is triggered at around 700 s at

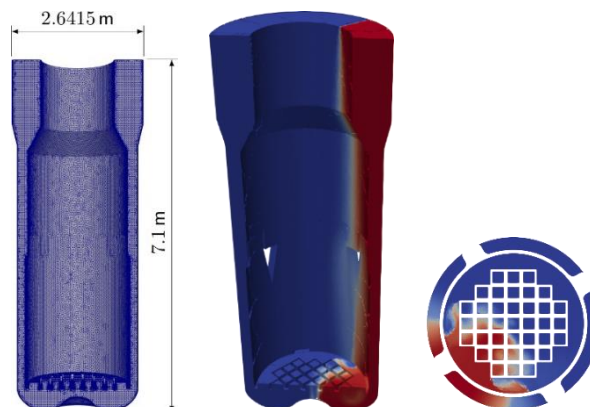


Figure 2. CFD mesh of NuScale downcomer and lower plenum (left); simulated distributions of a mixing scalar in the vessel (center) and in the core inlet plane (right).

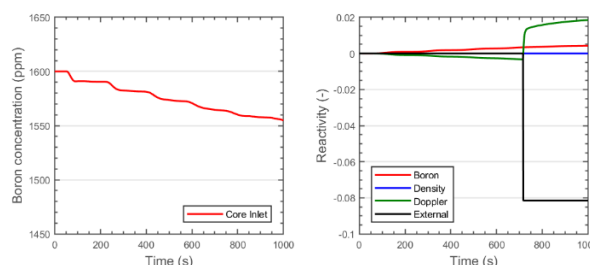


Figure 3. ATHLET results inside the core.

a core power exceeding 120 % nominal, due to major contribution from boron feedback. These results show an overprediction of mixing inside the vessel, which in turn delays reactor SCRAM with respect to FSAR. This issue is being dealt with. On the other hand, the result of a standalone CFD simulation under nominal conditions of operation is shown in Fig. 2. The coolant mixing in the downcomer and lower plenum regions is investigated by labelling the coolant with a scalar in a quarter sector of the inlet boundary. Disturbances of the coolant flow arise from core supporting structures in the downcomer and from flow inflection in the lower plenum, leading to substantial coolant mixing before entering the reactor core.

FUTURE WORK. Currently, an interface is developed that couples the system code ATHLET and the CFD package TrioCFD. It allows whole-plant simulations of reactor transients while capturing mixing phenomena in the pressure vessel in greater detail. The core behavior during transients largely depends on the feedback parameters which are to be provided as boundary conditions by the CFD part.

ACKNOWLEDGEMENTS. This project has received funding from the European Union's Horizon 2020 research and innovation program under grant agreement No. 945063.

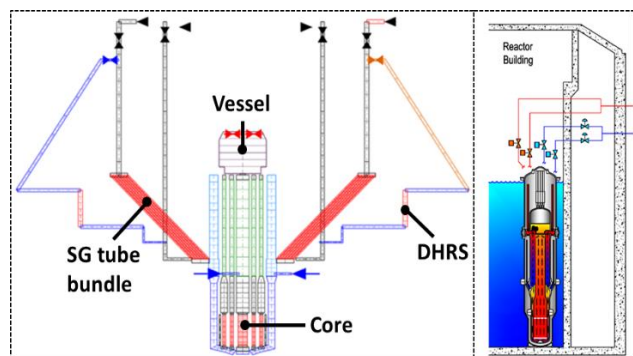


Figure 1. ATHLET model of NuScale SMR (left) and plant layout (right).

[1] Sanchez-Espinoza, V. et al. (2021) *Energies* **14**, 6348.
 [2] NuScale Power LLC (2018) NuScale Standard Plant Design Certification Application, U.S. Nuclear Regulatory Commission (NRC).

Numerical investigation of asymmetric cold-water injection into the primary circuit of a German KONVOI PWR during a Station Blackout sequence with ATHLET

E. Diaz-Pescador,¹ F. Schäfer, S. Kliem

¹Technische Universität Dresden, Dresden, Germany

This work summarizes the main insights from the investigation of fluid transport and mixing processes inside the reactor coolant system (RCS) of a German pressurized water reactor (PWR) during the numerical simulation of ROCOM Test 2.1 with the system code ATHLET.^[1,2] The experiment represents the asymmetric injection of cold water inside the RCS through cold leg #1 during a Station Blackout scenario to restore core cooling. The injected water is assumed at room temperature and boron-free, hence the risk of a core re-criticality is potentially given. Calculations are performed with a state-of-the-art thermohydraulic model of ROCOM based on multidimensional object topologies. The simulation results show agreement with experiment, demonstrating that the newly developed 3-D pipe concept enhances code predictive capabilities.

MOTIVATION. Coolant mixing inside the reactor pressure vessel (RPV) plays a major role during the progression of selected reactivity initiated accidents (RIAs), determining reactivity insertion rates and impact on operation and safety. Previous works from the authors have successfully addressed this issue in ATHLET for two of the most limiting RIAs, boron dilution and overcooling transient, by 3-D vessel modelling (Fig. 1).^[3,4] However, those works pointed out as well the need to enhance representation of transport processes prior to vessel arrival.^[9] This constitutes the motivation of this study and is achieved by the development of a novel pipe object topology, comprising three radial rings surrounding a central channel and overall 25 different vertical elevations, thereby giving rise to an interconnected network. Multiple fill-objects represent the ECC-Nozzle from ROCOM for the injection of cold-water under single-phase flow sub-cooled conditions (Fig.2).

RESULTS. The evolution of the injected water at cold leg #1 outlet is assessed by the mixing scalar, which is depicted in Fig.3. The results obtained with base case or ATHLET 3-D

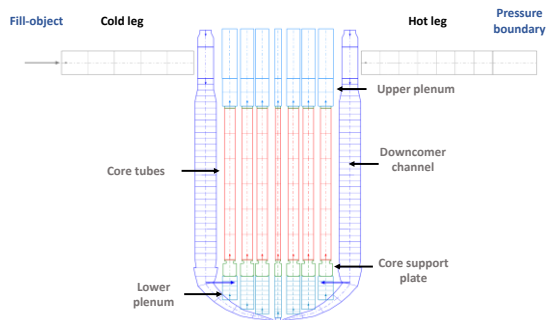


Figure 1. ATHLET model of ROCOM vessel.^[4]

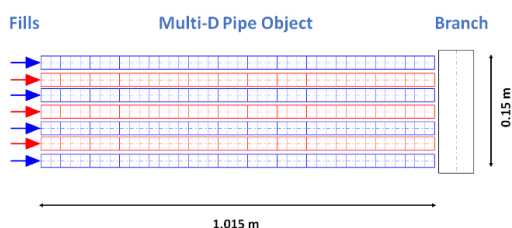


Figure 2. ATHLET cold leg #1 nodalization scheme.

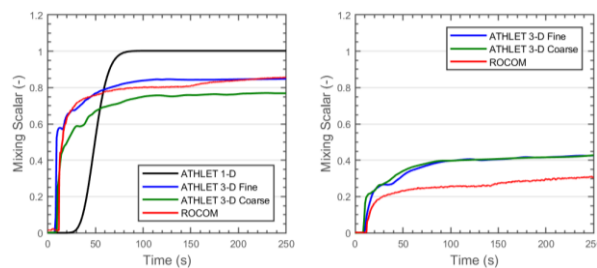


Figure 3. Cold leg #1 maximal (left) and averaged (right) mixing scalar.

Fine show a 3s early arrival of the injected water in ATHLET with respect to actual experiment, pointing out slightly higher momentum transport along cold leg #1. The orientation of the ECC-nozzle in ATHLET and ROCOM may justify this time deviation. Besides that, results from maximal mixing scalar show agreement with the experiment and depict an initial perturbation upon arrival of injected water, which stabilizes at 100s at around 0.85. A sensitivity study on the pipe nodalization shows that coarser 3-D nodalization lead to a plateau reached at slightly lower values, pointing out to a smoother share of the perturbation locally. On the other hand, the classic approach based on 1-D pipe topology fails to represent the behavior observed in the experiment, resulting in lower momentum transport and late arrival to the vessel at around 30 s. The single-channel configuration leads to over prediction regarding share of perturbation across the entire pipe cross-section area. The results from the average mixing scalar show nearly identical evolution between 3-D pipe topologies and over prediction of mixing scalar upon arrival against actual experiment, with an eventual deviation accounting for 0.1.

The latter seems to arise from the limitations of the system code posed by the lumped parameter approach and donor cell formulation of the finite volume approach.

CONCLUSIONS. The newly developed and implemented 3-D pipe configuration has notably improved code ability to represent transport and coolant mixing under complex flow conditions. Given the traditional limitations posed by system codes to model 3-D phenomena, the study shows discrepancies against the experiment, mainly in terms of stratification and water distribution. Those are to be dealt with in future works, supported by CFD calculations, reassessing and implementing enhanced closure relations in the governing equations. Criticality calculations resulting from replacement of highly-borated coolant at the core inlet are to be further assessed quantitatively by coupled ATHLET-DYN3D calculations applied to a full-plant PWR model.

ACKNOWLEDGEMENTS. This project was funded by the Federal Ministry for Economic Affairs and Climate Action (BMWK, grant no. 1501540).

- [1] Kliem, S. and Franz, R. (2016) *Institute Report HZDR\FWO\2016\01*.
- [2] Wielenberg, A. et al. (2019) *Nucl. Eng. Des.* **354**, 110211.
- [3] Diaz-Pescador, E. et al. (2020) *Nucl. Eng. Des.* **367**, 110776.
- [4] Diaz-Pescador, E. et al. (2021) *Nucl. Eng. Tech.* **53**, 3182 – 3195.

Activation calculations of selected RPV components' segments

R. Rachamin, J. Konheiser

By the end of 2022, all German nuclear power plants (NPPs) will have been shut down. This final shutdown is followed by a post-operational phase in which measures can be carried out to prepare for the NPPs dismantling and decommissioning. One of the important tasks in preparation for the dismantling is to acquire precise knowledge of the specific activities of the reactor pressure vessel (RPV) and its internal components. Such knowledge is essential for optimal planning of the disposal of these massive components and for minimizing the radioactive waste. In this study, the specific activities of selected RPV components' segments were calculated with a novel method based on the combined use of two Monte-Carlo codes, MCNP and FLUKA. The results of the calculations were obtained with great accuracy and evidenced that the used method can serve as a powerful and non-destructive tool for the radiological characterization of the RPV and its internals.

METHODOLOGY. High-resolution activation calculations of selected RPV components' segments (such as the RPV, core barrel, etc.) were performed using the MCNP-FLUKA codes sequence. At the first step, the MCNP code was used to calculate the neutron fluence rate characteristics (spectrum, distribution, and current entering the segment surfaces) in the studied segment using a 3D detailed model of a German PWR.^[1] A schematic view of the reactor model is shown in Fig. 1. The neutron fluence rate prediction capability of the MCNP model was validated *via* metal foil-activation measurements carried out in two German PWRs. The validation studies showed that the MCNP model is reliable and suitable for evaluating the neutron radiation field in the reactor for the ensuing activation calculations.^[2] At the second step, the FLUKA code was used to calculate the specific activity distribution in the studied segment using a 3D exact model of the segment and complex source terms built based on the neutron fluence rate parameters calculated using the MCNP code.^[3]

RESULTS AND DISCUSSION. The results of the RPV segment analysis are shown in Fig. 2 and Fig. 3. The studied segment has dimensions of $(r \times \theta \times z) = (25 \text{ cm} \times 5^\circ \times 12.2 \text{ cm})$ and is located parallel to the middle of the reactor core at an angle of 45° (see Fig. 1). Figure 2 presents the neutron fluence rate spectrum in the RPV segment obtained from the full model MCNP calculation and the segment calculation performed using the FLUKA code. As can be noted, a good agreement was obtained between the two codes, which evidenced that the neutron fluence rate characteristics were transferred adequately from the MCNP to the FLUKA calculations. Therefore, the FLUKA calculations can be considered as a direct continuation of the MCNP calculations. The specific activity distribution in the segment obtained from the FLUKA calculations is presented in Fig. 3 for four cooling times: end of life (EOL), and 1 y, 5 y, and 10 y after the EOL.

ACKNOWLEDGEMENTS. This work is funded as part of the PreussenElektra GmbH project "Activity calculation".

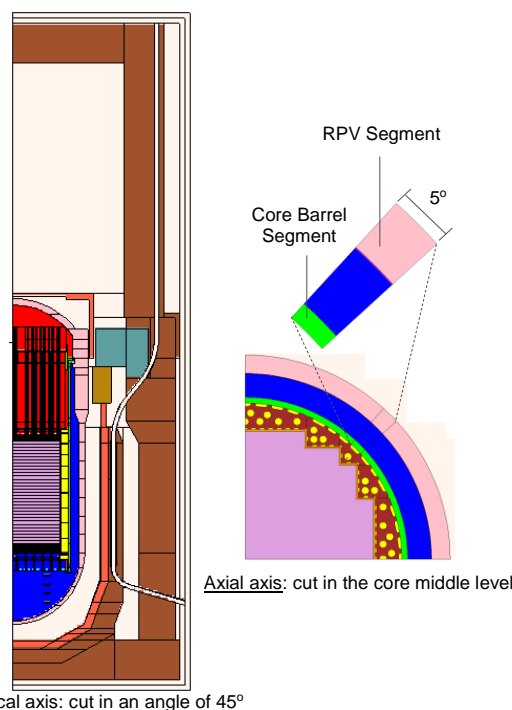


Figure 1. 3D model of a German PWR.

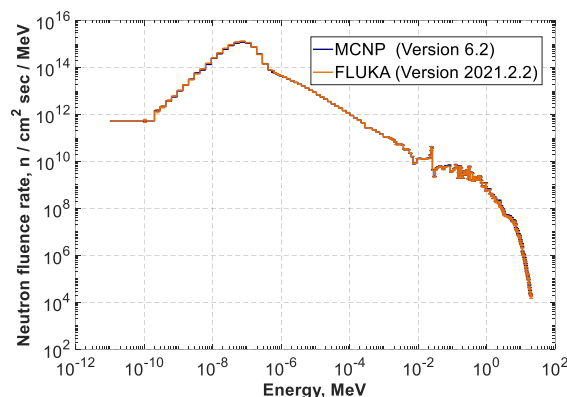


Figure 2. Neutron fluence rate in the RPV segment: MCNP vs. FLUKA.

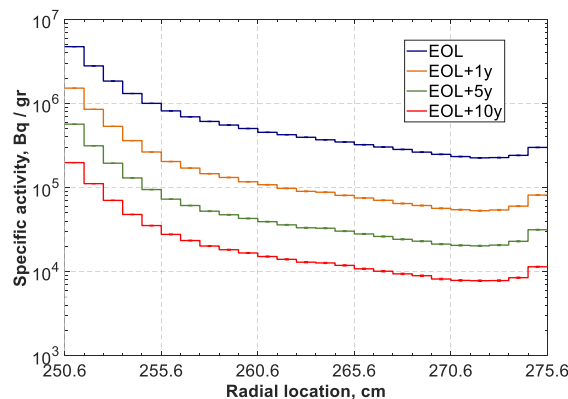


Figure 3. Specific activity in the RPV segment at different cooling times.

[1] Goorley, T. et al. (2012) *Nucl. Technol.* **180**, 298–315.

[2] Rachamin, R. et al. (2021) KONTEC 2021.

[3] Battistoni, G. et al. (2015) *Ann. Nucl. Energy* **82**, 10–18.

Fracture mechanics investigation of reactor pressure vessel steel by means of small scale specimen technique

A. Das,¹ E. Altstadt, P. Chekhonin, F. Obermeier²

¹Chair of Radiochemistry/Radioecology, Technische Universität Dresden, Dresden, Germany; ²Framatome GmbH, Erlangen, Germany

Neutron irradiation induced embrittlement of the reactor pressure vessel (RPV) reduces the operating lifetime of nuclear reactors. Therefore, knowledge of the fracture mechanics parameters of RPV steels before and after neutron irradiation is important but is limited by the shortage of irradiated material. To solve this, we tested sub-sized specimens manufactured from tested standard sized specimens using the master curve technique. Fractography was performed using scanning electron microscopy. The results from the small sized specimens are comparable to the standard specimens. After irradiation, RPV steels with higher impurities exhibit a larger increase in transition temperature with Mo particles initiating cleavage fracture predominantly.

The miniaturization of test specimens not only helps solve the limited material availability issue, but also reduces the active sample volume.^[1] The transferability of fracture mechanics data from small sized specimens to standard specimens is important and needs confirmation. This forms a key part of this study. Fracture mechanics testing is performed, on 0.16T compact tension C(T) specimens manufactured from already tested standard Charpy sized single edge bend (SE(B)), using the master curve technique in order to determine their transition temperature T_0 .^[2,3] The transition temperature T_0 is defined as the temperature at which the fracture toughness values is $100 \text{ MPa}\sqrt{\text{m}}$. Fractography is performed using the scanning electron microscope (SEM).

EXPERIMENTAL. Fracture mechanics testing of three RPV steels (2 base and 1 weld metal) was performed for both the unirradiated and irradiated conditions using 0.16T C(T) specimens in various orientations. Table 1 shows the material name, number of samples tested, orientation and neutron fluence. The nominal composition of JRQ is 0.15C, 0.24Si, 1.2Mn, 0.13Cr, 0.47Mo, 0.81Ni, 0.016P, 0.13Cu. JFL contains lower amounts of P (0.011 wt.-%) and Cu (0.02 wt.-%) while ANP-6 contains higher Ni (1.7 wt.-%) as compared to JRQ. The fracture surfaces were characterized using SEM and the fracture initiation sites were located.

Table 1. RPV materials along with their orientations and neutron fluences.

Material	Samples tested	Orientations	Fluence (10^{19} n/cm^2)
JRQ (Base)	32 Unirr, 16 Irr	T-L, T-S	9.82
JFL (Base)	41 Unirr, 36 Irr	L-T, T-S	8.67
ANP-6 (Weld)	23 Unirr, 8 Irr	T-L, T-S	5.63

RESULTS. JFL exhibits lower T_0 values as compared to the other materials in the unirradiated state (Fig. 1). An increase in T_0 is observed for all the materials after irradiation. The T_0 obtained for the sub-sized 0.16T C(T) specimens (gold) are comparable to that of standard Charpy 0.4 SE(B) specimens (blue) for both the unirradiated (solid) and irradiated conditions (dashed) demonstrating the applicability of small specimen techniques in safety assessment. Specimens from JRQ in the T-L orientation exhibit the highest increase in T_0 (solid black) closely followed by ANP-6 in

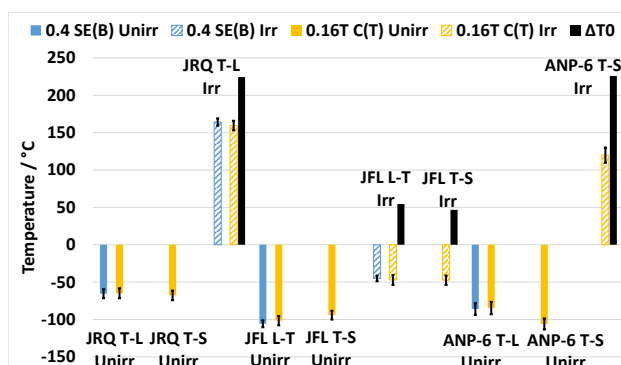


Figure 1. Comparison of the transition temperature T_0 of RPV steels between the standard Charpy SE(B) (blue) and sub-sized 0.16T C(T) specimens (gold) for both the unirradiated (solid) and irradiated (dashed) states along with the shift in transition temperature ΔT_0 after irradiation (solid black).

the T-S orientation. Samples from JFL exhibit relatively lower ΔT_0 irrespective of their testing orientation. The reason for the superior properties of unirradiated JFL is its microstructure which contains lower number density of Mo-particles that are responsible for cleavage fracture of the majority of the tested specimens as detected using SEM and EDX (Fig. 2). For the irradiated state, the lower contents of Cu, P and Ni in JFL results in lesser formation of precipitates, ultimately leading to lesser hardening and a smaller increase in T_0 as compared with the other materials.^[1]

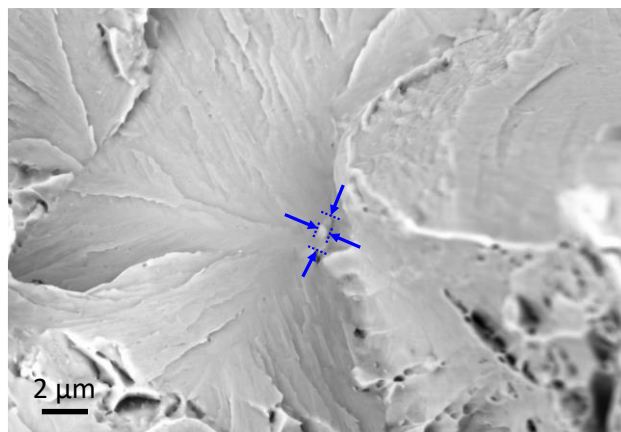


Figure 2. Fracture initiation particle as seen in a back scattered image using SEM from the fracture surface of a tested JRQ unirradiated specimen.

ACKNOWLEDGEMENTS. The authors thank W. Webersinke, M. Houska, M. Rossner and V. Reinke for their support.

- [1] Ballesteros, A. et al. (2014) *Nucl. Eng. Des.* **267**, 197–206.
- [2] Wallin, K. (1984) *Eng. Fract. Mech.* **19**, 1085–1093.
- [3] ASTM 1921 (2021), ASTM International.

Advanced microstructural characterization of reactor pressure vessel steels

P. Chekhonin, L. Lai

The microstructure of a reactor pressure vessel (RPV) steel was investigated by means of scanning- and transmission electron microscopy based techniques, in particular using electron backscatter diffraction (EBSD), energy dispersive X-ray spectroscopy (EDX) and scanning transmission electron microscopy.

The reactor pressure vessel is a critical component in a nuclear power plant which due to neutron irradiation embrittlement, from point of view of safety, ultimately limits its maximum life time. While there are many publications dealing with the neutron irradiation effects in bainitic steels,^[1] in many particular cases the image with respect to the microstructure of many particular steel is incomplete – the data is unavailable or unpublished.

One of the goals within the EURATOM funded project ENTENTE is the creation of a database of RPV steels with respect to their microstructural and mechanical properties, before and after neutron irradiation. It was identified that for many previously analyzed RPV steels the unirradiated bulk microstructure is incomplete or not available at all. However, a deeper understanding of the neutron irradiation effect and the subsequent hardening requires the input of the bulk microstructure (e.g. grain size, carbide size distribution, type of grain boundaries, dislocation density).

Within this project, HZDR agreed to provide a basic microstructural characterization of some chosen RPV steels and if possible, to identify and to complete data gaps. Here, such an analysis by means of scanning electron microscopy (SEM) and scanning transmission electron microscopy (STEM) will be presented using the low alloyed base metal RPV steel 22NiMoCr3-7, which is a 2nd/3rd generation RPV steel, which is actually used in power plants, as an example.

EXPERIMENTAL. Samples of the bainitic base steel forge 22NiMoCr3-7 were produced by electro discharge machining to a geometry of about $10 \times 10 \times 0.1 \text{ mm}^3$. With subsequent grinding and polishing procedures samples suitable for SEM, EDX and EBSD were produced. Classical preparation of thinned 3 mm discs was done for STEM analyses.

RESULTS. Figure 1a presents an EBSD mapping demonstrating the grain and grain boundary structure. The majority (63 %) of all grain boundaries are high angle grain boundaries (absolute misorientation $> 15^\circ$), those contribute to hardening and arresting of cracks.^[2] Furthermore, the EBSD mapping is used to calculate the average grain size to about $5.5 \mu\text{m}$ and additional data, such as grain size distribution, grain boundary misorientation distribution and the localiza-

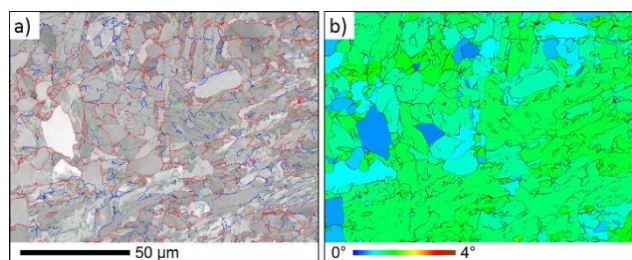


Figure 1. EBSD mapping with high and low angle grain boundaries plotted in red and blue, respectively (a). Kernel average misorientation plot of the same area (b).

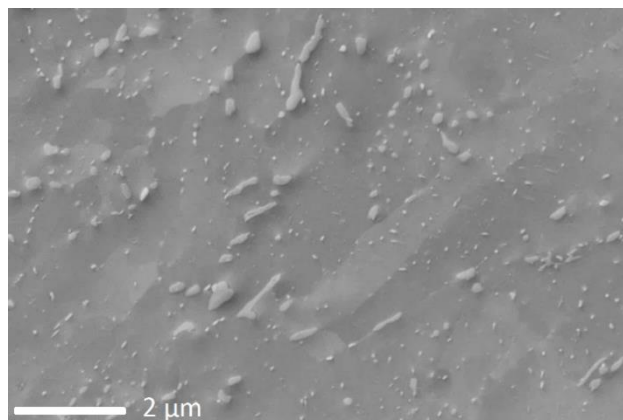


Figure 2. SE micrograph of an electro-polished surface.

tion of areas with lower dislocation density (blue areas in Fig. 1b), which may be ferrite islands.

Figure 2 shows a secondary electron (SE) micrograph of an electro-polished sample revealing the presence of precipitates and inclusions embedded in the steel. The majority of the precipitates is located on grain boundaries. EDX measurements demonstrate that there are two different carbide families: Mn rich and Mo rich carbides. In subsequent analysis images like this facilitate the determination of the carbide size distribution, which is essential to study and model the fracture toughness of the steel.

Figure 3 shows a STEM micrograph revealing the finest carbides and dislocations in the steel. Marking the dislocations and subsequently applying contrast recognition software, the dislocation line length was determined. In combination with thickness measurements of the transparent region by means of convergent beam electron diffraction, the average dislocation density (considering many different grains) was determined to amount $5 \times 10^{13} \text{ m}^{-2}$.

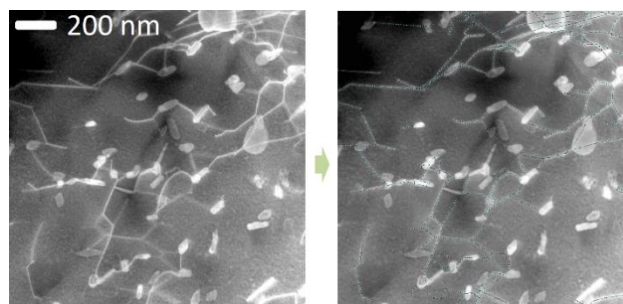


Figure 3. STEM micrograph before and after image processing. Dislocations are recognized by means of grey scale contrast and line intercept method.

ACKNOWLEDGEMENTS. This work was funded by the Euratom research and training program 2019-2020 under grant agreement No. 900018 (ENTENTE project). The authors would like to thank Ms. Michaela Rossner and Ms. Vanessa Reinke for SEM and TEM preparations.

[1] Was, G. S. (2003) *Fundamentals of Radiation Material Science*. Springer, Berlin Heidelberg.

[2] Lambert-Perlade A. et al. (2004) *Metal. Mater. Trans. A* **35**, 1039–1053.

Microstructure of oxide dispersion strengthened Fe-Cr-based tubes

A. Ulbricht, F. Bergner

Oxide-dispersion strengthened (ODS) steels are promising materials for nuclear components, such as cladding tubes, exposed to extreme service conditions. The improved properties of ODS ferritic/martensitic steels are directly connected with a uniform distribution of nanoparticles. The circumferential distribution and anisotropy of such particles in extruded cladding tubes were investigated by small-angle neutron scattering (SANS).

The application of SANS for the purpose of the characterization of oxide nanoparticles in ~1 mm thick compact samples of ODS alloys is well established.^[1-3] The objectives of the present set of experiments were, first, to apply SANS to the case of thin-walled tube material in order to characterize the oxide particles, and second, to derive a non-destructive testing method for circumferential and axial uniformity of tube quality.

EXPERIMENTAL. The ODS alloys of this study were fabricated at CEA, France, by way of mechanical alloying of Fe-Cr and Y₂O₃ powders followed by hot extrusion.^[4] Pieces of 30 mm length from ODS martensitic Fe-9%Cr and ODS ferritic Fe-14%Cr tubes distributed among partners of the MatISSE project were investigated. The thickness ($t = 0.55$ mm) and its uniformity (variation within 1% of t) in circumferential direction were measured by means of the ultrasonic pulse-echo technique. Both pieces were cut into two segments of 180° for the purpose of SANS. These experiments were performed at the instrument D22 at ILL Grenoble. The major instrument parameters were: wavelength 0.6 nm, sample-detector distance 2 m and 11.2 m, aperture 10 × 1 mm, no external magnetic field, six measuring positions at 45°, 90° and 135° for both segments of both tubes. Absolute calibration was done by means of a direct beam measurement.^[5] For data reduction, the software package GRASP was used.^[6] The transformation from scattering curves into particle-size distributions was performed using an in-house Monte Carlo code.^[7]

RESULTS. The scattered intensities as displayed by the neutron detector are shown in Figs. 1(a) and (b) for ODS Fe-9%Cr and ODS Fe-14%Cr, respectively. While ODS Fe-9%Cr exhibits an isotropic azimuthal distribution of intensities, the distribution obtained for ODS Fe-14%Cr shows a pronounced anisotropy. This difference is applicable to all tested positions of the materials. Therefore, it reflects a characteristic difference of the microstructures of the two alloys. The measured and fitted total scattering cross sections and the reconstructed size distributions in terms of volume fraction of scatterers per size increment are shown in Figs. 2 and 3 for both tubes. Oxide particles of radius between 0.5 and

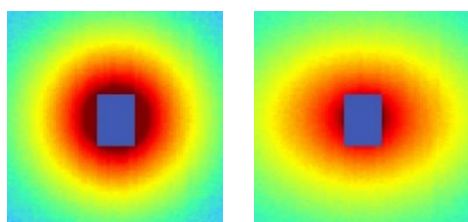


Figure 1. Measured scattering intensities in terms of detector counts for ODS Fe-9%Cr tube (left) and for ODS Fe-14%Cr tube. Horizontal and vertical directions of the figures correspond to circumferential and axial directions of the tube, respectively.

5 nm were observed for both materials. The mean size tends to be smaller for the 14Cr tube. As the scattering curves agree for each of the positions investigated, the size distributions also agree from position to position within measuring errors. The scattering of any probed volume of 9Cr tube was found to be perfectly isotropic. In contrast, a pronounced anisotropy of the scattered intensity between the circumferential and axial directions, the former being higher, was observed for the 14Cr tube. This anisotropy is assumed to be a consequence of the “background” scattering caused by extended features such as grain boundaries and may be due to heavily elongated grains and/or texture, in particular in combination with grain boundary segregation. This hypothesis was underpinned by means of electron-backscatter diffraction (EBSD) measurements.^[4] The findings and suggested interpretation about anisotropy are consistent with the known trend that ferritic microstructures such as for 14Cr tubes give rise to more pronounced textures than martensitic microstructures such as for 9Cr tubes. The link between microstructure and mechanical properties was worked out by the project partners and reported in a joint publication.^[4]

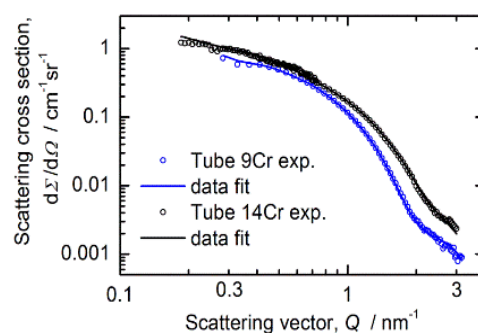


Figure 2. Measured and fitted total scattering cross sections of both tubes.

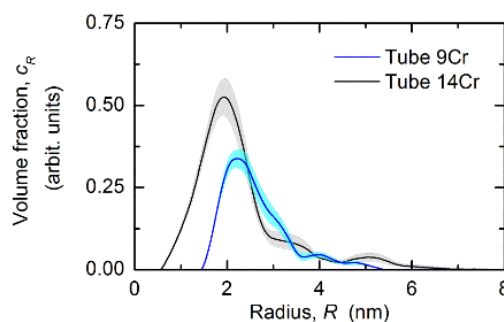


Figure 3. Size distribution of scatterers in terms of volume fraction per size increment.

ACKNOWLEDGEMENT. This work received funding from the European Commission within the FP7-Euratom-Fission project MatISSE, grant agreement No 604862.

[1] Mathon, M.-H. *et al.* (2012) *J. Nucl. Mater.* **428**, 147–153.
[2] Heintze, C. *et al.* (2011) *J. Nucl. Mater.* **416**, 35–39.
[3] Han, Y.-S. *et al.* (2014) *Appl. Phys. A*. **119**, 249–252.
[4] Sornin, D. *et al.* (2021) *Metall. Mater. Trans. A Phys. Metall. Mater. Sci.* **52**, 3541–3552.
[5] Lindner, P. (2002) in: *Neutron, X-Ray, Light Scatt. Methods Appl. Soft Condens. Matter*, p. 23–48, Elsevier, Amsterdam.
[6] Dewhurst, C. D. (2003) GRASP, ILL Grenoble.
[7] Wagner, A. *et al.* (2012) *Nucl. Instr. Meth. Phys. Res. B* **280**, 98–102.

Microstructure-informed prediction and measurement of nanoindentation hardness of an Fe-9Cr alloy irradiated with Fe-ions of 1 and 5 MeV energy

G. Kapoor, P. Chekhonin, C. Kaden, K. Vogel, F. Bergner

Hardening of Fe-9%Cr alloys exposed to irradiation with Fe²⁺ ions of two different energies, 1 and 5 MeV, is investigated using nanoindentation. Our study combines quantitative analysis of the ion-irradiated microstructures with the determination of the full depth dependence of irradiation hardening. The microstructure-informed model incorporates direct experimental evidence revealed by investigation using cross-sectional scanning transmission electron microscopy (STEM).^[1] For both ion energies, the observed microstructures consist of dislocation loops with band-like distributions and are concluded to be the dominant source of the measured irradiation-induced hardening. The model predictions are found to be in reasonable agreement with the as-measured nanoindentation response.

Fe-9%Cr model alloys are well suited for studying fundamental aspects of relevance for F/M steels (including the irradiation behavior) and for potential application in future generation fission and fusion devices.^[2,3] Ion irradiation may give rise to peculiar graded microstructures that essentially differ from microstructures observed under uniform irradiation, such as neutron irradiation.^[1,4] Here, the approach to predict the irradiation-induced nanohardness based on the as-measured depth-dependent microstructures is referred as microstructure-informed modeling or prediction. This model is based on (i) the dispersed barrier hardening (DBH) model linking the local hardness increase with the local number density N and size d of the irradiation-induced barriers (loops) and (ii) the assumption that the measured (target) hardening corresponds to the local hardening averaged over the indentation plastic zone.

EXPERIMENTAL. The binary Fe-Cr model alloy with 9.1 wt.-% Cr was irradiated with Fe²⁺ ions of two different energies, 1 and 5 MeV, at Ion Beam Center of HZDR. A FEI Talos F200X STEM operated at 200 kV was used to obtain the full depth dependence of the number density and size of irradiation-induced loops. Nanoindentation testing on irradiated samples was conducted using the UNAT device (ASMEC GmbH/Zwick Roell GmbH) equipped with a Berkovich indenter.

RESULTS. In this work, microstructure-informed modeling is applied to Fe-9Cr irradiated with Fe²⁺ ions of two different energies, 1 and 5 MeV, and compared with the as-measured hardening obtained by nanoindentation. Inspired by the band-like microstructure shown in Fig. 1, we divided the depth range of interest for nanoindentation into 4 and 6 layers for 1 and 5 MeV, respectively. These step-like profiles were used as input for the model.

Ion irradiation gives rise to a significant hardness increase for both ion energies with some characteristic differences (Fig. 2). The hardening is highest at small contact depths and decreases towards larger depths for the 1 MeV irradiation. In case of 5 MeV ions, the irradiation-induced hardness increase exhibits a peak. The peak position is reproduced best by assuming a half-sphere plastic zone of radius seven times larger than the contact depth. For both ion energies, the microstructure-informed prediction of the hardness increase agrees reasonably well with the as-measured hardness in-

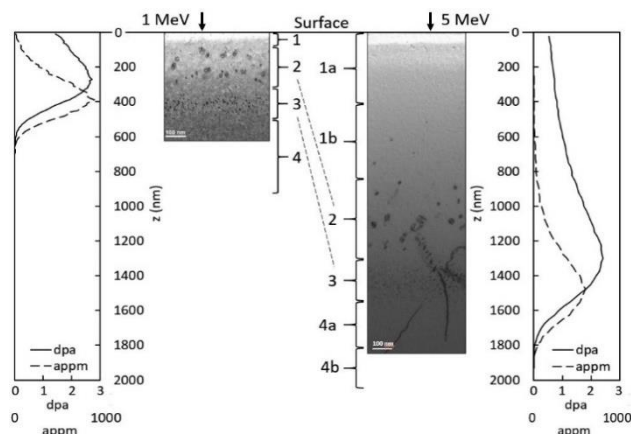


Figure 1. Comparison of Scheme to illustrate the relationships between damage profiles and irradiation-induced microstructures for 1 and 5 MeV.

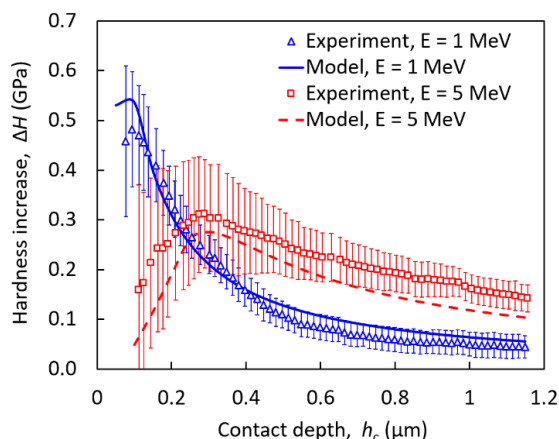


Figure 2. Comparison of predictions with size factor $c = 7$ and measured curves $\Delta H(h)$ for both ion energies.

crease, partly within experimental error. Only the results obtained for 5 MeV irradiation corresponding to the range of smallest contact depths of approximately 100 nm or below are transferable to the neutron case.

ACKNOWLEDGEMENTS. The work reported here received funding by the European Commission within the projects M4F (Grant Agreement No. 755039) and contributes to the Joint Programme on Nuclear Materials (JPNM) within the European Energy Research Alliance (EERA). The authors thank Dr. R. Hübner, W. Webersinke, M. Roßner, A. Kunz and the Ion Beam Center for their support.

- [1] Vogel, K. et al. (2021) *Nucl. Mater. Energy* **27**, 101007.
- [2] Klueh, R. L. et al. (2007) *J. Nucl. Mater.* **371**, 37–52.
- [3] Murty, K. L. et al. (2008) *J. Nucl. Mater.* **383**, 189–195.
- [4] Jin, H. H. et al. (2008) *Solid State Phenom.* **135**, 119–122.

Depth distribution of irradiation-induced dislocation loops in an ion-irradiated Fe-9Cr model alloy

K. Vogel, C. Kaden, P. Chekhonin, F. Bergner

Scanning transmission electron microscopy (STEM) was applied to characterize the distribution of irradiation-induced dislocation loops in an Fe-9Cr model alloy irradiated with 1 MeV and 5 MeV Fe²⁺ ions to address the effect of ion energy. Dislocation loops visible in the cross-sectional STEM images were found to be arranged within two bands with the depth position of these bands depending on the depth profiles of displacement damage and injected interstitials calculated by the binary collision code SRIM. The first and second band exhibit significantly different mean loop sizes and number densities. For the 5 MeV irradiation, an extended range between the sample surface and the first band was observed, where a decoration of pre-existing line dislocations with small loops is dominating. This microstructure resembles cases reported in several studies of neutron-irradiated Fe-Cr.

Fe-9Cr is a model alloy for studying irradiation effects that are relevant for a potential application of high-chromium ferritic/martensitic steels in nuclear energy devices. For investigation of the behavior of materials in nuclear environments, ion irradiations are often used because MeV ions can produce similar defects like neutrons with the advantage of shorter durations and lower costs of the irradiation experiments. One of the critical issues, however, is the limited penetration depth of the ions resulting in steep damage gradients and a depth dependent excess of interstitial atoms. Therefore, it is important to characterize the depth distribution of the structural defects introduced by the ion irradiation.

EXPERIMENTAL. Two samples of the Fe-9Cr model alloy were irradiated with Fe²⁺ ions, one sample with an ion energy of 1 MeV, and the second sample with an ion energy of 5 MeV. The irradiations were performed with the 3 MV tandemron accelerator of the Ion Beam Center at HZDR. The depth profiles of displacement damage and injected interstitials were calculated using the binary collision code SRIM-2013.00. Cross-sectional TEM samples were prepared by focused ion beam (FIB) lift-out technique. The microstructure was studied using a FEI Talos F200X scanning transmission electron microscope. Irradiation-induced dislocation loops were imaged under various diffraction conditions in bright-field and annular dark-field STEM mode. Bright-field images acquired with diffraction vector of type $g = \{110\}$ were used for counting loop numbers and for measuring the loop diameters. Details of STEM investigation and sample preparation can be found in literature.^[1]

RESULTS. For both ion energies, the loops visible in the cross-sectional STEM images are essentially arranged within two bands aligned parallel to the sample surface (Fig. 1). The first band contains relatively large dislocation loops, and the second band consists of a high number of very small loops (< 10 nm) that appear as black dots. In case of the 1 MeV irradiation (Fig. 1a), the first band starts close to the sample surface at a depth of approximately 0.1 μm and extends to a depth of approximately 0.3 μm , whereas the second band reaches from a depth of 0.3–0.45 μm . A comparison with the damage profiles calculated by SRIM revealed a strong correlation between the location of these bands and the depth po-

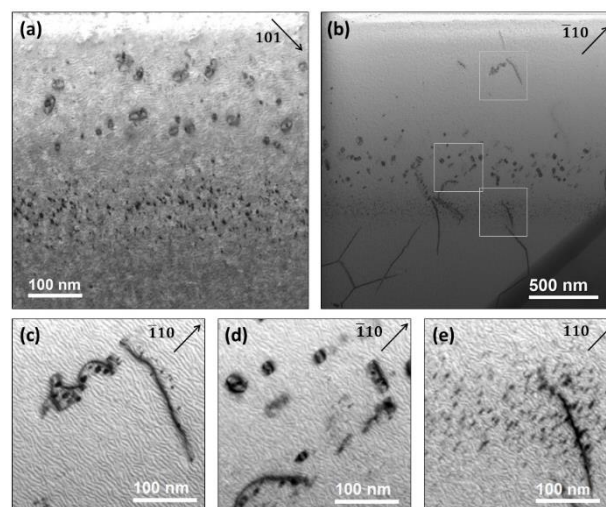


Figure 1. STEM images of ion-irradiated Fe-9Cr. Overview images of the samples irradiated with 1 MeV (a) and 5 MeV (b), higher magnified images of the rectangles in (b) (c–e).

sitions of the peaks of displacement damage and injected interstitials.^[1] In case of the 5 MeV irradiation (Fig. 1b), the first band starts at a depth of approximately 0.8 μm and extends to a depth of 1.3 μm , whereas the second band reaches from 1.3 to 1.5 μm . In the depth range between the sample surface and the first band, only a low number of loops is visible and almost all of these are located close to pre-existing line dislocations (Fig. 1c). This decoration of pre-existing dislocations with small dislocation loops resembles the arrangements of loops reported by Hernandez-Mayoral *et al.* and Dubinko *et al.* for neutron-irradiated Fe-Cr.^[2,3] Our result indicates a way how ion irradiations can be used in order to explore neutron-irradiation damage.

ACKNOWLEDGEMENTS. This work received funding from the European Commission within the project M4F (Euratom research and training programme 2014-2018 under grant agreement No 755039). The irradiations were carried out at the Ion Beam Center (IBC) at HZDR by Dr. S. Akhmadaliev. The use of the IBC TEM facilities and support by its staff is gratefully acknowledged. In particular, we thank Dr. R. Hübner for support during the STEM investigations and A. Kunz for the TEM sample preparation, and we want to thank M. Roßner for surface preparation.

- [1] Vogel, K. *et al.* (2021) *Nucl. Mater. Energy* **27**, 101007.
- [2] Hernandez-Mayoral, M. *et al.* (2016) *J. Nucl. Mater.* **472**, 88.
- [3] Dubinko, A. *et al.* (2020) *J. Nucl. Mater.* **540**, 152395.

Radiochemical analysis of ^{14}C and ^{60}Co in the activated RPV steel samples of Greifswald Nuclear Power Plant

G. Yassin, A. Barkleit

The concentrations of ^{60}Co and ^{14}C in the VVER steel shielding material of the Greifswald nuclear power plant were determined along the thickness of the reactor pressure vessel wall. The steel samples of the reactor pressure vessel were selected at different axial positions from the reactor core and at azimuthal locations of high neutron fluencies distribution.

During the decommissioning phase of nuclear power plants (NPPs), a comprehensive strategy including environmental assessment as well as radiological protection needs to be followed. We focus on the reactor pressure vessel (RPV) of the NPP, since it is considered as the main shielding barrier of the radioactive fuel to the environment.^[1] The aim of our work is the characterization of the activated products, radionuclides (RNs), and the determination of their activity distribution along the thickness of the RPV material. In this context, we report results that include the determination of gamma emitting ^{60}Co , and the long-lived beta emitting ^{14}C , both constitute an important concern in the safety assessment of deep geological repositories. ^{60}Co is important source of γ -irradiation, and ^{14}C may be released with different speciation under repository relevant conditions. In this study, their activity distribution along the RPV material was determined.

EXPERIMENTAL. Greifswald nuclear power plant represents the first generation of VVER-440/V230 Russian reactor type. The VVER steel samples had been irradiated with thermal neutron dose that were designed for operation of 30 effective full power years.^[2] The operation of the GW NPP was terminated in 1990 and shut down after 15-year operation period. Trepanns were sampled from the first decommissioned units at different sites from the reactor core. In this framework, we report the results of the activity of RPV Unit 1, at a selected axial position from the reactor core, which is followed by partitioning into four samples horizontally starting from the closest distance and going outward along the RPV thickness (Tab. 1).

Table 1. Sampling positions from the reactor core of RPV Unit 1.

Axial(mm)	Azimuthal(°)	Horizontal (mm)
3000	30, 60	7.5, 39, 71, 102.5

Our analysis is based on a multistep procedure that includes both nondestructive methods in determining gamma emitting RNs and destructive methods in determining the long lived difficult to measure RNs. Hence, ^{60}Co (gamma emitter) was determined using high purity Germanium detector (gamma-X HPGc). On the other hand, the long lived ^{14}C , beta emitter; $t_{1/2} = 5,740$ years), was determined by a destructive full combustion method using commercial oxidizer (Hidex 600 ox), and then followed by LSC measurements (Hidex 600 SL).

RESULTS. ^{60}Co concentrations in the VVER steel shielding material varied in the range from 736–223 Bq g⁻¹, showing a relevant decrease in its activity from the inner towards the outer position of the RPV wall, as shown in Fig. 1. Similarly, the ^{14}C concentrations within the RPV thickness wall were

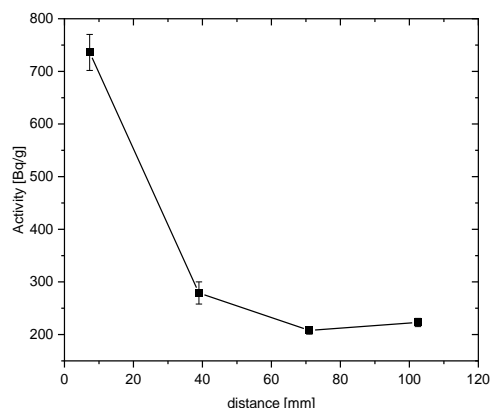


Figure 1. ^{60}Co activity along the VVER steel shielding material of the decommissioned RPV Unit 1 of GW NPP.

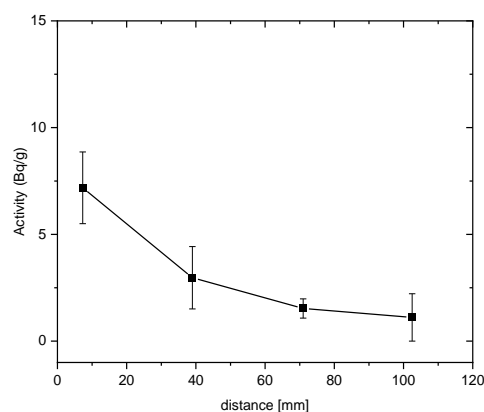


Figure 2. ^{14}C results along the VVER steel shielding material of the decommissioned RPV Unit 1 of GW NPP.

determined in the range from 7.18–1.11 Bq g⁻¹ as presented in Fig. 2; they confirm a high concentration in the region closest to the reactor core, which depletes toward the outward surface. Such detailed analysis may provide a holistic overview of the activity distribution of important RNs along the RPV, which may assist the decommissioning strategies of the RPVs in the future and implementing comprehensive decisions in their storage and final repositories.

ACKNOWLEDGEMENTS. This project is funded by the German Federal Ministry of Education and Research (BMBF) under the contract number 15S9412. The authors thank J. Konheiser for valuable discussions and collaboration.

[1] Yassin, G. et al. (2021) Report HZDR-113, p. 77.

[2] Viehriig, H.-W. et al. (2018) Report HZDR-088.

Greifswald NPP ex-vessel dosimetry revisited

E. Poenitz, J. Konheiser

For comparison with a measurement carried out at unit 1 of the Greifswald NPP in the late 1980s, reaction rates of activation detectors were calculated using the radiation transport codes MCNP and TRAMO. An explanation for the earlier observed good agreement in the center of the fission zone and deviations for the other measurement positions was found. It allows using the comprehensive data set to validate the newly developed geometry model of the NPP.

In the scope of the research project WERREBA, a detailed and extended geometry model of units 1–4 of the Greifswald NPP (VVER-440/230) was developed for the radiation transport code MCNP. To check and validate the model, experimental results were available as well as results obtained with the in-house code TRAMO. For this purpose, an ex-vessel activation detector measurement was chosen that was carried out during the 12th cycle of unit 1 of the Greifswald NPP.^[1] This comprehensive data set covers 393 data points (10 equidistant height positions from $h = -0.1$ cm to 250.1 cm with respect to the lower edge of the fission zone, five angles that cover one 60° sector, eight activation reactions sensitive to different regions of the neutron spectra). Radiation transport calculations with a version of TRAMO were already carried out earlier by Barz *et al.*^[2] Here, a good agreement between calculation and measurement was observed in the center of the fission zone but deviations at the other height positions were found. However, no data are given in this publication. It is therefore unknown whether calculations were indeed carried out for all ten heights.

RESULTS. As an example, the $^{54}\text{Fe}(n,p)^{54}\text{Mn}$ reaction rates R for an angle of 53.6° determined by measurement as well as by MCNP and new TRAMO calculations are shown in Fig. 1. A geometry model that covers the region of the fission zone was used for the TRAMO calculations. For this reason, the first and last height positions which are too close to the limits of the model were excluded. For the MCNP calculations, a geometry model that covers the complete reactor pressure vessel, reactor internals as well as the annular water tank was used and therefore allows calculating the reaction rates for all positions. An excellent agreement for the center of the fission zone (height positions 5 and 6, $h = 138.9$ cm and 111.1 cm, respectively) can be confirmed. For the other height positions, the deviation increases with increasing distance to the fission zone center showing a ratio of the calculated and experimental reaction rates $C/E < 1$ for the upper positions and $C/E > 1$ for the lower ones. To investigate the deviations, more calculations with modified input parameters were carried out including an assumed 11th height position also shown in Fig. 1. The best explanation is a misplacement of the activation detectors by approximately one monitor position. With the assumption of a height shift of the detector positions, a very good agreement was achieved for the majority of the data points. The C/E ratio for the $^{54}\text{Fe}(n,p)^{54}\text{Mn}$ reaction is shown in Fig. 2 for all five angles.

CONCLUSION AND OUTLOOK. While the reason will remain unknown, the assumption of a considerable misplacement of the activation detectors is strengthened by a comparison of unfolded neutron spectra by Mehner *et al.* with a power density profile measured by Dach *et al.*^[1,3] The assumed height shift provides an explanation for a discrepancy

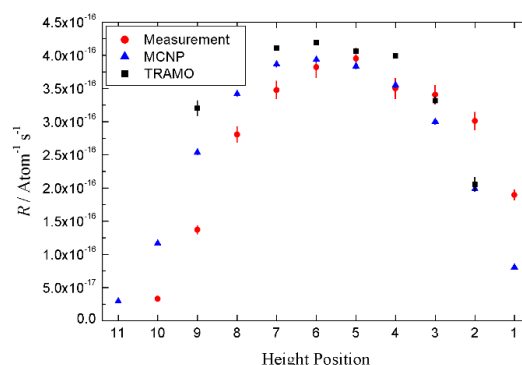


Figure 1. Experimental and calculated $^{54}\text{Fe}(n,p)^{54}\text{Mn}$ reaction rates for the angle 53.6°. Measurement and calculations appear to be shifted by approx. one height position.

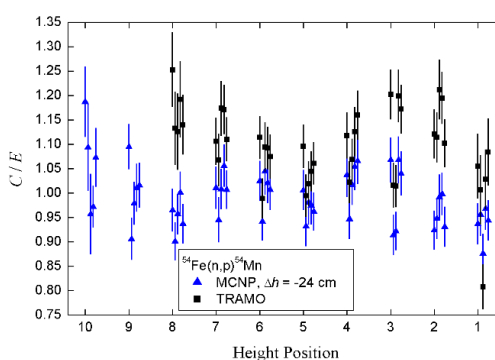


Figure 2. Ratio of the calculated and experimental $^{54}\text{Fe}(n,p)^{54}\text{Mn}$ reaction rates. A vertical shift of approx. one height position is applied. For better visibility, the data points for different angles have small offsets.

any observed 30 years ago. The comprehensive data set still provides an excellent opportunity to test the radiation transport simulations. Beside threshold reactions commonly used in reactor dosimetry, data for three (n,γ) reactions sensitive to thermal and epithermal neutrons are available. These data are especially valuable as the radionuclides produced by neutron activation relevant for decommissioning and final disposal are primarily produced by neutrons in these energy regions. Calculations of reaction rates for a second activation foil measurement including height positions outside the fission zone are currently carried out and will allow us to further validate the geometry model.^[4]

ACKNOWLEDGEMENTS. This work is supported within the research framework FORKA, German Federal Ministry of Research and Education (WERREBA project: Grant Number 15S9412).

- [1] Mehner, H.-C. *et al.* (1988) *Report ZfK-RPM 6/88*.
- [2] Barz, H.-U. *et al.* (1992) *Nucl. Eng. Des.* **137**, 71–75.
- [3] Dach, K. *et al.* (1980) *Kernenergie* **23**, 260–262.
- [4] Mehner, H.-C. *et al.* (1987) *Report ZfK-623*.

Neutron irradiated concrete: Material characterization and gamma dosimetry

Q. I. Roode-Gutzmer, A. Barkleit, J. Konheiser

The radionuclides that contribute to the highest dose rate in biological shielding concrete in the intermediate term after nuclear power plant shut down decay by gamma emission and include ^{60}Co , ^{152}Eu , ^{154}Eu and ^{133}Ba . Their appreciable activity and associated half-lives pose a problem not only during safe dismantling, but also in terms of processing the material to reduce the active waste volume for final disposal in a repository. Quartz amounts to around 50–60 wt.-% of concrete and accumulates defects into its structure proportional to the neutron fluence it has been subjected to. Few studies investigate intermediate neutron fluence prior to full amorphization of quartz. The ultimate objective of this work is to examine the increased reactivity of radiation-damaged quartz in the alkaline pore water of concrete, particularly in terms of the alkali silica reaction and its role in radionuclide transport.

EXPERIMENTAL. Inactive concrete powder was placed in a chamber passing through the first reactor shielding of an operating Konvoi nuclear power plant for 249 days. The neutron fluence at the sample position is estimated using Monte Carlo neutron transport calculations from a previous fuel cycle to be $\sim 4 \times 10^8 \text{ n/cm}^2$.^[1] The activated sample was analyzed by gamma spectroscopy using a coaxial high purity germanium (HPGe) detector (GMX, 30 % efficiency, Fa. Ortec-Ametek). A quadrupole Perkin Elmer NexION 350X Inductively Coupled Plasma Mass Spectroscopy (ICP-MS) was used to acquire elemental concentrations. Solid state ^{29}Si - and ^{27}Al -Magic-Angle-Spinning Nuclear Magnetic Spectroscopy was conducted using a Bruker Advance 300 MHz. X-ray diffraction (XRD) data was collected with a Rigaku Mini-Flex 600 diffractometer ($\text{CuK}_{\alpha 1} = 1.540562 \text{ \AA}$) using Si as internal standard.

RESULTS. Measured gamma activities are shown in Tab. 1. The NMR and XRD results (illustrated in Fig. 1) cannot be interpreted quantitatively. Phase compositional heterogeneity partly due to the non-trivial weight fraction of particles $> 125 \mu\text{m}$ is expected. The (100) peak for quartz is corrected for specimen displacement error, which is calculated from the shift in the Si(111) peak, where $d_{111} = 3.135 \text{ \AA}$. The hexagonal unit cell dimension in the basal plane is determined for the reference and irradiated quartz to be $a = 4.909 \text{ \AA}$ and 4.911 \AA , respectively. Our results can only be reported to the fourth significant figure and compares well with dimensions reported in the literature.^[4] To determine statistically significant unit-cell expansion as a function of neutron fluence, future measurements will be conducted with Synchrotron XRD. Further work will include defect characterization by Cathodoluminescence (CL) and Electron Paramagnetic Resonance (EPR) Spectroscopy in conjunction with Monte Carlo

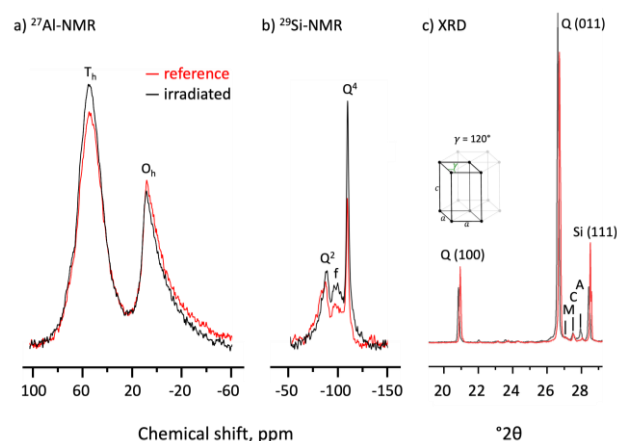


Figure 1. NMR-spectra of the reference and the neutron-irradiated concrete for ^{27}Al , illustrating the tetrahedral (T_h) and octahedral (O_h) binding sites for feldspars (a), ^{29}Si , showing the single Q^4 peak expected for quartz at 108 ppm (b). The fine structure between -92 and -102 ppm confirms the chemical shifts for T_2m , T_2O , and T_1O for both microcline and albite (f)^[2] with Q^2 associated with calcium silicate hydrate (C-S-H) phases at 85 ppm with an up-field shoulder for $Q^2(1Al)$.^[3] XRD patterns for the reference and neutron irradiated concrete showing the main peak for the silicon internal standard, (011) and (100) reflections for quartz, the (002) peaks for albite (A) and microcline (M), and the (104) peak for calcite (C) (c).

neutron transport calculations to obtain accurate neutron fluences.

ACKNOWLEDGEMENTS. This work is funded by the FORKA initiative of the German Federal Ministry of Research and Education (WERREBA project: Grant Number 15S9412). We are grateful to S. Beutner, S. Paasch and S. Shams Aldin Azzam for ICP-MS, NMR and XRD measurements, respectively.

- [1] Rachamin, R. *et al.* (2020) *Report HZDR-113*, p. 78
- [2] Smith, J. V. *et al.* (1984) *Nature* **309**, 140–142.
- [3] Walkley, B. *et al.* (2019) *Mat. Today Adv.* **1**, 1000007.
- [4] Ghiorso, M. S. *et al.* (1979) *Contrib. Mineral. Petrol.* **68**, 307–323.

Table 1. Measured gamma activities of irradiated concrete sample.

Nuclear reaction	Mother isotope abundance (%)	Thermal neutron cross section (barns)	Neutron-activated nuclide half-life (a)	Concentration mother nuclide (ppm)	Measured activity after $\sim 4 \times 10^8 \text{ n/cm}^2$ (Bq g^{-1})
$^{59}\text{Co} (n, \gamma) ^{60}\text{Co}$	100	37.8	5.27	4.75 ± 0.035	13.32 ± 0.360
$^{151}\text{Eu} (n, \gamma) ^{152}\text{Eu}$	47.8	9230	13.5	0.59 ± 0.005	9.11 ± 0.141
$^{153}\text{Eu} (n, \gamma) ^{154}\text{Eu}$	52.2	312	8.59	0.59 ± 0.005	2.10 ± 0.063
$^{132}\text{Ba} (n, \gamma) ^{133}\text{Ba}$	0.10	8.2	10.5	270.00 ± 1.000	0.33 ± 0.021

Examining zeta potential in the alkaline dissolution of quartz

Q. I. Roode-Gutzmer, R. Lessing

Quartz contributes more than half the weight of most concretes and is also the mineral most susceptible to radiation-induced metamictization.^[1] The first 20–30 cm of end-of-life biological shielding concrete from nuclear power reactors contains radionuclides and radiation-damaged silicate minerals. The objective of this work is to examine the reactivity of irradiated quartz in alkaline aqueous media, particularly in terms of the alkali silica reaction in concrete and its role in radionuclide transport. Despite vast amounts of literature on the dissolution of quartz and amorphous silica, studies relating the surface charge to the dissolution kinetics are lacking. We report preliminary results on the change in zeta potential observed for non-irradiated quartz during alkaline dissolution. This serves as a reference from which future results on alkaline dissolution of irradiated quartz can be compared to.

EXPERIMENTAL. Sample preparation is described elsewhere.^[2] A quadrupole Perkin Elmer NexION 350X Inductively Coupled Plasma Mass Spectrometry (ICP-MS) was used to acquire elemental concentrations. Unbuffered batch dissolution studies were done using 50 mg quartz sample (see Tab. 1) suspended in 50 mL solutions with pH 10, 11, 12 and 13 (using NaOH) and 0.1 M NaCl in polypropylene Falcon™ tubes, which were gently shaken for various lengths of times at 25 °C. Zeta potential was measured for samples in a polystyrol DTS1070 cuvette in a MALVERN Zetasizer Nano-ZS. The pH meter, WTW inoLab pH7110 with an Si Analytix BlueLine 16pH electrode, was regularly calibrated. Values for pH were measured each time prior to zeta potential measurements.

Table 1. Sample properties of the quartz used in the experiments.

	Quartz Merck (Q)	Ottendorf Kies (OK)
Purity* (% SiO ₂)	93.9	90.7
Al/Si molar ratio	0.53 × 10 ⁻³	0.93 × 10 ⁻³
Predominant particle-size fraction	20–32 μm 89 wt.-%	1–2 nm 95 wt.-%
Surface area N ₂ /BET, m ² g ⁻¹	0.35	4.82

*: all solutions contained < 10 μg L⁻¹ Fe.

RESULTS. The zeta potential for quartz changes very rapidly within the first 24 hours (Fig. 1). The increase in zeta potential in our case can be ascribed to the disturbed layer on the surface of the quartz, as well as the presence of more fines due to grinding, which leads to particle aggregation in solution. Crundwell derives a rate equation for quartz from first principles based on a surface-charge-driven dissolution mechanism.^[3] From this derivation it is possible to calculate the zeta potential for quartz under various dissolution conditions, which yields a constant value for pH > 8. Our results, however, show an increase in zeta potential as a function of pH for both quartz samples (Fig. 2). We observe an increase in the Al/Si molar ratio (10⁻³) in solution as a function of pH. Surface coverage of quartz with Al and Fe oxides and hydroxides is known to increase the zeta potential in a linearly additive manner.^[4,5] In this case, Al is present in trace concentrations with respect to Si. Therefore, we propose that Al scavenges OH⁻ ions within the Stern layer in the

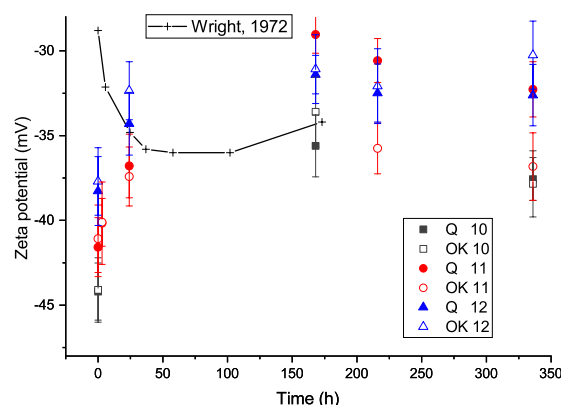


Figure 1. Zeta potential of Merck quartz (Q, filled symbols) and Ottendorf quartz (OK, unfilled symbols) as a function of time for pH 10, 11 and 12 at 25 °C (in 0.1 M NaCl). The zeta potential increases rapidly in the first 24 hours and then levels off. Data from Wright shows an opposite initial trend and this can be ascribed to the fact that their quartz was pre-treated with HF and NaOH, whereas our quartz underwent no pre-treatment after grinding.^[6]

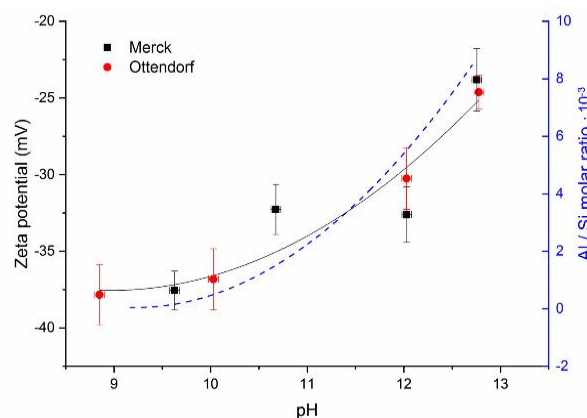


Figure 2. Zeta potential of Merck quartz (black squares) and Ottendorf quartz (red circles) as a function of pH after 14 days. The regression curve of both data sets is shown as a solid black line. The Al/Si molar ratio (10⁻³) in solution for Ottendorf quartz at seven days is shown as a dashed blue line. All experiments were conducted at 25 °C using a background electrolyte of 0.1 M NaCl.

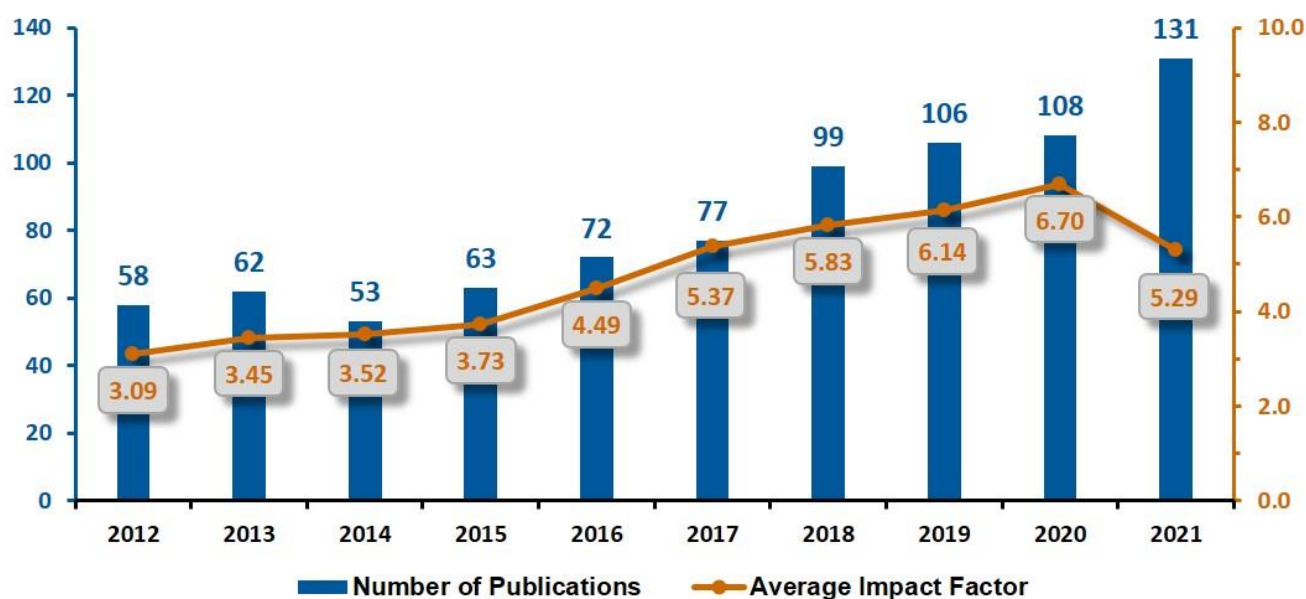
alkaline pH range, thereby catalytically enabling proton-mediated dissolution at the surface, which increases the zeta potential. This pH-dependent effect may disappear when a condition of steady state has been achieved.

ACKNOWLEDGEMENTS. This work is supported within the BMBF funding framework of FORKA (WERREBA project, 15S9412). We are grateful to S. Beutner, P. Fiala and H. Uhlig for ICP-MS, particle-size and N₂/BET analysis respectively.

[1] Douillard, L. *et al.* (1996) *Nucl. Instrum. Methods. Phys. Res. B* **107**, 212–217.
 [2] Lessing, R. L. (2021) Bachelor Thesis, TU Dresden, Germany.
 [3] Crundwell, F. (2017) *ACS Omega* **2**, 1116–1127.
 [4] Li, Z.-Y. *et al.* (2015) *Colloids Surf. A Physicochem. Eng. Asp.* **478**, 22–29.
 [5] Johnson, P. R. (1999) *J. Colloid Interface Sci.* **209**, 264–267.
 [6] Wright, H. J. L. (1972) Ph.D. Thesis, University of Sydney, Australia.

- ARTICLES (PEER-REVIEWED)
- FURTHER CONTRIBUTIONS
- EDITORIAL WORK
- ORAL PRESENTATIONS
- THESES

ARTICLES (PEER-REVIEWED)



Statistics on the publication activity of the Institute of Resource Ecology (IRE) within the last 10 years. The diagram considers peer-reviewed articles that were published under primary responsibility of the institute. Note that the given impact factors are based on data from 2020. The annual update might change the statistics retrospectively.

The following compilation provides peer-reviewed articles and further publications published in 2021 (online first) representing any contribution of members of the Institute of Resource Ecology.

Agrawal, P.; Till, B.; Raoof, A.; Iliev, O.; Fischer, C.; Wolthers, M.

The contribution of hydrodynamic processes to calcite dissolution rates and rate spectra

Geochimica et Cosmochimica Acta 307, 338–350 (2021).
DOI: 10.1016/j.gca.2021.05.003.

Altstadt, E.; Bergner, F.; Houska, M.

Use of the small punch test for the estimation of ductile-to-brittle transition temperature shift of irradiated steels

Nuclear Materials and Energy 26, 100918 (2021).
DOI: 10.1016/j.nme.2021.100918.

Amidani, L.; Retegan, M.; Volkova, A.; Popa, K.; Martin, P. M.; Kvashnina, K. O.

Probing the local coordination of hexavalent uranium and the splitting of 5f orbitals induced by chemical bonding.

Analytical Chemistry 60, 16286–16293 (2021).
DOI: 10.1021/acs.inorgchem.1c02107.

Amidani, L.; Vaughan, G. B. M.; Plakhova, T. V.; Romanchuk, A. Y.; Gerber, E.; Svetogorov, R.; Weiß, S.; Joly, Y.; Kalmykov, S. N.; Kvashnina, K. O.

The application of HEXS and HERFD XANES for accurate structural characterization of actinide nanomaterials: application to ThO₂.

Chemistry - A European Journal 27, 252–263 (2021).
DOI: 10.1002/chem.202003360.

Baker, U.; Margulis, M.; Shwageraus, E.; Fridman, E.;

Jiménez-Carrascosa, A.; García-Herranz, N.; Cabellos, O.; Gregg, R.; Krepel, J.

Evaluation of the ESFR End of Equilibrium Cycle State: Spatial Distributions of Reactivity Coefficients

Journal of Nuclear Engineering and Radiation Science 8, 011316 (2021).
DOI: 10.1115/1.4052121.

Bes, R.; Leinders, G.; Kvashnina, K.

Application of multi-edge HERFD-XAS to assess the uranium valence electronic structure in potassium uranate (K₂UO₇)

Journal of Synchrotron Radiation 29, 21–29 (2021).
DOI: 10.1107/S1600577521012431.

Bhat, V. J.; Vegesna, S. V.; Kiani, M.; Zhao, X.; Blaschke, D.; Du, N.; Vogel, M.; Kluge, S.; Raff, J.; Hubner, U.; Skorupa, I.; Rebohle, L.; Schmidt, H.

Detecting bacterial cell viability in few µl solutions from impedance measurements on silicon - based biochips

International Journal of Molecular Sciences 22, 3541 (2021).
DOI: 10.3390/ijms22073541.

Boelens, P.; Lei, Z.; Drobot, B.; Rudolph, M.; Li, Z.; Franzreb, M.; Eckert, K.; Lederer, F.

High-Gradient Magnetic Separation of Compact Fluorescent Lamp Phosphors: Elucidation of the Removal Dynamics in a Rotary Permanent Magnet Separator

Minerals 11, 1116 (2021).
DOI: 10.3390/min11101116.

- Börsig, N.; Scheinost, A. C.; Schild, D.; Neumann, T.
Mechanisms of selenium removal by partially oxidized magnetite nanoparticles for waste water remediation
Applied Geochemistry 132, 105062 (2021).
 DOI: 10.1016/j.apgeochem.2021.105062.
- de Bona, E.; Balice, L.; Cognini, L.; Holzhaeuser, M.; Popa, K.; Walter, O.; Cologna, M.; Prieur, D.; Wiss, T.; Baldinozzi, G.
Single-step, High Pressure, and Two-Step Spark Plasma Sintering of UO_2 nanopowders
Journal of the European Ceramic Society 41, 3655–3663 (2021).
 DOI: 10.1016/j.jeurceramsoc.2021.01.020.
- Buchholz, S.; Bonfigli, G.; Schäfer, F.; Kaczmarkiewicz, N.; Schuster, C.; Sporn, M.
Safety Cases for Design-Basis Accidents in LWRs Featuring Passive Systems Part 2 - Numerical Investigations
Nuclear Engineering and Design 372, 110996 (2021).
 DOI: 10.1016/j.nucengdes.2020.110996.
- Burger, A.; Weidinger, M.; Baumann, N.; Vesely, A.; Lichtscheidl, I.
The response of the accumulator plants *Nocca caerulea*, *Nocca goesingense* and *Plantago major* towards the uranium
Journal of Environmental Radioactivity 229–230, 106544 (2021).
 DOI: 10.1016/j.jenvrad.2021.106544.
- Cametti, G.; Scheinost, A. C.; Churakov, S. V.
 Cd^{2+} incorporation in small pores LEV/ERI intergrown zeolites: a multi-methodological study
Microporous and Mesoporous Materials 313, 110835 (2021).
 DOI: 10.1016/j.micromeso.2020.110835.
- Carocci, E.; Truche, L.; Cathelineau, M.; Bazarkina, E.
Tungsten (VI) speciation in hydrothermal solutions up to 400 °C as revealed by in-situ Raman spectroscopy
Geochimica et Cosmochimica Acta 317, 306–324, (2021).
 DOI: 10.1016/j.gca.2021.11.004.
- Davies, S.; Litskevich, D.; Rohde, U.; Detkina, A.; Merk, B.; Bryce, P.; Levers, A.; Ravindra, V.
DYN3D and CTF Coupling within a Multiscale and Multiphysics Software Development (Part I)
Energies 14, 5060 (2021).
 DOI: 10.3390/en14165060.
- Davies, S.; Rohde, U.; Litskevich, D.; Merk, B.; Bryce, P.; Levers, A.; Detkina, A.; Atkinson, S.; Ravindra, V.
CTF and FLOCAL Thermal Hydraulics Validations and Verifications within a Multiscale and Multiphysics Software Development
Energies 14, 1220 (2021).
 DOI: 10.3390/en14051220.
- Deev, D.; Rybkin, I.; Rijavec, T.; Lapanje, A.
When Beneficial Biofilm on Materials Is Needed: Electrostatic Attachment of Living Bacterial Cells Induces Biofilm Formation
Frontiers in Materials 8, 624631 (2021).
 DOI: 10.3389/fmats.2021.624631.
- Demnitz, M.; Molodtsov, K.; Schymura, S.; Schierz, A.; Müller, K.; Jankovsky, F.; Havlova, V.; Stumpf, T.; Schmidt, M.
Effects of surface roughness and mineralogy on the sorption of Cm(III) on crystalline rock
Journal of Hazardous Materials 423, 127006 (2022).
 DOI: 10.1016/j.jhazmat.2021.127006.
- Di Nora, V. A.; Fridman, E.; Nikitin, E.; Bilodid, Y.; Mikityuk, K.
Optimization of multi-group energy structures for diffusion analyses of sodium-cooled fast reactors assisted by simulated annealing – Part I: methodology demonstration
Annals of Nuclear Energy 155, 108183 (2021).
 DOI: 10.1016/j.anucene.2021.108183.
- Di Nora, V. A.; Fridman, E.; Nikitin, E.; Bilodid, Y.; Mikityuk, K.
Optimization of multi-group energy structures for diffusion analyses of sodium-cooled fast reactors assisted by simulated annealing – Part II: methodology application
Annals of Nuclear Energy 163, 108541 (2021).
 DOI: 10.1016/j.anucene.2021.108541.
- Diaz Pescador, E.; Schäfer, F.; Kliem, S.
Modelling of multidimensional effects in thermal-hydraulic system codes under asymmetric flow conditions – Simulation of ROCOM Tests 1.1 and 2.1 with ATHLET 3D-Module
Nuclear Engineering and Technology 53, 3182–3195 (2021).
 DOI: 10.1016/j.net.2021.04.015.
- Dixit, R.; Gupta, A.; Jordan, N.; Zhou, S.; Schild, D.; Weiß, S.; Guillon, E.; Jain, R.; Lens, P.
Magnetic properties of biogenic selenium nanomaterials
Environmental Science and Pollution Research (2021).
 DOI: 10.1007/s11356-020-11683-2.
- Dixon Wilkins, M. C.; Mottram, L. M.; Maddrell, E. R.; Stennett, M. C.; Corkhill, C. L.; Kvashnina, K. O.; Hyatt, N. C.
Synthesis, characterisation, and crystal structure of a novel U(V) brannerite $\text{UTi}_{1.23}\text{Al}_{0.77}\text{O}_6$ and the $\text{UTi}_{2-x}\text{Al}_x\text{O}_6$ system
Inorganic Chemistry 60, 18112–18121 (2021).
 DOI: 10.1021/acs.inorgchem.1c02733.
- Estevenon, P.; Dumas, T.; Solari, P. L.; Welcomme, E.; Szenknect, S.; Mesbah, A.; Kvashnina, K. O.; Moisy, P.; Poinssot, C.; Dacheux, N.
Formation of plutonium (IV) silicate species in very alkaline reactive media
Dalton Transactions 50, 12528–12536 (2021).
 DOI: 10.1039/D1DT02248B.

- Feig, M.; Akselrud, L.; Motylenko, M.; Bobnar, M.; Wagler, J.; Kvashnina, K. O.; Rafaja, D.; Leithe-Jasper, A.; Gumeniuk, R.
Valence fluctuations in the 3D+3 modulated Yb₃Co₄Ge₁₃ Remeika Phase
Dalton Transactions 50, 13580 (2021).
DOI: 10.1039/D1DT01972D.
- Fichter, S.; Radoske, T.; Ikeda, A.
Structure of the U₁₃ poly-oxo cluster, U₁₃O₈Cl_x(MeO)_{38-x} (x = 2.3, MeO: methoxide)
Acta Crystallographica Section E 77, 847–852 (2021).
DOI: 10.1107/S2056989021007623.
- Filimonova, O. N.; Trigub, A. L.; Nickolsky, M. S.; Chareev, D. A.; Kvashnina, K. O.; Kovalchuk, E. V.; Vikentyev, I. V.; Reukov, V. L.; Tagirov, B.
The state of platinum in pyrrhotite determined by X-ray absorption spectroscopy
Mineralogical Magazine (2021).
DOI: 10.1180/mgm.2021.76.
- Fischer, S.; Jain, R.; Krause, T.; Jain, P.; Tsushima, S.; Shevchenko, A.; Hübner, R.; Jordan, N.
Impact of the microbial origin and active microenvironment on the shape of biogenic elemental selenium nanomaterials
Environmental Science & Technology 55, 9161–9171 (2021).
DOI: 10.1021/acs.est.0c07217.
- Filipo, S.; Rosner, H.; Bobnar, M.; Kvashnina, K. O.; Leithe-Jasper, A.; Gumeniuk, R.
Thermoelectricity and electronic properties of Y_{1-x}Ce_xCrB₄
Physical Review B 103, 195121 (2021).
DOI: 10.1103/PhysRevB.103.195121.
- Fridman, E.; Álvarez-Velarde, F.; Romojaro-Otero, P.; Tsige-Tamirat, H.; Jiménez-Carrascosa, A.; García-Herranz, N.; Bernard, F.; Gregg, R.; Krepel, J.; Massara, S.; Pomerouly, S.; Girardi, E.; Mikityuk, K.
Neutronic analysis of the European Sodium Fast Reactor: Part I - fresh core results
Journal of Nuclear Engineering and Radiation Science 8, 011301 (2022).
DOI: 10.1115/1.4048905.
- Fridman, E.; Álvarez-Velarde, F.; Romojaro-Otero, P.; Tsige-Tamirat, H.; Jiménez-Carrascosa, A.; García-Herranz, N.; Bernard, F.; Gregg, R.; Krepel, J.; Massara, S.; Pomerouly, S.; Girardi, E.; Mikityuk, K.
Neutronic analysis of the European Sodium Fast Reactor: Part II - burnup results
Journal of Nuclear Engineering and Radiation Science 8, 011302 (2022).
DOI: 10.1115/1.4048765.
- García, M.; Bilodid, Y.; Basualdo Perello, J.; Tuominen, R.; Gommlich, A.; Leppanen, J.; Valtavirta, V.; Imke, U.; Ferraro, D.; van Uffelen, P.; Seidl, M.; Sanchez-Espinoza, V.
Validation of Serpent-SCF-TU full-core pin-by-pin burnup calculations using Pre-Konvoi PWR experimental data
Nuclear Engineering and Design 379, 111173 (2021).
DOI: 10.1016/j.nucengdes.2021.111173.
- García, M.; Vocka, R.; Tuominen, R.; Gommlich, A.; Leppanen, J.; Valtavirta, V.; Imke, U.; Ferraro, D.; Uffelen, P. v.; Milisdorfer, L.; Sanchez-Espinoza, V.
Validation of Serpent-SUBCHANFLOW-TRANSURANUS pin-by-pin burnup calculations using experimental data from the Temelín II VVER-1000 reactor
Nuclear Engineering and Technology 53, 3133–3150 (2021).
DOI: 10.1016/j.net.2021.04.023.
- Gerber, E.; Romanchuk, A. Y.; Weiss, S.; Bauters, S.; Schacherl, B.; Vitova, T.; Hübner, R.; Azzam, S. S. A.; Detollenaere, D.; Banerjee, D.; Butorin, S. M.; Kalmykov, S. N.; Kvashnina, K. O.
Insight into the structure-property relationship of UO₂ nanoparticles
Inorganic Chemistry Frontiers 8, 1102–1110 (2021).
DOI: 10.1039/D0QI01140A.
- Gericke, R.; Wagler, J.
Coordination and Electrochemical Switching on Paddle-Wheel Complexes Containing an As–Ru or a Sb–Ru Axis
Inorganic Chemistry (2021).
DOI: 10.1021/acs.inorgchem.1c02735.
- Gilbin, R.; Arnold, T.; Beresford, N. A.; Berthomieu, C.; Brown, J. E.; de With, G.; Horemans, N.; Madruga, M. J.; Masson, O.; Merroun, M.; Michalik, B.; Muikku, M.; O’Toole, S.; Mrdakovic Popic, J.; Nogueira, P.; Real, A.; Sachs, S.; Salbu, B.; Stark, K.; Steiner, M.; Sweek, L.; Vandenhove, H.; Vidal, M.; Vives i Batlle, J.
An updated strategic research agenda for the integration of radioecology in the european radiation protection research
Journal of Environmental Radioactivity 237, 106697 (2021).
DOI: 10.1016/j.jenvrad.2021.106697.
- Glasneck, F.; Roode-Gutzmer, Q.; Stumpf, T.; Kersting, B.
Tetra - substituted p - tert - butylcalix[4]arene with phosphoryl and salicylamide functional groups: synthesis, complexation and selective extraction of f - element cations
Chemistry - A European Journal, e202104301 (2022).
DOI: 10.1002/chem.202104301.
- Grahn, A.; Pescador, E. D.; Kliem, S.; Schäfer, F.; Höhne, T.
Modelling of complex boron dilution transients in PWRs – Validation of CFD simulation with ANSYS CFX against the ROCOM E2.3 experiment
Nuclear Engineering and Design 372, 110938 (2021).
DOI: 10.1016/j.nucengdes.2020.110938.

- Grote, L.; Zito, C. A.; Frank, K.; Dippel, A. C.; Reisbeck, P.; Pitala, K.; Kvashnina, K. O.; Bauters, S.; Detlefs, B.; Ivashko, O.; Pandit, P.; Rebber, M.; Harouna-Mayer, S. Y.; Nickel, B.; Koziej, D.
Emergence of cobalt oxide nano-assemblies: X-ray *in situ* studies bridging the molecular- and macro-length scales
Nature Communications 12, 4429 (2021).
DOI: 10.1038/s41467-021-24557-z.
- Gu, B.; Chekhonin, P.; Xin, S. W.; Liu, G. Q.; Ma, C. L.; Zhou, L.; Skrotzki, W.
Effect of temperature and strain rate on the deformation behavior of Ti5321 during hot-compression
Journal of Alloys and Compounds 876, 159938 (2021).
DOI: 10.1016/j.jallcom.2021.159938.
- Gu, B.; Chekhonin, P.; Xin, S. W.; Liu, G. Q.; Ma, C. L.; Zhou, L.; Skrotzki, W.
Microstructure and texture development during hot-compression of Ti5321
Materials Characterization 179, 111297 (2021).
DOI: 10.1016/j.matchar.2021.111297.
- Haubitz, T.; Drobot, B.; Tsushima, S.; Stuedtner, R.; Stumpf, T.; Kumke, M. U.
Quenching Mechanism of Uranyl(VI) by Chloride and Bromide in Aqueous and Non-Aqueous Solutions
Journal of Physical Chemistry A 125, 4380–4389 (2021).
DOI: 10.1021/acs.jpca.1c02487.
- Heller, A.; Pisarevskaja, A.; Bölicke, N.; Barkleit, A.; Bok, F.; Wober, J.
The effect of four lanthanides onto a rat kidney cell line (NRK-52E) is dependent on the composition of the cell culture medium
Toxicology 456, 152771 (2021).
DOI: 10.1016/j.tox.2021.152771.
- Huittinen, N. M.; Jessat, I.; Réal, F.; Vallet, V.; Starke, S.; Eibl, M.; Jordan, N.
Revisiting the complexation of Cm(III) with aqueous phosphates: what can we learn from the complex structures using luminescence spectroscopy and *ab initio* simulations?
Inorganic Chemistry 60, 10656–10673 (2021).
DOI: 10.1021/acs.inorgchem.1c01319.
- Jessat, J.; Sachs, S.; Moll, H.; John, W.; Stuedtner, R.; Hübner, R.; Bok, F.; Stumpf, T.
Bioassociation of U(VI) and Eu(III) by plant (*Brassica napus*) suspension cell cultures – A spectroscopic investigation
Environmental Science and Technology 55, 6718–6728 (2021).
DOI: 10.1021/acs.est.0c05881.
- Jiménez-Carrascosa, A.; García-Herranz, N.; Krepel, J.; Margulis, M.; Davies, U.; Shwageraus, E.; Fridman, E.; Gregg, R.
Decay heat characterization for the European Sodium Fast Reactor
Journal of Nuclear Engineering and Radiation Science 8, 011319 (2022).
DOI: 10.1115/1.4051798.
- Joos, J. J.; van der Heggen, D.; Amidani, L.; Seijo, L.; Barandiarán, Z.
Elucidation of the electron transfer mechanism in Eu²⁺ and Sm³⁺ codoped CaF₂: A step towards better understanding of trapping and detrapping in luminescent materials
Physical Review B 104, L201108 (2021).
DOI: 10.1103/PhysRevB.104.L201108.
- Kammerlander, K. K. K.; Köhler, L.; Huittinen, N. M.; Bok, F.; Stuedtner, R.; Oschatz, C.; Vogel, M.; Stumpf, T.; Brunner, E.
Sorption of Europium on Diatom Biosilica as Model of a “Green” Sorbent for f-Elements
Applied Geochemistry 126, 104823 (2021).
DOI: 10.1016/j.apgeochem.2020.104823.
- Kanj, A. B.; Bürck, J.; Vankova, N.; Li, C.; Mutruc, D.; Chandresh, A.; Hecht, S.; Heine, T.; Heinke, L.
Chirality Remote Control in Nanoporous Materials by Circularly Polarized Light
Journal of the American Chemical Society 143, 7059–7068 (2021).
DOI: 10.1021/jacs.1c01693.
- Kapoor, G.; Chekhonin, P.; Kaden, C.; Vogel, K.; Bergner, F.
Microstructure-informed prediction and measurement of nanoindentation hardness of an Fe-9Cr alloy irradiated with Fe-ions of 1 and 5 MeV energy
Nuclear Materials and Energy 30, 101105 (2022).
DOI: 10.1016/j.nme.2021.101105.
- Karimzadeh, L.; Fischer, C.
Implementing Heterogeneous Crystal Surface Reactivity in Reactive Transport Simulations: The Example of Calcite Dissolution
ACS Earth and Space Chemistry 5, 2408–2418 (2021).
DOI: 10.1021/acsearthspacechem.1c00099.
- Karpińska, M.; Liang, M.; Kempt, R.; Finzel, K.; Kamminga, M.; Zhang, N.; Knodlseder, C.; Maude, D. K.; Baranowski, M.; Ł, Ł.; Ye, J.; Kuc, A. B.; Plochocka, P.
Non-radiative energy transfer and selective charge transfer in a WS₂/(PEA)2PbI₄ heterostructure
ACS Applied Materials and Interfaces 13, 33677–33684 (2021).
DOI: 10.1021/acsami.1c08377.
- Kloditz, R.; Radoske, T.; Schmidt, M.; Heine, T.; Stumpf, T.; Patzschke, M.
Comprehensive Bonding Analysis of Tetravalent f-Element Complexes of the Type M(salen)₂
Inorganic Chemistry 60, 2514–2525 (2021).
DOI: 10.1021/acs.inorgchem.0c03424.

- Köhler, L.; Patzschke, M.; Schmidt, M.; Stumpf, T.; März, J.
How 5f electron polarizability drives covalency and selectivity in actinide N-donor complexes
Chemistry - A European Journal 27, 18058–18065 (2021).
 DOI: 10.1002/chem.202102849.
- Kolomiets, A. V.; Paukov, M.; Valenta, J.; Chatterjee, B.; Andreev, A. V.; Kvashnina, K. O.; Wilhelm, F.; Rogalev, A.; Drozdenko, D.; Minarik, P.; Kolorenc, J.; Richter, M.; Prchal, J.; Havela, L.
5f states in UGa₂ probed by x-ray spectroscopies
Physical Review B 104, 045119 (2021).
 DOI: 10.1103/PhysRevB.104.045119.
- Krawczyk-Bärsch, E.; Scheinost, A. C.; Rossberg, A.; Müller, K.; Bok, F.; Hallbeck, L.; Lehrich, J.; Schmeide, K.
Uranium and neptunium retention mechanisms in *Gallionella ferruginea* ferrihydrite systems for remediation purposes
Environmental Science and Pollution Research 28, 18342–18353 (2021).
 DOI: 10.1007/s11356-020-09563-w.
- Kretzschmar, J.; Tsushima, S.; Lucks, C.; Jäckel, E.; Meyer, R.; Steudtner, R.; Müller, K.; Rossberg, A.; Schmeide, K.; Brendler, V.
Dimeric and Trimeric Uranyl(VI)-Citrate Complexes in Aqueous Solution
Inorganic Chemistry 60, 7998–8010 (2021).
 DOI: 10.1021/acs.inorgchem.1c00522.
- Kuipers, G.; Morris, K.; Townsend, L. T.; Bots, P.; Kvashnina, K.; Bryan, N.; Lloyd, J. R.
Bio-mineralization of uranium-phosphates fueled by microbial 1 degradation of isosaccharinic acid (ISA)
Environmental Science & Technology 55, 4597–4606 (2021).
 DOI: 10.1021/acs.est.0c03594.
- Kvashnina, K. O.; Butorin, S. M.
High energy resolution X-ray spectroscopy at actinide M_{4,5} and ligand K edges: what we know, what we want to know, what we can know
Chemical Communications (2021).
 DOI: 10.1039/D1CC04851A.
- Levytskyi, V.; Wagler, J.; Hennig, C.; Feig, M.; Weigel, T.; Leithe-Jasper, A.; Meyer, D. C.; Gumenuik, R.
Sc₃Ir₄Si_{13+x} and Sc₄Ir₇Ge₆ – the perovskite-related crystal structures
Zeitschrift für Kristallographie 236, 313–323 (2022).
 DOI: 10.1515/zkri-2021-2055.
- Lippold, H.; Zedek, L.
Metal dissociation from humic colloids: Kinetics with time-dependent rate constants
Chemosphere 275, 130045 (2021).
 DOI: 10.1016/j.chemosphere.2021.130045.
- Liu, T. J.; Springer, M.; Heinsdorf, N.; Kuc, A. B.; Valenti, R.; Heine, T.
Semimetallic square-octagon two-dimensional polymer with high mobility
Physical Review B 104, 205419 (2021).
 DOI: 10.1103/PhysRevB.104.205419.
- Lopez Fernandez, M.; Jroundi, F.; Fresneda, M. A. R.; Merroun, M. L.
Microbial interaction with and tolerance of radionuclides: underlying mechanisms and biotechnological applications
Microbial Biotechnology 14, 810–828 (2021).
 DOI: 10.1111/1751-7915.13718.
- Lovisari, M.; Gericke, R.; Twamley, B.; McDonald, A. R.
Comparing Metal-Halide and -Oxygen Adducts in Oxidative C/O-H Activation: Au(III)-Cl versus Au(III)-OH
Inorganic Chemistry 60, 15610–15616 (2021).
 DOI: 10.1021/acs.inorgchem.1c02222.
- Lyu, K.; Fichter, S.; Gu, M.; März, J.; Schmidt, M.
An updated status and trends in actinide metal-organic frameworks (An-MOFs): from synthesis to application
Coordination Chemistry Reviews 446, 214011 (2021).
 DOI: 10.1016/j.ccr.2021.214011.
- Ma, F.; Jiao, Y.; Wu, W.; Liu, Y.; Yang, S. A.; Heine, T.
Half-Auxeticity and Anisotropic Transport in Pd Decorated Two-Dimensional Boron Sheets
Nano Letters 21, 2356–2362 (2021).
 DOI: 10.1021/acs.nanolett.0c04154.
- Maiwald, M. M.; Müller, K.; Heim, K.; Rothe, J.; Dardenne, K.; Rossberg, A.; Koke, C.; Trumm, M.; Skerencak-Frech, A.; Panak, P. J.
Complexation of Np(V) with the dicarboxylates malonate and succinate: complex stoichiometry, thermodynamic data and structural information
Inorganic Chemistry 60, 18674–18686 (2021).
 DOI: 10.1021/acs.inorgchem.1c01966.

- Malerba, L.; Caturla, M. J.; Gaganidze, E.; Kaden, C.; Konstantinović, M. J.; Olsson, P.; Robertson, C.; Rodney, D.; Ruiz-Moreno, A. M.; Serrano, M.; Aktaa, J.; Anento, N.; Austin, S.; Bakaev, A.; Balbuena, J. P.; Bergner, F.; Boioli, F.; Boleininger, M.; Bonny, G.; Castin, N.; Chapman, J. B. J.; Chekhonin, P.; Clozel, M.; Devincre, B.; Dupuy, L.; Diego, G.; Dudarev, S. L.; Fu, C. C.; Gatti, R.; Gélébart, L.; Gómez-Ferrer, B.; Gonçalves, D.; Guerrero, C.; Gueye, P. M.; Hähner, P.; Hannula, S. P.; Hayat, Q.; Hernández-Mayoral, M.; Jagielski, J.; Jennett, N.; Jiménez, F.; Kapoor, G.; Kraych, A.; Khvan, T.; Kurpaska, L.; Kuronen, A.; Kvashin, N.; Libera, O.; Ma, P. W.; Manninen, T.; Marinica, M. C.; Merino, S.; Meslin, E.; Momprou, F.; Mota, F.; Namburi, H.; Ortiz, C. J.; Pareige, C.; Prester, M.; Rajakrishnan, R. R.; Sauzay, M.; Serra, A.; Simonovski, I.; Soisson, F.; Spätig, P.; Tanguy, D.; Terentyev, D.; Trebala, M.; Trochet, M.; Ulbricht, A.; Vallet, M.; Vogel, K.; Yalcinkaya, T.; Zhao, J.
Multiscale modelling for fusion and fission materials: the M4F project
Nuclear Materials and Energy 29, 101051 (2021).
DOI: 10.1016/j.nme.2021.101051.
- Malinen, L.; Repo, E.; Harjula, R.; Huittinen, N.
The effect of UV-C irradiation and EDTA on the uptake of Co²⁺ by antimony oxide in the presence and absence of competing cations Ca²⁺ and Ni²⁺
Nuclear Engineering and Technology (2021).
DOI: 10.1016/j.net.2021.08.002.
- Mansel, A.; Franke, K.
Production of no-carrier-added ⁸⁹Zr at an 18 MeV cyclotron, its purification and use in investigations in solvent extraction
Journal of Radioanalytical and Nuclear Chemistry 328, 419–423 (2021).
DOI: 10.1007/s10967-021-07634-x.
- Matsuoka, M.; Tsushima, S.; Takao, K.
Fluorite-like hydrolyzed hexanuclear coordination clusters of Zr(IV) and Hf(IV) with syn-syn bridging N,N,N-trimethylglycine in soft crystal structures exhibiting cold-crystallization
Inorganica Chimica Acta 528, 120622 (2021).
DOI: 10.1016/j.ica.2021.120622.
- Mausolf, E. J.; Johnstone, E. V.; Mayordomo, N.; Williams, D. L.; Guan, E. Y. Z.; Gary, C. K.
Fusion-Based Neutron Generator Production of Tc-99m and Tc-101: A Prospective Avenue to Technetium Theranostics
Pharmaceuticals 14, 875 (2021).
DOI: 10.3390/ph14090875.
- Mayordomo, N.; Hernandez, D. M. R.; Rossberg, A.; Foerstendorf, H.; Heim, K.; Brendler, V.; Müller, K.
Analysis of technetium immobilization and its molecular retention mechanisms by Fe(II)-Al(III)-Cl layered double hydroxide.
Chemical Engineering Journal 408, 127265 (2021).
DOI: 10.1016/j.cej.2020.127265.
- Moll, H.; Barkleit, A.; Frost, L.; Raff, J.
Curium(III) speciation in the presence of microbial cell wall components
Ecotoxicology and Environmental Safety 227, 112887 (2021).
DOI: 10.1016/j.ecoenv.2021.112887.
- Moll, H.; Schmidt, M.; Sachs, S.
Curium(III) and europium(III) as luminescence probes for plant cell (*Brassica napus*) interactions with potentially toxic metals
Journal of Hazardous Materials 412, 125251 (2021).
DOI: 10.1016/j.jhazmat.2021.125251.
- Molodtsov, K.; Demnitz, M.; Schymura, S.; Jankovský, F.; Havlová, V.; Schmidt, M.
Molecular-level speciation of Eu(III) adsorbed on a migmatized gneiss as determined using μ TRLFS
Environmental Science and Technology 55, 4871–4879 (2021).
DOI: 10.1021/acs.est.0c07998.
- Moors, M.; An, Y.; Kuc, A. B.; Monakhov, K.
TiO_x/Pt₃Ti(111) Surface-Directed Formation of Electronically Responsive, Supramolecular Assemblies of Tungsten Oxide Clusters
Beilstein Journal of Nanotechnology 12, 203–212 (2021).
DOI: 10.3762/bjnano.12.16.
- Mull, T.; Wagner, T.; Bonfigli, G.; Buchholz, S.; Schäfer, F.; Schleicher, E.; Schuster, C.; Sporn, M.
Safety Cases for Design-Basis Accidents in LWRs Featuring Passive Systems Part 1 - Experimental Investigations
Nuclear Engineering and Design, 111095 (2021).
DOI: 10.1016/j.nucengdes.2021.111095.
- Neumann, J.; Brinkmann, H.; Britz, S.; Lützenkirchen, J.; Bok, F.; Stockmann, M.; Brendler, V.; Stumpf, T.; Schmidt, M.
A comprehensive study of the sorption mechanism and thermodynamics of f-element sorption onto K-feldspar
Journal of Colloid and Interface Science 591, 490–499 (2021).
DOI: 10.1016/j.jcis.2020.11.041.
- Neumann, J.; Qiu, C.; Eng, P.; Skanthakumar, S.; Soderholm, L.; Stumpf, T.; Schmidt, M.
Effect of Background Electrolyte Composition on the Interfacial Formation of Th(IV) Nanoparticles on the Muscovite (001) Basal Plane
Journal of Physical Chemistry C 125, 16524–16535 (2021).
DOI: 10.1021/acs.jpcc.1c03997.
- Panda, C.; Doyle, L. M.; Gericke, R.; McDonald, A. R.
Rapid Iron(III)-Fluoride Mediated Hydrogen Atom Transfer
Angewandte Chemie - International Edition 60, 26281–26286 (2021).
DOI: 10.1002/anie.202112683.

- Pinel-Cabello, M.; Jroundi, F.; Lopez Fernandez, M.; Geffers, R.; Jarek, M.; Jauregui, R.; Link, A.; Vilchez-Vargas, R.; Merroun, M. L.
Multisystem combined uranium resistance mechanisms and bioremediation potential of *Stenotrophomonas bentonitica* BII-R7: Transcriptomics and microscopic study
Journal of Hazardous Materials 405, 123858 (2021).
DOI: 10.1016/j.jhazmat.2020.123858.
- Podlech, C.; Matschiavelli, N.; Peltz, M.; Kluge, S.; Arnold, T.; Cherkouk, A.; Meleshyn, A.; Grathoff, G.; Warr, L. N.
Bentonite alteration in batch reactor experiments with and without fertilizing agents: implications for the disposal of radioactive waste
Minerals 11, 932 (2021).
DOI: 10.3390/min11090932.
- Ponomarev, A.; Mikityuk, K.; Fridman, E.; Nora, V. A. D.; Bubelis, E.; Schikorr, M.
Superphénix Benchmark Part II: Transient Results
Journal of Nuclear Engineering and Radiation Science 8, 011321 (2022),
DOI: 10.1115/1.4051877.
- Ponomarev, A.; Mikityuk, K.; Zhang, L.; Nikitin, E.; Fridman, E.; Álvarez-Velarde, F.; Romojaro-Otero, P.; Jiménez-Carrascosa, A.; García-Herranz, N.; Lindley, B.; Davies, U.; Seubert, A.; Henry, R.
Superphénix Benchmark Part I: Results of Static neutronics
Journal of Nuclear Engineering and Radiation Science 8, 011320 (2022),
DOI: 10.1115/1.4051449.
- Prieur, D.; Desagulier, M. M.; Neuville, D.; Guéneau, C.; Epifano, E.; Dardenne, K.; Rothe, J.; Martin, P.
A spectroscopic hike in the U-O phase diagram
Journal of Synchrotron Radiation 28, 1684–1691 (2021).
DOI: 10.1107/S1600577521010572.
- Prieur, D.; Vigier, J. F.; Popa, K.; Walter, O.; Dieste, O.; Varga, Z.; Beck, A.; Vitova, T.; Scheinost, A. C.; Martin, P.
Charge distribution in $U_{1-x}Ce_xO_{2+y}$ nanoparticles
Inorganic Chemistry 60, 14550–14556 (2021).
DOI: 10.1021/acs.inorgchem.1c01071.
- Prill, T.; Fischer, C.; Gavrilenko, P.; Iliev, O.
Implementing the Variability of Crystal Surface Reactivity in Reactive Transport Modeling
Transport in Porous Media 140, 535–557 (2021).
DOI: 10.1007/s11242-021-01697-w.
- Pukenas, A.; Chekhonin, P.; Scharnweber, J.; Chulist, R.; Oertel, C. G.; Freudenberger, J.; Skrotzki, W.
TiAl-based semi-finished material produced by reaction annealing of Ti/Al layered composite sheets
Materials Today Communications 30, 103083 (2022).
DOI: 10.1016/j.mtcomm.2021.103083.
- Rajabi, F.; Jessat, J.; Garimella, J. N.; Bok, F.; Steudtner, R.; Stumpf, T.; Sachs, S.
Uranium(VI) toxicity in tobacco BY-2 cell suspension culture - a physiological study
Ecotoxicology and Environmental Safety 211, 111883 (2021).
DOI: 10.1016/j.ecoenv.2020.111883.
- Ramzan, M. S.; Kunstmann, J.; Kuc, A. B.
Tuning valleys and wave functions of van der Waals heterostructures by varying the number of layers: A first-principles study
Small 17, 2008153 (2021).
DOI: 10.1002/sml.202008153.
- Reese, S.; Kaden, P.; Taylor, C. J.; Kloditz, R.; Schmidt, M.
Structure and Thermodynamics of Eu(III) and Cm(III) Complexes with Glucuronic Acid
Inorganic Chemistry 60, 14667–14678 (2021).
DOI: 10.1021/acs.inorgchem.1c01746.
- Rodriguez Hernandez, D. M.; Mayordomo, N.; Schild, D.; Azzam, S. S. A.; Brendler, V.; Müller, K.; Stumpf, T.
Reductive immobilization of $^{99}Tc(VII)$ by FeS_2 : the effect of marcasite
Chemosphere 281, 130904 (2021).
DOI: 10.1016/j.chemosphere.2021.130904.
- Roos, D. P.; Scheinost, A. C.; Churakov, S. V.; Nagashima, M.; Cametti, G.
On the nature of Pb species in Pb-(over)exchanged zeolite: a combined experimental and theoretical study
Microporous and Mesoporous Materials 327, 111444 (2021).
DOI: 10.1016/j.micromeso.2021.111444.
- Sanchez-Espinoza, V. H.; Gabriel, S.; Suikkanen, H.; Telkkä, J.; Valtavirta, V.; Bencik, M.; Kliem, S.; Queral, C.; Farda, A.; Abéguilée, F.; Smith, P.; Uffelen, P. v.; Ammirabile, L.; Seidl, M.; Schneidesch, C.; Grishchenko, D.; Lestani, H.
The H2020 McSAFER project: Main goals, technical work program, and status
Energies 14, 6348 (2021).
DOI: 10.3390/en14196348.
- Schabernack, J.; Kurganskaya, I.; Fischer, C.; Luttge, A.
Influence of Muscovite (001) Surface Nanotopography on Radionuclide Adsorption Studied by Kinetic Monte Carlo Simulations
Minerals 11, 468 (2021).
DOI: 10.3390/min11050468.
- Schaefer, S.; Steudtner, R.; Hübner, R.; Krawczyk-Bärsch, E.; Merroun, M. L.
Effect of temperature and cell viability on uranium biomineralization by the uranium mine isolate *Penicillium simplicissimum*
Frontiers in Microbiology 12, 802926 (2021).
DOI: 10.3389/fmicb.2021.802926

- Scheinost, A. C.; Claußner, J.; Exner, J.; Feig, M.; Findeisen, S.; Hennig, C.; Kvashnina, K. O.; Naudet, D.; Prieur, D.; Rossberg, A.; Schmidt, M.; Qiu, C.; Colomp, P.; Cohen, C.; Dettona, E.; Dyadkin, V.; Stumpf, T.
ROBL-II at ESRF: A synchrotron toolbox for actinide research
Journal of Synchrotron Radiation 28, 333–349 (2021).
DOI: 10.1107/S1600577520014265.
- Schmeide, K.; Rossberg, A.; Bok, F.; Azzam, S. S. A.; Weiß, S.; Scheinost, A.
Technetium immobilization by chukanovite and its oxidative transformation products: Neural network analysis of EXAFS spectra
Science of the Total Environment 770, 145334 (2021).
DOI: 10.1016/j.scitotenv.2021.145334.
- Schönberger, N.; Taylor, C. J.; Schrader, M.; Drobot, B.; Matys, S.; Lederer, F.; Pollmann, K.
Gallium-binding peptides as a tool for the sustainable treatment of industrial waste streams
Journal of Hazardous Materials 414, 125366 (2021).
DOI: 10.1016/j.jhazmat.2021.125366.
- Schymura, S.; Rybkin, I.; Uygan, S. S. S.; Drev, S.; Podlizec, R.; Rijavec, T.; Mansel, A.; Lapanje, A.; Franke, K.; Strok, M.
Dissolution-based uptake of CeO₂ nanoparticles by fresh water shrimp – A dual-radiolabelling study of the fate of anthropogenic cerium in water organisms
Environmental Science: Nano 8, 1934–1944 (2021).
DOI: 10.1039/d1en00264c.
- Shiryaev, A. A.; Trigub, A. L.; Voronina, E. N.; Kvashnina, K. O.; Bukhovets, V. L.
Behavior of implanted Xe and Kr in nanodiamond and thin graphene stacks: experiment and modeling
Physical Chemistry Chemical Physics 23, 21729–21737 (2021).
DOI: 10.1039/D1CP02600C.
- Singer, H.; Drobot, B.; Zeymer, C.; Steudtner, R.; Daumann, L.
Americium preferred: LanM, a natural lanthanide-binding protein favors an actinide over lanthanides
Chemical Science 12, 15581–15587 (2021).
DOI: 10.1039/D1SC04827A.
- Sonnendecker, C.; Oeser, J.; Richter, P. K.; Hille, P.; Zhao, Z.; Fischer, C.; Lippold, H.; Blázquez-Sánchez, P.; Engelberger, F.; Ramírez-Sarmiento, C. A.; Oeser, T.; Lihanova, Y.; Frank, R.; Jahnke, H. G.; Billig, S.; Abel, B.; Sträter, N.; Matysik, J.; Zimmermann, W.
Low Carbon Footprint Recycling of Post-Consumer PET Plastic with a Metagenomic Polyester Hydrolase
ChemSusChem (2021).
DOI: 10.1002/cssc.202101062.
- Sornin, D.; Ehrnsten, U.; Mozzani, N.; Rantala, J.; Walter, M.; Hobt, A.; Aktaa, J.; Onorbe, E.; Hernandez-Mayoral, M.; Ulbricht, A.; Gicquel, S.; Frank, L.; Carlan, Y. d.
Creep Properties of 9Cr and 14Cr ODS Tubes Tested by Inner Gas Pressure
Metallurgical and Materials Transactions A 52, 3541–3552 (2021).
DOI: 10.1007/s11661-021-06327-0.
- Stockmann, M.; Fritsch, K.; Bok, F.; Marques Fernandes, M.; Baeyens, B.; Steudtner, R.; Müller, K.; Nebelung, C.; Brendler, V.; Stumpf, T.; Schmeide, K.
New insights into U(VI) sorption onto montmorillonite from batch sorption and spectroscopic studies at increased ionic strength
Science of the Total Environment 806, 150653 (2022).
DOI: 10.1016/j.scitotenv.2021.150653.
- Subramanian, M.; Kielar, C.; Tsushima, S.; Fahmy, K.; Oertel, J.
DNA-Mediated Stack Formation of Nanodiscs
Molecules 26, 1647 (2021).
DOI: 10.3390/molecules26061647.
- Suksi, J.; Tullborg, E. L.; Pidchenko, I.; Krall, L.; Sandström, B.; Kaksonen, K.; Vitova, T.; Kvashnina, K. O.; Göttlicher, J.
Uranium remobilisation in anoxic deep rock-groundwater system in response to late Quaternary climate changes – Results from Forsmark, Sweden
Chemical Geology 584, 120551 (2021).
DOI: 10.1016/j.chemgeo.2021.120551.
- Takeyama, T.; Tsushima, S.; Takao, K.
Effects of Substituents on the Molecular Structure and Redox Behavior of Uranyl(V/VI) Complexes with N₃O₂-Donating Schiff Base Ligands
Inorganic Chemistry 60, 11435–11449 (2021).
DOI: 10.1021/acs.inorgchem.1c01449.
- Taylor, C. J.; Schönberger, N.; Laníková, A.; Patzschke, M.; Drobot, B.; Židek, L.; Lederer, F.
Investigation of the structure and dynamics of Gallium binding to high-affinity peptides elucidated by multi-scale simulation, quantum chemistry, NMR and ITC
Physical Chemistry Chemical Physics 23, 8618–8632 (2021).
DOI: 10.1039/d1cp00356a.
- Tian, Y. B.; Vankova, N.; Weidler, P.; Kuc, A. B.; Heine, T.; Wöll, C.; Gu, Z. G.; Zhang, J.
Oriented Growth of In-Oxo Chain based Metal-Porphyrin Framework Thin Film for High-Sensitive Photodetector
Advanced Science 8, 2100548 (2021).
DOI: 10.1002/adv.202100548.

- Verdel, N.; Rijavec, T.; Rybkin, I.; Erzin, A.; Ž, V.; Pintar, A.; Lapanje, A.
Isolation, identification and selection of bacteria with the proof-of-concept for bioaugmentation of whitewater from wood-free paper mills
Frontiers in Microbiology 12, 758702 (2021).
 DOI: 10.3389/fmicb.2021.758702.
- Viebach, M.; Lange, C.; Kliem, S.; Demaziere, C.; Rohde, U.; Hennig, D.; Hurtado, A.
Verification of the code DYN3D for calculations of neutron flux fluctuations
Annals of Nuclear Energy 166, 108735 (2022),
 DOI: 10.1016/j.anucene.2021.108735.
- Vogel, K.; Chekhonin, P.; Kaden, C.; Hernández-Mayoral, M.; Akhmadaliev, S.; Bergner, F.
Depth distribution of irradiation-induced dislocation loops in an Fe-9Cr model alloy irradiated with Fe ions: The effect of ion energy
Nuclear Materials and Energy 27, 101007 (2021).
 DOI: 10.1016/j.nme.2021.101007.
- Vogel, M.; Steudtner, R.; Fankhänel, T.; Raff, J.; Drobot, B.
Spatially resolved Eu(III) environments by chemical microscopy
Analyst 146, 6741–6745 (2021).
 DOI: 10.1039/D1AN01449H.
- Wöhner, K.; Wulf, T.; Vankova, N.; Heine, T.
Strong Binding of Noble Gases to [B₁₂X₁₁]: a theoretical study
Journal of Physical Chemistry A 125, 4760–4765 (2021).
 DOI: 10.1021/acs.jpca.1c01909.
- Wollenberg, A.; Drobot, B.; Hübner, R.; Kretzschmar, J.; Freitag, L.; Lehmann, F.; Günther, A.; Stumpf, T.; Raff, J.
Uranium(VI) bioassociation by different fungi – a comparative study into molecular processes
Journal of Hazardous Materials 411, 1–10 125068 (2021).
 DOI: 10.1016/j.jhazmat.2021.125068.
- Wu, B.; Kempt, R.; Kovalska, E.; Luxa, J.; Kuc, A. B.; Heine, T.; Sofer, Z.
Lithium-assisted Exfoliation and Photoelectrocatalytic Water Splitting of 2D Palladium Thiophosphate
ACS Applied Nano Materials 4, 441–448 (2021).
 DOI: 10.1021/acsanm.0c02775.
- Wulf, T.; Warneke, J.; Heine, T.
B₁₂X₁₁(H₂): Exploring the limits of isotopologue selectivity of hydrogen adsorption
RSC Advances 11, 28466–28475 (2021).
 DOI: 10.1039/D1RA06322G.
- Yuan, T.; Fischer, C.
Effective diffusivity prediction of radionuclides in clay formations using an integrated upscaling workflow
Transport in Porous Media 138, 245–264 (2021).
 DOI: 10.1007/s11242–021–01596–0.
- Yuan, T.; Schymura, S.; Bollermann, T.; Molodtsov, K.; Chekhonin, P.; Schmidt, M.; Stumpf, T.; Fischer, C.
Heterogeneous sorption of radionuclides predicted by crystal surface nanoroughness
Environmental Science & Technology 55, 15797–15809 (2021).
 DOI: 10.1021/acs.est.1c04413.
- Zhang, J.; Wenzel, M.; Schnaars, K.; Hennesdorf, F.; Schwedtmann, K.; März, J.; Rossberg, A.; Kaden, P.; Kraus, F.; Stumpf, T.; Weigand, J. J.
Coordination of Trivalent Lanthanum and Cerium, and Tetravalent Cerium and Actinides (An = Th(IV), U(IV), Np(IV)) by a 4-Phosphoryl 1H-Pyrazol-5-olate Ligand in Solution and the Solid State
Dalton Transactions 50, 3550–3558 (2021).
 DOI: 10.1039/D1DT00365H.
- Zhou, Y.; He, H.; Wang, J.; Liu, J.; Lippold, H.; Bao, Z.; Wang, L.; Lin, Y.; Fang, F.; Huang, Y.; Jiang, Y.; Xiao, T.; Yuan, W.; Wei, X.; Tsang, D. C. W.
Stable isotope fractionation of thallium as novel evidence for its geochemical transfer during lead-zinc smelting activities
Science of the Total Environment 803, 150036 (2022),
 DOI: 10.1016/j.scitotenv.2021.150036.
- Zhou, Z.; Springer, M.; Geng, W.; Zhu, X.; Li, T.; Li, M.; Jing, Y.; Heine, T.
Rational Design of Two-dimensional Binary Polymers from Heterotriangulenes for Photocatalytic Water Splitting
The Journal of Physical Chemistry Letters 12, 8134–8140 (2021).
 DOI: 10.1021/acs.jpcclett.1c02109.
- Zurita, C.; Tsushima, S.; Bresson, C.; Garcia-Cortes, M.; Solari, P. L.; Jeanson, A.; Creff, G.; Auwer, C. D.
How does iron storage protein ferritin interact with plutonium (and thorium)?
Chemistry - A European Journal 27, 2393–2401 (2021).
 DOI: 10.1002/chem.202003653.

○ FURTHER CONTRIBUTIONS

Bilodid, Y.; Leppänen, J.

Effect of the Uniform Fission Source method on local power variance in full core Serpent calculation

European Physical Journal Web of Conferences 247, 04024 (2021).

DOI: 10.1051/epjconf/202124704024.

Davies, U.; Margulis, M.; Shwageraus, E.; Fridman, E.;

Garcia-Herranz, N.; Jimenez-Carrascosa, A.;

Cabellos, O.; Gregg, R.

Evaluation of the ESFR End of Cycle State and Detailed Spatial Distributions of Reactivity Coefficients

European Physical Journal Web of Conferences 247, 02001 (2021).

DOI: 10.1051/epjconf/202124702001.

Ferraro, D.; García, M.; Imke, U.; Valtavirta, V.;

Tuominen, R.; Bilodid, Y.; Leppänen, J.; Sanchez-Espinoza, V.

SERPENT/SUBCHANFLOW coupled calculations for a VVER core at hot full power

European Physical Journal Web of Conferences 247, 04006 (2021).

DOI: 10.1051/epjconf/202124704006.

García, M.; Tuominen, R.; Gommlich, A.; Ferraro, D.;

Valtavirta, V.; Imke, U.; Uffelen, P. v.; Mercatali, L.;

Sanchez-Espinoza, V.; Leppänen, J.; Kliem, S.

SERPENT2-SUBCHANFLOW-TRANSURANUS pin-by-pin depletion calculations for a PWR fuel assembly

European Physical Journal Web of Conferences 247, 06016 (2021).

DOI: 10.1051/epjconf/202124706016.

Nikitin, E.; Fridman, E.; Mikityuk, K.; Radman, S.;

Fiorina, C.

Neutronic Modelling of the FFTF Control Rod Worth Measurements with Diffusion Codes

European Physical Journal Web of Conferences 247, 10017 (2021).

DOI: 10.1051/epjconf/202124710017.

Rytlewicz, W.; Fridman, E.; Shwageraus, E.

Modelling ASTRID-Like Sodium-Cooled Fast Reactor with Serpent DYN3D Code Sequence

European Physical Journal Web of Conferences 247, 02028 (2021).

DOI: 10.1051/epjconf/202124702028.

Viebach, M.; Lange, C.; Seidl, M.; Bilodid, Y.; Hurtado, A.

Neutron noise patterns from coupled fuel-assembly vibrations

European Physical Journal Web of Conferences 247, 02015 (2021).

DOI: 10.1051/epjconf/202124702015.

○ EDITORIAL WORK

Schmeide, K.; Philipp, T.; Wolter, J. M.; Kretschmar, J.;

Dullies, P.; Lippold, H.; Schymura, S.; Stumpf, T.

Joint project: Geochemical retention of radionuclides on cement alteration phases (GRaZ) - Subproject B

Wissenschaftlich-Technische Berichte / Helmholtz-Zentrum Dresden-Rossendorf; HZDR-114 (2021).

ORAL PRESENTATIONS

- Amidani, L.; Volkova, A.; Retegan, M.; Martin, P.; Kvashnina, K. O.
Understanding the M₄ edge HERFD XANES of U⁶⁺
Uranium Science, June 29–July 01, 2021, University of Bristol, U.K. (2021).
- Bok, F.; Moog, H. C.; Altmaier, M.; Freyer, D.; Thoenen, T.
THEREDA – Thermodynamic Reference Database for the nuclear waste disposal in Germany
Tage der Standortauswahl Freiberg 2021, February 11–12, 2021, Freiberg, Germany (2021).
- Bosbach, D.; Geckeis, H.; Heberling, F.; Kolditz, O.; Kühn, M.; Müller, K.; Stumpf, T.; Heberling, F.
An interdisciplinary view of the long-term evolution of repository systems across scales: the iCROSS project
SafeND Interdisziplinäres Forschungssymposium für die Sicherheit der nuklearen Entsorgung, November 10–12, 2021, Berlin, Germany (2021).
- Cametti, G.; Scheinost, A. C.; Churakov, S. V.
Combining X-ray diffraction, X-ray absorption spectroscopy, and molecular dynamics simulations to probe metals in zeolites: the case of intergrown Cd²⁺-LEV/ERI
XXV General Assembly and Congress of the International Union of Crystallography - IUCr 2021, August 14–22, 2021, Prague, Czech Republic (2021).
- Demnitz, M.; Molodtsov, K.; Schymura, S.; Schierz, A.; Müller, K.; Schmidt, M.
Spatially resolved sorption of Cm(III) on crystalline rock: influence of surface roughness and mineralogy
Goldschmidt 2021, July 04–09, 2021, Lyon, France (2021).
Interdisciplinary research symposium on the safety of nuclear disposal practices, November 10–12, 2021, Berlin, Germany (2021).
- Hilpmann, S.; Drobot, B.; Steudtner, R.; Bok, F.; Stumpf, T.; Cherkouk, A.
Sorption and reduction of uranium(VI) by a sulfate-reducing microorganism in synthetic Opalinus Clay pore water
Goldschmidt 2021, July 04–09, 2021, Lyon, France (2021).
- Hilpmann, S.; Drobot, B.; Steudtner, R.; Bok, F.; Stumpf, T.; Cherkouk, A.
Uranium(VI) reduction by a sulphate-reducing microorganism in Opalinus Clay pore water
Tage der Standortauswahl Freiberg 2021, February 11–12, 2021, Freiberg, Germany (2021).
- Huittinen, N. M.; Hennig, C.; Murphy, G. L.; Peters, L.; Tonnesen, T.; Winkler, B.
Fundamental investigations of actinide immobilization by incorporation into solid phases relevant for final disposal
MRS 2021 – 45th Scientific Basis for Nuclear Waste Management (SBNWM), October 24–29, 2021, Cologne, Germany (2021).
- Jessat, I.; Scheinost, A.; Rossberg, A.; Foerstendorf, H.; Jordan, N.
Investigation of Np(V) sorption onto the zircaloy corrosion product ZrO₂
MRS 2021 – 45th Scientific Basis for Nuclear Waste Management (SBNWM), October 24–29, 2021, Cologne, Germany (2021).
- Jessat, I.; Foerstendorf, H.; Jordan, N.
Sorption studies of Np(V) onto the zircaloy corrosion product ZrO₂
Goldschmidt 2021, July 04–09, 2021, Lyon, France (2021).
- Jessat, J.; Moll, H.; Bilke, M. L.; John, W.; Hübner, R.; Steudtner, R.; Drobot, B.; Bok, F.; Stumpf, T.; Sachs, S.
U(VI) and Eu(III) bioassociation behavior and uptake mechanisms of plant cells
Goldschmidt 2021, July 04–09, 2021, Lyon, France (2021).
- Jessat, J.; Moll, H.; John, W.; Steudtner, R.; Hübner, R.; Drobot, B.; Vogel, M.; Bok, F.; Stumpf, T.; Sachs, S.
Influence of plants on speciation and mobility of U(VI) and Eu(III)
45th Scientific Basis for Nuclear Waste Management Symposium, October 25–28, 2021, Jülich, Germany (2021).
- Jordan, N.; Huittinen, N. M.; Jessat, I.; Réal, F.; Vallet, V.; Starke, S.; Eibl, M.
Complexation of Cm(III) and Eu(III) with aqueous phosphates at elevated temperatures
Goldschmidt 2021, July 04–09, 2021, Lyon, France (2021).
- Köhler, L.; Patzschke, M.; März, J.; Schmidt, M.; Stumpf, T.
Pyrrol-Based Ligands as Salen Relatives: Complex Synthesis, Characterization and Comparison
ACS-Spring Meeting, April 12, 2021, U.S.A. (2021).
- Krawczyk-Bärsch, E.; Ramtke, J.; Drobot, B.; Steudtner, R.; Hübner, R.; Raff, J.
Magnetotactic bacteria as an effective sorbent for uranium in contaminated water
4th International Caparica Conference on Pollutant Toxic Ions and Molecules 2021, October 31–November 04, 2021, Caparica, Portugal (2021).
- Kretzschmar, J.; Tsushima, S.; Drobot, B.; Steudtner, R.; Schmeide, K.; Brendler, V.; Stumpf, T.
Dimeric and Trimeric Uranyl(VI)-Citrate Complexes: ¹⁷O-, ²³Na-, and ¹³⁹La-NMR – Helpful Probes for (Super-)Structure Determination
GDCh Jahrestagung der Fachgruppe Magnetische Resonanz (FGMR), September 27–October 01, 2021, Germany (2021).
- Kvashnina, K. O.
High energy resolution X-ray spectroscopy on uranium compounds
Uranium Science, June 28–July 01, 2021, Bristol, U.K. (2021).

- Kvashnina, K. O.
Towards The Bottom of The Periodic Table
Monday Meetings, March 22, 2021, Washington State University, U.S.A. (2021).
- Kvashnina, K. O.
X-ray Spectroscopy for Actinide Science
JDA-2021: 13th School on the Physics and Chemistry of Actinides, March 22–25, 2021, Rennes, France (2021).
- Kvashnina, K.
XAS Towards the Bottom of the Periodic Table
GlobalXAS, February 04, 2021, Washington, U.S.A. (2021).
- März, J.
Bonding Trends in a Series of Tetravalent Th-Pu Monosalen Complexes
Journées des Actinides, March 22–25, 2021, Rennes, France (2021).
- Matschiavelli, N.
Deutschlands Ausstieg aus der Atomkraft - Wie entsorgen wir den Müll und welche Rolle spielen Mikroorganismen?
Tag der Wissenschaften, November 23, 2021, Dresden, Germany (2021).
- Matschiavelli, N.
Die Rolle von Mikroorganismen bei der Lagerung von hoch-radioaktiven Abfällen - Mikrobiologie am HZDR
Girls` & Boys` day am HZDR, April 22, 2021, Dresden, Germany (2021).
- Matschiavelli, N.
UMB-II: 2nd video conference workshop
UMB-II project meeting, October 06, 2021, Brunswick, Germany (2021).
- Matschiavelli, N.; Sushko, V.; Dressler, M.; Neubert, T.; Kühn, L.; Schierz, A.; Cherkouk, A.
Can microorganisms significantly influence cast iron corrosion in a DGR?
EGU General Assembly 2021 vEGU21: Gather Online, April 19–30, 2021, Vienna, Austria (2021).
- Mayordomo, N.
The importance of understanding Technetium environmental chemistry- research at Institute of Resource Ecology
Research Talk at Helmholtz-Zentrum Dresden - Rossendorf, June 23, 2021, Dresden, Germany (2021).
- Mayordomo, N.; Rodriguez Hernandez, D. M.; Schild, D.; Rossberg, A.; Scheinost, A. C.; Brendler, V.; Müller, K.
Technetium immobilization by chloride green rust
TransRet2020, October 12–13, 2021, Karlsruhe, Germany (2021).
- Mayordomo, N.; Rodriguez Hernandez, D. M.; Schild, D.; Rossberg, A.; Scheinost, A. C.; Brendler, V.; Müller, K.
Technetium retention by green rust chloride
Goldschmidt2021, July 04–09, 2021, Lyon, France (2021).
- Müller, S.; Ferrari, A.; Knodel, O.; Rachamin, R.
The Mu2e experiment at Fermilab
2021 spring meeting of German Physical Society (DPG), section "Particle Physics", March 15–19, 2021, Dortmund (virtual), Germany (2021).
- Müller, S.; Ferrari, A.; Knodel, O.; Rachamin, R.
Probing charged lepton flavor violation with the Mu2e experiment
DPG Meeting SMUK, August 30–September 03, 2021, Germany (2021).
- Neumann, J.; Brinkmann, H.; Britz, S.; Lützenkirchen, J.; Bok, F.; Stockmann, M.; Brendler, V.; Stumpf, T.; Schmidt, M.
f-element sorption onto K-feldspar – A comprehensive characterization of mechanism and thermodynamics
Goldschmidt 2021, July 04–09, 2021, Lyon, France (2021).
- Neumann, J.; Brinkmann, H.; Britz, S.; Lützenkirchen, J.; Bok, F.; Stockmann, M.; Brendler, V.; Stumpf, T.; Schmidt, M.
Umfassende Untersuchung und Bestimmung thermodynamischer Daten der Sorption von dreiwertigen Metallionen an K-Feldspat
Tage der Standortauswahl Freiberg 2021, February 11–12, 2021, Freiberg, Germany (2021).
- Neumann, J.; Lessing, J.; Demnitz, M.; Eng, P.; Stubbs, J.; Stumpf, T.; Schmidt, M.
Structural Investigation of the Adsorption von Y(III) on Orthoclase (001) Single Crystals using Resonant Surface X ray Diffraction
TransRet Workshop: Processes Influencing Radionuclide Transport and Retention, October 12–13, 2021, Karlsruhe, Germany (2021).
- Newman-Portela, A. M.; Krawczyk-Bärsch, E.; Lopez-Fernandez, M.; Bok, F.; Kassahun, A.; Raff, J.; Merroun, M. L.
Bioremediación de aguas contaminadas: Estudio multidisciplinar de la reducción microbiana de uranio (U) en aguas de mina
XXVIII Congreso Nacional de Microbiología (SEM21), June 28–July 02, 2021, Spain (2021).
- Newman-Portela, A. M.; Krawczyk-Bärsch, E.; Lopez-Fernandez, M.; Bok, F.; Kassahun, A.; Raff, J.; Merroun, M. L.
Design of U mine water bioremediation strategy through U(VI) bioreduction process: Multidisciplinary characterization
10th International Symposium on Biomining (Biomining '21), June 07–09, 2021, Falmouth, Cornwall, U.K. (2021).
- Newman-Portela, A. M.; Krawczyk-Bärsch, E.; Lopez-Fernandez, M.; Bok, F.; Kassahun, A.; Raff, J.; Merroun, M. L.
Multidisciplinary Characterization of Mine Water from a Former Uranium Mine for Bioremediation Purposes
Goldschmidt 2021, July 04–09, 2021, Lyon, France (2021).

- Raff, J.
Bioleaching of uranium ores - microbiology, technical processes and resulting challenges
57th Meeting of the Joint OECD/NEA-IAEA Uranium Group, November 03–05, 2021, Paris, France (2021).
- Rodriguez, D.; Mayordomo, N.; Brendler, V.; Müller, K.; Schild, D.; Stumpf, T.
Reductive immobilization of ⁹⁹Tc(VII) by different crystalline phases of iron sulfide (FeS₂)
Tage der Standortauswahl Freiberg 2021, February 11–12, 2021, Freiberg, Germany (2021).
- Roode-Gutzmer, Q. I.; Schymura, S.; Barkleit, A.; Stumpf, T.
Examining out-of-plane expansion of aggregate minerals in ion-irradiated concrete
9. Radiochemischer Analytik Workshop, June 08–09, 2021, Rossendorf, Germany (2021).
- Schabernack, J.; Fischer, C.
Impact of Surface Reactivity on the Simulation of Mineral Dissolution Rates
EGU General Assembly 2021 vEGU21: Gather Online, April 19–30, 2021, Vienna, Austria (2021).
- Scheinost, A. C.
Interfacial redox reactions, X-ray absorption spectroscopy, and how they can contribute to the safety of radioactive-waste repositories
Fundamental Understanding of radionuclide Retention (FUTURE), 3rd Annual Meeting, November 16–17, 2021, Villigen, Switzerland (2021).
- Stockmann, M.; Noseck, U.; Flügge, J.; Gehrke, A.; Brendler, V.
Smart Kd-concept as efficient approach to improve geochemistry in reactive transport modelling for repository safety assessment
Tage der Standortauswahl Freiberg 2021, February 11–12, 2021, Freiberg, Germany (2021).
- Tsushima, S.; Takao, K.
Selective binding of UO₂²⁺ by different peptide families
The International Chemical Congress of Pacific Basin Societies 2021 (PACIFICHEM 2021), December 16–21, 2021, Honolulu, Hawaii, U.S.A. (2021).
- Yuan, T.; Yang, Y.; Deissmann, G.; Fischer, C.
Analysis of heterogeneity and anisotropy of diffusivity in the sandy facies of Opalinus Clay host rocks using multi-scale digital rock physics
Goldschmidt 2021, July 04–09, 2021, Lyon, France (2021).

THESES

(Technische Universität Dresden, 2021, except where noted)

DOCTORAL THESES

- An, Y.
Hydrogen Isotope Transport and Separation via Two-dimensional and Layered Materials
- Gerber, E.
High-energy resolution X-ray spectroscopy of f-electron systems
Lomonosov Moscow State University (2021)
- Kloditz, R.
Theoretische Untersuchungen von Actinid-Komplexen mit organischen Liganden
- Lösch, H.
Spektroskopische Untersuchungen zur Komplexierung und zum Einbau von Actiniden: Uran(VI) Komplexierung mit gelösten Silikaten und Stabilität von Europium(III) Xenotim Solid Solutions
- Neumann, J.
Strukturelle Untersuchung der Rückhaltung von Actiniden und ihrer Übergangsmetallhomologe an ausgewählten Alumosilikat-Phasen
- Ramzan, M. S.
Electronic and Transport Properties of Novel Two Dimensional Materials
Jacobs University Bremen gGmbH (2021).
- Rybkin, I.
Development of methods for electrostatic immobilization and coupling of different microbial cells
Jozef Stefan Internationa Postgraduate School (2021).
- Radoske, T.
Komplexierungsverhalten tetravalenter Actinidkomplexe mit N₂O-Donorliganden aus der Klasse Schiff'scher Basen
- Rodriguez Hernandez, D. M.
Technetium environmental chemistry: Mechanisms for the surface-mediated reduction of Tc(VII)
- Springer, M.
Towards Topological Two-Dimensional Polymers

Wollenberg, A.

Bioassoziation und Transport von ausgewählten Radionukliden und ihren Analoga durch Basidiomyzeten

Wulf, T.

The role of adsorption strength and quantum confinement on the isotopologue selectivity of H₂ complexation

MASTER THESES

Blei, M.

Synthese und Charakterisierung vierwertiger Actinid-Komplexe mit (ONNO)-tetradentaten Liganden vom Salen-Typ

Opitz, L.

Interaction of Ln (Ce, Eu, Gd) and Cm with ZrO(OH)₂ and their incorporation into m-ZrO₂

Claus, G.

Selektion hochaffiner Peptide zur Bindung von f-Elementen und deren physikochemische Charakterisierung

TU Dresden / Internationales Hochschulinstitut (IHI) Zittau (2021).

Näder, A.

Computergestützte Studien der Elektronenstruktur von An(IV)-Amidinat-Systemen und Berechnung spektroskopisch relevanter Parameter

Lessing, J.

Strukturelle Untersuchungen der Rückhaltung dreiwertiger Actiniden (Am, Cm) und Seltenen Erden (Eu, Y) an synthetischem Ca-Feldspat (Retention of trivalent actinides (Am, Cm) and rare earth elements (Eu, Y) by synthetic Ca-feldspar)

Padberg, G.

Uranium carbonates removal by Layered Double Hydroxides

Lessing, R.

Untersuchung der Oberflächenladung von Quarz zur Betrachtung der Auflösungskinetik vor dem Hintergrund der Alkali-Kieselsäure-Reaktion (AKR)

Puhlmann, M.

Wechselwirkung von Desulfosporosinus sp. mit Europium als Beitrag zur Endlagerproblematik. Hochschule für Technik und Wirtschaft (HTW) Dresden (2021)

Klotzsche, M.

Einfluss von Ionophoren auf die Aufnahme von Lanthaniden in Tabak BY-2-Zellen (Influence of ionophores on the uptake of Eu(III) in tobacco BY-2 cells)

Urbank, Ch.

Synthese und Charakterisierung von Actinoid-Tetrel-Komplexen

Koch, T.

Die Abrasivität ausgewählter Reinigungsapplikationen an alterierten Natursteinen quantifiziert mittels Rauheitsparametern

Georg-August-Universität Göttingen (2021)

Waurick, L.

Berechnung des Einflusses von Halogensubstituenten auf die Elektronenstruktur von An(IV)-Salen-Komplexen

DIPLOMA THESIS

Fankhänel, T.

Nutzung von Liposomen zur Akkumulation und Separation von Lanthanoiden (Application of liposomes for the accumulation and separation of lanthanides)

BACHELOR THESIS

Balas, J.

Synthese und Charakterisierung von Uranyl-Komplexen mit Pyrrol-basierten Liganden

Bilke, M.-L.

Studien zu Aufnahmemechanismen von Europium(III) und Uran(VI) in Pflanzenzellen

Kahle, L.

Untersuchung von Abbauraten während der enzymatischen Hydrolyse von Polyethylenterephthalat
Universität Leipzig (2021)

Kühn, L.

Der mikrobielle Einfluss auf die Korrosion von Gusseisen unter endlagerrelevanten Bedingungen.
Hochschule Zittau/Görlitz (2021)

Lessing, R.

Untersuchung der Oberflächenladung von Quarz zur Betrachtung der Auflösungskinetik vor dem Hintergrund der Alkali-Kieselsäure-Reaktion (AKR)

Ramtke, J.

Untersuchung der Wechselwirkung von magnetotaktischen Bakterien mit Uran in wässrigen Systemen
Hochschule Zittau/Görlitz (2021)

SCIENTIFIC ACTIVITIES

○ WEBINARS

○ AWARDS

○ SEMINARS

○ TEACHING ACTIVITIES

Scientific Activities

○ CONTRIBUTIONS TO THE FRAMEWORK OF IAEA'S CPR2016: "IMPLEMENTING EXPLORATION TECHNIQUES FOR PALEOCHANNEL SANDSTONE-HOSTED URANIUM DEPOSITS AND FLUID-ROCK INTER- ACTION IN IN-SITU LEACHING PROCESSES"

The IAEA's objective is to promote and support the research, development and practical use of nuclear energy and its applications for peaceful purposes worldwide. To this end, and to network international research institutions, the IAEA conducts, among other things, so-called Coordinated Research Projects (CRP). Within the framework of CPR2016 "Implementing Exploration Techniques for Paleochannel Sandstone-Hosted Uranium Deposits and Fluid-Rock Interaction in In-Situ Leaching Processes", the Institute of Resource Ecology provided the following contributions this year:

- Presentation on the webinar
"Uranium Mining by *In situ* Leaching and Groundwater Remediation"
Organized by DLAMO, the World Nuclear University, School of Uranium Production, and IAEA.
May 31–June 04, 2021

Raff, J.
Bioleaching of sulphide ores and remediation – Methods and techniques

- Organization of the webinar
"Uranium Mining and Remediation"
Co-organized by HZDR, CSA Global, Mining Industry Consultants, and IAEA
October 12–14, 2021

Speakers of HZDR:

Drobot, B.
Spectroscopic methods for the determination of uranium speciation – Advanced methods

Raff, J.
Bioleaching of (uranium) ores and remediation – Theory, methods and techniques

Bio-remediation concepts for uranium contaminated sites and water

Sachs, S.
Natural occurring radioactive materials (NORM) – Overview and research activity

Steudtner, R.
Spectroscopic methods for the determination of uranium speciation – An introduction

○ AWARDS

Fichter, S.
Synthesis and Characterization of Tri- and Tetravalent Actinide Amidinates
HZDR
PhD Recognition Awards 2020

Kielar, C.
DNA-Origami nanostructures in biomedicine: Beyond drug delivery
Outstanding Thesis Prize 2020
Paderborn University

Kvashnina, K. O.
Admission to AcademiaNet (International Database for Excellent Researchers)
nominated by Swiss National Science Foundation (SNSF) for outstanding academic qualifications

Forbes Russia named Dr. K. Kvashnina under the Top 10 strong female scientists 2021

Schöne, S.
„Kids-mit-Grips“ experiments in the kindergarten „Hutbergstrolche“ in Dresden Weißig
HZDR
Award for Scientific Communication 2020

○ SEMINARS (TALKS OF VISITORS)

Tapio, Kosti

University of Jyväskylä, Finland

DNA as a multifunctional material

September 29 (2021)

Charlet, Laurent

University of Grenoble Alpes, France

Oxyanion behavior in the context of radwaste research

December 16 (2021)

○ TEACHING ACTIVITIES

(Winter term: WT; summer term: ST)

Lectures

Bok, F.

Friedrich-Schiller-Universität, Jena

ST 2021

Geochemische Modellierung mit Geochemist's Workbench®

Huittinen, N.

Technische Universität Dresden

ST 2021

Radioecology

Brendler, V.

Dresden University of Applied Sciences

ST 2021

Radiochemistry

Kuc, A. B.

Universität Leipzig

WT 2020/2021

Computational Chemistry of Solids

WT 2021/2022

Computational Spectroscopy

Fahmy, K.

Technische Universität Dresden

WT 2020/2021, WT 2021/2022

Molecular Biophysics: Concepts and Methods

ST 2021

Biological Thermodynamics

Lippold, H.

Universität Leipzig

ST 2021

Entstehung und Eigenschaften ionisierender Strahlung

WT 2020/2021, WT 2021/2022

Radioanalytik

Radiochemische Analysenmethoden

Fischer, C.

Universität Bremen

ST 2021

Diagenese

Universität Leipzig

WT 2020/2021, WT 2021/2022

Moderne Methoden in der Materialwissenschaft

Raff, J.

Dresden University of Applied Sciences

WT 2020/2021, WT 2021/2022

Mikrobiologie

Technische Universität Dresden

WT 2020/2021, WT 2021/2022

Mikrobielle Laugung

Heine, T.

Technische Universität Dresden

WT 2020/2021, WT 2021/2022

PC II (Theorie der Chemischen Bindung)

PC III (Einführung in die Computerchemie)

Theoretische Chemie

Computational Spectroscopy

WT 2020/2021

Quantum Chemistry

Schmidt, M.

Technische Universität Dresden

ST 2021

Chemistry of the f-elements

Yonsei University Seoul, Korea

ST 2021

Artificial Intelligence and Machine Learning

Schymura, S.

Universität Leipzig

WT 2020/2021, WT 2021/2022

Radioanalytik

Stumpf, T.

Technische Universität Dresden

WT 2020/2021, WT 2021/2022

Radiochemistry

Courses

☞ The laboratory course “Radiochemistry” was provided from August 23–September 03, 2021, as a part of a module of the chemistry master degree program at the Technische Universität Dresden.

Advisers:

Bezzina, J.	Jordan, N.
Butscher, D.	Kaden, P.
Demnitz, M.	Mayordomo Herranz, N.
Dornbusch, D.	Neumann, J.
Duckworth, T.	Patzschke, M.
Hilpmann, S.	Rodriguez Hernandez, D. M.
Hong, Boseok	Sieber, C.
Jessat, I.	Sushko, V.
Jessat, J.	Zimmermann, T.
John, W.	

☞ Biophysics course of the Dresden-International-Graduate School (WT 2020/2021 & WT 2021/2022).

Advisers:

Fahmy, K.	Oertel, J.	Philipp, J.
-----------	------------	-------------

☞ Courses and seminars were held referring to the following lectures:

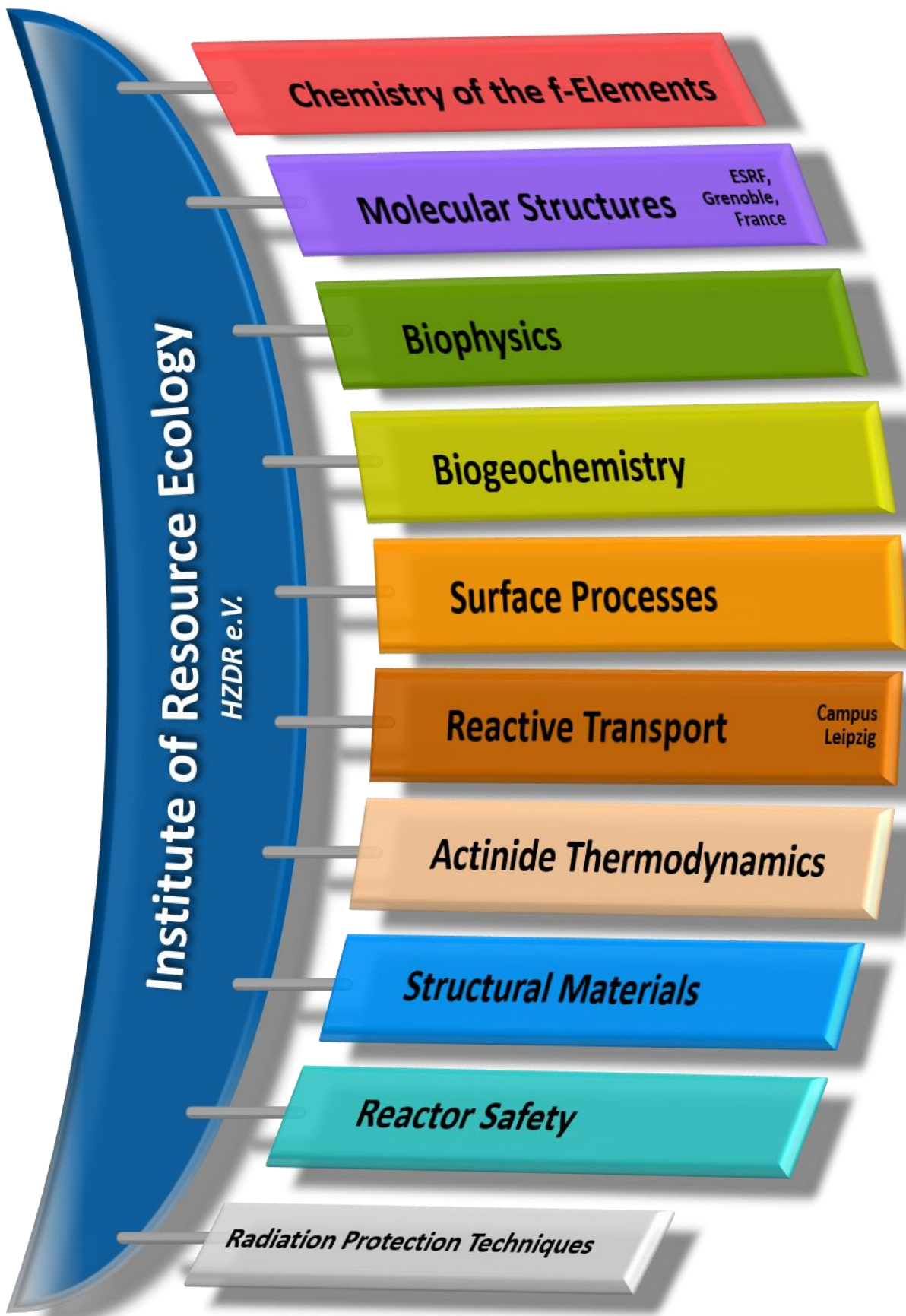
Fahmy, K.
Technische Universität Dresden,
 WT 2020/2021
Biophysics course of the Dresden-International-Graduate School

Faria Oliveira, A.
Technische Universität Dresden,
 WT 2020/2021
Spektroskopie mit dem Computer
 WT 2021/2022
Theorie der chemischen Bindung

Kuc, A. B.
Universität Leipzig,
 WT 2020/2021
Spektroskopie (PC)
 WT 2020/2021
Computational Chemistry for Solids
 WT 2021/2022
Computational Spektroskopie

Springer, M.
Technische Universität Dresden,
 WT 2020/2021, WT 2021/2022
Theorie der chemischen Bindung

PERSONNEL



HEAD OF INSTITUTE: Prof. Dr. Thorsten Stumpf

ADMINISTRATION:

Office Dresden: Gorzitze, Jana; Theunert, Bettina;
Kovacs, Jenny; Kunde, Kerstin; Rott, Sonja
Office Leipzig: Gerstner, Katrin; Meinken, Roswitha; Pedrosa Gil, Nadja

PROJECT COORDINATION:

Dr. Arnold, Thuro

RADIATION PROTECTION:

Bachmann, Stefanie; Dräger, Eric; Eisold, Silke; Falkenberg, Dirk;
Henke, Stefan; Jimenez Hernandez, Susana; Nebe, Kathrin
Sysad (IT): Berndt, Konny

ACTINIDE THERMODYNAMICS

PROF. DR. BRENDLER, VINZENZ

Dr. Abbasova, Dinara
Dr. Bok, Frank
Dr. Brinkmann, Hannes
Fankhänel, Tobias*
Dr. Kretschmar, Jérôme
Dr. Richter, Anke
Dr. Pospiech, Solveig
Dr. Schierz, Arlette
Dr. Schneide, Katja
Shams Aldin Azzam, Salim
Sieber, Claudia*

Dr. Stockmann, Madlen
Zechel, Susanne

ANALYTICS
Dr. Foerstendorf, Harald
Beutner, Sabina
Eckardt, Carola
Goldbach, Dominik
Heim, Karsten
Schöne, Sylvia

BIOGEOCHEMISTRY

DR. RAFF, JOHANNES

Bertheau, Rahel
Dressler, Magdalena*
Dr. Drobot, Björn
Flemming, Katrin
Dr. Günther, Alix
Jesat, Jenny*
Dr. John, Warren
Klotzsche, Max*
Dr. Krawczyk-Bärsch, Evelyn
Dr. Mandel, Poulami
Dr. Moll, Henry
Dr. Sachs, Susanne

Seibt, Jana
Dr. Stalke, Sebastian
Dr. Steudtner, Robin

MICRONUT
Dr. Cherkouk, Andrea
Hilpmann, Stephan*
Klüge, Sindy
Dr. Lopez-Fernandez, Margarita
Dr. Matschavelli, Nicole
Sushko, Vladyslav*
Dr. Wei, Ting-Shyang

BIOPHYSICS

PROF. DR. FAHMY, KARIM

Dornbusch, Daniel*
Dr. Kietlar, Charlotte
Nucke, Lisa*
Dr. Oertel, Jana

Philipp, Jenny
Prof. Dr. Tsushima, Satoru
Subramanian, Madhunarai*

REACTIVE TRANSPORT

PDDR. FISCHER, CORNELIUS

Becker, Alexandra*
Bollermann, Till*
CardenasRivera, MariaAlgardia*
Dr. Franke, Karsten
Grubne, Stefan
Dr. Kulenkampff, Johannes
Dr. Lippold, Holger
Lösel, Dagmar
Dr. Mansel, Alexander
Raj, Abhishek*
PROF. DR. HEINE, THOMAS, Chair Theor. Chem.- TU Dresden/
PDDR. KUC, AGNIESZKA BEATA

Campus Leipzig

Schabernack, Jonas*
Schößler, Claudia
Dr. Yuan, Tao
Zhou, Wenyu

NANOSAFETY
Dr. Schymura, Stefan
Rybkin, Jaroslav*
Uygan, Serisha Sinala Su*

CHEMISTRY OF THE F-ELEMENTS

PDDR. SCHMIDT, MORITZ

Dr. Bezina, James P.
Dr. Gericke, Robert
Dr. Kaden, Peter
Dr. Neumann, Julia
Dr. Patzschke, Michael
Ramakrishnan, Sreerivas
Dr. Taylor, Corey

METAL ORGANIC ACTINIDE CHEMISTRY
Dr. März, Juliane
Dr. Bansal, Deepak
Duckworth, Tamara*
Dr. Fichter, Sebastian
Hong, Boeok*
Köhler, Luisa*

MOLECULAR STRUCTURES

DR. HABIL. SCHEINOST, ANDREAS C.

Dr. Baumann, Nils
Dr. Estevanon, Paul
Exner, Jörg
Dr. De Bona, Emanuelle
Dr. Faria Oliveira, Augusto
Dr. Hennig, Christoph
Naudet, Damien
Dr. Prieur, Damien
Dr. Rossberg, André

ESRF, Grenoble

Dr. Svilyk, Volodymyr
Zimmermann, Thomas*

ERC GRANT:
Dr. Kravshina, Kristina O.
Dr. Amidani, Lucia
Dr. Bauters, Stephen
Dr. Bazarkina, Elena
Galenzew, Juri

REACTIVE TRANSPORT

PDDR. FISCHER, CORNELIUS

Becker, Alexandra*
Bollermann, Till*
CardenasRivera, MariaAlgardia*
Dr. Franke, Karsten
Grubne, Stefan
Dr. Kulenkampff, Johannes
Dr. Lippold, Holger
Lösel, Dagmar
Dr. Mansel, Alexander
Raj, Abhishek*
PROF. DR. HEINE, THOMAS, Chair Theor. Chem.- TU Dresden/
PDDR. KUC, AGNIESZKA BEATA

Campus Leipzig

Schabernack, Jonas*
Schößler, Claudia
Dr. Yuan, Tao
Zhou, Wenyu

NANOSAFETY
Dr. Schymura, Stefan
Rybkin, Jaroslav*
Uygan, Serisha Sinala Su*

REACTOR SAFETY

DR. KIEM, SÖREN

Berger, Torsten
Dr. Baier, Silvio
Bastrakova, Kseniia*
Dr. Bilodid, Yurii
Di Nora, Vincenzo
Diaz, Pescador Eduard*
Dr. Fridman, Emil
Gommlich, André
Dr. Grahm, Alexander

Jobst, Matthias
Konheiser, Jörg
Dr. Nikitin, Evgeny
Dr. Pöritz, Erik
Dr. Ponomarev, Alexander
Dr. Rachamin, Reuven
Dr. Schäfer, Frank
Yadav, Pratibha*

STRUCTURAL MATERIALS

DR. ALTSTADT, EBERHARD

Dr. Bergner, Frank
Dr. Brandenburg, Jann-Erik
Dr. Chekonnin, Paul
Engelmann, Hans-Jürgen
Houska, Mario
Dr. Kaden, Cornelia
Dr. Kapoor, Garima

Lai, Libang*
Pletsch, Jens
Röbner, Michaela
Dr. Ulbricht, Andreas
Dr. Vogel, Karin
Webersinke, Wolfgang
Welz, Tilo

SURFACE PROCESSES

DR. MÜLLER, KATHARINA

Butscher, Daniel*
Chlupka, Althe
Demnitz, Maximilian*
Dietze, Alexandra
Friedrich, Sebastian*
Jesat, Isabelle*
Dr. Jordan, Norbert
Dr. Mayordomo Herranz, Natalia
Müller, Christa
Dr. Rodríguez Hernandez, Diana M.

Weiss, Stephan

INCORPORATION INTO SOLID PHASES
Dr. Hattinen, Nina
Dr. Barkleit, Astrid
Braga Ferreira dos Santos, Luzia*
Dr. Gilson, Sara
Roode-Gutzmer, Quirina
Dr. Yassin, Ghada

*: Ph.D. student (as of 2021/12/31)

GUEST SCIENTISTS

Brumme, Thomas	<i>Technische Universität Dresden, Germany</i>
Das, Aniruddh	<i>Technische Universität Dresden, Germany</i>
Dykas, Jakob	<i>Technische Universität Dresden, Germany</i>
Heller, Anne	<i>Technische Universität Dresden, Germany</i>
Kai, Lyu	<i>Chinese Science Council</i>
Reinke, Vanessa	<i>Technische Universität Dresden, Germany</i>
Richter, Tony	<i>Technische Universität Dresden, Germany</i>
Romanchuk, Anna	<i>Moscow State University, Russia</i>
Sayed, Ahmed M. T.	<i>Technische Universität Dresden, Germany</i>
Vogel, Manja	<i>HZDR Innovation GmbH</i>

CO-FUNDED PH.D. STUDENTS

An, Yun	<i>University of Leipzig, Germany / China Scholarship Council, Beijing, China</i>
Asghar, Umm-e-hani	<i>Jacobs University Bremen gGmbH, Germany</i>
Gerber, Evgeny	<i>Lomonosov Moscow State University, Moscow, Russia</i>
He, Yihua	<i>Laboratoire de physique subatomique et des technologies associées (Subatech), Nantes, France</i>
Kempt, Roman	<i>Technische Universität Dresden, Germany</i>
Kirsch, Klemens	<i>Bundesanstalt für Materialforschung und -prüfung (BAM), Berlin, Germany</i>
Newman Portela, Antonio	<i>UGR Granada, Spain</i>
Wöhner, Kevin	<i>Universität Leipzig, Germany</i>

MASTER/DIPLOMA/BACHELOR

Balas, Johannes	Hadlich, Christoph	Näder, Adrian	Urbank, Christian
Blei, Magdalena	Kühn, Luise	Opitz, Lucas	Waurick, Lukas
Bilke, Marie-Louise	Lessing, Jessica	Padberg, Gero	
Cariven, Claire	Lessing, Richard	Puhlmann, Michael	
Claus, Gerda	Mphirime, Moipone Doreen	Ramtke, Justus	

GRADUATE ASSISTANTS, STUDENT ASSISTANTS, TRAINEES

Brokemper, Jan	Kola, Naga Suresh	Michak, Marvin Lukas	Weiske, Hendrik
Huang, Yun-Hsuan	Lambert, Mara Harriet	Stricker, Alexandra	
Jeschke, Isabelle	Lessing, Richard	Uhlitzsch, Lucie	

ACKNOWLEDGEMENTS

The Institute of Resource Ecology is one of the eight institutes of the Helmholtz-Zentrum Dresden–Rossendorf e.V. (HZDR). As registered, non-profit institution, the HZDR is supported by the authorities of the Federal Government and the Free State of Saxony. In addition to the basic funding, the financial support of the projects listed below by the given organizations and companies is gratefully acknowledged.

FUNDING ORGANIZATION / COMPANY	PROJECT TITLE	CONTRACT NO. (if applicable)
Commission of the European Communities (EU)	COMET – Two dimensional lattices of covalent- and metal-organic frameworks for the Quantum Hall resistance standard	20FUN03
	ENTENTE – European Database for Multiscale Modelling of Radiation Damage	H2020-900018
	ESFR-SMART – European SFR – Safety Measures Assessment and Research Tools	H2020-754501
	EURAD – European Joint Programme on Radioactive Waste Management ConCorD, CORI, DONUT, FUTURE T2 + T3, MAGIC, SFC, UMAN, KMSoK	H2020-847593
	FRACTESUS – Fracture mechanics testing of irradiated RPV steels by means of sub-sized specimens	H2020-900014
	INSIDER – Improved Nuclear Site characterization for waste minimization in DD operations under constrained Environment	H2020-755554
	M4F – Multiscale Modeling for Fusion and Fission Materials	H2020-755039
	McSAFER – High-Performance Advanced Methods and Experimental Investigations for the Safety Evaluation of Generic Small Modular Reactors	H2020-945063
	R2CA: Reduction of Radiological Consequences of Design Basis and Design Extension Accidents	H2020-847656
	RadoNorm – Towards effective radiation protection based on improved scientific evidence and social considerations – focus on radon and NORM + RadoNorm Open Call Grant	H2020-900009
	Sol2H2 – Computational Design of Materials for Photocatalytic Hydrogen Generation and Separation	H2020-101031846
	STRUMAT-LTO – STRUctural MATerials research for safe Long Term Operation of LWR NPPs	H2020-945272
	SurfBio – Innovation hub for surface and colloid biology research	H2020-952379
	TOP – ERC Starting Grant – Towards the Bottom of the Periodic Table	H2020-759696
Federal Ministry for Economic Affairs and Climate Action (BMWK) & Federal Ministry of Education and Research (BMBF)	AcE – Grundlegende Untersuchungen zur Immobilisierung von Actiniden mittels Einbau in endlagerrelevante Festphasen	02NUK060A
	EMPRADO – Entwicklung einer Methode zur Pre-Aktivitäts- und Dosisleistungsberechnung von reaktornahen Bauteilen auf Basis von Neutronenflussverteilungen Berechnung der Neutronenflussverteilung in reaktornahen Bauteilen und deren Validierung an Experimenten als Basis der Aktivitätsrechnungen	15S9409A
	f-Char – Verbundprojekt – Spektroskopische Charakterisierung von f-Element-Komplexen mit soft donor-Liganden	02NUK059B

FUNDING ORGANIZATION / COMPANY	PROJECT TITLE	CONTRACT NO. (if applicable)
	FENABIUM – Struktur-Wirkungsbeziehungen zwischen f-Elementen und organischen Ligandsystemen mit Naturstoff-basierten Bindungsfunktionen in Hinblick auf eine mögliche Mobilisierung in der Umwelt	02NUK046B
	GRaZ II – Verbundvorhaben Geochemische Radionuklidrückhaltung an Zementalterationsphasen	02E11860B
	iCross – BMBF Verbundprojekt iCross Integrität von Endlagersystemen für radioactive Abfälle – Skalenübergreifendes Systemverständnis	02NUK053B
	KRIMI Verbundprojekt Kinetik der Radionuklidimmobilisierung MgO-S3 Spritzbeton für Streckenverschlüsse für HAW-Endlager im Steinsalz	02NUK056C 02E11769B
	PANAS – Verbundvorhaben Untersuchungen zu passiven Nachzerfallswärme-Abfuhrsystemen; Teilprojekt B: Untersuchungen zu Kondensationsprozessen im Notkondensator und numerische Simulation einer passiven Wärmeabfuhrkette	02NUK041B
	PepTight – Lasst die Biologie ran – Peptide umgarnen entscheidende Rohstoffe: die "natürliche" Trennung von Lanthaniden, Teilprojekt A	031B1122A
	RADEKOR – Verbundprojekt Speziation und Transfer von Radionukliden im Menschen unter besonderer Berücksichtigung von Dekorporationsmitteln	02NUK057A
	RENA – Biologische Radionuklidentfernung durch Nutzung natürlicher Assoziationsprozesse, Teilprojekt A	02NUK066A
	ResKin_Move – Geschwindigkeitsfeld-Analyse mit Positronen-Emissions-Tomografie (PET): Parametrisierung und Validierung von Transportmodellen (Plug-Skala)	03G0900A
	SMILE – Smart-K _d in der Langzeitsicherheitsanalyse – Anwendungen, Teilprojekt B	02E11668B
	STROEFUN III – Strömungstechnischer Funktionsnachweis für Verschlussbauwerke und flüssigkeitsgestützte Abdichtung des Kontaktbereiches Phase III: Vertiefung Kenntnisstand Kontaktbereich & Injektionsmittel, <i>in situ</i> -Versuche	02E11748B
	TRANS-LARA – Verbundprojekt Transport- und Transferverhalten langlebiger Radionuklide entlang der kausalen Kette Grundwasser-Boden-Oberfläche-Pflanze unter Berücksichtigung langfristiger klimatischer Veränderungen, Teilprojekt B	02NUK051B
	TransForm – Transnationale Forschungsinfrastruktur und multidisziplinäre akademische Nachwuchsförderung	01DT20004
	ULTRASENS – Ultrasensitiver spektraler Sensor zur indirekten Messung ionisierender Strahlung	03THWSN004
	UMB II – Umwandlungsmechanismen in Betonitbarrieren II	02E11870B

FUNDING ORGANIZATION / COMPANY	PROJECT TITLE	CONTRACT NO. (if applicable)
	VESPA II – Verbundprojekt Verhalten langlebiger Spalt- und Aktivierungsprodukte im Nahfeld eines Endlagers und Möglichkeiten ihrer Rückhaltung	02E11607B
	WERREBA – Wege zum effizienten Rückbau von Reaktorkomponenten und Betonabschirmung: Berechnung des Aktivitätsinventars und deren Validierung an Bohrkernen sowie Mobilitätsuntersuchungen von Radionukliden	15S9412
	WTZ-Granit – Vorhersage der heterogenen Radionuklidsorption auf Kluff- und Störungsflächen in granitischen Gesteinen: Parametrisierung und Validierung verbesserter reaktiver Transportmodelle	02E11911A
Deutsche Forschungsgemeinschaft (DFG, German Research Foundation)	DFG-Programmpauschalen ab 2014 – Verwaltung von 25 % der ab 2014 zu den DFG-Projekten bewilligten Programmpauschalen	
	DNA-Struktur Molekulare Mechanismen der Interaktion chaotroper Salze mit natürlichen und künstlichen DNA-Strukturen	FA 248/8-1
	Graduiertenkolleg „Wasserstoff-Isotope 1,2,3H“	GRK 2721/1
	SFB 1415 – Sonderforschungsbereich 1415 „Chemie der synthetischen zweidimensionalen Materialien“	SFB 1415/1 2020
Deutscher Akademischer Austauschdienst (DAAD, German Academic Exchange Service)	DAAD PPP Frankreich 2020–2021 – Programm des projektbezogenen Personenaustausches mit Frankreich 2020–2021	57512305
Framatome, SAS	DYN3D Support Service Framatome	
Bundesgesellschaft für Endlagerung mbH (BGE)	THEREDA IV	
Helmholtz-Gemeinschaft Deutscher Forschungszentren e.V. (HGF, Helmholtz Association)	HEP CROSSING – Crossing borders and scales – an interdisciplinary approach	PIE-0007
	Exzellenznetzwerk-Phase 3 "Physics of Life – The Dynamic Organization of Living Matter"	ExNet-0029-Phase2-3
	LiqCounter – New Liquid Scintillation Counter	HE-2021-06-FSF
	NUSAFE / iCross	SO-093
HZDR Innovation GmbH	Extract	
Hochschule für Technik und Wirtschaft (HTW, University of Applied Science), Dresden	Altstahl – bruchmechanische Prüfung im Rahmen eines Forschungsprojektes der HTW	
PreussenElektra GmbH	Berechnung hochaufgelöste Neutronenspektren an ausgesuchten Positionen des Reaktordruck-behälters und der daraus resultierenden Aktivitäten	4500355585
	Gekoppelte Dyn3D/Athlet-Analysen	4500355625/PME/0701
	Monitoring – Rekursive Berechnung von Neutronenfeldern in Räumen außerhalb der biologischen Abschirmung	4500353697
	Strömungseffekte	4500351063

FUNDING ORGANIZATION / COMPANY	PROJECT TITLE	CONTRACT NO. (if applicable)
South African Medical Research Council (SAMRC), Cape Town, South Africa	Haarproben – Analyse von Uran in einzelnen Haarproben von Kindern, die in der Nähe von Minenhalden in Südafrika leben	
TÜV NORD	Prüfung geologischer Fragen Konsultation	<i>M.ASS.06.015.01.F70</i>
TÜV SÜD	DYN3D Wartung TÜV S 2020/2021– FWOR TÜV VVER 1200 code 1 – Support and consulting services WWER AP03	<i>500603389</i>
ÚJV Řež, a.s., Czech Republic	DYN3D für UJV Wartung 2020/2021, 2021/2022	<i>VT1100028</i>

INDEX OF AUTHORS

AUTHOR.....	PAGE
Alibert, M.	23
Aloin, C.	23
Altstadt, E.	80
Amidani, L.	25
Baeyens, B.	43
Balas, J.	17
Baranowski, M.	28
Barkleit, A.	85, 87
Barnouin, L.	23
Bazarkina, E. F.	24
Bergner, F.	82, 83, 84
Bezzina, J.	47
Bilodid, Y.	76
Blei, M. K.	16
Bok, F.	18, 43, 47, 49, 54
Bollermann, T.	38
Brendler, V.	18, 41, 43, 47, 50
Brinkmann, H.	44
Bukaemskiy, A. A.	53
Butorin, S. M.	26
Caprani, R.	23
Čeh, M.	69
Chekhonin, P.	38, 80, 81, 83, 84
Clavier, N.	23
Cologna, M.	22
Dardenne, K.	27
Das, A.	80
Daumann, L. J.	66
De Bona, E.	22
Demnitz, M.	42
Den Auwer, C.	67
Desagulier, M.-M.	27
Di Nora, V. A.	76
Diaz-Pescador, E.	77, 78
dos Santos, L. B. F.	52
Drev, S.	70
Drobot, B.	59, 62, 63, 65, 66, 68
Dyksik, M.	28
Eng, P. J.	44
Epifano, E.	27
Fahmy, K.	64
Fankhänel, T.	63, 65
Findeisen, S.	19
Finzel, K.	28
Fischer, C.	35, 37, 38, 40
Foerstendorf, H.	45, 51
Franke, K.	70
Fridman, E.	75, 76
Fritsch, K.	43
Gabriel, G.	23
Gehrke, A.	36
Gericke, R.	29
German, S.	69

AUTHOR.....	PAGE
Gilson, S. E.	53
Gorin, D.	69
Grahn, A.	77
Grossmann, K.	71
Gruhne, S.	39
Gu, Z.-G.	31
Guéneau, C.	27
Heine, T.	30, 31
Heinemann, F. W.	13
Henkes, M. K.	53
Hennig, C.	19, 20, 22, 52
Hübner, R.	57
Huittinen, N.	15, 21, 52, 53
Jessat, I.	15, 45
Jessat, J.	57
John, W. A.	57, 61
Jordan, N.	15, 45, 51
Kaden, C.	83, 84
Kaden, P.	14
Kamminga, M.	28
Kapoor, G.	83
Karpinska, M.	28
Kassahun, A.	62
Kempt, R.	28, 30
Kestel, B.	13
Kielar, C.	64
Kliem, S.	78
Kloditz, R.	14
Kłopotowski, Ł.	28
Knodlseder, C.	28
Koblar, M.	69
Köhler, L.	17
Konheiser, J.	79, 86, 87
Kovalska, E.	30
Krawczyk-Bärsch, E.	59, 62
Kretzschmar, J.	18
Kuc, A.	28, 30, 31
Kulenkampff, J.	39
Kvashnina, K. O.	16, 24, 25, 26
Lai, L.	81
Lanikova, A.	68
Lapanje, A.	69, 70
Lebreton, F.	23
Lederer, F.	68
Lee, S. S.	44
Lessing, J.	47
Lessing, R.	88
Liang, M.	28
Lippold, H.	40
Lopez-Fernandez, M.	62
Lösel, D.	39
Lu, R.	36
Lützenkirchen, J.	47
Luxa, J.	30

AUTHOR.....	PAGE
Mansel, A.	70
Marques Fernandes, M.	43
Martin, P.	23
Martin, P. M.	25, 27
Martinez, J.	23
März, J.	16, 17
Matschi, S.	61
Maude, D. K.	28
Mayordomo, N.	46, 48, 50
Merroun, M. L.	62
Meyer, K.	13
Miehlich, M. E.	13
Miollan, O.	23
Moll, H.	58
Molodtsov, K.	38
Moog, H. C.	54
Müller, K.	18, 42, 43, 46, 50
Murphy, G. L.	53
Nebelung, C.	43
Neumann, J.	42, 44, 47
Neuville, D. R.	27
Newman-Portela, A. M.	62
Nikitin, E.	75, 76
Nucke, L.	65
Obermeier, F.	80
Oertel, J.	64
Opitz, L.	21
Padberg, G.	46
Patzschke, M.	13, 16, 68
Picard, L.	23
Pinyaev, S.	69
Pividori, D.	13
Plochocka, P.	28
Podlipec, R.	70
Poenitz, E.	86
Ponomarev, A.	75
Popa, K.	22, 25
Pospiech, S.	41
Prieur, D.	22, 23, 27, 57
Pyataev, N.	69
Rachamin, R.	79
Raff, J.	59, 62, 63
Rajabi, F.	60
Ramtke, J.	59
Réal, F.	15
Reese, S.	14
Retegan, M.	25
Richter, A.	54
Rijavec, T.	70
Rodriguez, D. M.	46, 50
Roode-Gutzmer, Q. I.	87, 88
Rossberg, A.	18, 48, 49, 57
Rothe, J.	27
Rybkin, I.	69, 70

AUTHOR.....	PAGE
Sachs, S.	57, 58, 60, 61
Schäfer, F.	78
Scheinost, A. C.	22, 49
Scheurer, A.	13
Schmeide, K.	18, 43, 49
Schmidt, M.	14, 17, 38, 42, 44, 47, 58
Schönberger, N.	68
Schymura, S.	38, 42, 70
Sevilla, J.-R.	23
Shams Aldin Azzam, S.	49
Signoret, P.	23
Sindeeva, O.	69
Singer, H.	66
Sofer, Z.	30
Sonnendecker, C.	40
Stalke, S.	71
Starke, S.	15
Staudtner, R.	18, 43, 59, 63, 65, 66, 71
Stockmann, M.	36, 43
Strok, M.	70
Stubbs, J. E.	44
Stumpf, T.	17, 38, 43, 44, 47
Subramanian, M.	64
Sukhorukov, G.	69
Svitlyk, V.	19, 20, 52
Taylor, C. J.	14, 68
Tian, Y.-B.	31
Tsushima, S.	18, 64, 67
Ulbricht, A.	82
Uygan, S. S. S.	70
Vallet, V.	15
Vankova, N.	31
Vogel, K.	83, 84
Vogel, M.	63
Volkova, A.	25
Wagler, J.	29
Walter, O.	22
Waurick, L. K.	16
Weidler, P.	31
Weiss, S.	20, 49
Wöll, C.	31
Wu, B.	30
Yassin, G.	85
Ye, J.	28
Yuan, T.	37, 38
Zechel, S.	54
Zeymer, C.	66
Zhang, J.	31
Zhang, N.	28
Zidek, L.	68
Zurita, C.	67



Institute of Resource Ecology
Bautzner Landstrasse 400
01328 Dresden/Germany
Phone +49 351 260-3210
Fax +49 351 260-3553
Email contact.resourceecology@hzdr.de
<http://www.hzdr.de>

Member of the Helmholtz Association